Rational Design of Novel Irreversible Inhibitors for Human Arginase and Applications of
Nanoparticles for Catalytic Reactions

by

Xuefeng Guo

B. S., University of Science and Technology of China, China, 2014

M. A., Brown University, 2018

A dissertation submitted in partial fulfillment of the

requirements for the Degree of Doctor of Philosophy

in the Department of Chemistry at Brown University

Providence, Rhode Island

May 2019

This dissertation by Xuefeng Guo is accepted in its present form by
the Department of Chemistry as satisfying the dissertation requirement
for the degree of Doctor of Philosophy.

Date _____   _____
                                          Dr. Christopher T. Seto, Advisor

                         Recommended to the Graduate Council

Date _____   _____
                                             Dr. Amit Basu, Reader

Date _____   _____
                                           Dr. Shouheng Sun, Reader

                          Approved by the Graduate Council

Date _____   _____
                                          Dr. Andrew G. Campbell
                                          Dean of the Graduate School

Curriculum Vitae

Xuefeng Guo was born in Shenyang, China, in 1991. He attended the University of Science and Technology of China in 2010, where he obtained a Bachelor of Science degree in Chemistry with a thesis on "An efficient synthesis of amides from alcohols and azides catalyzed by a bifunctional catalyst Au/DNA under mild conditions". Upon completion of his Bachelors degree in 2014, Xuefeng began graduate studies in the Department of Chemistry at Brown University under the supervision of Prof. Christopher T. Seto. His research focused on rational design of arginase inhibitors and applications of nanoparticles for catalytic reactions. During his time at Brown University, Xuefeng has co-authored the following publications:

[1] Guo, X.; Chen, Y.; Seto, C. T. Rational design of novel irreversible inhibitors for human arginase. *Bioorganic & medicinal chemistry*, **2018**, *26*, 3939–3946.

[2] Guo, X.; Yu, C.; Yin, Z.; Sun, S.; Seto, C. T. Hydrodehalogenation of polyhalogenated aromatics catalyzed by NiPd nanoparticles supported on nitrogen-doped graphene. *ChemSusChem*, **2018**, *11*, 1617–1620.

[3] Yu, C.; Guo, X.; Xi, Z.; Muzzio, M.; Yin, Z.; Shen, B. et al. AgPd nanoparticles deposited on $WO_{2.72}$ nanorods as an efficient catalyst for one-Pot conversion of nitrophenol/nitroacetophenone into benzoxazole/quinazoline. *Journal of the American Chemical Society*, **2017**, *139*, 5712–5715.

[4] Yu, C.; Guo, X.; Shen, M.; Shen, B.; Muzzio, M.; Yin, Z. et al. Maximizing the catalytic activity of nanoparticles through monolayer assembly on nitrogen-doped graphene.

Angewandte Chemie International Edition, **2018**, *57*, 451–455.

[5] Yu, C.; Guo, X.; Shen, B.; Xi, Z.; Li, Q.; Yin, Z. et al. One-pot formic acid dehy-drogenation and synthesis of benzene-fused heterocycles over reusable $AgPd/WO_{2.72}$ nanocatalyst. *Journal of Materials Chemistry A*, **2018**, *6*, 23766–23772.

[6] Yu, C.; Guo, X.; Muzzio, M.; Seto, C. T.; Sun, S. Self-assembly of nanoparticles into two-dimensional arrays for catalytic applications. *ChemPhysChem*, **2019**, *20*, 23–30.

Acknowledgements

I would like to express my gratitude to my advisor, Prof. Christopher T. Seto, for his support, patience, and encouragement throughout my graduate studies. I am fortunate to have such an amazing advisor who let me explore freely on my own ideas, and at the same time guided me when I encounter difficulties. He taught me to have confidence in my work and to pay attention to the smallest details in research. I am enormously grateful for all that he has done for me, and I could not have imagined having a better advisor for my Ph.D study.

Besides my advisor, I would like to thank my committee members: Prof. Amit Basu, Prof. Jason Sello and Prof. Shouheng Sun, for their encouragement, insightful comments, and guidance during my graduate studies. During the collaboration between Seto and Sun's group in developing new catalytic reactions, I learnt a great deal about nanocatalyst synthesis and characterization from Prof. Sun, and he always inspired me to think about problem from another angle.

Great thanks to the lab members in Seto and Sun lab: Dr. Yiming Chen, Dr. Chao Yu, Dr. Zheng Xi, Dr. Bo Shen, Junrui Li, Zhouyang Yin, Michelle Muzzio, Mengqi Shen, Honghong lin and Joshua Dunn. Without their help, I could not finish my research projects. I also want to thank Dr. Tun-Li Shen for his help and instructions on the mass spectrometry.

Finally, I want to thank my dear parents for their love and support throughout my life. Thank you for encouraging me in all of my pursuits and inspiring me to follow my dreams.

Contents

List of Schemes

List of Figures

List of Tables

Chapter 1

Introduction of Arginase and Activity-Based Probes

1.1 Arginase

Arginase is a manganese-dependent metalloenzyme that catalyzes the hydrolysis of L-arginine to form L-ornithine and urea.[1] In mammals, there are two isoenzymes: arginase I and arginase II. They catalyze the same chemical reaction but differ in cellular location. Arginase I is expressed in the liver, and constitutes the final step of urea biogenesis. Arginase II is expressed in mitochondria and is located in a variety of tissues such as red blood cells, glands and kidneys. The main function of arginase II is to produce ornithine, which is a biosynthetic precursor to proline and polyamines.

In humans, the two isozymes are encoded by separate genes. Human arginase I contains 322 amino acids while human arginase II contains 354.[2] The two isoforms share 60% homology, have almost identical structures and have similar mechanisms of action.[3] Both are trimers and require two manganese atoms in order to function (Figure 1.1). As Shown in Figure 1.2, the active site holds arginine in place via hydrogen bonding between the guanidinium group of Arg and the side chain of Glu 277. Nucleophilic attack by a metal-associated hydroxide ion on the guanidinium group leads to a tetrahedral intermediate, which is stabilized by hydrogen bonding with Asp 128 and Glu 277. Breakdown of the tetrahedral intermediate through proton transfer generates urea and ornithine as products.
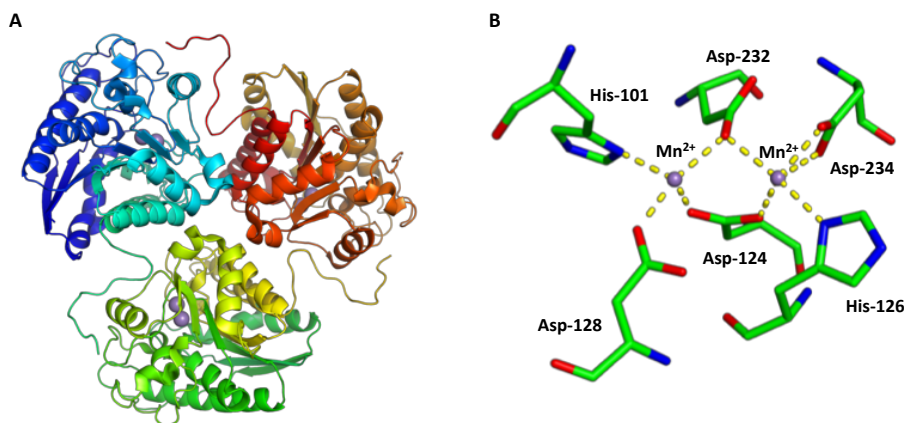
Figure 1.1 Arginase trimer structure and binuclear manganese cluster (pdb 2aeb).
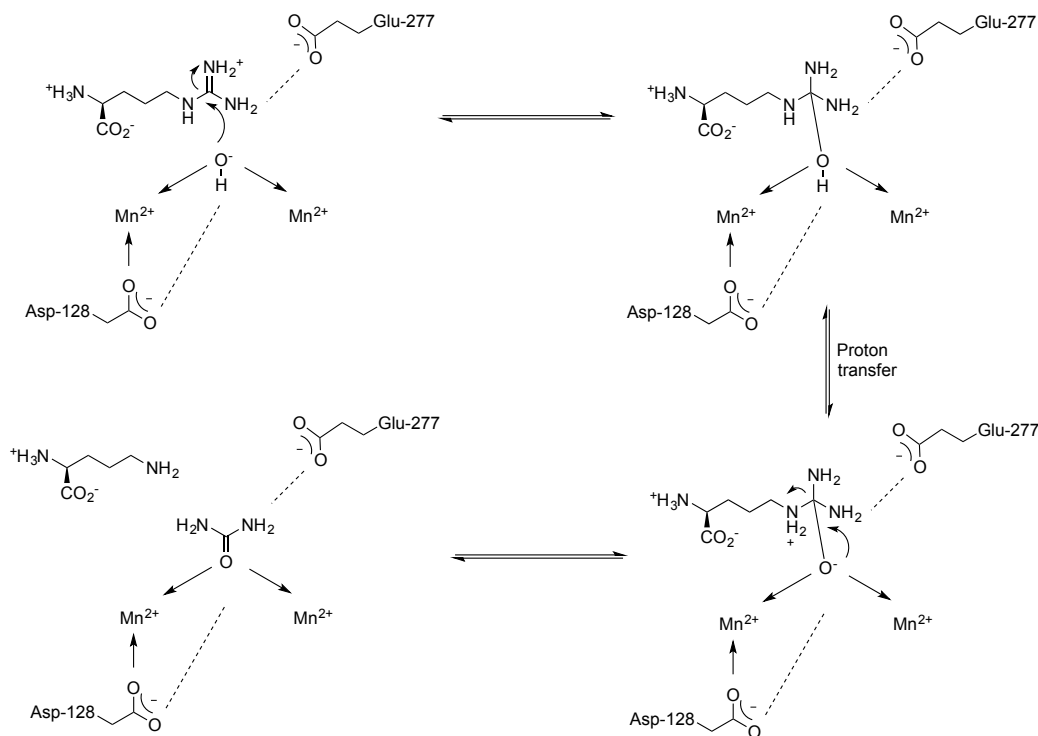
Figure 1.2 Mechanism of arginase catalyzing arginine to ornithine and urea.

1.2   Immune function and related diseases

Arginase plays an important role in the immune function because arginine is also the substrate for nitric oxide synthase (NOS). In the cellular environment, arginase competes with NOS for the same arginine molecules as substrates (Scheme 1.1).[4] When the concentration of arginine is low, NOS produces less NO and uses more oxygen to form superoxide. The superoxide reacts with the NO to form peroxynitrite, thus further decreasing the concentration of NO.[5] As a result, an increase in arginase activity leads to decreased levels of arginine and lowers the level of NO. In short, arginase and NOS are reciprocally regulated under some conditions and up-regulation of arginase has been demonstrated in several diseases including hypertension and Chagas disease.

Hypertension   Also known as high blood pressure, hypertension is a long-term medical condition in which blood pressure is persistently elevated. High blood pressure can result
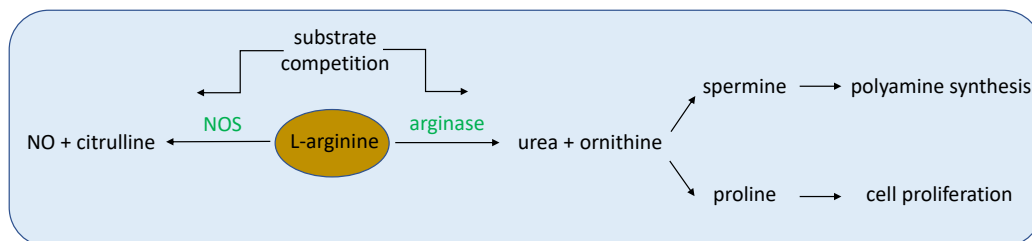
Scheme 1.1 Scheme for the catabolism of arginine by arginase and NO synthase.

from obesity, diabetes and kidney disease, and may lead to heart attack and stroke. Approximately 85 million people in the United States have hypertension, and it is accountable for 13% of deaths globally.[6]

Recently, studies have demonstrated that high blood pressure is associated with increased arginase activity. Endothelial dysfunction induces an increase in reactive oxygen species (ROS) via NADPH oxidase which causes an increase in endothelial arginase expression. Low amounts of arginine causes the "uncoupled" endothelial nitric oxide synthase (eNOS) to produces superoxide instead of NO, resulting in the production of hydrogen peroxide and peroxynitrite, and finally leading to the production of adhesive molecules that block blood vessel (Scheme 1.2).[7] Thus, inhibition of arginase increases the bioavailability of NO and reduces the levels of superoxide, resulting in improved endothelial function. This pathway may offer an alternative method to treat high blood pressure.
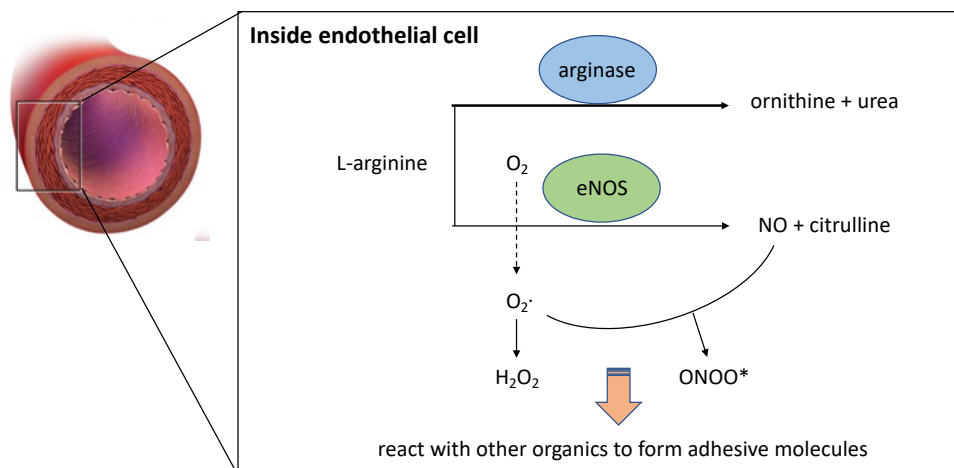
Scheme 1.2 Schematic illustration of how arginase regulates NO bio-availability and vascular function.

Chagas' disease Also known as American trypanosomiasis, Chagas disease is a tropical parasitic disease caused by the protist *Trypanosoma cruzi*. The disease is mostly spread by "kissing bugs" and the symptoms include fever, fatigue, body aches, headache, local swelling, enlarged heart and finally heart failure. Chagas disease affects over 16 million people in Latin America, causing about 50,000 deaths per year.[8]

One interesting finding about the parasite is that after invasion it can evade the human immune response and escape NO toxicity by activating the host's arginase (Scheme 1.3).[9] The activation of arginase leads to (1) depletion of arginine leading to decreased NO production, which is toxic to parasites; (2) increased production of polyamines, which are necessary for parasite growth and differentiation; and (3) enhancement of the polyamine biosynthetic precursor for trypanothione, a molecule that is essential for parasites to maintain their intracellular redox system. Therefore, small molecules inhibitors for arginase might be used as new antiparasitic chemotherapeutics.
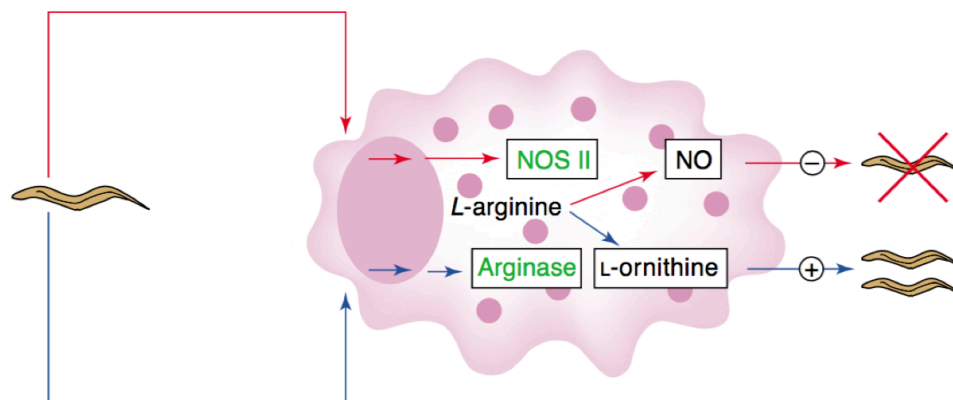
Scheme 1.3 Schematic illustration of how parasites escape NO toxicity. Reprinted with permission from ref [9]. Copyright 2003 Elsevier.

1.3   Arginase inhibitors

Since all of the above diseases involve up-regulation of arginase activity, small arginase inhibitors may show promise as new drugs to treat these diseases. To date, a variety of arginase inhibitors have been reported and some of these are already being applied to pre-clinical use in humans. The first arginase inhibitor is NOHA, an intermediate formed during the production of NO by NOS (Figure 1.3).[10] However, NOHA causes many side effects because of its low specificity and the high concentrations required for efficient inhibition.

Recently, competitive inhibitors have been developed, which show greater specificity for arginase. Based on the structure and mechanism of arginase, the Christianson group developed boronic acid analogs of L-arginine (ABH and BEC).[11] Both inhibitors contain a boronic acid in place of the guanidinium group in arginine. The inhibitors bind to the active site of arginase, and react with a Mn^{2+} bound hydroxide ion to give a tetrahedral boronate species. These species have a higher affinity for arginase than the substrate L-arginine, and thus block the activity site and result in competitive inhibition.
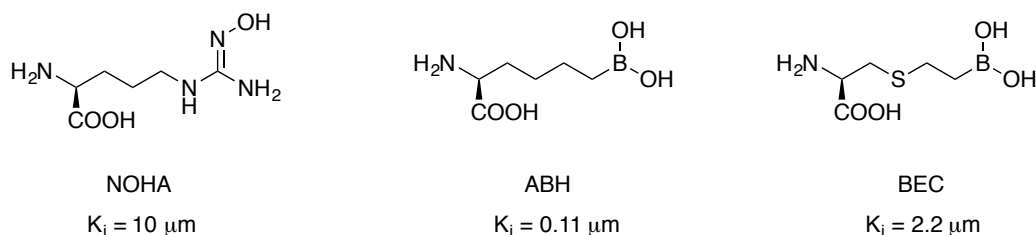
Figure 1.3 Variety of arginase inhibitors.

Several arginase inhibitors, including ABH and BEC, have been used in humans for pre-clinical trials and show promising results in the treatment of type 2 diabetes,[12] heart failure[13] and hypertension.[14] However, the safety of long-term treatment using these inhibitors still remains an open question due to the fact that arginase plays an important role in the urea cycle and synthesis of ornithine, proline and polyamines. Another concern is that arginase inhibitors may have adverse effects on tissue repair and thus may not be good treatments for many cardiovascular diseases.[15] Also, the boronic acid inhibitors

have relatively poor pharmacokinetic profiles and bio-availabilities, which further limit their potential as chemotherapeutic reagents.[16]

1.4   Assays for measuring arginase activity

Because of the significant role played by arginase in biology, revealing the activities of these enzymes has attracted a lot of interest. Both radiochemical assays and spectrophotometric assays have been developed for measuring the activity of arginase.

Radiochemical assay

In 1980, Ruegg and Russell developed a fixed-point assay, which uses a radioactive substrate [^{14}C] guanidine-L-arginine to generate [^{14}C] urea (Scheme 1.4).[17] The radioactive urea is then quantified by scintillation counting. However, this kind of fixed-point assay requires expensive equipment and toxic radio-labeled materials and are usually very time consuming.
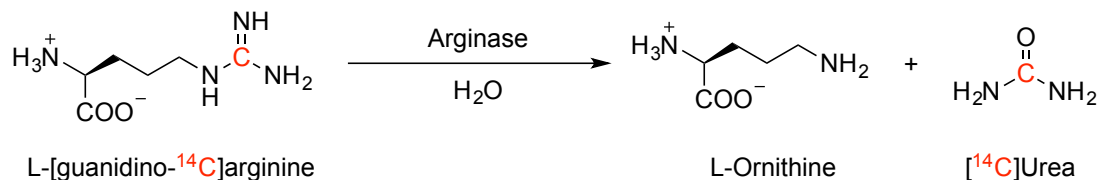
Scheme 1.4 Schematic illustration of the fixed-point assay for measuring arginase activity.

Spectrophotometric assay

In 2002, Viola and coworkers developed a spectrophotometric assay by using thioarginine, which is a good mimic of natural L-arginine as substrate.[18] After hydrolysis by arginase, the free thiol group can react with DTNB by cleaving the disulfide bond to give TNB (Scheme 1.5). TNB has a yellow color and can be quantified in a spectrophotometer by measuring the absorbance of visible light at 412 nm. However, Ellman's reagent (DTNB) can only be used within a narrow pH range (6 - 8), which is different from the optimum pH for arginase activity (8.5 – 10.5).
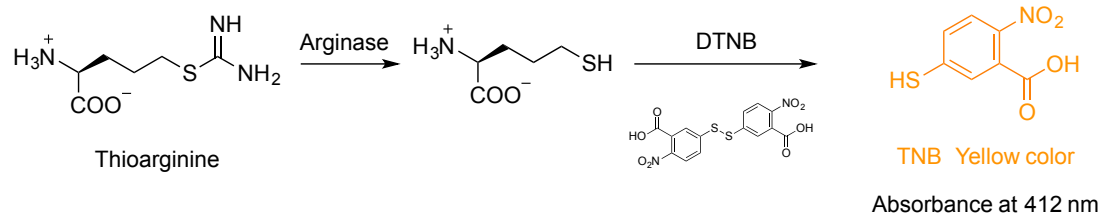
Scheme 1.5 Schematic illustration of the spectrophotometric assay based on the thiol-DTNB reaction.

In 2008, Woods and coworkers developed a colorimetric assay for determining arginase activity based on the ornithine-ninhydrin reaction.[19] After hydrolysis by arginase, the primary amino group in ornithine can react with ninhydrin to form a purple compound with strong absorbance at 570 nm (Scheme 1.6). However, the samples are require to be heated to 100 °C before reading in a spectrophotometer to make sure all the amino groups are coupled with ninhydrin. Correction calculations are also needed since the original L-arginine can also react with ninhydrin.
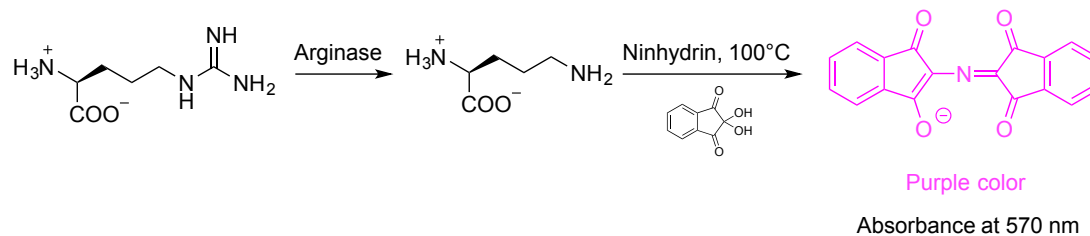
Scheme 1.6 Schematic illustration of the spectrophotometric assay based on the ornithine-ninhydrin reaction.

Even though the above methods can measure arginase activity indirectly, there are still many limitations. Moreover, these available methods cannot monitor the activity of arginase *in vivo*. Activity-based protein profiling is a novel approach for detecting enzyme activities.

1.5 Activity-based probe

Activity-based probes are designed to react with the active forms of enzymes. They can discern between active and inactive enzymes and target the activity of the enzyme instead of the abundance of the protein. Compared to traditional protein profiling methods, activity-based protein profiling provides a more comprehensive view of the enzyme's activity in the biological system.

1.5.1 Structure of activity-based probes

Most activity-base probes share a similar design and have three structural components: (1) a reactive group that reacts with the enzyme covalently; (2) a linker that connects the reactive group with a tag and (3) a tag group for further enrichment or visualization (Figure 1.4).
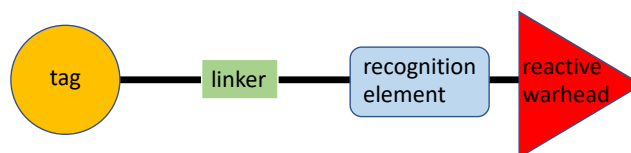
Figure 1.4 Structure of a typical activity-based probe.

Reactive group   Also known as the warhead, the reactive group can react with a proximal nucleophilic residue in the active site, and results in irreversible covalent labeling of the enzyme. Based on the catalytic mechanism, small irreversible inhibitors can be transformed into activity-based probes by attaching proper report tags. Various reactive groups have been developed for different enzymes. For example fluoromethyl ketones are highly reactive towards cysteine proteases[20] while bromobenzylphosphonates are highly reactive towards tyrosine phosphatases.[21]

Linker   The linker is like a bridge that connects the reactive group and the tag together. The main purpose of using a linker is to reduce the steric effect between those two groups and

improve the probe accessibility. Long carbon chains or polyethylene glycols are commonly used as linkers. In some cases, a specially designed linker can be used to increase probe selectivity and specificity. For example, a short peptide that mimics the natural protein substrate can be used as a linker to target proteases. By changing the amino acid sequences, different subfamilies of proteases can be specifically targeted.[22]

Tag The tag group in the activity-based probe enables visualization and purification of the labeled proteins. Radioisotopes (^{125}I and ^{3}H) were first introduced into activity-based probes as tags for visualization.[23] However, due to the half-life problems and special handling procedures, the radio-labeled probes are not widely used today. Nowadays, fluorescent tags are most commonly used in labs. A number of commercial fluorophores have been developed with different excitation and emission wavelengths (Figure 1.5). The combination of fluorescent tags with SDS-PAGE analysis enables fast and sensitive determination of successful labeling. On the other hand, affinity tags are commonly used for isolation and purification of tagged proteins. Biotin is the most widely used affinity tag due to the strong interaction between biotin and avidin/streptavidin. Incorporation of a biotin tag enables efficient enrichment even when low abundant targets are labeled. This reduces the complexity of biological samples which facilitates further analysis by mass spectrometry.
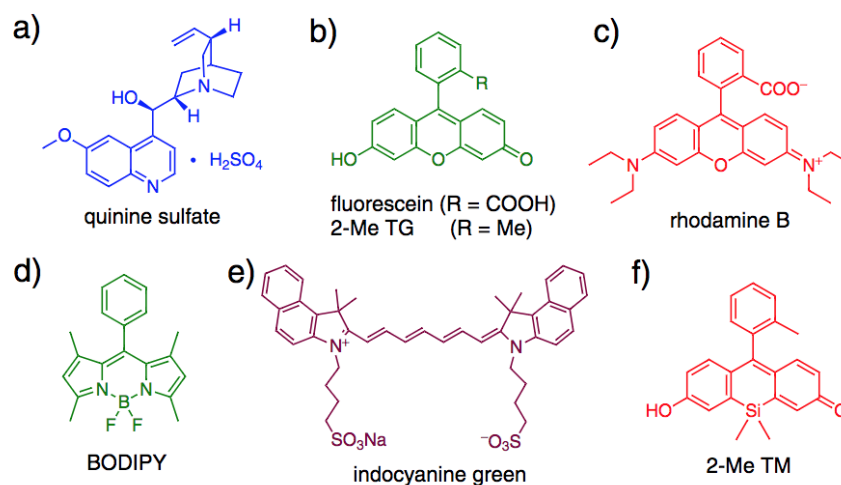
Figure 1.5 Small-molecule fluorophores with different visible colors.

Tag-free two step labeling Even though tags are commonly used in activity-based probes, poor cell permeability limits their use for *in situ* and *in vivo* experiments. To resolve this problem, tag-free activity-based probes were developed utilizing click chemistry. A small conjugation group (alkyne) is connected to the probe instead of a bulky tag. After labeling, a biotin tag or fluorescent tag can be added by cycloaddition of an azide with the alkyne in the presence of a copper catalyst (Scheme 1.7).[24]
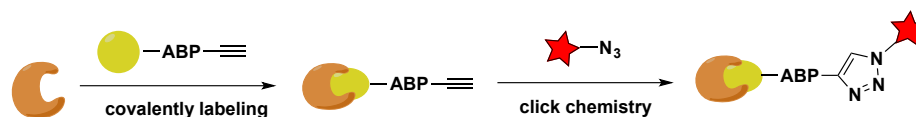
Scheme 1.7 Schematic illustration of two steps labeling using click chemistry.

1.5.2 Activity-based probes for serine proteases

Serine proteases are enzymes that use serine as the nucleophilic amino acid to cleave peptide bonds in proteins.[25] In humans, they are involved in many biological processes including digestion, inflammation and blood clotting. Most serine proteases use a Ser/His/Asp catalytic triad. The -OH group of the serine side chain acts as a nucleophile to attack the carbonyl carbon in the amide substrate. One nitrogen atom in the histidine abstracts the hydroxyl proton and thus increases serine's nucleophilicity. The carboxylate group in aspartic acid accepts a proton during the process, making the nitrogen on histidine more basic. Based on this mechanism, several activity-based probes have been developed to covalently label the nucleophilic serine residue. The electrophilic warhead in these probes include phosphonates,[26] 4-chloroisocoumarins[27] and sulfonyl fluorides.[28] For example, the binding mechanism of phosphoramidates is in shown in Scheme 1.8.[29]
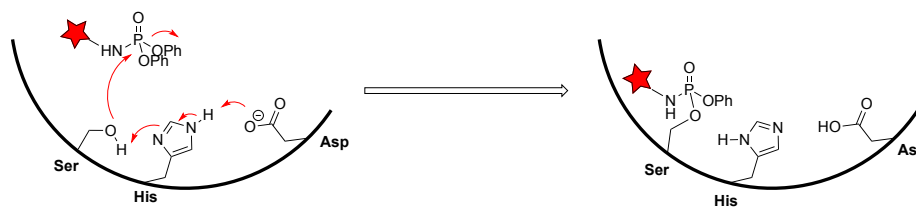
Scheme 1.8 The mechanism of the phosphoramidate-based probe for serine proteases.

1.5.3   Activity-based probes for kinases

Kinases are enzymes that catalyze the transfer of a phosphate group from adenosine triphosphate to the substrates, producing a phosphorylated substrate and adenosine diphosphate.[30] There are over 500 kinases in humans, and they play important roles in cell signaling, transportation and metabolism. Activity-based probes for kinases are different from serine proteases probes, because kinases catalyze phosphoryl transfer by a direct mechanism that does not involve a covalent-enzyme intermediate. In other words, the kinase active site does not contain a nucleophilic residue for catalysis. Based on the sequences of kinases, it has been found that all protein kinases have at least one conserved lysine residue within their active sites.[31] The Patricelli group designed an activity-based probe for kinases based on this common structural feature. The biotinylated acyl phosphate reacts with the amine in the lysine side chain to form a stable amide bond and thus label the kinase.[32]
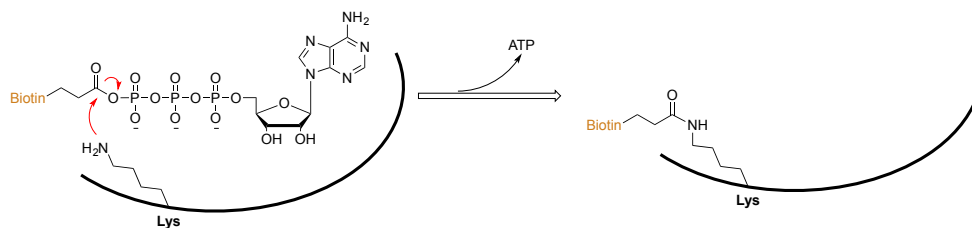
Figure 1.6 The mechanism of the ATP-based probe for protein kinases.

Aim of this work

There are several competitive reversible inhibitors available for arginase. However, there are no reports of irreversible inhibitors. The first part of my thesis research focuses on developing new mechanism-based irreversible arginase inhibitors. These small molecule inhibitors for arginase may show therapeutic potential for the treatment of a range of pathological conditions, and have promise as new anti-parasitic drugs. The irreversible inhibitor can further be transformed into activity-based probes by attaching proper tags, which provides a new way to profile arginase and arginase activity in humans.

References

[1] Christianson, D. W. Arginase: structure, mechanism, and physiological role in male and female sexual arousal. *Accounts of chemical research* **2005**, *38*, 191–201.

[2] Caldwell, R. B.; Toque, H. A.; Narayanan, S. P.; Caldwell, R. W. Arginase: an old enzyme with new tricks. *Trends in pharmacological sciences* **2015**, *36*, 395–405.

[3] Di Costanzo, L.; Sabio, G.; Mora, A.; Rodriguez, P. C.; Ochoa, A. C.; Centeno, F.; Christianson, D. W. Crystal structure of human arginase I at 1.29-Å resolution and exploration of inhibition in the immune response. *Proceedings of the National Academy of Sciences* **2005**, *102*, 13058–13063.

[4] Rath, M.; Müller, I.; Kropf, P.; Closs, E. I.; Munder, M. Metabolism via arginase or nitric oxide synthase: two competing arginine pathways in macrophages. *Frontiers in immunology* **2014**, *5*, 532.

[5] Pacher, P.; Beckman, J. S.; Liaudet, L. Nitric oxide and peroxynitrite in health and disease. *Physiological reviews* **2007**, *87*, 315–424.

[6] others,, et al. A call to action and a lifecourse strategy to address the global burden of raised blood pressure on current and future generations: the Lancet Commission on hypertension. *The Lancet* **2016**, *388*, 2665–2712.

[7] Förstermann, U.; Xia, N.; Li, H. Roles of vascular oxidative stress and nitric oxide in the pathogenesis of atherosclerosis. *Circulation research* **2017**, *120*, 713–735.

[8] Moncayo, Á.; Silveira, A. C. *American Trypanosomiasis Chagas Disease*; Elsevier, 2017; pp 59–88.

[9] Vincendeau, P.; Gobert, A. P.; Daulouède, S.; Moynet, D.; Mossalayi, M. D. Arginases in parasitic diseases. *Trends in parasitology* **2003**, *19*, 9–12.

[10] Bratt, J. M.; Zeki, A. A.; Last, J. A.; Kenyon, N. J. Competitive metabolism of L-arginine: arginase as a therapeutic target in asthma. *Journal of biomedical research* **2011**, *25*, 299–308.

[11] Shin, H.; Cama, E.; Christianson, D. W. Design of amino acid aldehydes as transition-state analogue inhibitors of arginase. *Journal of the American Chemical Society* **2004**, *126*, 10278–10284.

[12] Kövamees, O.; Shemyakin, A.; Checa, A.; Wheelock, C. E.; Lundberg, J. O.; Östenson, C.-G.; Pernow, J. Arginase inhibition improves microvascular endothelial function in patients with type 2 diabetes mellitus. *The Journal of Clinical Endocrinology & Metabolism* **2016**, *101*, 3952–3958.

[13] Pernow, J.; Jung, C. Arginase as a potential target in the treatment of cardiovascular disease: reversal of arginine steal. *Cardiovascular research* **2013**, *98*, 334–343.

[14] Steppan, J.; Nyhan, D.; Berkowitz, D. Development of novel arginase inhibitors for therapy of endothelial dysfunction. *Frontiers in immunology* **2013**, *4*, 278.

[15] Schlüter, K.-D.; Schulz, R.; Schreckenberg, R. Arginase induction and activation during ischemia and reperfusion and functional consequences for the heart. *Frontiers in physiology* **2015**, *6*, 65.

[16] others,, et al. Boron chemicals in diagnosis and therapeutics. *Future medicinal chemistry* **2013**, *5*, 653–676.

[17] Rüegg, U. T.; Russell, A. S. A rapid and sensitive assay for arginase. *Analytical biochemistry* **1980**, *102*, 206–212.

[18] Han, S.; Viola, R. E. A spectrophotometric assay of arginase. *Analytical biochemistry* **2001**, *295*, 117–119.

[19] Iyamu, E. W.; Asakura, T.; Woods, G. M. A colorimetric microplate assay method for high-throughput analysis of arginase activity in vitro. *Analytical biochemistry* **2008**, *383*, 332–334.

[20] Bedner, E.; Smolewski, P.; Amstad, P.; Darzynkiewicz, Z. Activation of caspases measured in situ by binding of fluorochrome-labeled inhibitors of caspases (FLICA): correlation with DNA fragmentation. *Experimental cell research* **2000**, *259*, 308–313.

[21] Kumar, S.; Zhou, B.; Liang, F.; Wang, W.-Q.; Huang, Z.; Zhang, Z.-Y. Activity-based probes for protein tyrosine phosphatases. *Proceedings of the National Academy of Sciences* **2004**, *101*, 7943–7948.

[22] Bedner, E.; Smolewski, P.; Amstad, P.; Darzynkiewicz, Z. Activation of caspases measured in situ by binding of fluorochrome-labeled inhibitors of caspases (FLICA): correlation with DNA fragmentation. *Experimental cell research* **2000**, *259*, 308–313.

[23] Sadaghiani, A. M.; Verhelst, S. H.; Bogyo, M. Tagging and detection strategies for activity-based proteomics. *Current opinion in chemical biology* **2007**, *11*, 20–28.

[24] Speers, A. E.; Adam, G. C.; Cravatt, B. F. Activity-based protein profiling in vivo using a copper (I)-catalyzed azide-alkyne [3+ 2] cycloaddition. *Journal of the American Chemical Society* **2003**, *125*, 4686–4687.

[25] Kraut, J. Serine proteases: structure and mechanism of catalysis. *Annual review of biochemistry* **1977**, *46*, 331–358.

[26] Hawthorne, S.; Hamilton, R.; Walker, B. J.; Walker, B. Utilization of biotinylated diphenyl phosphonates for disclosure of serine proteases. *Analytical biochemistry* **2004**, *326*, 273–275.

[27] Kam, C. M.; Abuelyaman, A. S.; Li, Z.; Hudig, D.; Powers, J. C. Biotinylated iso-coumarins, new inhibitors and reagents for detection, localization, and isolation of serine proteases. *Bioconjugate chemistry* **1993**, *4*, 560–567.

[28] Yan, X.; Luo, Y.; Zhang, Z.; Li, Z.; Luo, Q.; Yang, L.; Zhang, B.; Chen, H.; Bai, P.; Wang, Q. Europium-labeled activity-based probe through click chemistry: absolute serine protease quantification using 153Eu isotope dilution ICP/MS. *Angewandte Chemie International Edition* **2012**, *51*, 3358–3363.

[29] Haedke, U. R.; Frommel, S. C.; Hansen, F.; Hahne, H.; Kuster, B.; Bogyo, M.; Verhelst, S. H. Phosphoramidates as novel activity-based probes for serine proteases. *Chembiochem* **2014**, *15*, 1106–1110.

[30] Endicott, J. A.; Noble, M. E.; Johnson, L. N. The structural basis for control of eukaryotic protein kinases. *Annual review of biochemistry* **2012**, *81*, 587–613.

[31] Nolen, B.; Taylor, S.; Ghosh, G. Regulation of protein kinases: controlling activity through activation segment conformation. *Molecular cell* **2004**, *15*, 661–675.

[32] Patricelli, M. P.; Szardenings, A. K.; Liyanage, M.; Nomanbhoy, T. K.; Wu, M.; Weissig, H.; Aban, A.; Chun, D.; Tanner, S.; Kozarich, J. W. Functional interrogation of the kinome using nucleotide acyl phosphates. *Biochemistry* **2007**, *46*, 350–358.

Chapter 2

Rational Design of Novel Irreversible Inhibitors for Human Arginase[†]

2.1   Abstract

Parasites have developed a variety of strategies for invading hosts and escaping their immune response. A common mechanism by which parasites escape nitric oxide (NO) toxicity is the activation of host arginase. This activation leads to a depletion of L-arginine, which is the substrate for NO synthase, resulting in lower levels of NO and increased production of polyamines that are necessary for parasite growth and differentiation. For this reason, small molecule inhibitors for arginase show promise as new anti-parasitic chemotherapeutics. However, few arginase inhibitors have been reported. Here, we describe the discovery of novel irreversible arginase inhibitors, and their characterization using biochemical, kinetic, and structural studies. Importantly, we determined the site on human arginase that is labeled by one of the small molecule inhibitors. The tandem mass spectra data show that the inhibitor occupies the enzyme active site and forms a covalent bond with Thr135 of arginase. These findings pave the way for the development of more potent and selective irreversible arginase inhibitors.

2.2   Introduction

Arginase is a manganese metalloenzyme that catalyzes the hydrolysis of arginine to form ornithine and urea.[1] In the liver, this reaction constitutes the final step of urea biogenesis.[2] In other non-hepatic tissues such as red blood cells, mammary glands and kidneys, the main function of arginase is thought to be the production of ornithine, which serves as a biosynthetic precursor to proline and polyamines.[3] Recent studies suggest that arginase also plays an important role in modulating the immune response since it regulates arginine levels, and arginine is the substrate for nitric oxide synthases (NOS) (Figure 2.1).[4,5] When the level of extra-hepatic arginase is elevated, arginine availability as a substrate for NOS is limited due to the enhanced consumption of arginine by arginase. Thus, arginase and NOS appear to be reciprocally regulated under some conditions. Up-regulation of arginase has been observed in several diseases including Chagas disease and sleeping sickness.[6,7] These

diseases are caused by parasitic protozoa of the genus *Trypanosoma*. These parasites evade the human immune response and escape NO toxicity by activating the host's arginase.[8–10] The activation of arginase leads to (1) depletion of arginine leading to decreased NO production; (2) increased production of polyamines, which are necessary for parasite growth and differentiation; and (3) enhancement of the polyamine biosynthetic precursor for trypanothione, a molecule that is essential for parasites to maintain their intracellular redox system.
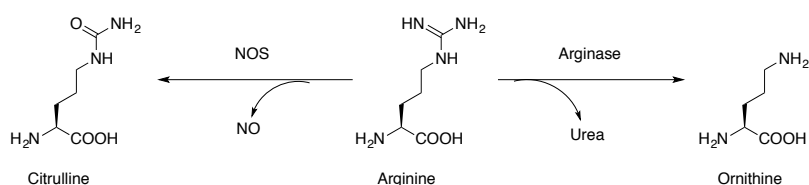
Figure 2.1 Two enzymes that use arginine as a substrate.

Recently, arginase and polyamine biosynthetic pathways have been being targeted for the treatment of African sleeping sickness and Chagas disease.[11,12] Potent arginase inhibitors are valuable chemical tools for deciphering the complex immune response mediated by arginase, and for testing biological and therapeutic hypotheses associated with parasitic diseases. However, only a few arginase inhibitors have been reported to date (Figure 2.2).[13–15] The boronic acid analogs of L-arginine (Figure 2.2, ABH and BEC) have been widely used as reversible arginase inhibitors to study the biological function of arginase. Both inhibitors contain a boronic acid in place of the guanidinium group in arginine. The inhibitors bind to the active site of arginase, and react with a Mn^{2+} bound hydroxide ion to give a tetrahedral boronate species. These boronic acid inhibitors often have high toxicity, and relatively poor pharmacokinetic profiles, selectivities and bioavailabilities.[16,17] Thus, their potential applications as chemotherapeutic reagents are limited. The development of novel arginase inhibitors is an urgent need.

Irreversible inhibitors typically contain a reactive functional group that reacts with amino acid side chains to form a covalent adduct. A higher level of selectivity can be
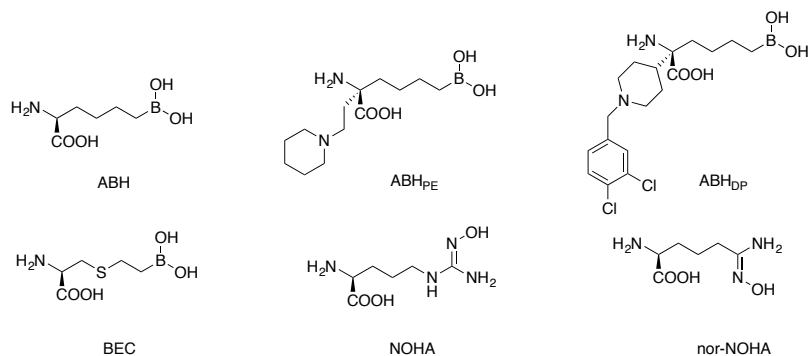
Figure 2.2 Reversible arginase inhibitors.

achieved if the reactive functional group is only unmasked as a consequence of an enzyme-catalyzed reaction. In this way, such mechanism-based inactivators generate the reactive group in the active site of the target enzyme, and avoid non-specific reaction with other proteins. Irreversible inhibitors have been developed for a variety of enzyme families, including proteases,[18,19] kinases[20,21] and phosphatases.[22,23] In 2011, researchers estimated that 26 covalent drugs accounted for over \$33 billion in annual worldwide sales.[24] Inspired by the natural structure of arginine, we designed and synthesized two mechanism-based irreversible arginase inhibitors. We characterized these compounds in biochemical and kinetic assays. Furthermore, we determined the labeling site on human arginase 1 that reacts with inhibitor 1. Such small molecule inhibitors for human arginase may show therapeutic potential for the treatment of a range of pathological conditions, and have promise as new anti-parasitic drugs.

2.3 Results and discussion

2.3.1 Design

The inhibitors have three structural components: (1) the 4-guanidinobenzyl group that mimics the side chain of L-arginine; (2) a leaving group that triggers formation of a reactive electrophile in the active site;[25–28] and (3) a carboxyl group that anchors the inhibitor in the active site through hydrogen bonds with several amino acid side chains. The proposed

mechanism is shown in Scheme 2.1. After binding to the active site of arginase, the guanidinium group on the inhibitor is first hydrolyzed by arginase to generate an aromatic amine. This intermediate undergoes rapid 1,6-elimination to give a para-azaquinone methide, which is a strong electrophile. The azaquinone methide reacts with a proximal nucleophilic residue in the active site of arginase, and results in irreversible covalent labeling of the enzyme. Two leaving groups, fluoride and acetate, were chosen due to their stability in aqueous solution and reasonable leaving group ability.
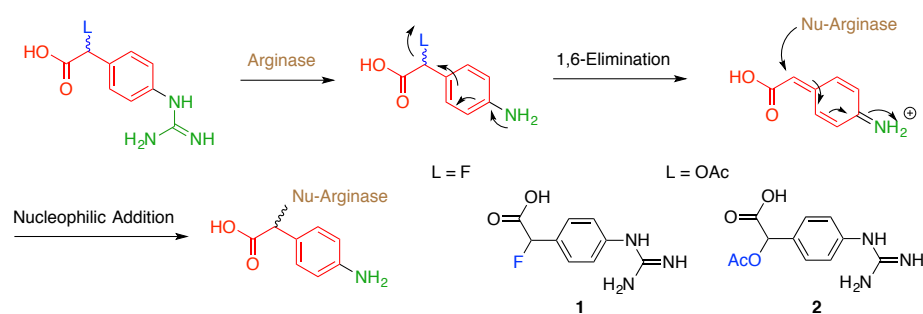
Scheme 2.1 Proposed mechanism of action of the irreversible inhibitors.

We generated a computer-based model of inhibitor 1 docked into the active site of arginase using the crystal structure of the arginase-ABH complex (PDB 2AEB)[29] in conjunction with a flexible side chain docking strategy. The ABH molecule in the crystal structure was first removed, then inhibitor 1 was docked and energy minimized in the binding site. Figure 2.3A illustrates that the guanidinium group of inhibitor 1 can hydrogen bond with the side chains of His126, Asp128, Asp232 and Asp234, while the carboxylate can hydrogen bond with Asn130, Ser137 and Asn139. An overlay of the crystal structure of ABH with the model of inhibitor 1 suggests that the two inhibitors can bind in a similar manner (Figure 2.3B). Similar docking studies with inhibitor 2 (Figure 2.3C and D) suggest that inhibitor 2 also fits into the binding site, but with less favorable interactions compared with inhibitor 1.
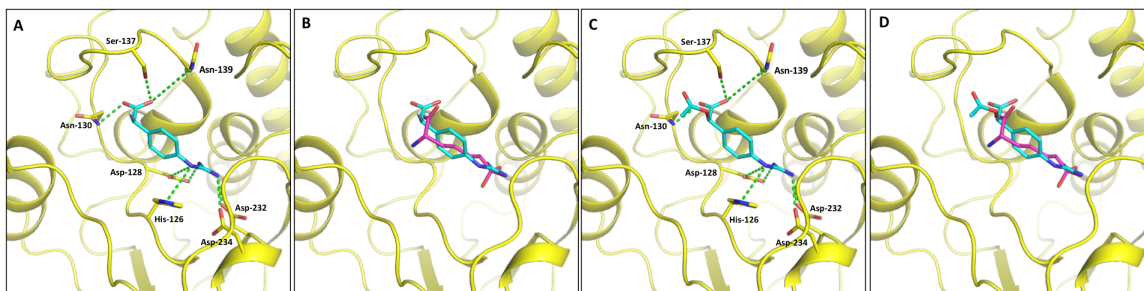
Figure 2.3 (A) Docking of inhibitor 1 (cyan) in the active site of arginase (yellow). Hydrogen bonds are shown as green dotted lines. (B) Overlay of the docking model of inhibitor 1 (cyan) with the crystal structure of ABH (magenta) bound in the active site of arginase. (C) Docking of inhibitor 2 (cyan) in the active site of arginase (yellow). Hydrogen bonds are shown as green dotted lines. (D) Overlay of the docking model of inhibitor 2 (cyan) with the crystal structure of ABH (magenta) bound in the active site of arginase.

2.3.2 Synthesis

Inhibitors 1 and 2 were synthesized as shown in Scheme 2.2. 2-(4-Nitrophenyl)acetic acid 3 was esterified to give methyl 2-(4-nitrophenyl)acetate 4. Bromination followed by hydrolysis of the intermediate benzylic bromide 5 gave alcohol 6. The nitro group was reduced using Pd/C and H_2, and the resulting aromatic amine 7 was reacted with 1,3-bis(tert-butoxycarbonyl)-2-methyl-2-thiopseudourea to form the Boc protected guanidine compound 8. Inhibitor 1 was then prepared from 8 by converting the alcohol to a fluoride using DAST, and removing the methyl ester and Boc protecting groups with aqueous KOH and TFA, respectively. Inhibitor 2 was synthesized from 8 by saponifying the methyl ester, followed by acylating the benzylic alcohol with acetic anhydride to give compound 12. TFA removed the Boc protecting groups to give inhibitor 2.

2.3.3 Kinetic Assays of Irreversible Inhibitors with Arginase

We used the substrate thioarginine, in conjunction with the colorimetric reagent 5,5-dithio-bis-(2-nitrobenzoic acid) (DTNB), to measure the activity of arginase.[30] After thioarginine is hydrolyzed by arginase, the resulting free thiol group undergoes thiol-disulfide interchange with DTNB to give 2-nitro-5-thiobenzoate (TNB). TNB has a yellow color and can be quantified by measuring its absorbance at 412 nm (Scheme 2.3). We used this substrate
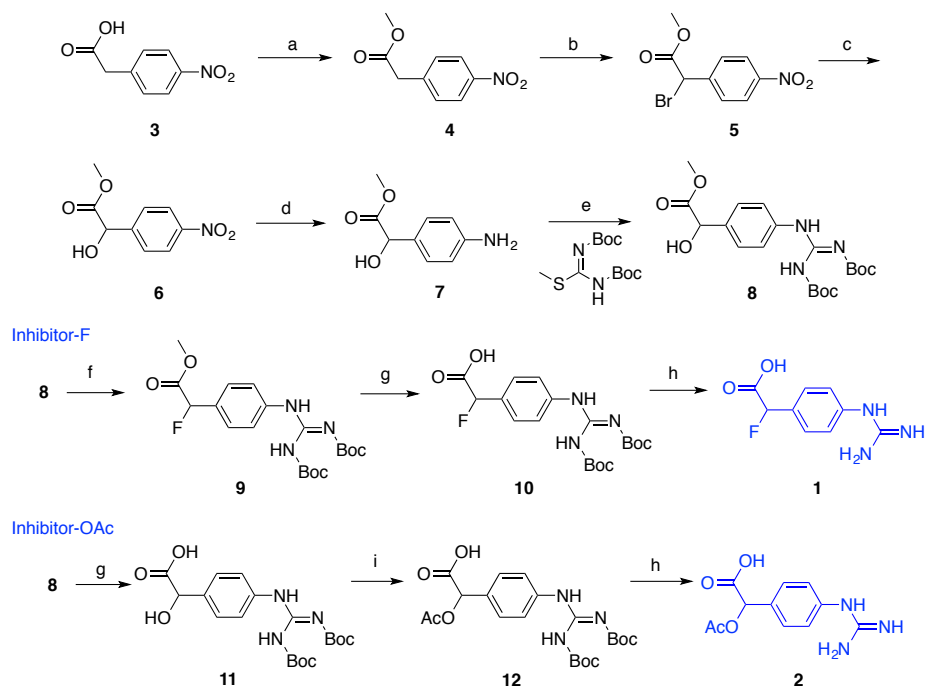
Scheme 2.2 Synthesis of inhibitors 1 and 2. Reagents and conditions: (a) MeOH, H_2SO_4, reflux, 5 h; (b) AIBN, NBS, CCl_4, reflux, overnight; (c) Ag_2SO_4, dioxane:water = 1:1, reflux, 3 h; (d) 5% Pd/C, H_2, rt, overnight; (e) $AgNO_3$, TEA, rt, overnight; (f) DAST, 0 °C, 1 h; (g) 1M KOH, rt, 3 h; (h) TFA:DCM = 1:1, rt, 24 h; (i) Ac_2O, DMAP, DCM, rt, 5 h.

to measure K_m and V_{max} values for arginase 1 and 2 that are similar to the values reported in the literature (Figure 2.4).[31,32] The minor differences between our experimental and literature values are likely due to minor differences in the assay conditions including temperature, pH, and the presence of additives.
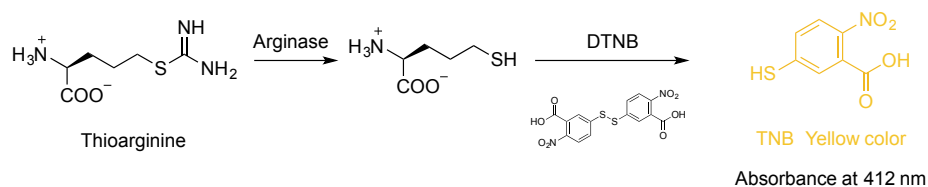
Scheme 2.3 Colorimetric assay to measure arginase activity.

Inhibitors 1 and 2 were assayed against arginase using thioarginine as the substrate.
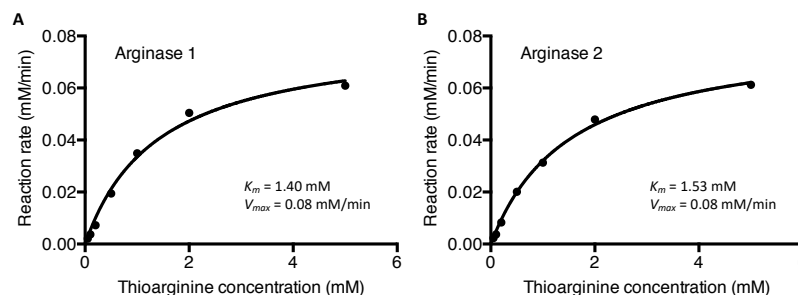
Figure 2.4 Data for thioarginine hydrolysis by arginase. (A) for arginase 1 and (B) for arginase 2. The solid line represents a fit of the data to the Michaelis-Menten equation.

Based upon our mechanistic proposal, we expected to observe time- and concentration-dependent irreversible inhibition. Arginase 1 and 2 were incubated with varying concentrations of the inhibitors, and at several time points aliquots were removed and assayed for remaining enzyme activity by measuring the initial hydrolysis rate of the substrate using a UV-Vis micro-plate reader. The apparent exponential decay rate constant (k_{app}) was plotted against the inhibitor concentration according to the equation $k_{app} = k_{inact} \times [inhibitor]/(K_I + [inhibitor])$ to calculate inhibition constants K_I and inactivation rate constants k_{inact}. The full data set is shown in the Figure 2.5 and the inhibition results are summarized in Table 2.1. The K_I values of both inhibitors are significantly lower than the K_m values for the thioarginine substrate (1.4 and 1.5 mM for arginase 1 and 2, respectively). This may be due to the greater hydrophobicity of the inhibitors compared to the substrate. Inhibitor 1 is slightly more potent than inhibitor 2 against both enzymes. This observation is consistent with our docking studies that indicate that the smaller fluoride leaving group allows inhibitor 1 to make more favorable contacts with the active site when compared with the larger acetate leaving group of inhibitor 2. The inhibitors have similar inactivation rate constants k_{inact} against both enzymes, suggesting a similar mechanism of action. While the K_I values reported here are higher than those for the reversible inhibitors shown in Figure 2.2 (for example, BEC, $K_I = 20$ μM), compounds 1 and 2 may show significant selectivity since they are mechanism-based inhibitors that are designed to react only with the active form of arginase.
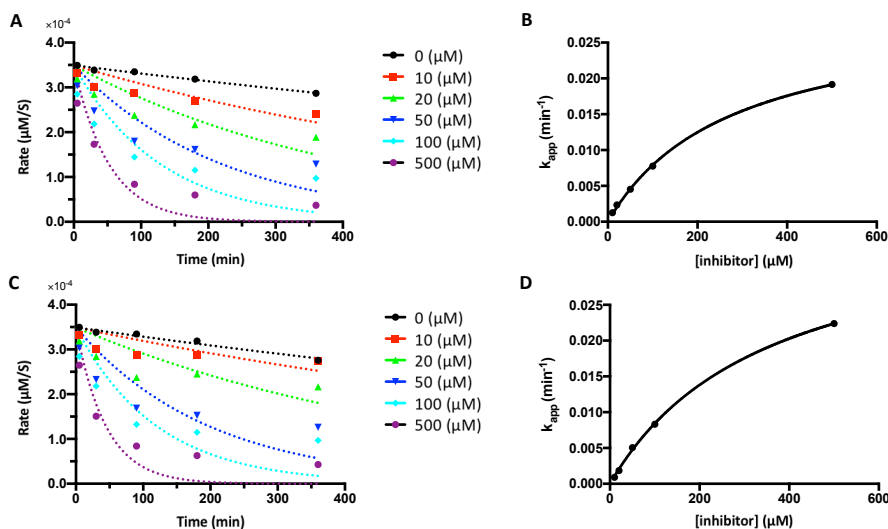
Figure 2.5 Measurement of kinetic parameters for inhibitors 1 and 2 with arginase 1. (A) Time and concentration-dependent inhibition of arginase 1 by inhibitor 1. (B) Apparent inhibition rate constant (k_{app}) vs. inhibitor concentration for inhibitor 1. (C) Time and concentration-dependent inhibition of arginase 1 by inhibitor 2. (D) Apparent inhibition rate constant (k_{app}) vs. inhibitor concentration for inhibitor 2.

Table 2.1 Kinetic inhibition parameters with arginase.

	Arg 1 - Inh 1	Arg 1 - Inh 2	Arg 2 - Inh 1	Arg 2 - Inh 2
$K_I(\mu M)$	275 ± 19	382 ± 68	322 ± 32	437 ± 41
$k_{inact}(min^{-1})$	0.029 ± 0.001	0.032 ± 0.003	0.048 ± 0.002	0.033 ± 0.002

2.3.4 Tandem Mass Spectra of Arginase 1 - Inhibitor 1 Complex

Since the kinetic assays demonstrated that the inhibitors are irreversible, we wanted to determine the site or sites on the enzyme that are covalently labeled by the inhibitor. To determine the labeling site(s), we analyzed proteolytic digests of arginase 1 that had been incubated with inhibitor 1. After the incubation, arginase 1 was digested using chymotrypsin, and the resulting peptides were analyzed by tandem mass spectrometry. By matching the masses of the precursor and fragment ions, we observed only one labeled peptide. The precursor ion (m/z = 797.879, MH^{+2}) corresponds to the peptide $T_{134}\underline{T}TSGNLHGQPVSF_{147}$, where the underline denotes the modified Thr135 residue. In the tandem mass spectrum, we observed masses corresponding to a number of labeled and unlabeled peptide fragments

(Figure 2.6). Peptide fragment ions are indicated by b if the charge is retained on the N-terminal fragment and by y if the charge is retained on the C-terminal fragment. B/y ions indicate that the peptide has been cleaved on both the C and N termini. In the b-ion series, we observe labeled fragments that contain at a minimum T134 and T135 (b2). In the y-ion series, we do not observe labeled fragments that contain any of the residues from S137 to F147. However, we do observe the labeled y13 fragment corresponding to T135-F147. In the b/y ion series, we do not observer labeled fragments that contain any of the residues from T136 to S146. Taken together, these data are consistent with Thr135 as the primary site on arginase 1 that is labeled by inhibitor 1. In the tandem MS we also observe the benzylic cation at m/z = 150.05 (4-aminophenylacetic acid fragment as shown in Figure 2.6) that results from breakage of the peptide-inhibitor fragment bond. Benzyl-modified residues can undergo benzylic cleavage under collision induced dissociation (CID) conditions.[33] In the case of the labeled peptide, the peptide-inhibitor fragment bond is particularly labile, since the resulting benzylic cation is stabilized by resonance from the amino group at the 4-position of the aromatic ring. The docking model is also consistent with Thr135 as the site of covalent modification by inhibitor 1. The distance between the side chain hydroxyl group of Thr135 and the benzylic carbon of inhibitor 1 is 5 Å (Figure 2.7).

2.4 Conclusion

We have described the design and synthesis of two irreversible inhibitors that label the active site of arginase 1 and 2. Kinetic assays demonstrated that treatment of arginase with the inhibitors causes irreversible inactivation in a time- and concentration-dependent manner. Tandem mass spectrometry shows that arginase forms a covalent bond with the inhibitor through the nucleophilic side chain of Thr135 near the active site. In summary, we have developed a new type of irreversible inhibitors for arginase that can serve as the basis for therapeutics to treat parasitic infections, and also as tools to more fully explore the biology of arginases.
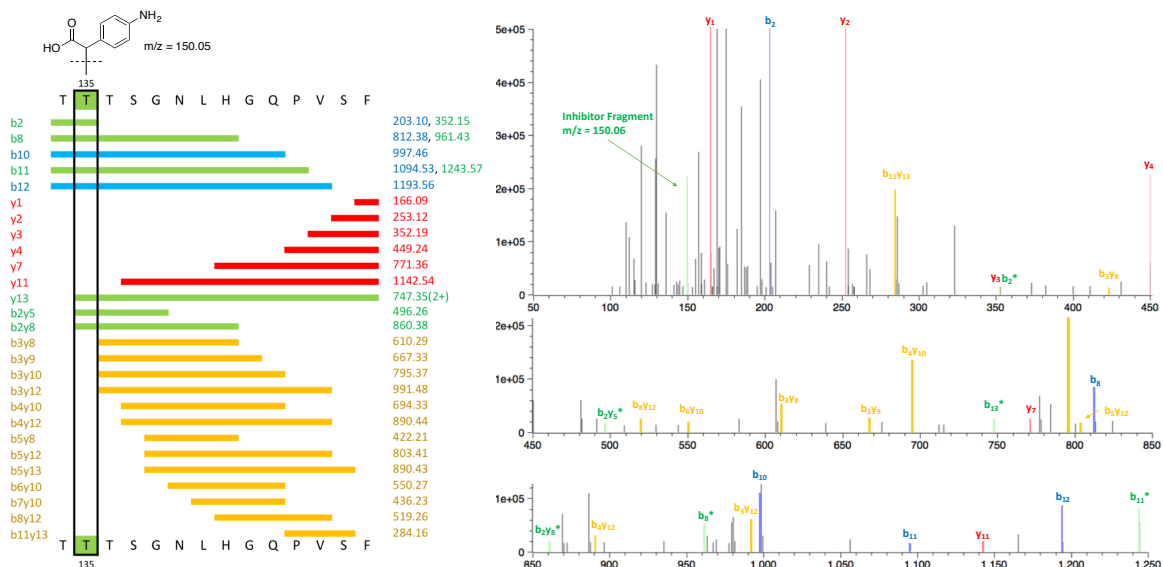
Figure 2.6 The tandem mass spectrum of the peptide from arginase 1 (residues 134-147) that is labeled by inhibitor 1. The unlabeled y-, b- and b/y-ions are colored in red, blue and yellow, respectively. The y- and b-ions that are labeled by the inhibitor (+149.05 Da) are colored in green. Masses of the unlabeled and labeled ions are color coded, and shown on the right side of the figure. All ions have a +1 charge unless indicated otherwise in parentheses next to the observed mass.
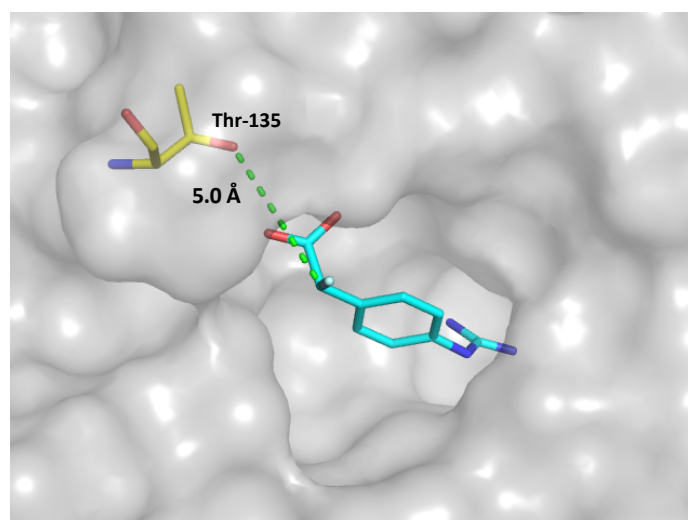
Figure 2.7 The structure of the energy-minimized complex between inhibitor 1 and arginase 1 determined using a docking model (same data as shown in Figure 2.3). This structure indicates that side chain hydroxyl group of Thr135 is 5 Å from the electrophilic benzylic carbon of inhibitor 1.

2.5 Experimental section

2.5.1 Docking procedure for arginase with inhibitors 1 and 2

The 3D structures of inhibitors 1 and 2 were created using Avogadro software. The arginase structure (PDB 2AEB) was used as the template for docking of the ligands into the active site of the enzyme using AutoDock Vina. Before docking, the existing ligand was removed from the complex structure of the PDB file. In order to obtain the initial docking positions of the inhibitors, the covalent single bonds in the inhibitors were allowed to rotate freely to generate the energy-minimized complex between inhibitors and arginase.

2.5.2 Arginase irreversible inhibition kinetic assay

To determine the kinetics of arginase inhibition by the inhibitors, arginase (2.8 µM) was incubated in buffer (50 mM Tris, 50 mM NaCl, 10% glycerol, pH = 9) with various concentrations (0, 10, 20, 50, 100, 500 µM) of inhibitors at room temperature. To 40 µL of thioarginine (400 µM) buffer solution was added 10 µL of the incubation mixture at various time points (5, 30, 90, 180, 360 min) during the incubation. The rates of thioarginine hydrolysis were measured using a UV micro-plate reader (λ_{abs} = 412 nm) at each time point. Each kinetic experiment was performed twice. The remaining arginase activity at each time point was fitted to an exponential decay rate expression $A_t = A_0 \times e^{-k_{app}t}$ determine the apparent inhibition rate constant (k_{app}) at specific inhibitor concentrations [$inhibitor$]. The k_{app} vs. [$inhibitor$] data were fit to the irreversible inhibition rate equation $k_{app} = k_{inact} \times [inhibitor]/(K_I + [inhibitor])$ to obtain the inhibition constant (K_I) and inactivation rate constant (k_{inact}), as shown in Figure 2.5.

2.5.3 Tandem mass spectra of the labeled arginase 1 active site

Arginase 1 (10 µg) was pre-incubated in Tris buffer (50 mM Tris, 50 mM NaCl, 10% glycerol, pH = 9) with 500 µM of inhibitor 1 at room temperature. Labeled arginase 1 protein was then re-suspended in 150 µL of 50 mM Tris buffer (pH = 8.0). To this solution was added

2.0 μg of chymotrypsin (4 μL of a 0.5 μg/μL stock, Promega). The digestion was incubated at 37 °C for 16 h, and then terminated by acidification with 1% formic acid. Subsequently, Ziptip C18 pipette tips (EMD Millipore) were utilized to purify the digest. The eluent was then injected into the Thermo Fisher Q Exactive mass spectrometer for analysis. Tandem MS data were analyzed with a mass match tolerance of 40 ppm using ProteoWizard to identify sites of covalent modification. The analysis indicates that inhibitor 1 modified Thr135, which is located proximal to the catalytic residue near the active site.

2.5.4 Synthesis of compound 4

To a solution of 4-nitrobenzene acetic acid (9.0 g, 50 mmol) in absolute methanol (60 mL), concentrated sulfuric acid (1 mL) was added. The reaction mixture was refluxed for 5 hours. After the completion of the reaction, the residue was concentrated under vacuum, poured into deionized water (20 mL) and then extracted with ethyl acetate (3×10 mL). The organic layers were combined and washed with saturated aqueous NaCl (10 mL), dried over anhydrous sodium sulfate and concentrated under vacuum. The crude product was purified by silica gel column chromatography using ethyl acetate/hexane (1:8, v:v) as an eluent to afford 4 as yellow solid. Yield: 8.9 g (91%, 45.5 mmol). ^{1}H-NMR (400 MHz, CDCl$_3$) δ [ppm] = 8.21 (d, ^3J(H,H) = 8.8 Hz, 2H), 7.48 (d, ^3J(H,H) = 8.8 Hz, 2H), 3.76 (s, 2H), 3.75 (s, 3H). ^{13}C-NMR (100 MHz, CDCl$_3$) δ [ppm] = 170.6, 147.2, 141.3, 130.3, 123.8, 52.4, 40.8. GC-MS (M)$^+$ calculated for C$_9$H$_9$NO$_4$ 195.05, found 195.0.

2.5.5 Synthesis of compound 5

Compound 4 (7.8 g, 40 mmol), N-bromosuccinimide (7.8 g, 44 mmol) and azobisisobutyronitrile (AIBN, 820 mg, 5 mmol) were mixed in tetrachloromethane (60 mL). The reaction mixture was then refluxed overnight. After the completion of the reaction, the residue was poured into deionized water (100 mL) and then extracted with CH$_2$Cl$_2$ (3×50 mL). The organic layers were combined and washed with saturated aqueous NaCl (150 mL), dried over anhydrous sodium sulfate and concentrated under vacuum. The crude product was

purified by silica gel column chromatography using ethyl acetate/hexane (1:8, v:v) as an eluent to afford 5 as a white solid. Yield: 8.3 g (76%, 30.4 mmol). ^{1}H-NMR (400 MHz, CDCl$_3$) δ [ppm] = 8.22 (d, ^3J(H,H) = 8.8 Hz, 2H), 7.74 (d, ^3J(H,H) = 8.8 Hz, 2H), 5.42 (s, H), 3.82 (s, 3H). ^{13}C-NMR (100 MHz, CDCl$_3$) δ [ppm] = 168.0, 148.2, 142.5, 129.9, 124.0, 53.8, 44.2. GC-MS (M)$^+$ calculated for C$_9$H$_8$BrNO$_4$ 272.96, found 273.0.

2.5.6   Synthesis of compound 6

Compound 5 (5.5 g, 20 mmol) and silver sulfate (7.5 g, 24 mmol) were dissolved in 60 mL of a mixed solvent of dioxane/deionized water (1:1, v:v). The reaction mixture was then refluxed for 3 hours. After the completion of the reaction, the residue was concentrated under vacuum and then extracted with ethyl acetate (3×15 mL). The organic layers were combined and washed with saturated aqueous NaCl (30 mL), dried over anhydrous sodium sulfate and concentrated under vacuum. The crude product was purified by silica gel column chromatography using ethyl acetate/hexane (1:6, v:v) as an eluent to afford 6 as white solid. Yield: 3.1 g (73%, 14.6 mmol). ^{1}H-NMR (400 MHz, CDCl$_3$) δ [ppm] = 8.22 (d, ^3J(H,H) = 8.8 Hz, 2H), 7.65 (d, ^3J(H,H) = 8.4 Hz, 2H), 5.32 (s, H), 3.80 (s, 3H). ^{13}C-NMR (100 MHz, CDCl$_3$) δ [ppm] = 172.9, 147.9, 145.0, 127.5, 123.7, 72.0, 53.6. HRMS [M+H]$^+$ calculated for C$_9$H$_9$NO$_5$: 212.0561 found 212.0569.

2.5.7   Synthesis of compound 7

Compound 6 (3.0 g, 14 mmol) and 5% Pd/C (300 mg) were combined in methanol (20 mL). The reaction mixture was then stirred at room temperature overnight under an atmosphere of H$_2$ using a ballon filled with H$_2$. After the reaction was complete, the residue was filtered, and the organic solution was concentrated under vacuum. The crude product was purified by silica gel column chromatography using ethyl acetate/hexane (1:3, v:v) as an eluent to afford 7 as white solid. Yield: 2.4 g (95%, 13.3 mmol). ^{1}H-NMR (400 MHz, CD$_3$OD) δ [ppm] = 7.15 (d, ^3J(H,H) = 8.0 Hz, 2H), 6.70 (d, ^3J(H,H) = 8.4 Hz, 2H), 5.05 (s, H), 3.69 (s, 3H). ^{13}C-NMR (100 MHz, CD$_3$OD) δ [ppm] = 174.0, 147.9, 129.4, 127.6, 114.8, 72.8,

51.1. HRMS $[M+H]^+$ calculated for $C_9H_{11}NO_3$: 182.0819 found 182.0824.

2.5.8 1,3-Bis(tert-butoxycarbonyl)-2-methyl-2-thiopseudourea

S-methylisothiourea sulfate (6.95 g, 50 mmol) was dissolved in a mixture of H_2O (80 mL) and dioxane (80 mL) followed by addition of 2 M aq NaOH solution (50 mL, 100 mmol) and di-tert-butyl dicarbonate (26.2 g, 120 mmol, 1.2 equiv). The reaction mixture was stirred at room temperature overnight. After the completion of the reaction, the residue was concentrated under vacuum and then extracted with ethyl acetate (3×30 mL). The organic layers were combined and washed with saturated aqueous NaCl (50 mL), dried over anhydrous sodium sulfate and concentrated under vacuum. The crude product was purified by silica gel column chromatography using ethyl acetate/ hexane (1:8, v:v) as an eluent to afford product as white solid. Yield: 11.9 g (82%, 41 mmol). ^{1}H-NMR (400 MHz, CDCl$_3$) δ [ppm] = 2.37 (s, 3H), 1.50 (s, 9H), 1.49 (s, 9H). ^{13}C-NMR (100 MHz, CDCl$_3$) δ [ppm] = 171.5, 146.7, 85.1, 28.2, 28.0, 27.8, 27.4, 14.4. HRMS $[M+H]^+$ calculated for $C_{12}H_{22}N_2O_4S$: 291.1380 found 291.1371.

2.5.9 Synthesis of compound 8

Compound 7 (1.8 g, 10 mmol), 1,3-bis(tert-butoxycarbonyl)-2-methyl-2-thiopseudourea (3.2 g, 11 mmol), silver nitrate (2.0 g, 12 mmol), and triethylamine (1.7 ml, 12 mmol) were mixed in CH_2Cl_2 (60 mL). The reaction mixture was stirred at room temperature overnight. After the completion of the reaction, the residue was poured into deionized water (50 mL) and then extracted with ethyl acetate (3×30 mL). The organic layers were combined and washed with saturated aqueous NaCl (50 mL), dried over anhydrous sodium sulfate and concentrated under vacuum. The crude product was purified by silica gel column chromatography using ethyl acetate/hexane (1:6, v:v) as an eluent to afford 8 as white solid. Yield: 3.1 g (74%, 7.4 mmol). ^{1}H-NMR (400 MHz, CDCl$_3$) δ [ppm] = 11.65 (br s, H), 10.36 (br s, H), 7.59 (d, ^3J(H,H) = 8.8 Hz, 2H), 7.36 (d, ^3J(H,H) = 8.4 Hz, 2H), 5.13 (s, H), 3.73 (s, 3H), 3.56 (br s, H), 1.53 (s, 9H), 1.50 (s, 9H). ^{13}C-NMR (100 MHz, CDCl$_3$) δ [ppm] = 174.0, 153.5,

153.3, 136.9, 134.6, 127.2, 122.3, 83.8, 79.7, 72.4, 53.0, 29.7, 29.6, 29.4, 28.1, 28.0. HRMS $[M+H]^+$ calculated for $C_{20}H_{29}N_3O_7$: 424.2086 found 424.2082.

2.5.10 Synthesis of compound 9

Compound 8 (846 mg, 2 mmol) was dissolved in CH_2Cl_2 (20 mL) followed by addition of diethylaminosulfur trifluoride (289 µL, 354 mg, 2.2 mmol) in CH_2Cl_2 (5.0 mL). The reaction mixture was stirred at 0 °C for 30 min, and was then quenched by addition of a saturated solution of NaCl (10 mL), and allowed to stir for an additional 15 min. After the completion of the quenching reaction, the residue was poured into deionized water (30 mL), and then was extracted with CH_2Cl_2 (3×10 mL). The organic layers were combined and washed with saturated aqueous NaCl, dried over anhydrous sodium sulfate and concentrated under vacuum. The crude product was purified by silica gel column chromatography using ethyl acetate/hexane (1:8, v:v) as an eluent to afford 9 as white solid. Yield: 697 mg (82%, 1.64 mmol). ^{1}H-NMR (400 MHz, CDCl$_3$) δ [ppm] = 11.65 (s, H), 10.42 (s, H), 7.67 (d, ^3J(H,H) = 6.8 Hz, 2H), 7.43 (d, ^3J(H,H) = 6.8 Hz, 2H), 5.76 (d, ^2J(H,F) = 47.6 Hz, H), 3.78 (s, 3H), 1.55 (s, 9H), 1.52 (s, 9H). ^{13}C-NMR (100 MHz, CDCl$_3$) δ [ppm] = 169.1, 168.8, 163.4, 153.5, 153.3, 138.1, 130.3, 130.1, 127.5, 127.4, 122.3, 89.0 (d, ^1J(C,F) = 184 Hz), 84.0, 79.9, 52.7, 28.2, 28.1. ^{19}F-NMR (376 MHz) δ [ppm] = -178.8 (d, ^2J(H,F) = 48.8 Hz). HRMS $[M+H]^+$ calculated for $C_{20}H_{28}FN_3O_6$: 426.2042 found 426.2051.

2.5.11 Synthesis of compound 10 and inhibitor 1

Compound 9 (553 mg, 1.3 mmol) was dissolved in a mixture of H_2O (2 mL) and methanol (2 mL) followed by addition of 1 M aq KOH solution (2 mL) dropwise. The reaction mixture was stirred at room temperature for 3 hours. After this time, methanol was removed under reduced pressure. The residual aqueous solution was diluted with H_2O (5 mL) and extracted with Et_2O (2×10 mL). The aqueous layer was then acidified with 1 M aqueous HCl which resulted in the precipitation of a white solid. The aqueous phase was then extracted with Et_2O (3×5 mL). The organic layers were combined and washed with saturated aqueous

NaCl (10 mL), dried over anhydrous sodium sulfate and concentrated under vacuum. The crude product 10 was dissolved in a mixture of CH_2Cl_2/TFA (1:1; 2 mL) and stirred at room temperature for 24 h, after which time the CH_2Cl_2 and TFA were removed under reduced pressure. The crude product was purified by HPLC to afford inhibitor 1 as a white solid. Yield: 78 mg (29%, 0.37 mmol). ^{1}H-NMR (400 MHz, CD_3OD) δ [ppm] = 7.63 (d, [3]J(H,H) = 7.2 Hz, 2H), 7.38 (d, [3]J(H,H) = 6.8 Hz, 2H), 5.77 (d, [2]J(H,F) = 48.4 Hz, H). ^{13}C-NMR (100 MHz, CD_3OD) δ [ppm] = 178.0, 153.3, 138.2, 129.9, 127.6, 124.5, 89.0 (d, [1]J(C,F) = 185 Hz). ^{19}F-NMR (376 MHz) δ [ppm] = -178.9 (d, [2]J(H,F) = 48.8 Hz). HRMS [M+H][+] calculated for $C_9H_{10}FN_3O_2$: 212.0837 found 212.0845.

2.5.12   Synthesis of compound 11

Compound 8 (846 mg, 2 mmol) was dissolved in a mixture of H_2O (2 mL) and methanol (2 mL) followed by addition of 1 M aq KOH solution (2 mL) dropwise. The reaction mixture was stirred at room temperature for 3 hours, after which time the methanol was removed under reduced pressure. The residual aqueous solution was diluted with H_2O (5 mL) and extracted with Et_2O (2×10 mL). The aqueous layer was then acidified with 1M aqueous HCl, which resulted in the precipitation of a white solid. The aqueous phase was then extracted with Et_2O (3×5 mL). The organic layers were combined and washed with saturated aqueous NaCl (10 mL), dried over anhydrous sodium sulfate and concentrated under vacuum. The crude product was purified by silica gel column chromatography using ethyl acetate/hexane (1:1, v:v) as an eluent to afford 11 as white solid. Yield: 654 mg (80%, 1.6 mmol). ^{1}H-NMR (400 MHz, CD_3OD) δ [ppm] = 7.58 (d, [3]J(H,H) = 8.8 Hz, 2H), 7.35 (d, [3]J(H,H) = 8.4 Hz, 2H), 5.12 (s, H), 1.52 (s, 9H), 1.49 (s, 9H). ^{13}C-NMR (100 MHz, CD_3OD) δ [ppm] = 178.0, 153.6, 153.3, 137.1, 134.6, 127.3, 122.4, 84.0, 79.9, 72.8, 28.6, 28.3. HRMS [M+H][+] calculated for $C_{19}H_{27}N_3O_7$: 410.1929 found 410.1933.

2.5.13 Synthesis of compound 12 and inhibitor 2

Compound 11 (531 mg, 1.3 mmol), pyridine (0.5 mL), acetic anhydride (306 mg, 3 mmol) and 4-dimethylaminopyridine (10 mg) were mixed in CH_2Cl_2 (10 mL). The reaction mixture was stirred at room temperature for 5 hours. After the completion of the reaction, the reaction mixture was poured into deionized water (10 mL), acidified with 1M aqueous HCl and then extracted with CH_2Cl_2 (3×10 mL). The organic layers were combined and washed with saturated aqueous NaCl (30 mL), dried over anhydrous sodium sulfate and concentrated under vacuum. The crude product 12 was dissolved in a mixture of CH_2Cl_2/TFA (1:1, 2 mL) and stirred at room temperature for 24 h. After this time the CH_2Cl_2 and TFA were removed under reduced pressure. The crude product was purified by HPLC to afford inhibitor 2 as white solid. Yield: 83 mg (25%, 0.33 mmol). ^{1}H-NMR (400 MHz, CD_3OD) δ [ppm] = 7.61 (d, ^3J(H,H) = 8.4 Hz, 2H), 7.40 (d, ^3J(H,H) = 8.8 Hz, 2H), 6.05 (s, H), 2.15 (s, 3H). ^{13}C-NMR (100 MHz, CD_3OD) δ [ppm] = 178.5, 168.7, 153.2, 138.5, 129.5, 128.1, 125.3, 73.1, 20.2. HRMS [M+H]$^+$ calculated for $C_{11}H_{13}N_3O_4$: 252.0986 found 252.0991.

2.6 Characterization of compounds

Spectra of compound (4)

^{1}H-NMR
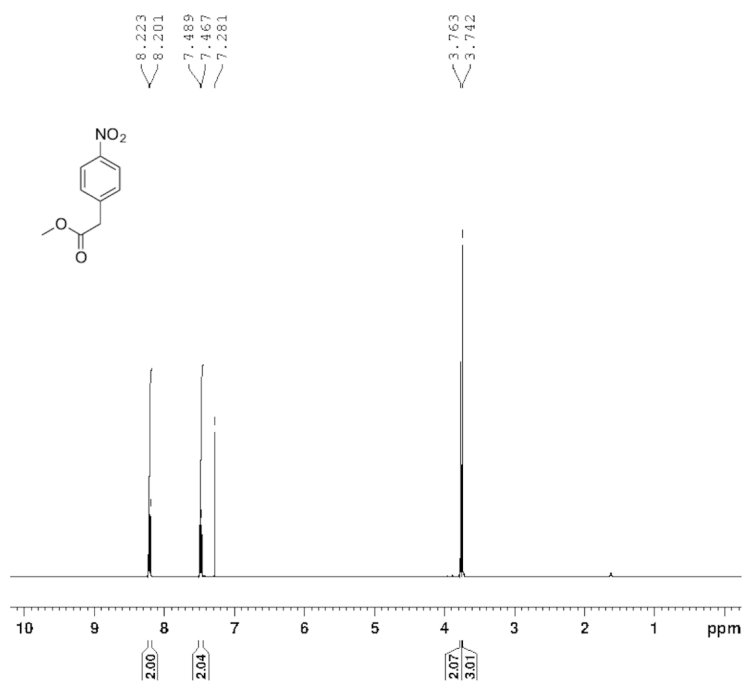
^{13}C-NMR
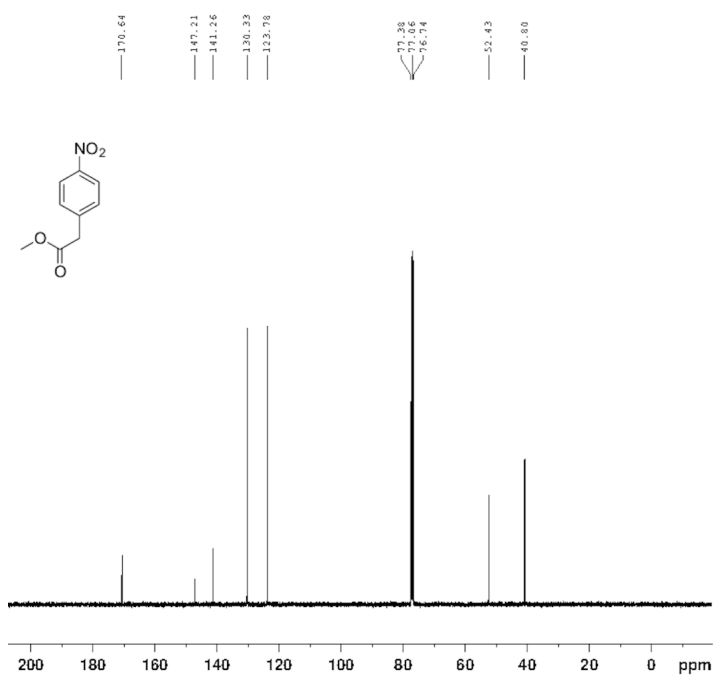
Spectra of compound (5)

^{1}H-NMR
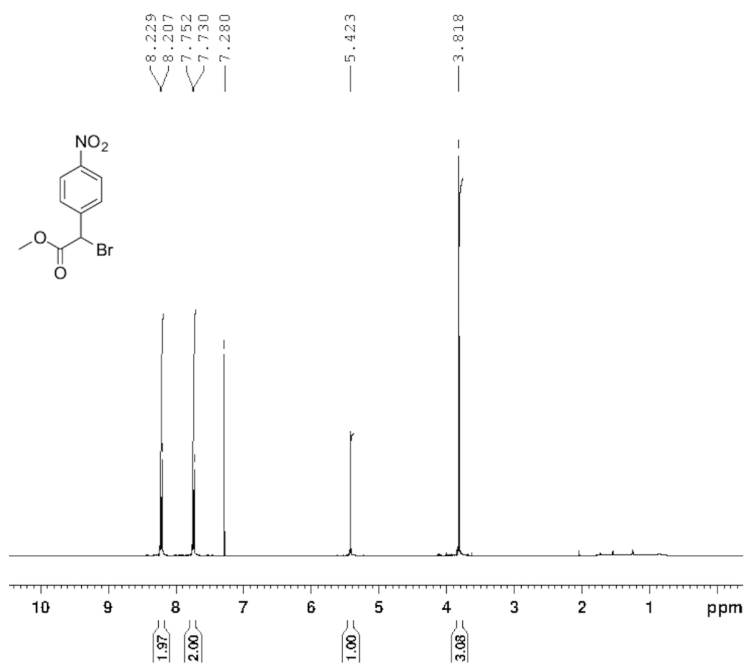
^{13}C-NMR
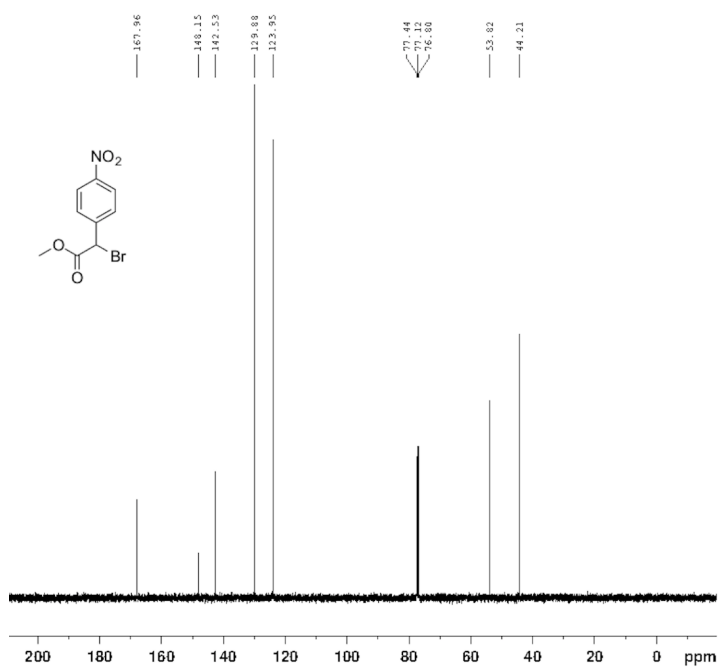
Spectra of compound (6)

¹H-NMR
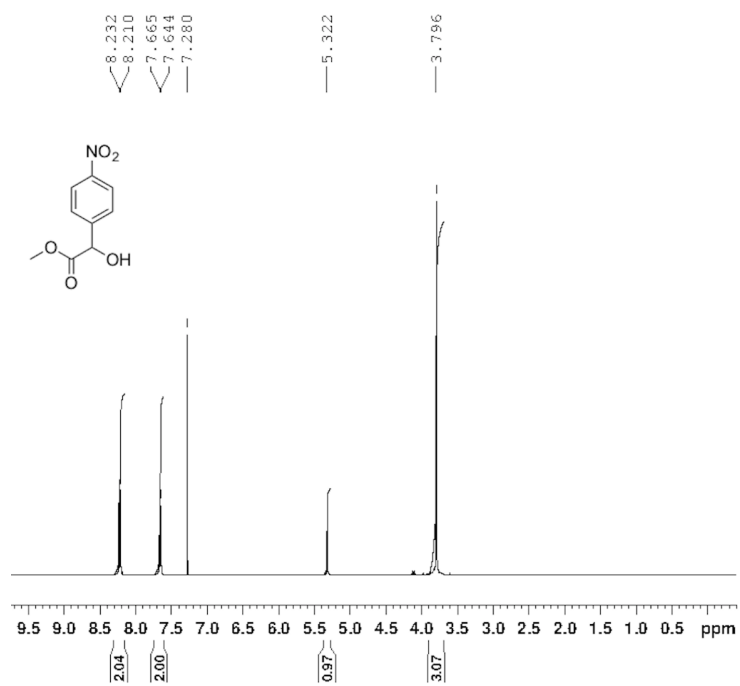
¹³C-NMR
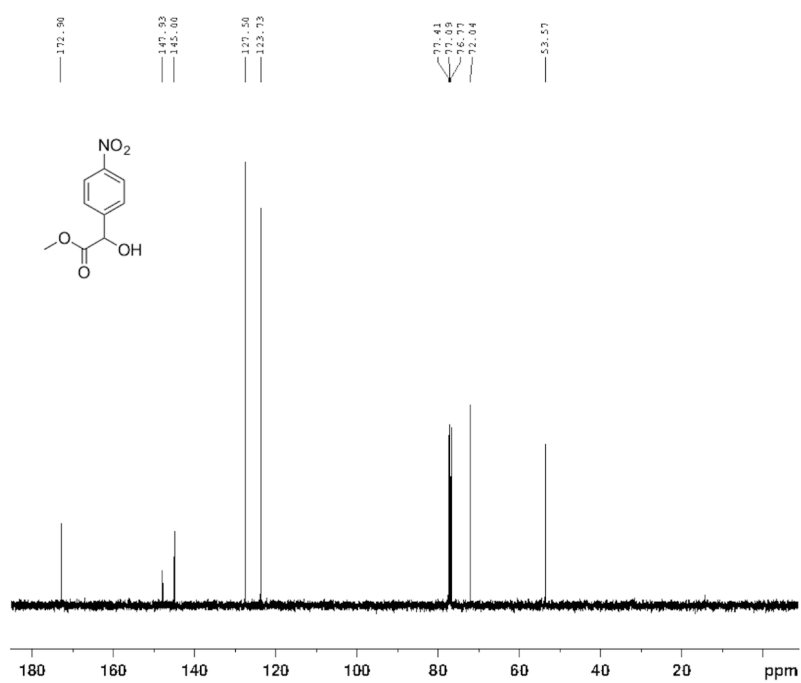
Spectra of compound (7)

^{1}H-NMR
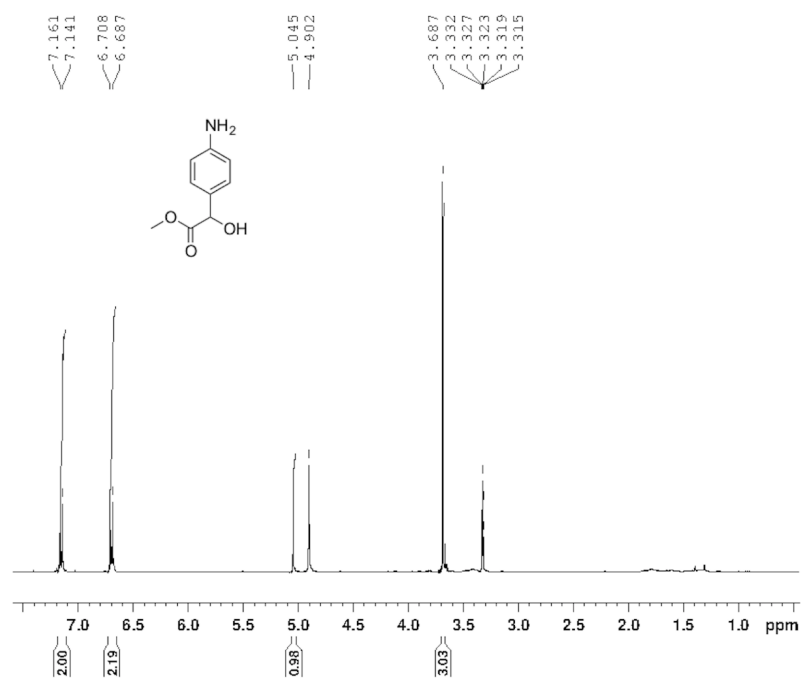
^{13}C-NMR
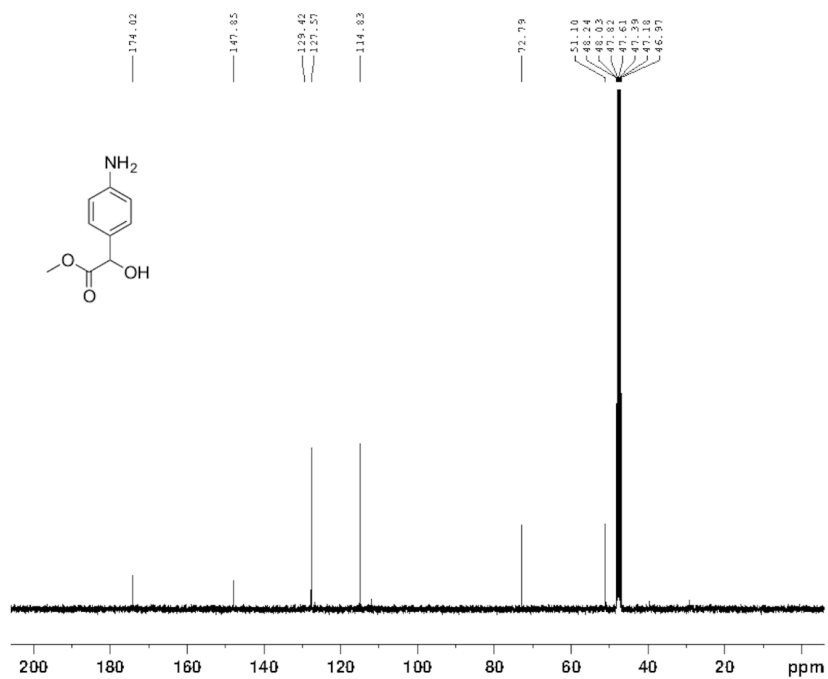
Spectra of 1,3-bis(tert-butoxycarbonyl)-2-methyl-2-thiopseudourea

^{1}H-NMR
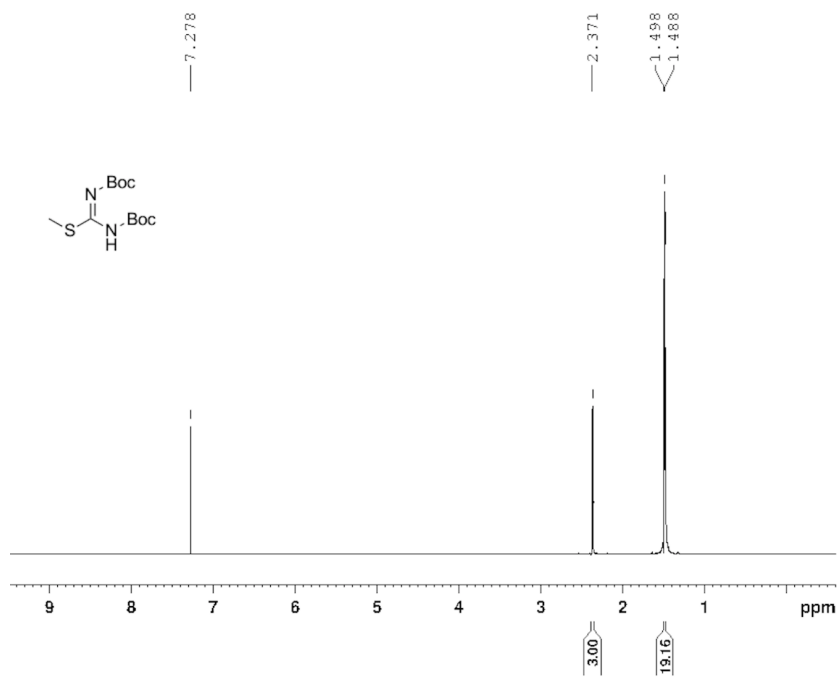
^{13}C-NMR
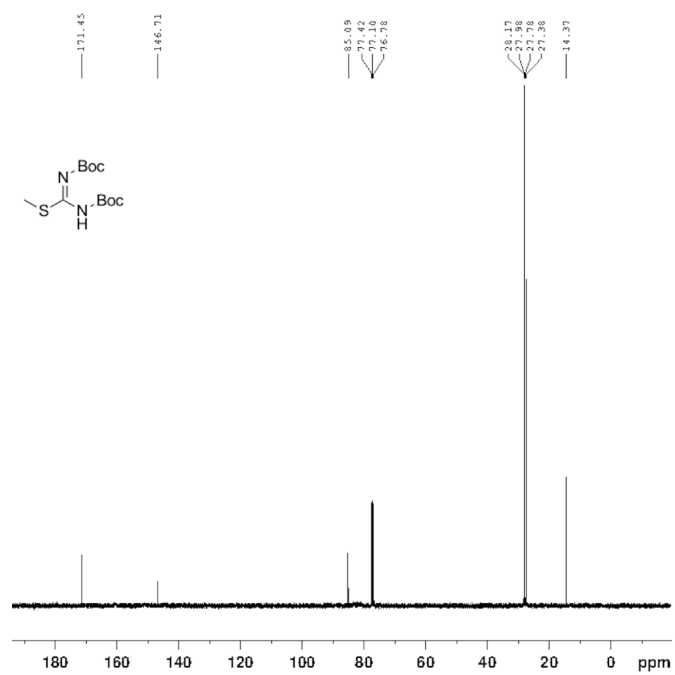
Spectra of compound (8)

¹H-NMR
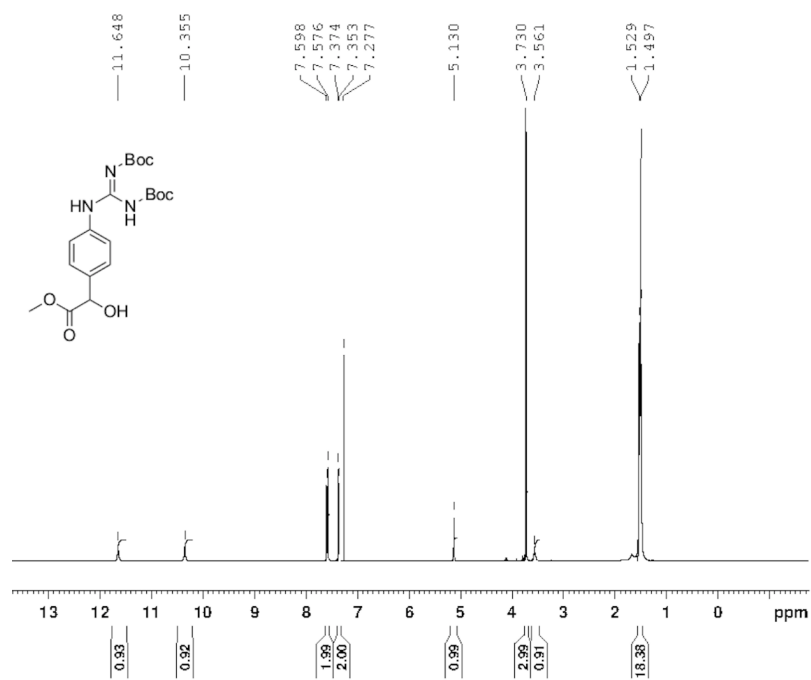
¹³C-NMR
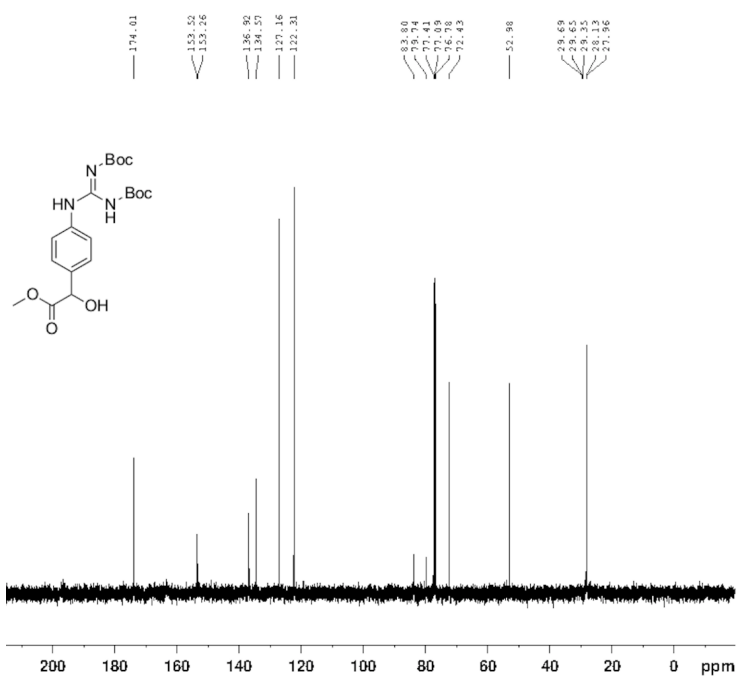
Spectra of compound (9)

¹H-NMR

¹³C-NMR

¹⁹F-NMR

^{19}F-NMR

11.646
10.427
7.676
7.659
7.439
7.422
7.272
5.819
5.700
3.776
1.547
1.518

0.97   0.97   2.05 2.01   1.00   3.00   18.52
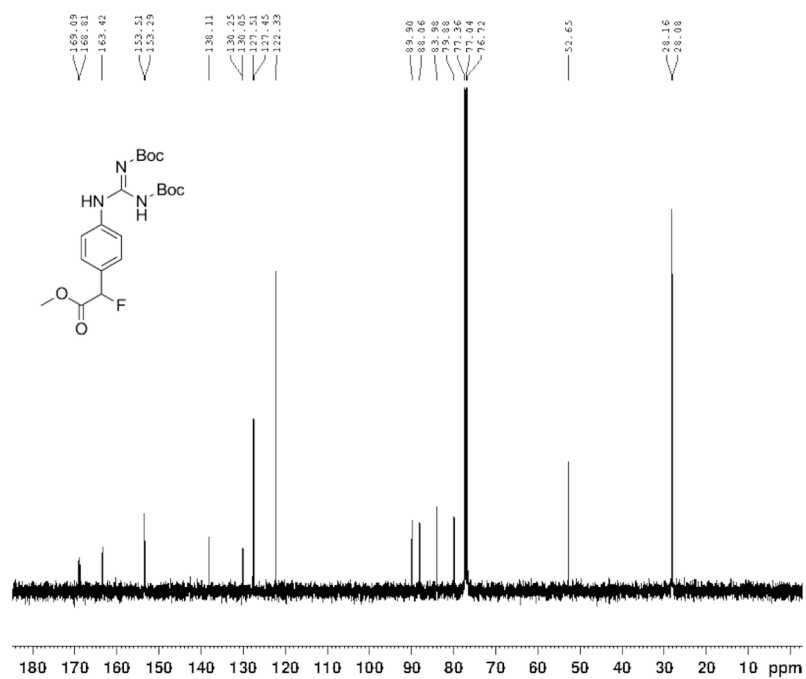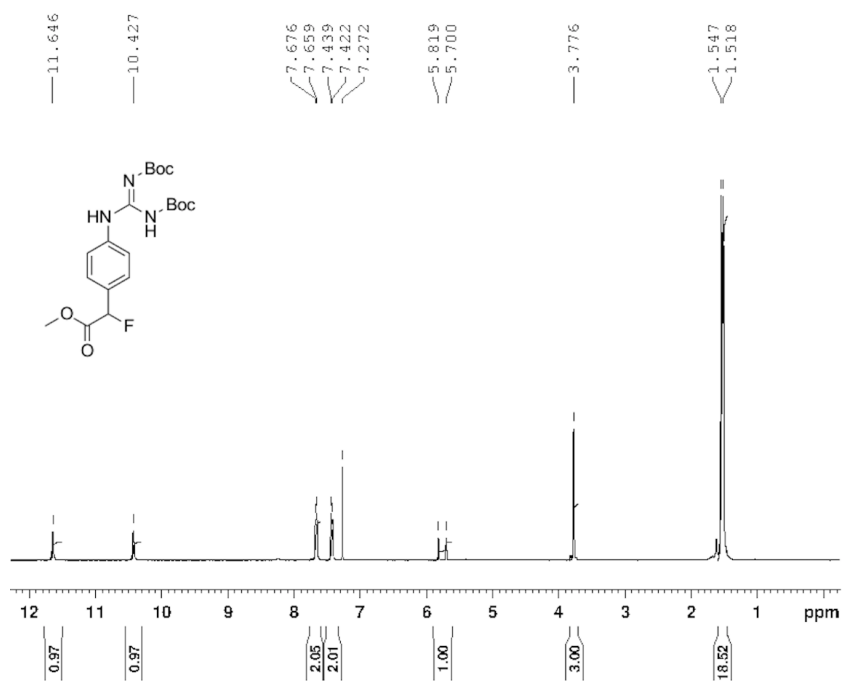
Spectra of inhibitor (1)

¹H-NMR

^{1}H-NMR

7.637
7.619
7.399
7.372
5.876
5.670
4.912
3.332
3.327
3.323
3.319
3.315

2.07 2.02   1.00
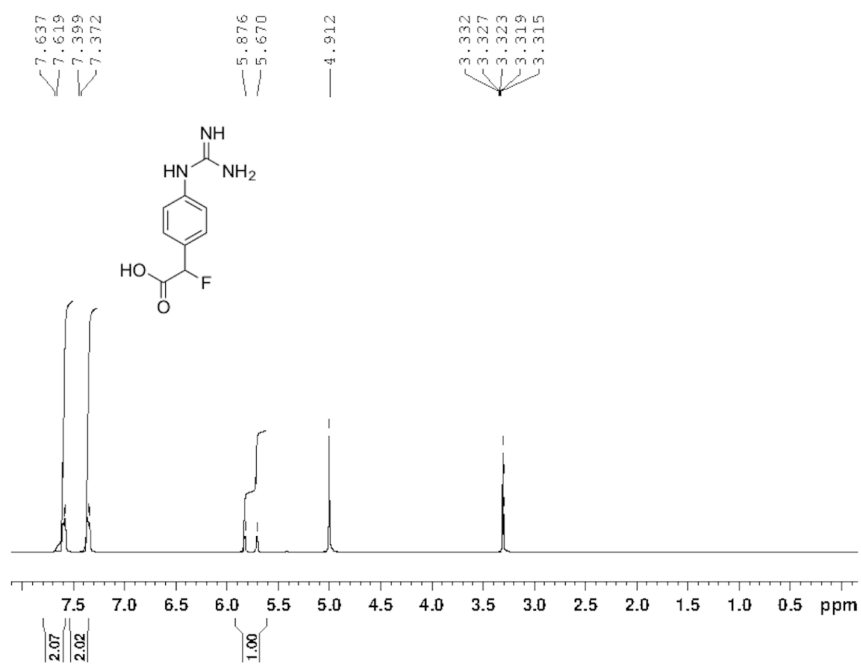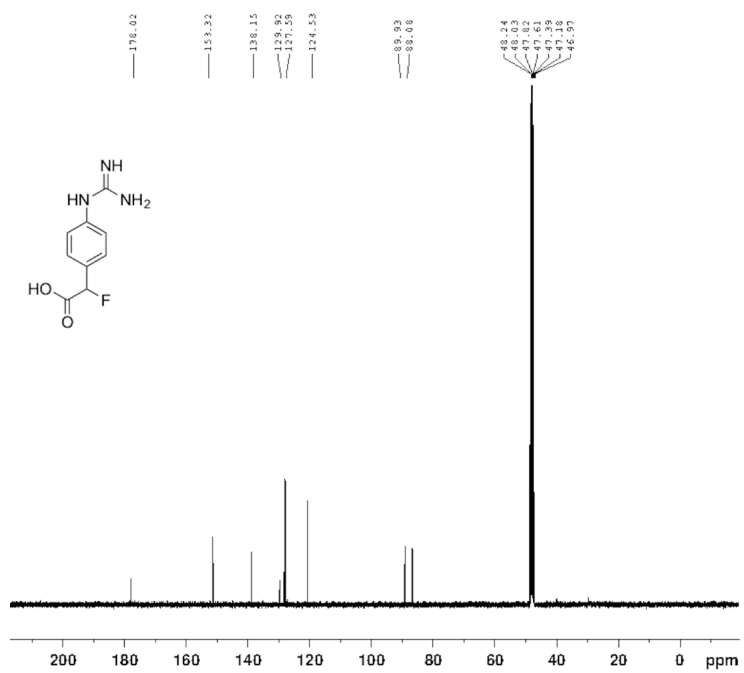
^{13}C-NMR

^{19}F-NMR
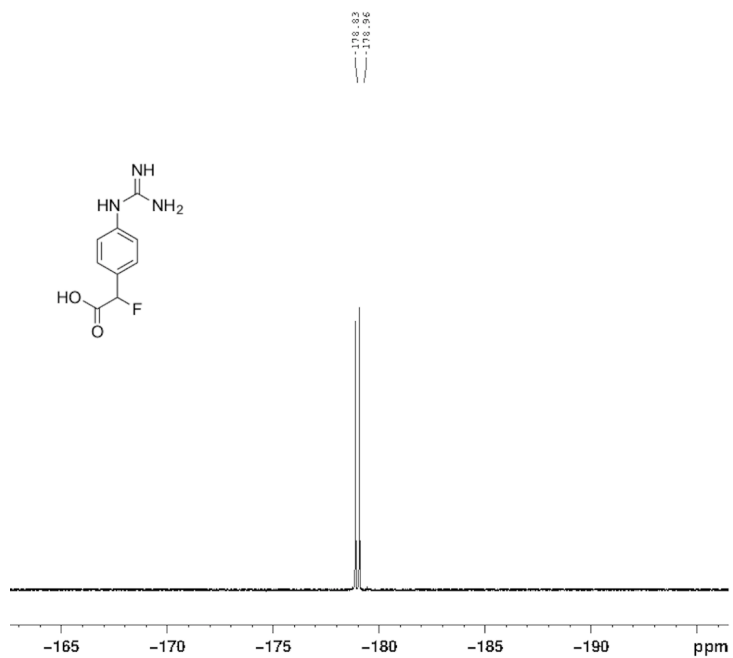
Spectra of compound (11)

^{1}H-NMR
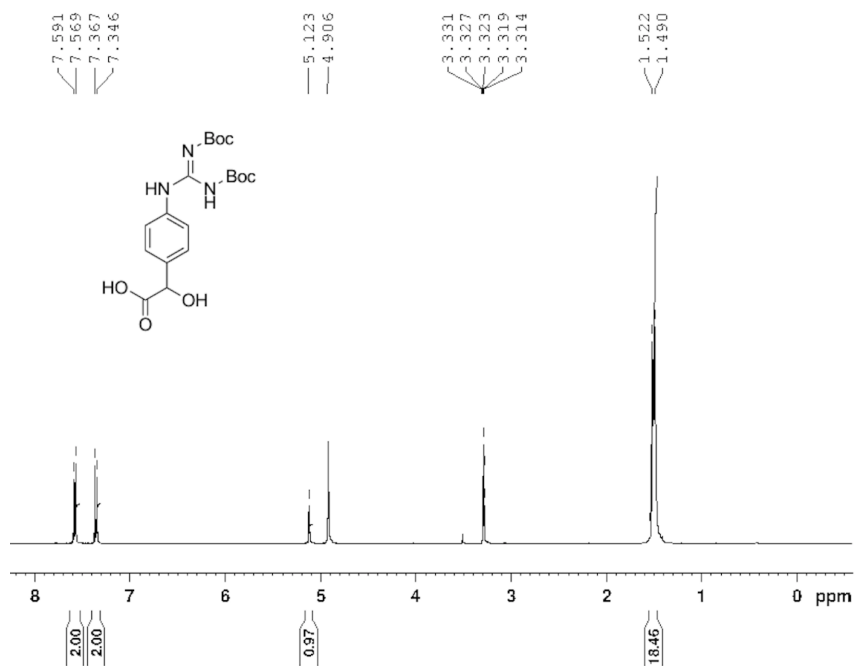
^{13}C-NMR
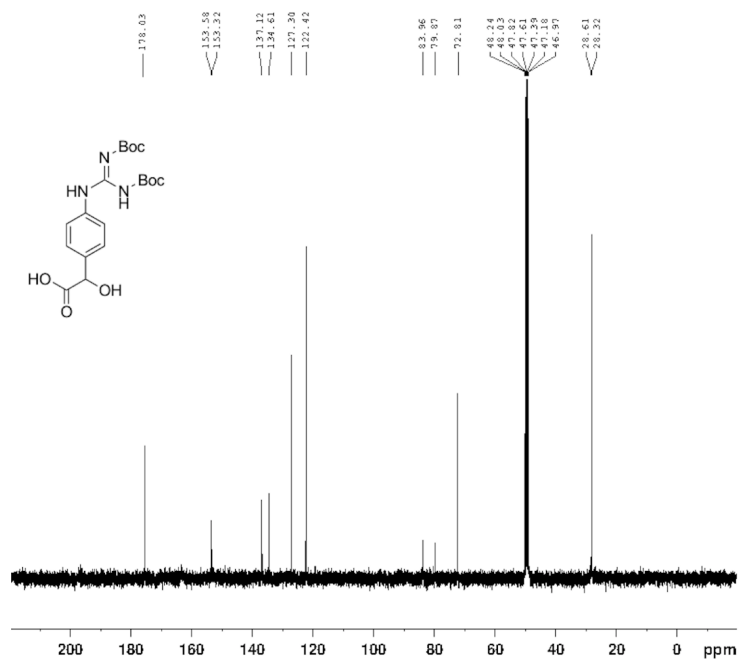
Spectra of inhibitor (2)

^{1}H-NMR
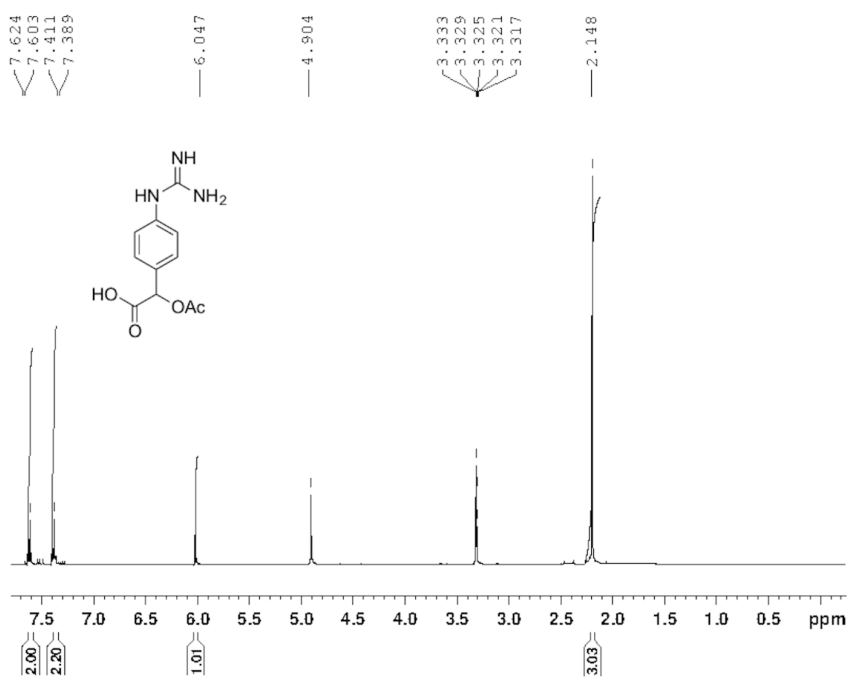
^{13}C-NMR
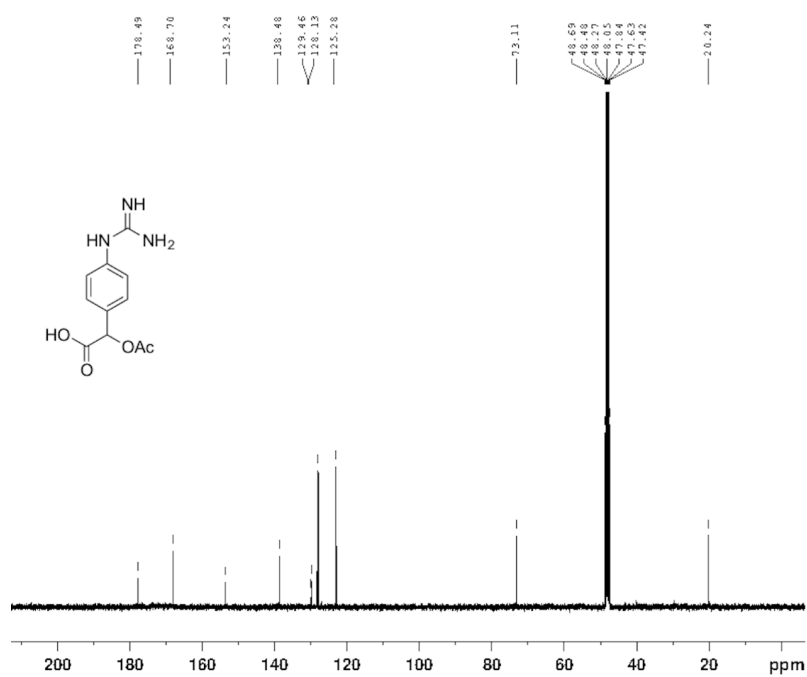
References

[1] Ash, D. E. Structure and function of arginases. *The Journal of Nutrition* **2004**, *134*, 2760S–2764S.

[2] Maarsingh, H.; Zaagsma, J.; Meurs, H. Arginase: a key enzyme in the pathophysiology of allergic asthma opening novel therapeutic perspectives. *British Journal of Pharmacology* **2009**, *158*, 652–664.

[3] Guoyao, W.; Morris, S. M. Arginine metabolism: nitric oxide and beyond. *Biochemical Journal* **1998**, *336*, 1–17.

[4] Elms, S.; Chen, F.; Wang, Y.; Qian, J.; Askari, B.; Yu, Y.; Pandey, D.; Iddings, J.; Caldwell, R. B.; Fulton, D. J. Insights into the arginine paradox: evidence against the importance of subcellular location of arginase and eNOS. *American Journal of Physiology-Heart and Circulatory Physiology* **2013**, *305*, H651–H666.

[5] Morris Jr, S. M. Recent advances in arginine metabolism: roles and regulation of the arginases. *British Journal of Pharmacology* **2009**, *157*, 922–930.

[6] Duleu, S.; Vincendeau, P.; Courtois, P.; Semballa, S.; Lagroye, I.; Daulouède, S.; Boucher, J.-L.; Wilson, K. T.; Veyret, B.; Gobert, A. P. Mouse strain susceptibility to trypanosome infection: an arginase-dependent effect. *The Journal of Immunology* **2004**, *172*, 6298–6303.

[7] Stijlemans, B.; Caljon, G.; Van Den Abbeele, J.; Van Ginderachter, J. A.; Magez, S.;

De Trez, C. Immune evasion strategies of Trypanosoma brucei within the mammalian host: progression to pathogenicity. *Frontiers in Immunology* **2016**, *7*, 233.

[8] Das, P.; Lahiri, A.; Lahiri, A.; Chakravortty, D. Modulation of the arginase pathway in the context of microbial pathogenesis: a metabolic enzyme moonlighting as an immune modulator. *PLOS Pathogens* **2010**, *6*, e1000899.

[9] Drennan, M. B.; Stijlemans, B.; Van Den Abbeele, J.; Quesniaux, V. J.; Barkhuizen, M.; Brombacher, F.; De Baetselier, P.; Ryffel, B.; Magez, S. The induction of a type 1 immune response following a Trypanosoma brucei infection is MyD88 dependent. *The Journal of Immunology* **2005**, *175*, 2501–2509.

[10] Oladiran, A.; Belosevic, M. Immune evasion strategies of trypanosomes: a review. *Journal of Parasitology* **2012**, *98*, 284–292.

[11] DAntonio, E. L.; Ullman, B.; Roberts, S. C.; Dixit, U. G.; Wilson, M. E.; Hai, Y.; Christianson, D. W. Crystal structure of arginase from Leishmania mexicana and implications for the inhibition of polyamine biosynthesis in parasitic infections. *Archives of Biochemistry and Biophysics* **2013**, *535*, 163–176.

[12] Heby, O.; Persson, L.; Rentala, M. Targeting the polyamine biosynthetic enzymes: a promising approach to therapy of African sleeping sickness, Chagas disease, and leishmaniasis. *Amino Acids* **2007**, *33*, 359–366.

[13] Di Costanzo, L.; Ilies, M.; Thorn, K. J.; Christianson, D. W. Inhibition of human arginase I by substrate and product analogues. *Archives of Biochemistry and Biophysics* **2010**, *496*, 101–108.

[14] Busnel, O.; Carreaux, F.; Carboni, B.; Pethe, S.; Vadon-Le Goff, S.; Mansuy, D.; Boucher, J.-L. Synthesis and evaluation of new ω-borono-α-amino acids as rat liver arginase inhibitors. *Bioorganic & Medicinal Chemistry* **2005**, *13*, 2373–2379.

[15] Baggio, R.; Emig, F. A.; Christianson, D. W.; Ash, D. E.; Chakder, S.; Rattan, S. Biochemical and functional profile of a newly developed potent and isozyme-selective arginase inhibitor. *Journal of Pharmacology and Experimental Therapeutics* **1999**, *290*, 1409–1416.

[16] Golebiowski, A.; Beckett, R. P.; Van Zandt, M.; Ji, M. K.; Whitehouse, D.; Ryder, T. R.; Jagdmann, E.; Andreoli, M.; Mazur, A.; Padmanilayam, M. 2-Substituted-2-amino-6-boronohexanoic acids as arginase inhibitors. *Bioorganic & Medicinal Chemistry Letters* **2013**, *23*, 2027–2030.

[17] Das, B. C.; Thapa, P.; Karki, R.; Schinke, C.; Das, S.; Kambhampati, S.; Banerjee, S. K.; Van Veldhuizen, P.; Verma, A.; Weiss, L. M. Boron chemicals in diagnosis and therapeutics. *Future Medicinal Chemistry* **2013**, *5*, 653–676.

[18] Rut, W.; Zhang, L.; Kasperkiewicz, P.; Poreba, M.; Hilgenfeld, R.; Drąg, M. Extended substrate specificity and first potent irreversible inhibitor/activity-based probe design for Zika virus NS2B-NS3 protease. *Antiviral Research* **2017**, *139*, 88–94.

[19] Kathman, S. G.; Xu, Z.; Statsyuk, A. V. A fragment-based method to discover irreversible covalent inhibitors of cysteine proteases. *Journal of Medicinal Chemistry* **2014**, *57*, 4969–4974.

[20] Kung, A.; Chen, Y.-C.; Schimpl, M.; Ni, F.; Zhu, J.; Turner, M.; Molina, H.; Overman, R.; Zhang, C. Development of specific, irreversible inhibitors for a receptor tyrosine kinase EphB3. *Journal of the American Chemical Society* **2016**, *138*, 10554–10560.

[21] Henise, J. C.; Taunton, J. Irreversible Nek2 kinase inhibitors with cellular activity. *Journal of Medicinal Chemistry* **2011**, *54*, 4133–4146.

[22] Tjin, C. C.; Otley, K. D.; Baguley, T. D.; Kurup, P.; Xu, J.; Nairn, A. C.; Lombroso, P. J.; Ellman, J. A. Glutathione-responsive selenosulfide prodrugs as a platform strategy for potent and selective mechanism-based inhibition of protein tyrosine phosphatases. *ACS Central Science* **2017**, *3*, 1322–1328.

[23] Ge, L.; Li, K.-s.; Li, M.-m.; Xiao, P.; Hou, X.-b.; Chen, X.; Lin, A.; Yu, X.; Ren, G.-j.; Fang, H. Identification of a benzo imidazole thiazole derivative as the specific irreversible inhibitor of protein tyrosine phosphatase. *Bioorganic & Medicinal Chemistry Letters* **2016**, *26*, 4795–4798.

[24] Singh, J.; Petter, R. C.; Baillie, T. A.; Whitty, A. The resurgence of covalent drugs. *Nature Reviews Drug Discovery* **2011**, *10*, 307.

[25] Kuo, C.-C.; Chu, C.-Y.; Lin, J.-J.; Lo, L.-C. Selective activation of SHP2 activity by cisplatin revealed by a novel chemical probe-based assay. *Biochemical and Biophysical Research Communications* **2010**, *391*, 230–234.

[26] Shen, K.; Qi, L.; Ravula, M.; Klimaszewski, K. Synthesis and peptide incorporation of an unnatural amino acid containing activity-based probe for protein tyrosine phosphatases. *Bioorganic & Medicinal Chemistry Letters* **2009**, *19*, 3264–3267.

[27] Lo, L.-C.; Chiang, Y.-L.; Kuo, C.-H.; Liao, H.-K.; Chen, Y.-J.; Lin, J.-J. Study of the preferred modification sites of the quinone methide intermediate resulting from the latent trapping device of the activity probes for hydrolases. *Biochemical and Biophysical Research Communications* **2004**, *326*, 30–35.

[28] Lo, L.-C.; Pang, T.-L.; Kuo, C.-H.; Chiang, Y.-L.; Wang, H.-Y.; Lin, J.-J. Design and synthesis of class-selective activity probes for protein tyrosine phosphatases. *Journal of Proteome Research* **2002**, *1*, 35–40.

[29] Di Costanzo, L.; Sabio, G.; Mora, A.; Rodriguez, P. C.; Ochoa, A. C.; Centeno, F.; Christianson, D. W. Crystal structure of human arginase I at 1.29-Å resolution and exploration of inhibition in the immune response. *Proceedings of the National Academy of Sciences* **2005**, *102*, 13058–13063.

[30] Han, S.; Viola, R. E. A spectrophotometric assay of arginase. *Analytical Biochemistry* **2001**, *295*, 117–119.

[31] Alarcón, R.; Orellana, M. S.; Neira, B.; Uribe, E.; García, J. R.; Carvajal, N. Mutational analysis of substrate recognition by human arginase type I- agmatinase activity of the N130D variant. *The FEBS Journal* **2006**, *273*, 5625–5631.

[32] López, V.; Alarcón, R.; Orellana, M. S.; Enríquez, P.; Uribe, E.; Martínez, J.; Carvajal, N. Insights into the interaction of human arginase II with substrate and manganese ions by site-directed mutagenesis and kinetic studies. *The FEBS Journal* **2005**, *272*, 4540–4548.

[33] Simon, E. S.; Papoulias, P. G.; Andrews, P. C. Gas-phase fragmentation characteristics of benzyl-aminated lysyl-containing tryptic peptides. *Journal of the American Society for Mass Spectrometry* **2010**, *21*, 1624–1632.

Chapter 3

NiPd Nanoparticles Assembled on Nitrogen-Doped Graphene for the Synthesis of Quinazolines[†]

3.1 Abstract

We report a facile interface assembly method to assemble a monolayer array of nitrogen-doped graphene (NG) and nanoparticles (NPs) and then to transfer the dual monolayers onto a solid substrate. Using 3 nm NiPd NPs as an example, we demonstrate that NiPd-NG-Si can function as a catalyst probe and show maximum NiPd catalysis for the hydrolysis of ammonia borane (H$_3$NBH$_3$, AB) with a TOF $= 4896.8$ h^{-1} and $E_a = 18.8$ kJ/mol. The NiPd-NG-Si is also highly active for catalyzing transfer hydrogenation from AB to nitro groups, leading to the green chemistry synthesis of quinazolines in water. Our assembly method can be extended to other graphene and NP catalyst materials, providing a new 2D NP catalyst platform for catalyzing multiple reactions in one-pot with maximum efficiency.

3.2 Introduction

The recent push for green chemistry syntheses of functional molecules and materials requires new and efficient catalysts that are able to catalyze multiple chemical reactions. Such catalysts can also serve as models for developing a better understanding of how to design and optimize multifunctional catalysts. One way that this problem has been addressed is to have catalysts arranged in a two-dimensional (2D) array so that each single catalyst unit is exposed to reactants equally for a specific reaction. This is conventionally achieved by using the lithography process in which a catalytically active material is deposited on a pre-patterned substrate.[1–8] Recently, self-assembly techniques have advanced to a level that functional nanoparticles (NPs) can be deposited on a flat surface[9–16] and serve as a catalyst layer to achieve higher catalytic activity.[17–22] However, this approach has been limited to NP deposition on bulk solid surfaces. Efforts to deposit NPs on a flat nanoscale support, such as graphene (G), have met with only limited success for catalytic applications because of difficulties in controlling monodisperse NP deposition on a flat G surface,[14,23–27] or in unfolding the NP-modified G into a flat NP-G array.[28–32]

Here we report a facile assembly approach to consecutive monolayer assembly of nitrogen-doped G (NG) and NPs to achieve a monolayer NP deposition on NG and further on a flat solid substrate, as outlined in Figure 3.1. Our assembly strategy is based on liquid/liquid self-assembly of NPs reported as a way for rapid fabrication of 2D nanostructures.[33–35] By controlling solvent types and solvent evaporation on the water phase, we are able to assemble a monolayer array of NG (Figure 3.1a), and then a monolayer assembly of NPs (Figure 3.1b). By lifting a solid substrate (S) from a water phase, we can transfer the monolayer assembly of NPs and NG onto S, giving NPs-NG-S (Figure 3.1c). The assembly method can be extended to G in general, but pristine G cannot stabilize NPs well enough to survive the NP activation process tested in this paper for catalysis. NG is a better choice for anchoring/stabilizing NPs for catalytic studies due to the N-doping induced disruption of the π-electron cloud on the G surface.[14,36,37] When proper NPs are chosen for the assembly, the NPs-NG-S can serve as a convenient catalyst probe: Inserting the probe into a solution containing all required reactants will trigger a series of cascade reactions, while pulling the probe out of the solution will stop the reactions (Figure 3.1c). In this way, we can achieve rational control of reaction kinetics and product formation.
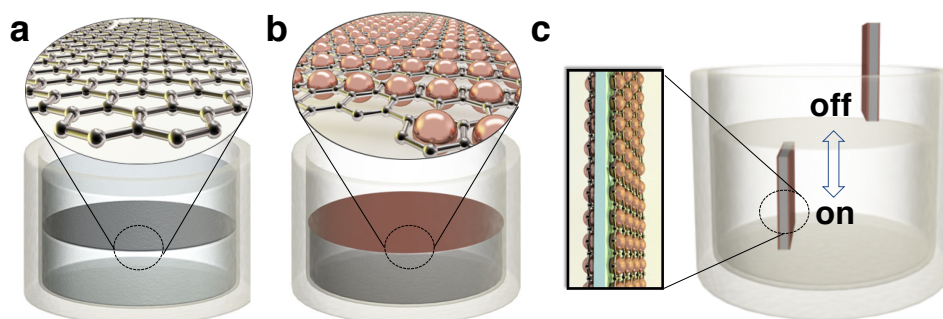
Figure 3.1 (a) Schematic illustration of the interface assembly of monolayer NG. (b) Interface assembly of NPs-NG. (c) Assembled NPs-NG on both sides of S as a probe to catalyze a solution phase reaction with "on" representing the probe insertion to trigger the catalytic reaction, and "off" indicating the pulling of the probe from the solution to stop the reaction.

3.3   Results and discussion

We first demonstrate our new strategy to prepare NPs-NG-S. NG was synthesized as reported,[38] and was dispersed in ethanol. Representative NPs of 3 nm $Ni_{30}Pd_{70}$ (denoted as NiPd in this paper),[39] 8 nm Fe_3O_4[40] and 9 nm Pd[41] were also prepared as reported. We modified a previous report on the assembly of graphene oxide (GO)[34,42] and performed our assembly by dropping pentane (5 mL) onto a water (5 mL) surface (20 cm^2) to create a pentane-water inter-surface. Then we added 1 mL of ethanol dispersion of NG (0.05 mg/mL) via a syringe into the water phase without disrupting the interface. Evaporation of half of the pentane at room temperature led to formation of a reflective NG film at the interface. When we added 2.5 mL of NP pentane dispersion (0.012 mg/mL) dropwise at this stage and let the pentane completely evaporate, we obtained a monolayer array of NPs directly on the NG film. The film was collected on a SiO-coated Cu grid or a silicon wafer by lifting the substrate up through the water phase, and dried in air. During this process, lifting the substrate at different stages can give us either NG-Si or NPs-NG-Si.

The NG-Si was characterized by atomic force microscope (AFM, Figure 3.2a). Line scanning across a representative sheet gave a height profile and film thickness of 0.6 nm, corresponding to the thickness of a single layer of NG.[38,43] The transmission electron microscope (TEM) images clearly show the monolayer assembly of 3 nm NiPd NPs on NG (Figure 3.2b). The NP arrays can be further characterized by AFM analysis (Figure 3.2c). For example, the average thickness of the NiPd-NG is measured to be 3.1 nm. Subtracting the NG thickness of 0.6 nm (Inset of Figure 3.2a) gives a NP height of 2.5 nm, close to the average NP size measured by TEM, indicating the successfully preparation of a dual-monolayer assembly of NPs and NG (AFM measurements often give smaller dimensions than TEM measurements, especially for NPs with dimensions less than 10 nm due to tip-sample interactions).[44–46] Under these assembly conditions with a properly controlled NP dispersion concentration, we did not observe NP deposition on the non-NG area of S, indicating that our assembly approach is very selective for the formation of NPs-NG. However,
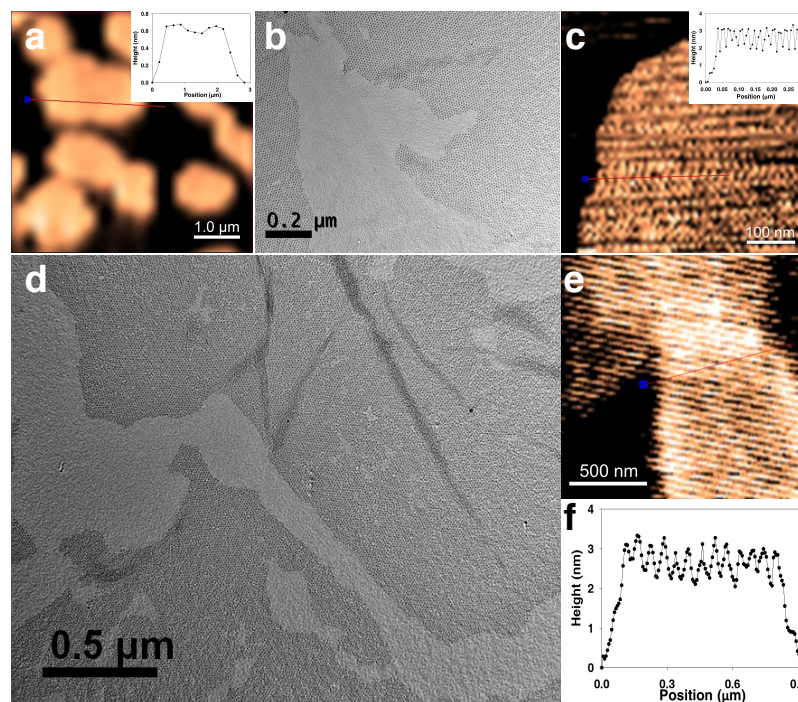
Figure 3.2 (a) AFM image of NG-S (S = Si). Inset: line profile of scanning across the NG. (b) TEM image of 3 nm NiPd-NG-S (S = SiO Type-A supported Cu grid). (c) AFM image of NiPd-NG-Si. Inset: line profile of scanning across part of the NiPd-NG-Si. (d) TEM image of 3 nm NiPd-NG-S (S = SiO Type-A supported Cu grid) annealed at 400 °C. (e) AFM image of the annealed NiPd-NG-Si. (f) AFM height profile of line scanning across the annealed NiPd-NG-Si in e).

increasing the NP concentration to 0.016 mg/mL or higher caused the NPs to stack in multi-layers at the interface (Figure 3.3a), denoted as $(NiPd)_{>1}-NG-Si$, while reduction of the NP dispersion concentration to 0.008 mg/mL or below resulted in patchy NP assemblies on the NG surface (Figure 3.3b), denoted as $(NiPd)_{<1}-NG-Si$.

Monolayer assembly of NPs on NG allows maximum exposure of NPs for catalysis. The NG serves as a Lewis basic support, providing anchoring sites not only for the NPs, but also for Lewis acidic reactants, facilitating the enhancement of NP catalysis.[47–50] For comparison purposes, we also prepared NiPd-G-Si (Figure 3.4), as well as a physical mixture of NiPd+NG (or G) by mixing NPs and NG (or G) (mass ratio 3/5) in hexane followed by hexane washing. These NPs were activated by annealing in Ar at 400 °C for 2 h. The NiPd-NG-Si shows no NP aggregation (Figure 3.2d). The AFM image of a representative patch
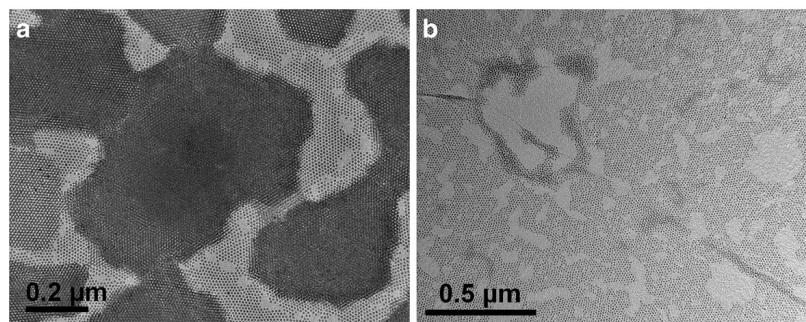
Figure 3.3 TEM images of NiPd-NG obtained from deposition of NiPd NPs at the concentration of (a) 0.016 mg/mL and (b) 0.08 mg/mL.

of the annealed sample shows nearly the same height (3.0 nm) when compared to the height measured for a freshly-deposited, unannealed sample (Inset of Figure 3.2c). However, the NiPd NPs in the NiPd-G-Si structure shows signs of stacking after this annealing treatment (Figure 3.4c). These observations indicate that the NG indeed provides anchoring sites that stabilize the NPs during the NP activation process.
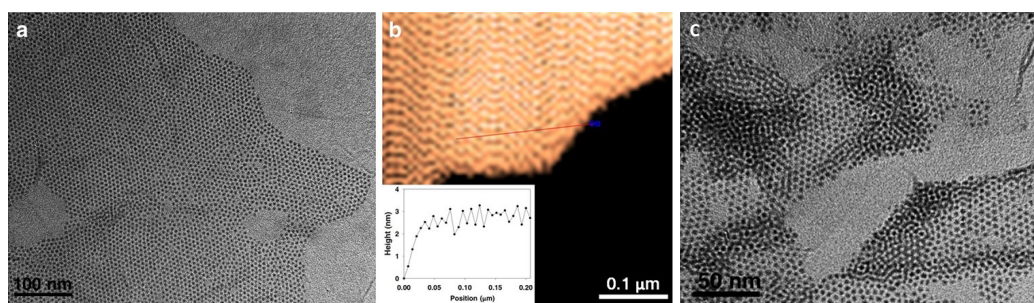
Figure 3.4 (a) TEM image of NiPd-G-S (S = SiO Type-A supported Cu grid). (b) AFM image of NiPd-G-Si. Inset: Height profile along the red line in (b). (c) TEM image of NiPd-G-S after annealing.

We first tested the assembled NiPd NPs as a catalyst for the hydrolysis of ammonia borane (AB) (the assembled Pd and Fe_3O_4 NPs were much less active than the NiPd NPs). We used the reaction conditions that have been optimized for the NiPd NP catalyst (10 mL of 300 mM AB at 298 K)[39] for comparison purposes, and plotted the data in Figure 3.5a and b. Compared with other controls, the NiPd-NG-Si catalyst shows much-enhanced activity for AB hydrolysis. $(NiPd)_{>1}-NG-Si$, $(NiPd)_{<1}-NG-Si$ and even NiPd-G-Si are all less active than the monolayer assembly NiPd-NG-Si. NiPd + NG (or G) is much less active than

the NiPd-NG-Si and requires that the NiPd loading be increased to 0.15 mg/mL for the rate of H_2 production to be comparable with the NiPd-NG-Si (1.5 ppm). These results indicate that 1) monolayer assembly can indeed maximize NiPd catalysis; and 2) the presence of NG enhances the NiPd catalysis due to the NG's role in stabilizing the NiPd NPs and activating H_3N-BH_3 bonding by the $NG-BH_3$ interaction. The temperature dependence of the catalytic reaction from 298 K–328 K was also measured as shown in Figure 3.5c. From the slope of the linear plot of ln TOF versus 1/T in Figure 3.5d, we calculated the activation energy for H_2 evolution from AB to be $E_a = 18.8\ kJ/mol$, and TOF to be $4896.8\ mol_{H_2}mol_{NiPd}^{-1}min^{-1}$. The NiPd-NG-Si has the lowest E_a and highest initial TOF ever reported for AB hydrolysis.[51,52]
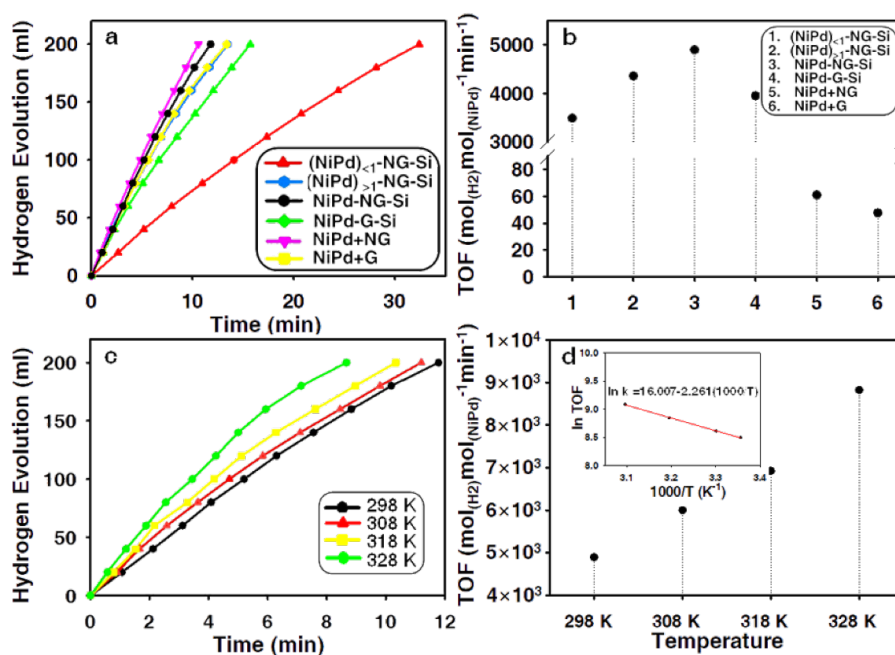
Figure 3.5 (a) Stoichiometric hydrogen evolution from AB hydrolysis catalyzed by NiPd-S prepared via different assembly methods ([AB] = 300 mM, T = 298 K. For NiPd-NG-Si or NiPd-G-Si, [NiPd] = 1.5 ppm and 1.7 ppm, respectively. For $(NiPd)_{<1}-NG-Si$ and $(NiPd)_{>1}-NG-Si$, [NiPd] = 1.0 ppm and 2.1 ppm, respectively. For NiPd + Support, [NiPd] = 0.15 mg/mL). (b) TOF values of NiPd-S prepared via different assembly methods. (c) Stoichiometric hydrogen evolution at different temperatures ([AB] = 300 mM, [NiPd] = 1.5 ppm). (d) TOF values of NiPd-NG at different temperatures. Inset: Arrhenius plot of ln TOF vs (1/T).

Since AB hydrolysis has been used directly in transfer hydrogenation reactions for organic reductions,[18,53–56] we explored the advantages of our new catalyst probe for the AB-initiated transfer hydrogenation and for the high-yield synthesis of quinazolines - the key components present in heterocycle compounds for displaying antibacterial, antifungal and anticancer activities.[57–59] Our NiPd-NG-Si catalyzed the one-pot synthesis of quinazolines from o-nitroacetophenone and benzaldehydes with AB hydrolysis providing the necessary H_2 and NH_3 ($NH_4^+ \rightleftharpoons NH_3 + H^+$) sources, as summarized in Figure 3.6a. We screened reaction conditions and found that reaction in water at 60 °C for 8 h to be optimal. The NiPd-NG-Si was the most active catalyst, giving 4-methyl-2-phenylquinazoline in an excellent yield of 99% in the presence of only 0.016 mol% of NiPd. We tested the NiPd-NG-Si catalyst for similar reactions and found it to be equally active in producing quinazoline derivatives (1a-5a) regardless of the presence of electron-donating or electron-withdrawing groups on the benzaldehyde. Furthermore, an aliphatic aldehyde, which is much less active under conventional reaction conditions, also reacts well to give 6a in 84% yield. In the synthesis, we simply inserted the NiPd-NG-Si probe into the solution to initiate the one-pot reaction. From the reaction system photos (Figure 3.6b), we can see that after the probe is inserted into the reaction solution, the balloon expands quickly due to the fast release of H_2 from AB hydrolysis. As the reaction proceeds, the balloon shrinks due to the consumption of H_2 during the subsequent transfer hydrogenation and other reactions. We can pull the catalyst probe out from the reaction system to stop the reaction and to separate the reaction product. Using the reaction leading to the formation of 1a, we tested the stability of the NiPd-NG-Si catalyst after 5 consecutive reaction runs. In each case, after pulling the catalyst from the reaction solution and washing it with water, the catalyst was ready for the next round of reaction. We found no significant loss of catalytic activity (1a yield stayed >95%, Figure 3.6c) and no obvious change in catalyst morphology, indicating that the NiPd-NG-Si catalyst is not only active, but also stable under the reaction conditions.

We further performed three control experiments (Figure 3.7) to study the possible reaction mechanism. From control experiment 1, we can see that the reaction without aldehyde
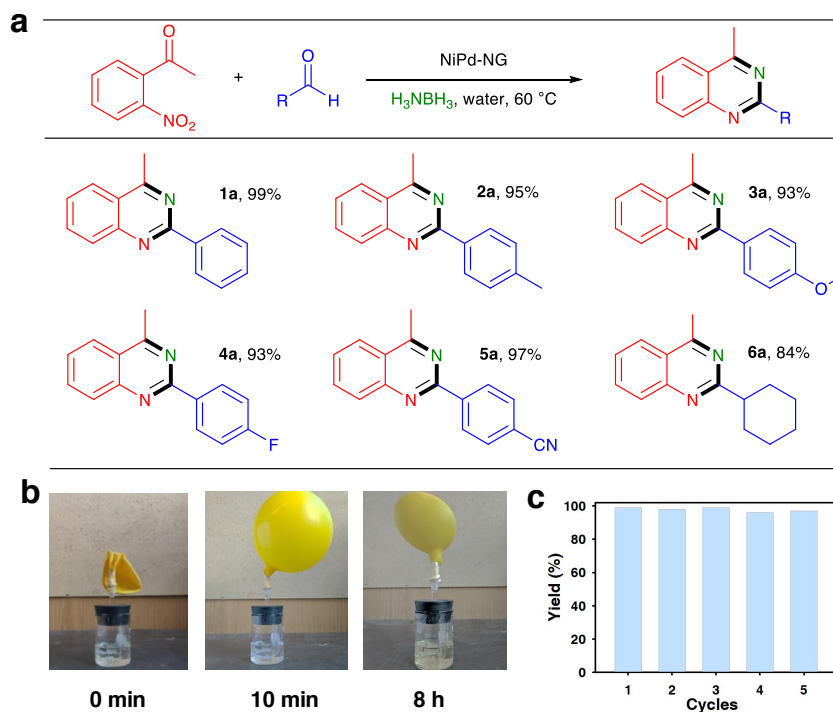
Figure 3.6 (a) Reaction results of 2-nitroacetophenone and various aldehydes. Reaction conditions: 2-nitroacetophenone (1 mmol), aromatic or aliphatic aldehyde (1.2 mmol), NiPd-NG-Si (0.016 mol%), water (20 mL) and AB (3 mmol), 60 °C, 8 h. (b) Schematic photos showing the NiPd-NG-catalyzed one-pot synthesis of quinazolines using AB in water. (c) Separation yields of quinazoline 1a in successive runs using recycled NiPd-NG-Si.

gave aromatic amines. The formation of amine and imine products shows that the hydrolysis of AB provides both H_2 and NH_3 for the reactions. Control experiment 2 indicates that NH_3 is a reaction component required for the formation of quinazoline. Control experiment 3 confirms that the catalyst is active for dehydro-aromatization, and can further catalyze a second transfer hydrogenation reaction to C=C of styrene. Based on these control experiments and previous reports,[60–63] we can propose a possible mechanism to explain how the reactions proceed to form the final product (Scheme 3.1). Overall, compared with previous syntheses of quinazolines,[64–67] our new catalyst probe shows maximum activity for catalyzing one-pot cascade reactions for the formation of quinazolines in water under mild conditions without the addition of any other additives or oxidants.
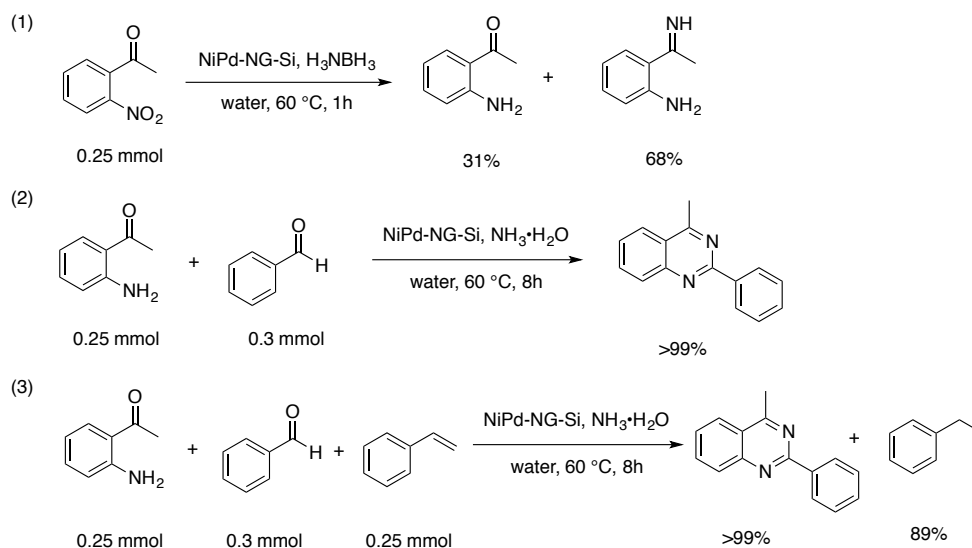
Figure 3.7 (1) The reaction of 2-nitroacetophenone catalyzed by NiPd-NG-Si in the presence of AB at 60 °C for 1 h; (2) The reaction of 2-aminoacetophenone and benzaldehyde catalyzed by NiPd-NG-Si in the presence of ammonia at 60 °C for 8 h; (3) The reaction of 2-aminoacetophenone, benzaldehyde and styrene catalyzed by NiPd-NG-Si in the presence of ammonia at 60 °C for 8 h.

3.4 Conclusion

We have developed a facile interfacial assembly method to prepare a monolayer array of NG and NPs consecutively, and to transfer the NPs-NG onto a solid substrate (S), obtaining the dual NP and NG assemblies on S, NPs-NG-S. This NPs-NG-S can be used as a catalyst probe to turn a catalytic reaction on by inserting the probe into the reaction solution and off by pulling the probe out of the solution. Using 3 nm NiPd NPs as an example, we have demonstrated that the monolayer NiPd-NG-Si shows the maximum catalysis not only for AB hydrolysis, but also for the following transfer hydrogenation, imine formation, and condensation of aromatic nitro-compounds and aldehydes, leading to the one-pot, high-yield synthesis of quinazolines in water with only 0.016 mol% catalyst loading. Our assembly method can be extended to other G and NPs, providing a new 2D NP platform for catalyzing reactions with optimum efficiency.
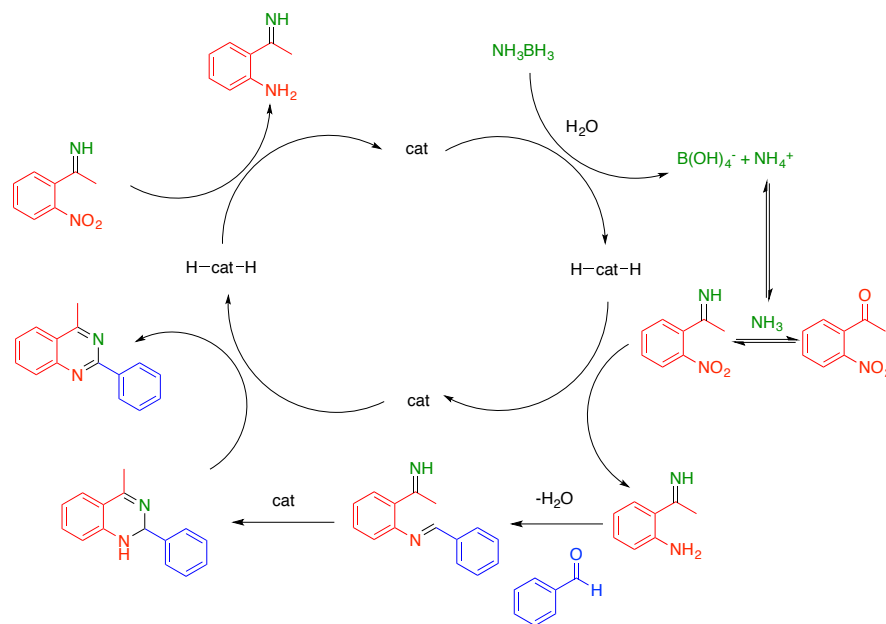
Scheme 3.1 Plausible reaction mechanism for the one-pot aromatization of 2-nitroacetophenone and benzaldehyde.

3.5 Experimental section

Synthesis of Ni$_{30}$Pd$_{70}$ NPs 0.2 mmol of Pd(acac)$_2$ and 0.2 mmol of Ni(acac)$_2$ were dissolved in 3 mL of OAm. The precursor mixture was quickly injected into a mixture of 200 mg of BBA, 3 mL of OAm, and 7 mL of ODE at 100 °C under magnetic stirring in an argon environment. The reaction was allowed to proceed for 1 h and cooled to room temperature. Then acetone/ethanol (v/v = 7/3) was added, and the NP product was separated by centrifugation at 9000 rpm for 10 min. The NPs were redispersed in hexane and then stored for further use.

Synthesis of Fe$_3$O$_4$ NPs Fe(acac)$_3$ (2 mmol) was dissolved in benzyl ether (10 mL) and OAm (10 mL). The above mixture solution was dehydrated at 110 °C for 1 h under a flow of nitrogen, and under a blanket of nitrogen, was heated to 300 °C and kept at this temperature for 2 h. The black-brown mixture was cooled to room temperature. Ethanol (40 mL) was added to the mixture and precipitate was collected by centrifugation at 8000 rpm. Finally, the product was redispersed in hexane.

Synthesis of Pd NPs   In a reaction flask with a continuous N_2 flow and magnetic stirring, 0.5 mmol of Pd(acac)$_2$ was dissolved in 15 mL of OAm, and the solution was heated to 40 °C. After 30 min of heating at 40 °C, 2.5 mmol of borane morpholine complex pre-dissolved in 4 mL of OAm was injected into the solution, leading to an instant color change from transparent yellow to black-brown. The solution was then heated to 90 °C at a rate of 3 °C /min and kept at this temperature for 1 h. Once cooled down to room temperature, the Pd NPs were collected by adding ethanol and centrifugation. The NPs were further purified with hexane/ethanol and redispersed in hexane for further use.

Synthesis of nitrogen-doped graphene (NG)   2.0 g melamine and 0.4 g single-layered GO were mixed in 400 mL deionized water and stirred at room temperature for 48 h. Water was then evaporated at 60 °C. The resulting solid product was first annealed at 350 °C for 0.5 h and then at 900 °C for 1 h in a N_2 atmosphere. After cooled to room temperature, the powder was ready for further use.

Monolayer assembly of NPs-NG-S   Pentane (5 mL) was firstly added on the top of water (5 mL) to form a biphasic interface between pentane and water phase. NG was mixed with ethanol (0.05 mg/mL) and 1 mL of its solution was injected into the water phase. Once half of pentane was evaporated at room temperature, 2.5 mL of NPs/pentane solution (0.012 mg/mL for $Ni_{30}Pd_{70}$, 0.02 mg/mL for Fe_3O_4, 0.02 mg/mL for Pd) was added dropwise to the pentane phase. After pentane evaporation, a monolayer array was assembled on the water surface and was transferred onto S (14×6 mm silicon wafer (RCA clean process) or SiO Type-A supported Cu grid) for characterization.

AB hydrolysis   A two-necked reaction flask (25 mL) containing a Teflon-coated stir bar was placed on a magnetic stirrer and thermostated to 25.0 °C by using a constant tempera-ture bath. A gas burette filled with water was connected to one neck of the flask (the other neck was sealed) to measure the volume of hydrogen gas evolved from the reaction. The catalyst deposited on both side of silicon wafer was added into 10 mL of water containing

100.0 mg (3 mmol) of AB under stirring. The volume of hydrogen gas evolved was measured by recording the volume of water displaced. The reaction was considered to cease when hydrogen gas generation was no longer observed.

General procedure for producing quinazolines via NiPd-NG-Si   2-Nitroaceto- phenone (1 mmol), aldehyde (1.2 mmol) and water (20 mL) were stirred for 5 min in the reactor at 60 °C. The NiPd-NG-Si was inserted into the solution and AB (3 mmol) was added to the reaction mixture (the flask was sealed by a balloon). The solution was stirred at 800 rpm at 60 °C for 8 h. Once the reaction was completed, the catalyst was taken out and washed with water for the next reaction. The organic product was extracted with ethyl acetate and the organic phase was evaporated under vacuum. The residue was purified by flash column chromatography (hexane/ethyl acetate = 8:1) to give the solid product.

Catalyst stability test   After each model reaction, the catalyst probe was pulled out, washed with water and dried. Then the probe was reused directly in the subsequent reaction.

3.5.1   Characterization data of products

4-methyl-2-phenylquinazoline (1a) ^{1}H-NMR (400 MHz, CDCl$_3$) δ [ppm] = 8.66-8.63 (m, 2H), 8.11-8.09 (m, 2H), 7.90-7.86 (m, 2H) 7.62-7.52(m, 4H), 3.04 (s, 3H); ^{13}C-NMR (100 MHz, CDCl$_3$) δ [ppm] = 168.2, 160.1, 150.3, 138.2, 133.5, 130.4, 129.2, 128.6, 128.5, 126.8, 125.0, 123.0, 22.0. HRMS [M+H]$^+$ calculated for C$_{15}$H$_{13}$N$_2$: 221.1084 found 221.1076.

4-methyl-2-p-tolylquinazoline (2a) ^{1}H-NMR (400 MHz, CDCl$_3$) δ [ppm] = 8.54 (d, J = 8.8 Hz, 2H), 8.10-8.06 (m, 2H), 7.89-7.85 (m, 1H), 7.60-7.56 (m, 1H), 7.37-7.34 (m, 2H), 3.03 (s, 3H), 2.46 (s, 3H); ^{13}C-NMR (100 MHz, CDCl$_3$) δ [ppm] = 168.1, 160.2, 150.4, 140.5, 135.5, 133.4, 129.3, 129.1, 128.4, 126.6, 125.0, 122.9, 22.0, 21.5. HRMS [M+H]$^+$ calculated for C$_{16}$H$_{15}$N$_2$: 235.1239 found 235.1231.

2-(4-methoxyphenyl)-4-methylquinazoline (3a) ^{1}H-NMR (400 MHz, CDCl$_3$) δ [ppm] = 8.60 (d, J = 8.4 Hz, 2H), 8.09-8.03 (m, 2H), 7.87-7.83 (m, 1H), 7.58-7.54 (m, 1H), 7.05 (d, J = 9.2 Hz, 2H), 3.92 (s, 3H), 3.01 (s, 3H); ^{13}C-NMR (100 MHz, CDCl$_3$) δ [ppm] = 168.0, 161.6, 160.0, 150.4, 133.4, 130.9, 130.1, 129.0, 126.4, 125.0, 122.7, 113.8, 55.4, 22.0. HRMS [M+H]$^+$ calculated for C$_{16}$H$_{15}$N$_2$O: 251.1188 found 251.1180.

2-(4-fluorophenyl)-4-methylquinazoline (4a) ^{1}H-NMR (400 MHz, CDCl$_3$) δ [ppm] = 8.67-8.64 (m, 2H), 8.11-8.06 (m, 2H), 7.90-7.86 (m, 1H), 7.62-7.58 (m, 1H), 7.24-7.19 (m, 2H), 3.03 (s, 3H); ^{13}C-NMR (100 MHz, CDCl$_3$) δ [ppm] = 168.3, 165.8, 163.3, 159.2, 150.3, 134.4, 133.6, 130.7, 129.1, 126.9, 125.0, 122.9, 115.4, 22.0. HRMS [M+H]$^+$ calculated for C$_{15}$H$_{12}$N$_2$F: 239.0985 found 239.0977.

4-(4-methylquinazolin-2-yl)benzonitrile (5a) ^{1}H-NMR (400 MHz, CDCl$_3$) δ [ppm] = 8.75 (d, J = 8.4 Hz, 2H), 8.16-8.10 (m, 2H), 7.95-7.91 (m, 1H), 7.82 (d, J = 8.8 Hz, 2H), 7.69-7.65 (m, 1H), 3.05 (s, 3H); ^{13}C-NMR (100 MHz, CDCl$_3$) δ [ppm] = 168.7, 158.1, 150.1, 142.3, 134.0, 132.3, 129.3, 129.0, 127.8, 125.1, 123.2, 119.0, 113.5, 22.0. HRMS [M+H]$^+$ calculated for C$_{16}$H$_{12}$N$_3$: 246.1033 found 246.1025.

2-cyclohexyl-4-methylquinazoline (6a) ^{1}H-NMR (400 MHz, CDCl$_3$) δ [ppm] = 8.05 (d, J = 8.0 Hz, 1H), 7.97 (d, J = 8.4 Hz, 2H), 7.85-7.81 (m, 1H), 7.57-7.53 (m, ^{1}H), 3.00-2.96 (m, 1H), 2.94 (s, 3H), 2.10-2.06 (m, 2H), 1.92-1.88 (m, 2H), 1.80-1.76 (m, 3H), 1.50-1.35 (m, 3H); ^{13}C-NMR (100 MHz, CDCl$_3$) δ [ppm] = 170.1, 167.9, 150.0, 133.2, 128.6, 126.4, 124.8, 122.6, 47.9, 31.9, 26.3, 26.0, 21.8. HRMS [M+H]$^+$ calculated for C$_{15}$H$_{19}$N$_2$: 227.1550 found 227.1541.

3.6 Characterization of compounds

Spectra of 4-methyl-2-phenylquinazoline (1a)
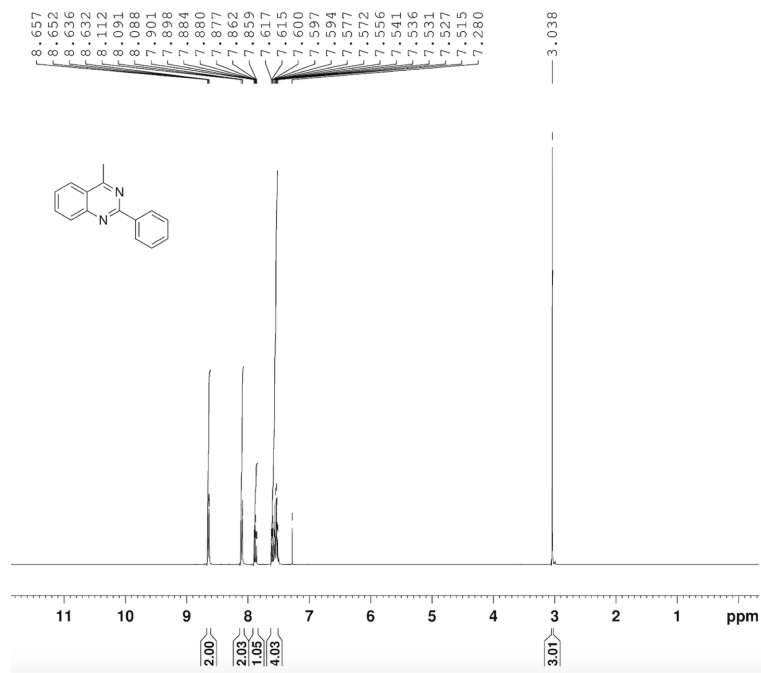
¹H-NMR

¹³C-NMR
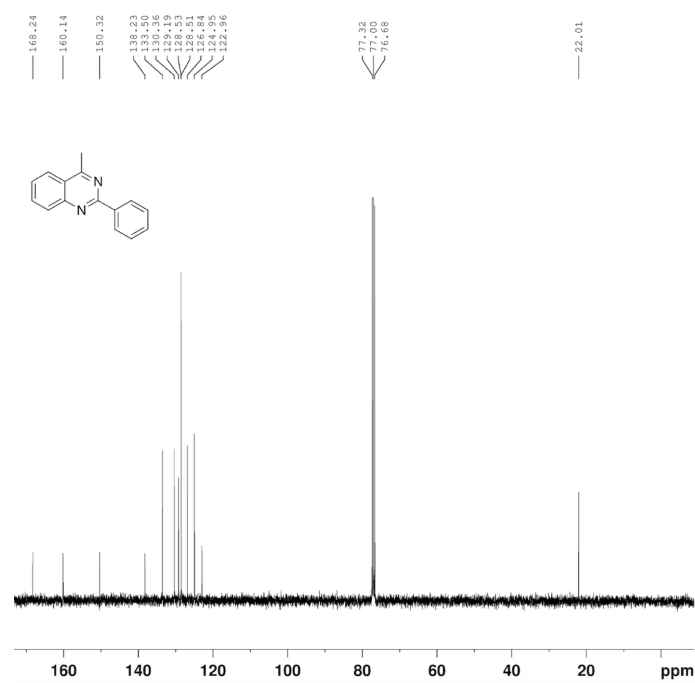
Spectra of 4-methyl-2-p-tolylquinazoline (2a)
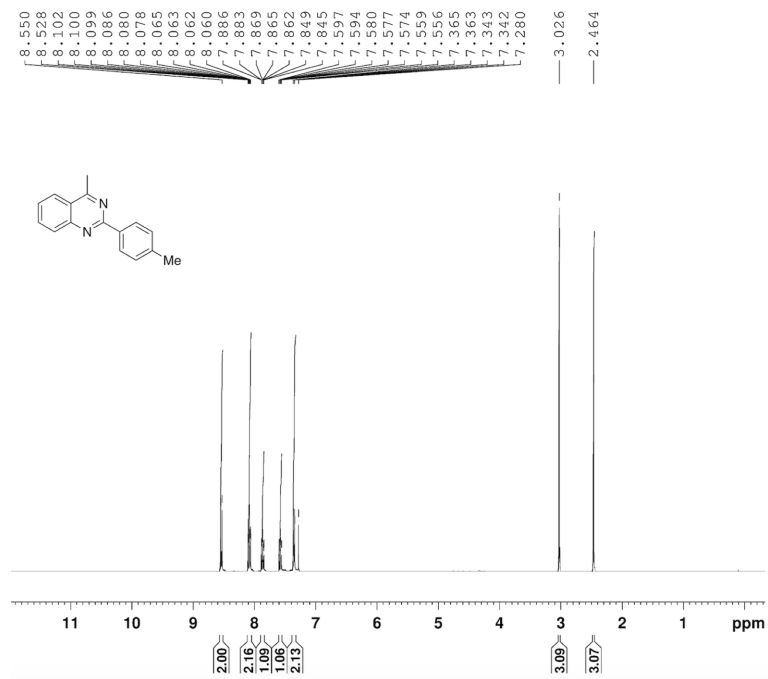
^{1}H-NMR

^{13}C-NMR
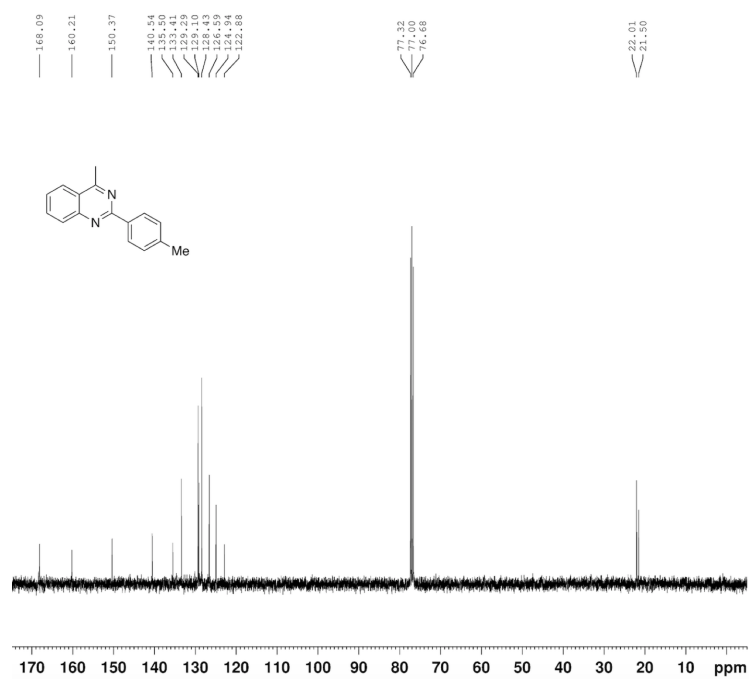
Spectra of 2-(4-methoxyphenyl)-4-methylquinazoline (3a)
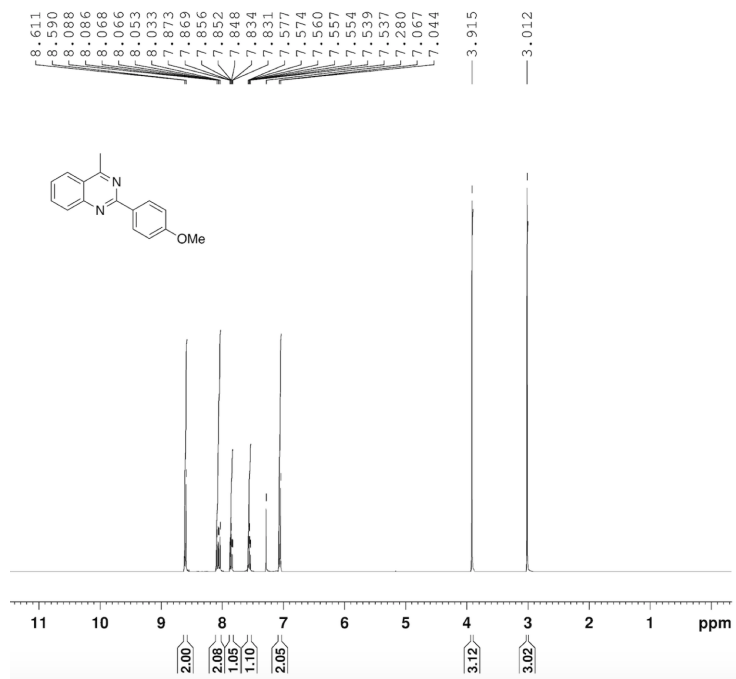
^{1}H-NMR

^{13}C-NMR
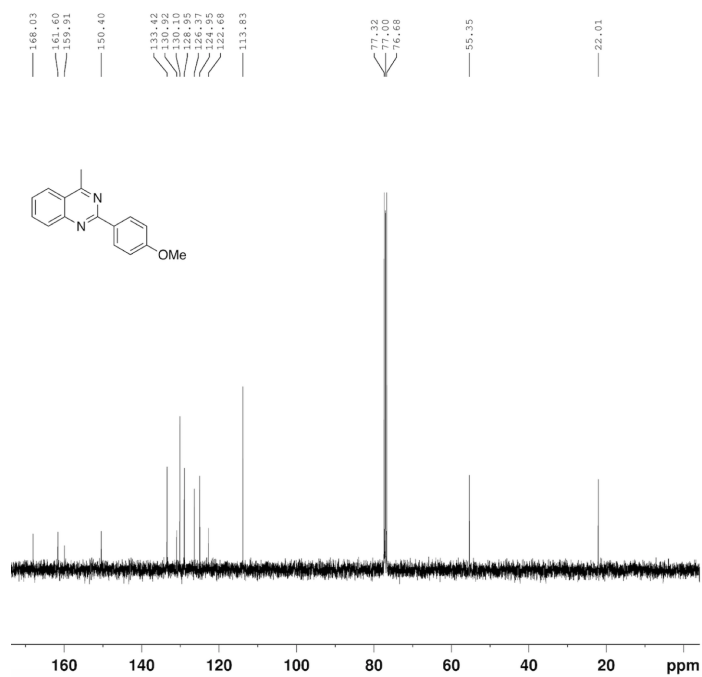
Spectra of 2-(4-fluorophenyl)-4-methylquinazoline (4a)
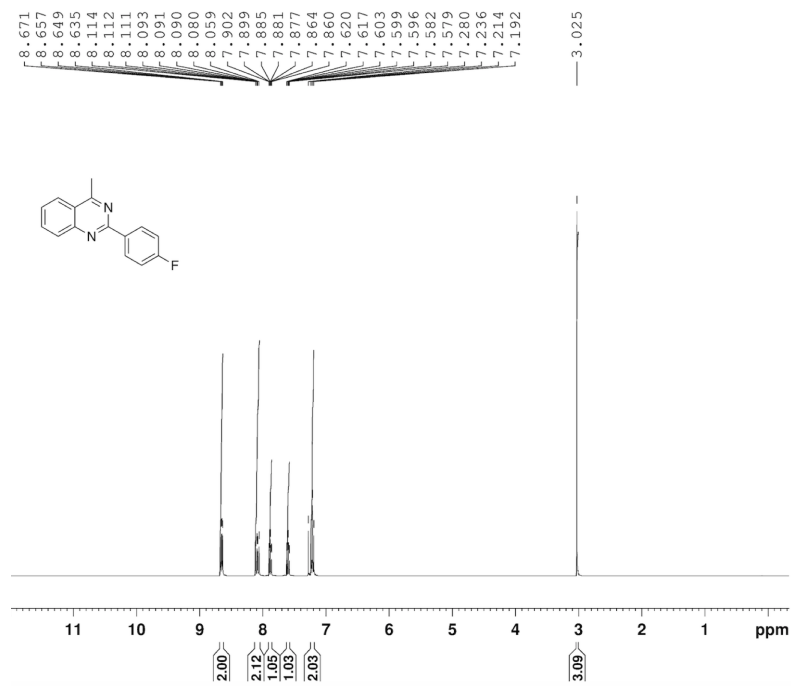
^{1}H-NMR

^{13}C-NMR
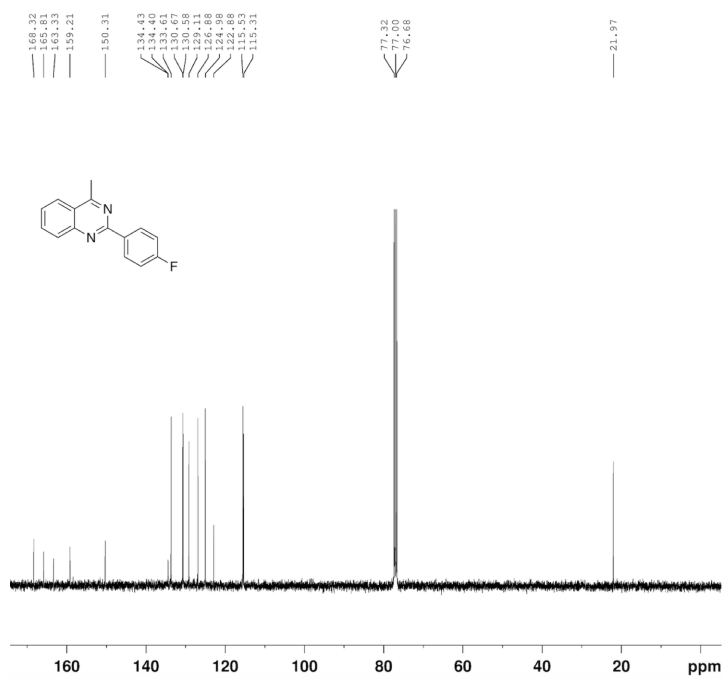
Spectra of 4-(4-methylquinazolin-2-yl)benzonitrile (5a)
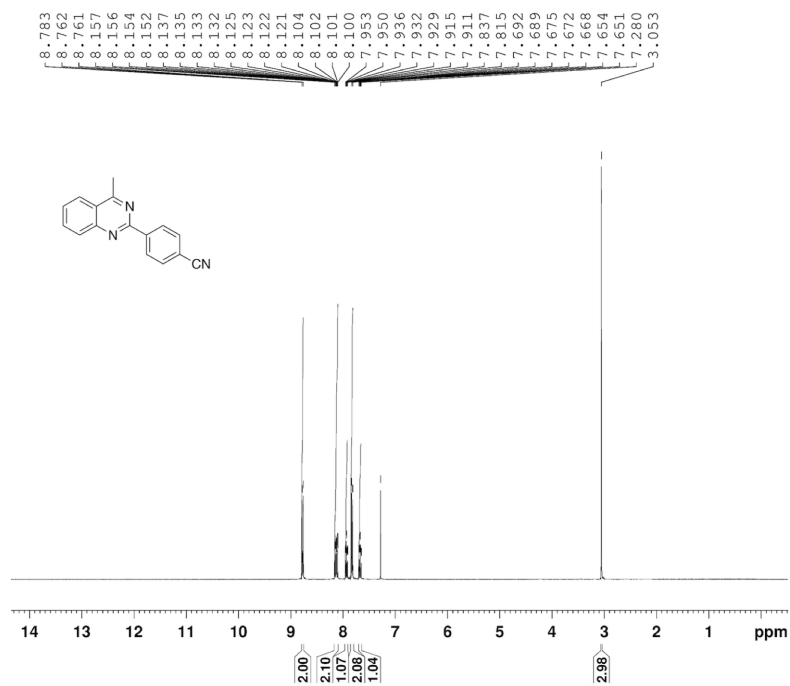
^{1}H-NMR

^{13}C-NMR
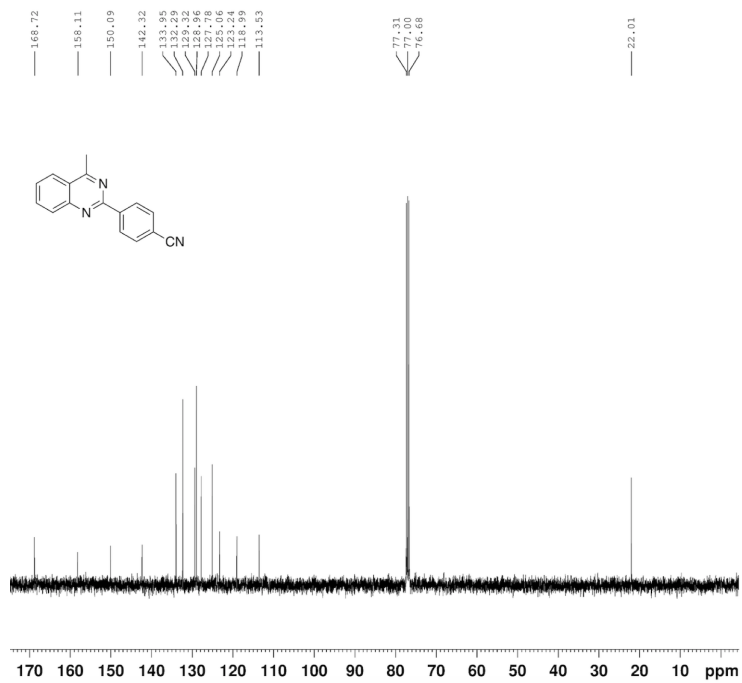
Spectra of 2-cyclohexyl-4-methylquinazoline (6a)

^{1}H-NMR
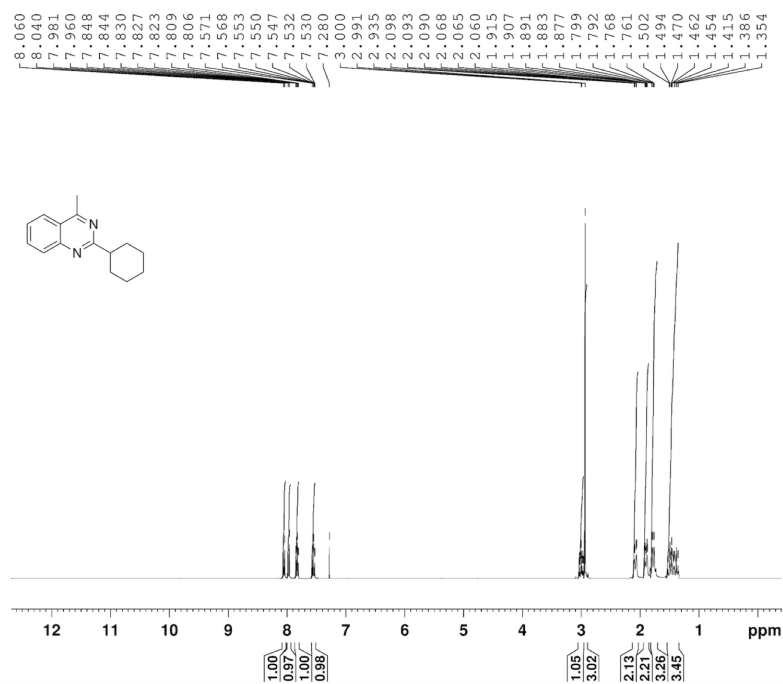
^{13}C-NMR
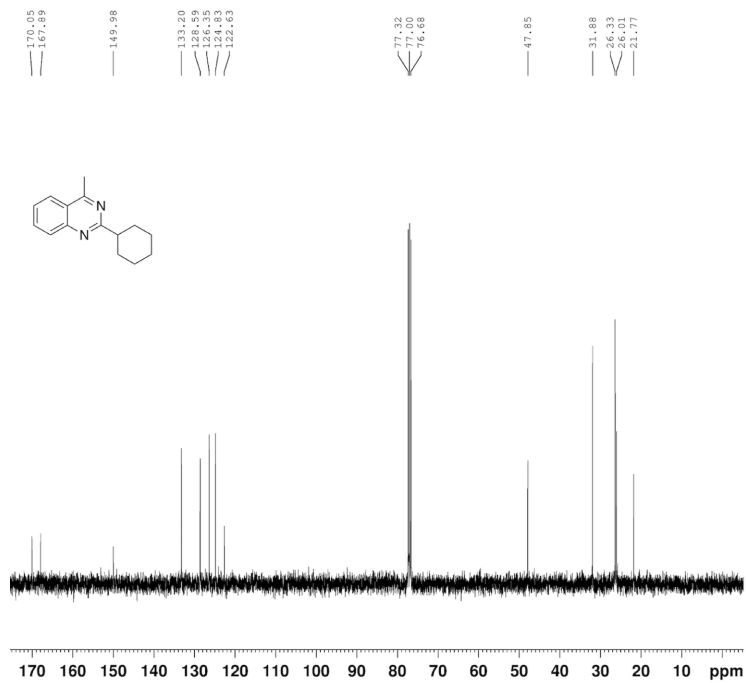
References

[1] Flauraud, V.; Mastrangeli, M.; Bernasconi, G. D.; Butet, J.; Alexander, D. T.; Shahrabi, E.; Martin, O. J.; Brugger, J. Nanoscale topographical control of capillary assembly of nanoparticles. *Nature Nanotechnology* **2017**, *12*, 73.

[2] Edwardson, T. G.; Lau, K. L.; Bousmail, D.; Serpell, C. J.; Sleiman, H. F. Transfer of molecular recognition information from DNA nanostructures to gold nanoparticles. *Nature Chemistry* **2016**, *8*, 162.

[3] Etschel, S. H.; Portilla, L.; Kirschner, J.; Drost, M.; Tu, F.; Marbach, H.; Tykwinski, R. R.; Halik, M. Region-selective deposition of core–shell nanoparticles for 3 D hierarchical assemblies by the Huisgen 1, 3-dipolar cycloaddition. *Angewandte Chemie International Edition* **2015**, *54*, 9235–9238.

[4] Zheng, Y.; Lalander, C. H.; Thai, T.; Dhuey, S.; Cabrini, S.; Bach, U. Gutenberg-style printing of self-assembled nanoparticle arrays: electrostatic nanoparticle immobilization and DNA-mediated transfer. *Angewandte Chemie International Edition* **2011**, *123*, 4490–4494.

[5] Zhang, J.; Li, Y.; Zhang, X.; Yang, B. Colloidal self-assembly meets nanofabrication: From two-dimensional colloidal crystals to nanostructure arrays. *Advanced Materials* **2010**, *22*, 4249–4269.

[6] Peng, K.; Wu, Y.; Fang, H.; Zhong, X.; Xu, Y.; Zhu, J. Uniform, axial-orientation

alignment of one-dimensional single-crystal silicon nanostructure arrays. *Angewandte Chemie International Edition* **2005**, *117*, 2797–2802.

[7] Santhanam, V.; Andres, R. P. Microcontact printing of uniform nanoparticle arrays. *Nano Letters* **2004**, *4*, 41–44.

[8] Cui, Y.; Björk, M. T.; Liddle, J. A.; Sönnichsen, C.; Boussert, B.; Alivisatos, A. P. Integration of colloidal nanocrystals into lithographically patterned devices. *Nano Letters* **2004**, *4*, 1093–1098.

[9] Toth, P. S.; Velický, M.; Bissett, M. A.; Slater, T. J.; Savjani, N.; Rabiu, A. K.; Rakowski, A. M.; Brent, J. R.; Haigh, S. J.; O'Brien, P. Asymmetric MoS2/Graphene/metal sandwiches: preparation, characterization, and application. *Advanced Materials* **2016**, *28*, 8256–8264.

[10] Arciniegas, M. P.; Stasio, F. D.; Li, H.; Altamura, D.; De Trizio, L.; Prato, M.; Scarpellini, A.; Moreels, I.; Krahne, R.; Manna, L. Self-assembled dense colloidal Cu2Te nanodisk networks in P3HT thin films with enhanced photocurrent. *Advanced Functional Materials* **2016**, *26*, 4535–4542.

[11] Toth, P. S.; Velický, M.; Ramasse, Q. M.; Kepaptsoglou, D. M.; Dryfe, R. A. Symmetric and asymmetric decoration of graphene: Bimetal-graphene sandwiches. *Advanced Functional Materials* **2015**, *25*, 2899–2909.

[12] Xu, L.; Zhou, X.; Tian, W. Q.; Gao, T.; Zhang, Y. F.; Lei, S.; Liu, Z. F. Surface-confined single-layer covalent organic framework on single-layer graphene grown on copper foil. *Angewandte Chemie International Edition* **2014**, *126*, 9718–9722.

[13] Lee, K. H.; Shin, H.-J.; Kumar, B.; Kim, H. S.; Lee, J.; Bhatia, R.; Kim, S.-H.; Lee, I.-Y.; Lee, H. S.; Kim, G.-H. Nanocrystalline-graphene-tailored hexagonal boron nitride thin films. *Angewandte Chemie International Edition* **2014**, *53*, 11493–11497.

[14] Li, Z.; Liu, J.; Xia, C.; Li, F. Nitrogen-functionalized ordered mesoporous carbons as multifunctional supports of ultrasmall Pd nanoparticles for hydrogenation of phenol. *Acs Catalysis* **2013**, *3*, 2440–2448.

[15] Huang, X.; Li, M.; Green, D. C.; Williams, D. S.; Patil, A. J.; Mann, S. Interfacial assembly of protein–polymer nano-conjugates into stimulus-responsive biomimetic protocells. *Nature Communications* **2013**, *4*, 2239.

[16] Reina, A.; Jia, X.; Ho, J.; Nezich, D.; Son, H.; Bulovic, V.; Dresselhaus, M. S.; Kong, J. Large area, few-layer graphene films on arbitrary substrates by chemical vapor deposition. *Nano Letters* **2008**, *9*, 30–35.

[17] Zhao, J.; Chen, Z. Single Mo atom supported on defective boron nitride monolayer as an efficient electrocatalyst for nitrogen fixation: A Computational Study. *Journal of the American Chemical Society* **2017**, *139*, 12480–12487.

[18] Yu, C.; Fu, J.; Muzzio, M.; Shen, T.; Su, D.; Zhu, J.; Sun, S. CuNi nanoparticles assembled on graphene for catalytic methanolysis of ammonia borane and hydrogenation of nitro/nitrile compounds. *Chemistry of Materials* **2017**, *29*, 1413–1418.

[19] Huang, Y.; Zhao, M.; Han, S.; Lai, Z.; Yang, J.; Tan, C.; Ma, Q.; Lu, Q.; Chen, J.; Zhang, X. Growth of Au nanoparticles on 2D metalloporphyrinic metal-organic framework nanosheets used as biomimetic catalysts for cascade reactions. *Advanced Materials* **2017**, *29*, 1700102.

[20] Deng, D.; Novoselov, K.; Fu, Q.; Zheng, N.; Tian, Z.; Bao, X. Catalysis with two-dimensional materials and their heterostructures. *Nature Nanotechnology* **2016**, *11*, 218.

[21] Yao, Y.; Fu, Q.; Zhang, Y.; Weng, X.; Li, H.; Chen, M.; Jin, L.; Dong, A.; Mu, R.; Jiang, P. Graphene cover-promoted metal-catalyzed reactions. *Proceedings of the National Academy of Sciences* **2014**, *111*, 17023–17028.

[22] Chen, X.; Zhang, J.; Fu, X.; Antonietti, M.; Wang, X. Fe-g-C3N4-catalyzed oxidation of benzene to phenol using hydrogen peroxide and visible light. *Journal of the American Chemical Society* **2009**, *131*, 11658–11659.

[23] Xu, S.; Man, B.; Jiang, S.; Wang, J.; Wei, J.; Xu, S.; Liu, H.; Gao, S.; Liu, H.; Li, Z. Graphene/Cu nanoparticle hybrids fabricated by chemical vapor deposition as surface-enhanced Raman scattering substrate for label-free detection of adenosine. *ACS Applied Materials & Interfaces* **2015**, *7*, 10977–10987.

[24] Lv, Y.; Fang, Y.; Wu, Z.; Qian, X.; Song, Y.; Che, R.; Asiri, A. M.; Xia, Y.; Tu, B.; Zhao, D. In-situ confined growth of monodisperse Pt nanoparticle@ graphene nanobox composites as electrocatalytic nanoreactors. *Small* **2015**, *11*, 1003–1010.

[25] Geng, D.; Wang, H.; Yu, G. Graphene single crystals: size and morphology engineering. *Advanced Materials* **2015**, *27*, 2821–2837.

[26] Liu, J.; Lu, R.; Xu, G.; Wu, J.; Thapa, P.; Moore, D. Development of a seedless floating growth process in solution for synthesis of srystalline ZnO micro/nanowire arrays on graphene: Towards high-performance nanohybrid ultraviolet photodetectors. *Advanced Functional Materials* **2013**, *23*, 4941–4948.

[27] Zhou, X.; Huang, X.; Qi, X.; Wu, S.; Xue, C.; Boey, F. Y.; Yan, Q.; Chen, P.; Zhang, H. In situ synthesis of metal nanoparticles on single-layer graphene oxide and reduced graphene oxide surfaces. *The Journal of Physical Chemistry C* **2009**, *113*, 10842–10846.

[28] Wu, L.; Willis, J. J.; McKay, I. S.; Diroll, B. T.; Qin, J.; Cargnello, M.; Tassone, C. J. High-temperature crystallization of nanocrystals into three-dimensional superlattices. *Nature* **2017**, *548*, 197.

[29] Gaulding, E. A.; Diroll, B. T.; Goodwin, E.; Vrtis, Z. J.; Kagan, C. R.; Murray, C. B. Deposition of wafer-scale single-component and binary nanocrystal superlattice thin films via dip-coating. *Advanced Materials* **2015**, *27*, 2846–2851.

[30] Dong, A.; Chen, J.; Vora, P. M.; Kikkawa, J. M.; Murray, C. B. Binary nanocrystal superlattice membranes self-assembled at the liquid–air interface. *Nature* **2010**, *466*, 474.

[31] Bigioni, T. P.; Lin, X.-M.; Nguyen, T. T.; Corwin, E. I.; Witten, T. A.; Jaeger, H. M. Kinetically driven self assembly of highly ordered nanoparticle monolayers. *Nature Materials* **2006**, *5*, 265.

[32] Li, M.; Schnablegger, H.; Mann, S. Coupled synthesis and self-assembly of nanoparticles to give structures with controlled organization. *Nature* **1999**, *402*, 393.

[33] Han, W.; Lin, Z. Learning from coffee rings: ordered structures enabled by controlled evaporative self-assembly. *Angewandte Chemie International Edition* **2012**, *51*, 1534–1546.

[34] Chen, F.; Liu, S.; Shen, J.; Wei, L.; Liu, A.; Chan-Park, M. B.; Chen, Y. Ethanol-assisted graphene oxide-based thin film formation at pentane–water interface. *Langmuir* **2011**, *27*, 9174–9181.

[35] Biswas, S.; Drzal, L. T. A novel approach to create a highly ordered monolayer film of graphene nanosheets at the liquid- liquid interface. *Nano Letters* **2008**, *9*, 167–172.

[36] Li, Q.; Zhu, W.; Fu, J.; Zhang, H.; Wu, G.; Sun, S. Controlled assembly of Cu nanoparticles on pyridinic-N rich graphene for electrochemical reduction of CO 2 to ethylene. *Nano Energy* **2016**, *24*, 1–9.

[37] Li, B.; Dai, F.; Xiao, Q.; Yang, L.; Shen, J.; Zhang, C.; Cai, M. Nitrogen-doped activated carbon for a high energy hybrid supercapacitor. *Energy & Environmental Science* **2016**, *9*, 102–106.

[38] Sheng, Z.-H.; Shao, L.; Chen, J.-J.; Bao, W.-J.; Wang, F.-B.; Xia, X.-H. Catalyst-free synthesis of nitrogen-doped graphene via thermal annealing graphite oxide with melamine and its excellent electrocatalysis. *ACS Nano* **2011**, *5*, 4350–4358.

[39] Goksu, H.; Ho, S. F.; Metin, O.; Korkmaz, K.; Mendoza Garcia, A.; Gultekin, M. S.; Sun, S. Tandem dehydrogenation of ammonia borane and hydrogenation of nitro/nitrile compounds catalyzed by graphene-supported nipd alloy nanoparticles. *ACS Catalysis* **2014**, *4*, 1777–1782.

[40] Xi, P.; Cheng, K.; Sun, X.; Zeng, Z.; Sun, S. Magnetic Fe3O4 nanoparticles coupled with a fluorescent Eu complex for dual imaging applications. *Chemical Communications* **2012**, *48*, 2952–2954.

[41] Jiang, G.; Zhu, H.; Zhang, X.; Shen, B.; Wu, L.; Zhang, S.; Lu, G.; Wu, Z.; Sun, S. Core/shell face-centered tetragonal FePd/Pd nanoparticles as an efficient non-Pt catalyst for the oxygen reduction reaction. *ACS Nano* **2015**, *9*, 11014–11022.

[42] Wang, Y.; Fu, H.; Huang, Q.; Cui, Y.; Sun, Y.; Jiang, L. Experimental study of direct contact vaporization heat transfer on n-pentane-water flowing interface. *Energy* **2015**, *93*, 854–863.

[43] He, C.; Li, Z.; Cai, M.; Cai, M.; Wang, J.-Q.; Tian, Z.; Zhang, X.; Shen, P. K. A strategy for mass production of self-assembled nitrogen-doped graphene as catalytic materials. *Journal of Materials Chemistry A* **2013**, *1*, 1401–1406.

[44] Cargnello, M.; Wieder, N. L.; Montini, T.; Gorte, R. J.; Fornasiero, P. Synthesis of dispersible Pd@ CeO2 core- shell nanostructures by self-assembly. *Journal of the American Chemical Society* **2009**, *132*, 1402–1409.

[45] Mechler, Á.; Kopniczky, J.; Kokavecz, J.; Hoel, A.; Granqvist, C.-G.; Heszler, P. Anomalies in nanostructure size measurements by AFM. *Physical Review B* **2005**, *72*, 125407.

[46] Ebenstein, Y.; Nahum, E.; Banin, U. Tapping mode atomic force microscopy for nanoparticle sizing: tip- sample interaction effects. *Nano Letters* **2002**, *2*, 945–950.

[47] Cui, X.; Li, Y.; Bachmann, S.; Scalone, M.; Surkus, A.-E.; Junge, K.; Topf, C.; Beller, M. Synthesis and characterization of iron–nitrogen-doped graphene/core–shell catalysts: Efficient oxidative dehydrogenation of N-heterocycles. *Journal of the American Chemical Society* **2015**, *137*, 10652–10658.

[48] Bi, Q.-Y.; Lin, J.-D.; Liu, Y.-M.; He, H.-Y.; Huang, F.-Q.; Cao, Y. Dehydrogenation of formic acid at room temperature: boosting Palladium nanoparticle efficiency by coupling with pyridinic-nitrogen-doped carbon. *Angewandte Chemie International Edition* **2016**, *55*, 11849–11853.

[49] Chen, F.; Surkus, A.-E.; He, L.; Pohl, M.-M.; Radnik, J.; Topf, C.; Junge, K.; Beller, M. Selective catalytic hydrogenation of heteroarenes with N-graphene-modified cobalt nanoparticles (Co3O4–Co/NGr@ α-Al2O3). *Journal of the American Chemical Society* **2015**, *137*, 11718–11724.

[50] Zheng, Y.; Jiao, Y.; Ge, L.; Jaroniec, M.; Qiao, S. Z. Two-step boron and nitrogen doping in graphene for enhanced synergistic catalysis. *Angewandte Chemie International Edition* **2013**, *125*, 3192–3198.

[51] Zhan, W.-W.; Zhu, Q.-L.; Xu, Q. Dehydrogenation of ammonia borane by metal nanoparticle catalysts. *ACS Catalysis* **2016**, *6*, 6892–6905.

[52] Rossin, A.; Peruzzini, M. Ammonia–borane and amine–borane dehydrogenation mediated by complex metal hydrides. *Chemical Reviews* **2016**, *116*, 8848–8872.

[53] Shao, Z.; Fu, S.; Wei, M.; Zhou, S.; Liu, Q. Mild and selective Cobalt-catalyzed chemodivergent transfer hydrogenation of nitriles. *Angewandte Chemie International Edition* **2016**, *55*, 14653–14657.

[54] Rej, S.; Hsia, C.-F.; Chen, T.-Y.; Lin, F.-C.; Huang, J.-S.; Huang, M. H. Facet-dependent and light-assisted efficient hydrogen evolution from ammonia borane ssing Gold–Palladium core–shell nanocatalysts. *Angewandte Chemie International Edition* **2016**, *128*, 7338–7342.

[55] Brown, H. C.; Chandrasekharan, J. Mechanism of hydroboration of alkenes with borane-Lewis base complexes. Evidence that the mechanism of the hydroboration reaction proceeds through a prior dissociation of such complexes. *Journal of the American Chemical Society* **1984**, *106*, 1863–1865.

[56] Ryschkewitsch, G. E. Amine boranes. I. Kinetics of acid hydrolysis of trimethylamine borane. *Journal of the American Chemical Society* **1960**, *82*, 3290–3294.

[57] Colotta, V.; Catarzi, D.; Varano, F.; Lenzi, O.; Filacchioni, G.; Costagli, C.; Galli, A.; Ghelardini, C.; Galeotti, N.; Gratteri, P. Structural investigation of the 7-chloro-3-hydroxy-1 H-quinazoline-2, 4-dione scaffold to obtain AMPA and kainate receptor selective antagonists. synthesis, pharmacological, and molecular modeling studies. *Journal of Medicinal Chemistry* **2006**, *49*, 6015–6026.

[58] Ma, Z.; Hano, Y.; Nomura, T. Luotonin A: a lead toward anti-cancer agent development. *Heterocycles* **2005**, *65*, 2203–2219.

[59] Plé, P. A.; Green, T. P.; Hennequin, L. F.; Curwen, J.; Fennell, M.; Allen, J.; Lambert-van der Brempt, C.; Costello, G. Discovery of a new class of anilinoquinazoline inhibitors with high affinity and specificity for the tyrosine kinase domain of c-Src. *Journal of Medicinal Chemistry* **2004**, *47*, 871–887.

[60] Yu, C.; Guo, X.; Xi, Z.; Muzzio, M.; Yin, Z.; Shen, B.; Li, J.; Seto, C. T.; Sun, S. AgPd nanoparticles deposited on WO2.72 nanorods as an efficient catalyst for one-pot conversion of nitrophenol/nitroacetophenone into benzoxazole/quinazoline. *Journal of the American Chemical Society* **2017**, *139*, 5712–5715.

[61] Tang, L.; Zhao, X.; Zou, G.; Zhou, Y.; Yang, X. Heterogeneous gold-catalyzed cascade hydrogen-transfer strategy for selective synthesis of quinazolinones in water. *Asian Journal of Organic Chemistry* **2016**, *5*, 335–339.

[62] Tang, L.; Yang, Y.; Wen, L.; Zhang, S.; Zha, Z.; Wang, Z. Supported gold-catalyzed

and ammonia-promoted selective synthesis of quinazolines in aqueous media. *Organic Chemistry Frontiers* **2015**, *2*, 114–118.

[63] Tang, L.; Guo, X.; Yang, Y.; Zha, Z.; Wang, Z. Gold nanoparticles supported on titanium dioxide: an efficient catalyst for highly selective synthesis of benzoxazoles and benzimidazoles. *Chemical Communications* **2014**, *50*, 6145–6148.

[64] Chen, Z.; Chen, J.; Liu, M.; Ding, J.; Gao, W.; Huang, X.; Wu, H. Unexpected copper-catalyzed cascade synthesis of quinazoline derivatives. *The Journal of Organic Chemistry* **2013**, *78*, 11342–11348.

[65] Yan, Y.; Zhang, Y.; Feng, C.; Zha, Z.; Wang, Z. Selective iodine-catalyzed intermolecular oxidative amination of C (sp3) H bonds with ortho-carbonyl-substituted anilines to give quinazolines. *Angewandte Chemie International Edition* **2012**, *51*, 8077–8081.

[66] Liu, X.; Fu, H.; Jiang, Y.; Zhao, Y. A simple and efficient approach to quinazolinones under mild copper-catalyzed conditions. *Angewandte Chemie International Edition* **2009**, *121*, 354–357.

[67] Jiarong, L.; Xian, C.; Daxin, S.; Shuling, M.; Qing, L.; Qi, Z.; Jianhong, T. A new and facile synthesis of quinazoline-2, 4 (1 H, 3 H)-diones. *Organic Letters* **2009**, *11*, 1193–1196.

Chapter 4

NiPd Nanoparticles Assembled on Nitrogen-Doped Graphene for the Reductive Hydrodehalogenation Reactions[†]

[†]This chapter was adapted and modified from: Guo, X.; Yu, C.; Yin, Z.; Sun, S.; Seto, C. T. Hydrodehalogenation of polyhalogenated aromatics catalyzed by NiPd nanoparticles supported on nitrogen-doped graphene. *ChemSusChem*, **2018**, *11*, 1617–1620.

4.1 Abstract

We report a $Ni_{30}Pd_{70}$/nitrogen-doped graphene (NG) catalyst that hydrodehalogenates halogenated aromatics under mild reaction conditions. It reduces mono- or dichloroarenes to the corresponding dehalogenated arenes in >90% yield in 10% aqueous isopropanol solvent at or below 50 °C within 5 hours. Tests on a variety of substrates containing various functional groups show that the catalyst is selective for reduction of C-Cl and C-Br bonds. In addition, this catalyst completely hydrodehalogenates high concentration solutions of dioxin, polychlorinated biphenyls (PCBs), chloroaromatic constituents of the defoliant agent orange, and polybrominated diphenyl ethers (PBDEs) in 12 hours. The catalyst is reusable and shows no morphological or compositional changes after 5 cycles. This methodology offers a powerful, low-cost and safe technology for the degradation of polyhalogenated aromatics, and may be useful for preventing proliferation of these toxins in the environment from causing serious health issues.

4.2 Introduction

Polyhalogenated aromatics (PHAs), such as polychlorinated biphenyls (PCBs) and polybrominated diphenyl ethers (PBDEs), are a class of persistent organic pollutants that adversely affect human health. Due to the stability of C_{Ar}-Cl (97.1 kcal/mol) and C_{Ar}-Br (84.0 kcal/mol) bonds,[1] these PHAs are extremely difficult to degrade in the natural environment, and can accumulate and pass from one organism to another through the food chain.[2–4] Activation of C_{Ar}-X (X = Cl or Br) bonds to achieve full conversion to C_{Ar}-H is the key step in PHA degradation. Conventional methods to accomplish this transformation rely on hydrodehalogenation reactions in the presence of a catalyst with either isopropanol or pressurized H_2 as the hydrogen source. Transition metal complexes of Pd,[5–7] Rh,[8–10] Ni,[11] Co,[12] or Fe,[13,14] are often selected as hydrodehalogenation catalysts under homogeneous reaction conditions, but these complexes often show limited stability and re-usability. For example, a Rh[8] catalyst requires strong base (*t*BuOK), high temperature (100 °C)

and a long reaction time (24 h) to dehalogenate chlorobenzene. Mild biological reagents have also been developed to degrade halogenated pollutants, but these systems require extremely long reaction times, and only work with low concentrations of PHAs. For example, bio-remediation processes using microalgae[15–17] or cyanobacteria[18,19] to dechlorinate PHAs require weeks to months to achieve only partial dechlorination of low concentrations of PHAs in soil.

Recently, a nanostructured composite of Fe(0) and Pd(0) was studied as a catalyst to degrade PHAs in water.[20,21] Fe reacts with water to generate H_2 for the subsequent Pd catalyzed-hydrodechlorination reaction. In this process, Fe(0) is oxidized and must be regenerated by a stronger reducing agent such as sodium borohydride for the catalysis to proceed. Still, the composite catalyst is not efficient for the dechlorination of high concentrations of PHAs. Supported transition metal catalysts have also been developed for hydrodehalogenation reactions.[22–24] However, these reactions often use pressured hydrogen gas, which makes them difficult to apply outside of the lab to remediate polluted soil or water. As part of the development of the hydrogen economy, ammonia borane (AB, H_3NBH_3) has emerged as an appealing sustainable fuel source because it is a solid with a high hydrogen storage capacity. In addition, energy-efficient chemical processes have been developed to regenerate AB from its dehydrogenation products, making it an attractive alternative to H_2 gas for hydrodehalogenation reactions.[25–27] Pd-based NPs catalyze the dehydrogenation of AB for subsequent hydrogenation of nitro compounds to amines.[28–32] Combining the Pd-catalyzed C_{Ar}-X reduction with the AB-initiated transfer hydrogenation, here we report an efficient NiPd nanoparticle (NP) catalyst for hydrodehalogenation of high concentrations of chlorinated and brominated aromatics to the corresponding aromatics in near quantitative yield. The NP catalyst is comprised of 3 nm NiPd NPs assembled on nitrogen-doped graphene (NG). It catalyzes the one-pot dehydrogenation of AB and subsequent hydrodehalogenation of halogenated aromatics in 10% aqueous isopropanol at or below 50 °C. It is effective for converting C_{Ar}-X to C_{Ar}-H, not only for monohalogenated aromatics, but also for PHAs, including PCBs and PBDEs.

4.3   Results and discussion

We first tested MPd (M = Ni, Co, Fe) NP catalysts for AB-initiated C_{Ar}-Cl conversion to C_{Ar}-H. 3-4 nm MPd NPs were first prepared and deposited onto the carbon (C) or graphene (G) supports in order to study their roles in catalyzing AB-initiated hydrodechlorination of chlorobenzene.[33,34] We found NiPd NPs to be more active than either CoPd or FePd. To further enhance NiPd catalysis, we deposited these NPs on nitrogen-doped graphene (NG)[35,36] so that the NPs are better anchored to the surface, and to guard against aggregation via pyridine-N coordination. In the reaction, the NG serves as a NP anchor, while NG and AB neutralize the HCl generated during the reaction, enhancing catalysis and stabilizing the catalyst. We assembled 3 nm $Ni_{30}Pd_{70}$ NPs on NG by mixing and sonicating a hexane dispersion of NPs and NG. We tested the assembly conditions and used a 1:1 w/w mixture of NPs/NG to form a well-dispersed monolayer of NPs on the NG surface (Figure 4.1a). We further prepared $Ni_{30}Pd_{70}$/C, $Ni_{30}Pd_{70}$/G, $Ni_{54}Pd_{46}$/NG, $Ni_{67}Pd_{33}$/NG and Pd/NG (Table 4.1 and Figure 4.1b-d). After testing the AB-initiated transfer hydrogenation and hydrodechlorination of chlorobenzene and dichlorobenzene, we found $Ni_{30}Pd_{70}$/NG to be the most efficient catalyst for the hydrodechlorination reaction (Table 4.1).

To demonstrate that AB is the source of hydrogen in the reactions, and not isopropanol, we performed the hydrodechlorination of dichlorobenzene in 10% aqueous isopropanol without adding AB and found the yield of dechlorinated products to be less than 3%. We also tested the reaction in aqueous AB solution without adding isopropanol as a cosolvent, and obtained a 76% yield of benzene. The reduction in yield from 99% (10% aqueous isopropanol solvent) to 76% (pure water as the solvent) is likely caused by the poor solubility of dichlorobenzene in pure water. When 10% isopropanol was added to improve the dichlorobenzene solubility, the reaction was completed within 5 hours and all the dichlorobenzene was converted to benzene. AB serves as both the hydrogen source, and as a base to neutralize the hydrochloric acid generated during the reaction, which is key to maintaining the pH of the reaction mixture and to stabilizing the NiPd/NG catalyst.
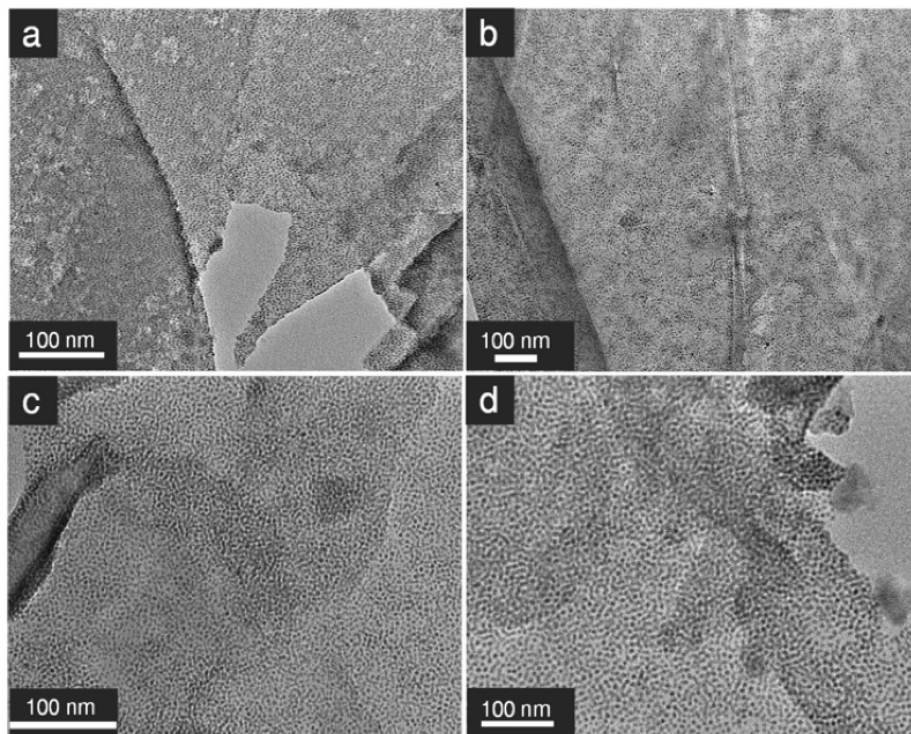
Figure 4.1 (a) TEM image of 3.0 nm $Ni_{30}Pd_{70}$/NG, (b) TEM image of 3.4 nm $Ni_{54}Pd_{46}$/NG, (c) TEM image of 3.8 nm $Ni_{67}Pd_{33}$/NG, (d) TEM image of 4.0 nm Pd/NG. These NiPd/NG samples were prepared by mixing hexane dispersions of NiPd NPs and NG in 1:1 mass ratio. Each TEM sample was prepared by adding a drop of hexane dispersion of NiPd/NG on an amorphous carbon coated Cu grid followed by hexane evaporation under ambient conditions.

Using $Ni_{30}Pd_{70}$/NG (abbreviated as NiPd/NG) as the catalyst, we studied the time-dependent AB initiated hydrodechlorination of chlorobenzene at 40 °C. Figure 4.2 shows the concentration changes of chlorobenzene and benzene over time in the presence of 3 mol% NiPd/NG. The disappearance of chlorobenzene and growth of benzene follows the exponential concentration changes of a first order reaction, indicating that the reaction proceeds without formation of other detectable intermediates.

Using these reaction conditions, we examined a series of other mono-halogenated aromatic compounds (Table 4.2). NiPd/NG is an efficient and selective hydrodechlorination catalyst for these substrates. Chlorobenzene, 2-chloronaphthylene and 3-chloropyridine are reduced in greater than 94% yield (entries 1-3). The reaction is effective for substrates with

Table 4.1 Hydrodehalogenation of dichlorobenzene catalyzed by Pd-based catalysts on different carbon supports[a]

Entry	Catalyst	Yield[b] (%)
1	$Ni_{30}Pd_{70}$/C	81
2	$Ni_{30}Pd_{70}$/G	84
3	**$Ni_{30}Pd_{70}$/NG**	**99**
4	Pd/NG	69
5	$Ni_{54}Pd_{46}$/NG	72
6	$Ni_{67}Pd_{33}$/NG	44

[a] Reaction conditions: dichlorobenzene (1 mmol), ammonia borane (6 mmol), 10% aqueous isopropanol (3.0 mL) and catalyst (3 mol %) for 5 h at 50 °C. [b] Yields determined by GC-MS.

either electron-donating (entries 4-9, 13-14) or electron-withdrawing groups (entries 10-12, 15). The conversion is not sensitive to the position of the halogen atom relative to other functional groups (entries 4-12). Hydroxyl, amine, amide, and carboxylic acid groups are not reduced under the reaction conditions. Furthermore, the reaction can be extended to brominated substrates (entries 16-21).

Encouraged by the general applicability of NiPd/NG to mono-halogenated substrates, we extended the study to substrates containing multiple Cl or Br atoms. Using 1,2-dicholorobenzene as an example, we examined its time-dependent hydrodechlorination at 50 °C. As shown in Figure 4.3, the first hour of the reaction gives exponential decay of dichlorobenzene accompanied by an increase in both the chlorobenzene and benzene concentrations. This pattern is typical of a stepwise process in which the two chlorine atoms are reduced sequentially. The chlorobenzene concentration reaches a maximum at two hours, and subsequently decreases with a corresponding increase in the concentration of the benzene final product. The reaction is complete after 5 hours. During the course of the reaction

Figure 4.2 Time-dependent hydrodechlorination of chlorobenzene catalyzed by NiPd/NG catalyst. Reaction conditions: chlorobenzene (1 mmol), ammonia borane (2 mmol), 10% aqueous isopropanol (3.0 mL) and NiPd/NG (3 mol%) at 40 °C.

we do not detect any other intermediates by GC-MS.

Using these reaction conditions, we examined other polyhalogenated substrates (Table 4.3). Dichlorinated substrates (entries 1-6) are dehalogenated to their parent compounds in high yield. The environmental pollutants 2,4-dichlorophenoxyacetic acid, 2,4,5-trichlorophenoxyacetic acid and 2,3,7,8-tetrachlorodibenzodioxin (entries 7-9) are all completely dechlorinated in high yield under the reaction conditions. We also examined five chlorinated biphenyl substrates (entries 10-14). Compounds 10-12 that contain chlorine atoms meta and/or para to the biphenyl bond are fully reduced under the standard conditions. In contrast, substrates with chlorine atoms ortho to the biphenyl bond are reduced more slowly (entries 13 and 14). These are the most sterically hindered positions in the molecule, and the ortho chlorine substituents enforce a perpendicular geometry of the two phenyl rings. These substrates require 12 hours to achieve complete reduction of all of the C-Cl bonds. In a similar manner, the four bromine atoms in PBDE (entry 12) that are ortho to the ether oxygen reside in sterically hindered positions, and PBDE also requires 12 hours for full dehalogenation.

Table 4.2 Hydrodehalogenation of mono-halogen substituted compounds[a]

Entry	Ar-X	Yield[b] (%)	Entry	Ar-X	Yield[b] (%)	Entry	Ar-X	Yield[b] (%)
1		99[c]	2		94[c]	3		98[c]
4		98[c]	5		99[c]	6		99[c]
7		91	8		91	9		93
10		97	11		97	12		98
13		87	14		90	15		92
16		99[c]	17		97[c]	18		99[c]
19		99[c]	20		96	21		97

[a] Reaction conditions: aryl halides (1 mmol), ammonia borane (2 mmol), 10% aqueous isopropanol (3.0 mL) and NiPd/NG (3 mol%) for 3 h at 40 °C. [b] Isolated yield except where noted otherwise. [c] Yield determined by GCMS.

We have also examined if the NiPd/NG catalyst can be recycled through several sequential hydrodehalogenation reactions. We measured the stability of the catalyst by observing NiPd NP morphology and composition changes before and after the hydrodechlorination of dichlorobenzene. After the first reaction was complete, we separated the catalyst from the reaction solution by filtration, and washed it with water and isopropanol. We then re-used it in the next hydrodehalogenation reaction. Our tests showed that after the 5th reaction/separation cycle, the catalyst had no obvious loss in activity and the product yield remained >91%. TEM and ICP-AES analyses of the catalyst after the 5th reaction cycle
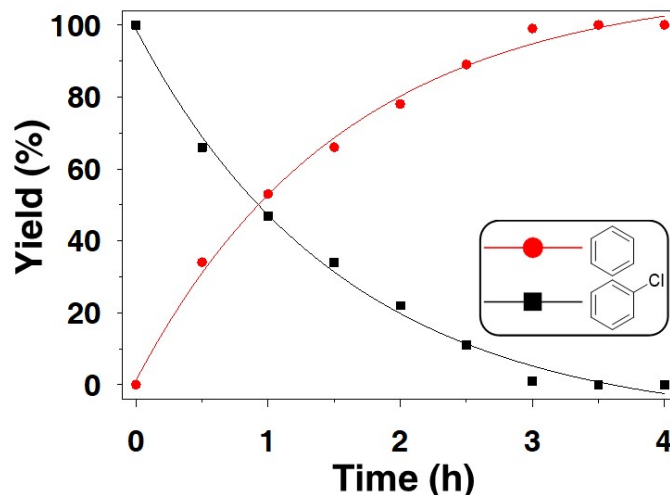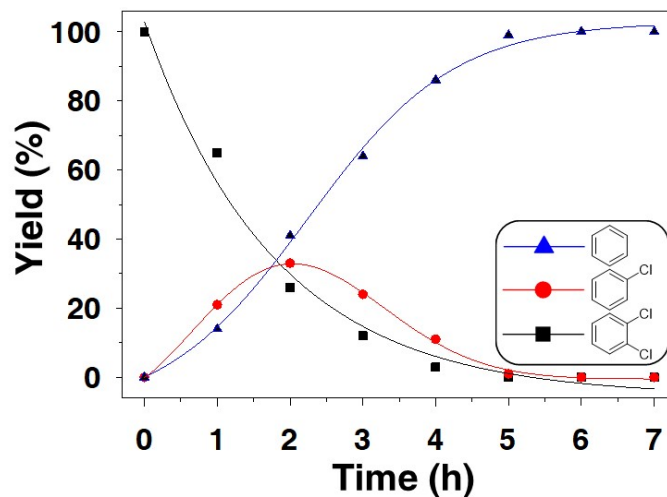
Figure 4.3 Time-dependent hydrodechlorination of dichlorobenzene catalyzed by NiPd/NG catalyst. Reaction conditions: dichlorobenzene (1 mmol), ammonia borane (6 mmol), 10% aqueous isopropanol (3.0 mL) and NiPd/NG (3 mol%) at 50 °C.

showed that the NPs display no obvious morphology changes or aggregation (Figure 4.4), and the NP composition is stabilized at $Ni_{28}Pd_{72}$. These results suggest that NG offers the necessary anchoring sites to stabilize NiPd NPs against aggregation. The combination of NG and AB neutralizes the hydrochloric acid generated during the reaction, and prevents Ni from leaching out of the NiPd NPs.
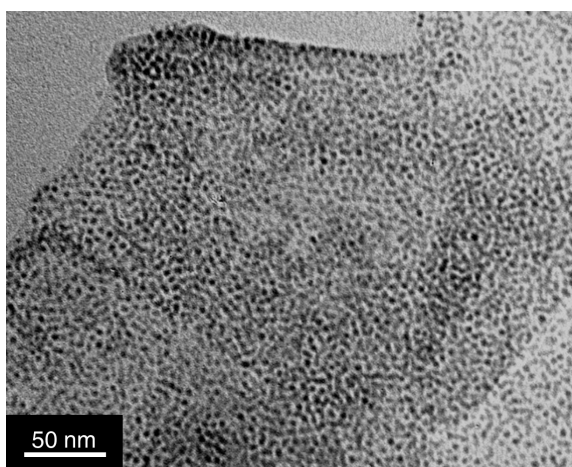
Figure 4.4 TEM of NiPd/NG after 5th recycling.

Table 4.3 Hydrodehalogenation of multi-halogen substrates[a]

Entry	Ar-X	Yield[b] (%)	Entry	Ar-X	Yield[b] (%)	Entry	Ar-X	Yield[b] (%)
1		98[c]	2		97[c]	3		98[c]
4		97	5		90	6		93
7		90	8		87	9		92[c,d]
10		99[c]	11		99[c]	12		98[c]
13		97[c,e]	14		94[c,e,f]	15		97[c,e]

[a] Reaction conditions: organic halides (1 mmol), ammonia borane (3.0 equiv with respect to halogen atoms), 10% aqueous isopropanol (3.0 mL) and NiPd/NG (3 mol%) at 50 °C. [b] Isolated yield except where noted. [c] Yield determined by GCMS. [d] 0.003 mmol (1 mg) of dioxin was used in the reaction. [e] Reaction was run for 12 h. [f] 0.04 mmol of decachlorobiphenyl was used in the reaction.

4.4   Conclusion

In conclusion, the NiPd/NG catalyst reported here shows superior performance for the hydrodehalogenation of PHAs under mild and environmentally friendly reaction conditions. Dehalogenation reactions often require strong bases, strong reducing agents and harsh reaction conditions including high temperatures. In contrast, this NiPd/NG system uses ammonia borane as the hydrogen source and base, and an aqueous solvent system. The reaction is compatible with a variety of functional groups including hydroxyl groups, amines, amides and carboxylic acids. Under these mild conditions, the NiPd/NG catalyst promotes the complete dehalogenation of several severe environmental contaminants including the components of agent orange, dioxins, PCBs and PBDEs, which are extremely difficult to decontaminate using conventional methods. This concept of exploiting nanoparticles for

green chemistry applications may provide a promising avenue for the rational design and assembly of nanostructured catalysts for solving long-standing problems in environmental chemistry.

4.5   Experimental section

Synthesis of Pd NPs   Under a gentle flow of N_2, 200 mg of BBA, 6 mL of OAm, and 4 mL of ODE were mixed, stirred by a magnetic bar and heated to 120 °C for 10 min. The solution was kept at this temperature for another 30 min before it was cooled to 100 °C. In a separate vial, 4.0 mmol of $Pd(acac)_2$ was dissolved in 3 mL of ODE and the solution was added via a syringe quickly into the 100 °C solution. The mixed solution was stirred at 100 °C for 1 h and cooled to room temperature. Then ethanol was added, and the NP product was separated by centrifugation at 9000 rpm for 15 min. Next, the NPs were washed with hexane/ethanol (v/v= 1:15) by centrifugation at 9000 rpm for 20 min. The obtained powder was dispersed in hexane for further use.

Synthesis of $Ni_{30}Pd_{70}$ alloy NPs   The synthesis was similar to what was described in the synthesis of Pd NPs except that in a separate vial, 2.0 mmol of $Pd(acac)_2$ and 3.0 mmol of $Ni(acac)_2$ were dissolved in 3 mL of ODE.

Synthesis of $Co_{31}Pd_{69}$ alloy NPs   The synthesis was similar to what was described in the synthesis of Pd NPs except that in a separate vial, 1.5 mmol of $Pd(acac)_2$ and 3.5 mmol of $Co(acac)_3$ were dissolved in 3 mL of ODE.

Synthesis of $Cu_{31}Pd_{69}$ alloy NPs   The synthesis was similar to what was described in the synthesis of Pd NPs except that in a separate vial, 2.2 mmol of $Pd(acac)_2$ and 2.8 mmol of $Cu(acac)_2$ were dissolved in 3 mL of ODE.

Synthesis of $Fe_{32}Pd_{68}$ alloy NPs   The synthesis was similar to what was described in the synthesis of Pd NPs except that in a separate vial, 1.3 mmol of $Pd(acac)_2$ and 3.7 mmol

of Fe(acac)$_3$ were dissolved in 3 mL of ODE.

Synthesis of Ni$_{54}$Pd$_{46}$ alloy NPs   The synthesis was similar to what was described in the synthesis of Pd NPs except that in a separate vial, 2.0 mmol of Pd(acac)$_2$ and 4.0 mmol of Ni(acac)$_2$ were dissolved in 3 mL of ODE.

Synthesis of Ni$_{67}$Pd$_{33}$ alloy NPs   Synthesis of Ni67Pd33 Alloy NPs: The synthesis was similar to what was described in the synthesis of Pd NPs except that in a separate vial, 1.5 mmol of Pd(acac)$_2$ and 4.0 mmol of Ni(acac)$_2$ were dissolved in 3 mL of ODE.

Synthesis of nitrogen-doped graphene (NG)   2.0 g melamine and 0.4 g single-layered graphene oxide were mixed in 400 mL deionized water and stirred at room temperature for 48 h. Water was then evaporated at 60 °C. The resulting solid product was first annealed at 350 °C for 0.5 h and then at 900 °C for 1 h under a N$_2$ atmosphere. After cooled to room temperature, the powder was ready for further use.

Assembly of NPs on NG   10 mg of the NPs were dispersed in 5.0 mL of hexane and the dispersion was added drop-wise into a suspension of 10.0 mg of NG in ethanol (60 mL) in an ultrasonic environment. After the addition of the NP dispersion, the ethanol/hexane mixture was sonicated for 2 h to ensure complete adsorption of the NPs onto NG.

Synthesis of the PCB substrates   Chloroaryl bromide (5 mmol), chloroaryl boronic acid (5 mmol), K$_3$PO$_4$ (10 mmol), Pd(OAc)$_2$ (10 mg) and 20 mL of DMF/H$_2$O (v/v = 1/1) were added to a round bottom flask. The reaction mixture was stirred at room temperature for 24 hours. The aqueous phase was extracted with EtOAc (3×20 mL), the combined organic extracts were washed with H$_2$O (3×50 mL), dried over Na$_2$SO$_4$ and the solvents were removed in vacuo. The crude product was purified by flash column chromatography.

General procedure for the hydrodehalogenation reactions   Aryl halide (1 mmol), NPs/NG (10 mg, 3 mol %), H$_3$NBH$_3$ (3 mmol) and 10% aqueous isopropanol (3 mL) were

stirred in a 10 mL sealed tube at 50 °C for 5 hours. After the reaction was complete, the catalyst was filtered and the mixture was extracted with ethyl acetate. The organic phase was evaporated under vacuum and purified by flash column chromatography (hexane/ethyl acetate = 8:1) to give the final product.

Cl balance during reaction   After the dehalogenation of dichlorobenzene, the catalysts was separated from reaction mixture and titrated in the product solution with $AgNO_3$. AgCl rapidly precipitated from the reaction mixture as a white solid. We separated, dried and weighed the AgCl precipitate, and calculated that 93% of the Cl was recovered. This confirmed that Cl is present as chloride ion after the dehydrohalogenation reactions.

Catalyst re-use   After the reaction was complete, the NPs/NG catalyst was filtered from the reaction mixture and washed with water and isopropanol. The catalyst was then dried, weighed, and used directly for the next round of reaction.

4.5.1   Characterization data of products

Phenol ^{1}H-NMR (400 MHz, CDCl$_3$) δ [ppm] = 7.36 (t, J = 7.4 Hz, 2H), 7.08 (t, J = 7.4 Hz, 1H), 6.99 (d, J = 8.0 Hz, 2H), 6.514 (bs, 1H); ^{13}C-NMR (100 MHz, CDCl$_3$) δ [ppm] = 155.1, 130.0, 121.3, 115.6.

Anisole ^{1}H-NMR (400 MHz, CDCl$_3$) δ [ppm] = 7.38 (t, J = 7.4 Hz, 2H), 7.06-6.99 (m, 3H), 3.88 (s, 3H); ^{13}C-NMR (100 MHz, CDCl$_3$) δ [ppm] = 159.6, 129.5, 120.7, 114.0, 55.2.

Benzoic acid ^{1}H-NMR (400 MHz, CDCl$_3$) δ [ppm] = 13.10 (bs, 1H), 8.19 (d, J = 7.6 Hz, 2H), 7.66 (t, J = 7.4 Hz, 1H), 7.52 (t, J = 7.4 Hz, 2H); ^{13}C-NMR (100 MHz, CDCl$_3$) δ [ppm] = 172.8, 133.9, 130.2, 129.4, 128.5.

Aniline ^{1}H-NMR (400 MHz, CDCl$_3$) δ [ppm] = 7.28 (t, J = 7.4 Hz, 2H), 6.89 (t, J = 7.4 Hz, 1H), 6.77 (d, J = 7.6 Hz, 2H), 3.70 (bs, 2H); ^{13}C-NMR (100 MHz, CDCl$_3$) δ [ppm] = 146.6, 129.4, 118.6, 115.24.

2-phenoxyacetic acid ^{1}H-NMR (400 MHz, CDCl$_3$) δ [ppm] = 11.67 (bs, 1H), 7.35 (t, J = 7.2 Hz, 2H), 7.06 (t, J = 7.2 Hz, 1H), 6.96 (d, J = 7.6 Hz, 2H), 4.72 (s, 2H); ^{13}C-NMR (100 MHz, CDCl$_3$) δ [ppm] = 175.1, 157.4, 129.7, 122.2, 114.7, 64.8. HRMS calculated for C$_8$H$_8$O$_3$ (M-H)$^-$ 151.0393, found 151.0395.

4-chloro-1,1'-biphenyl ^{1}H-NMR (400 MHz, CDCl$_3$) δ [ppm] = 7.62-7.56 (m, 4H), 7.52-7.40 (m, 5H); ^{13}C-NMR (100 MHz, CDCl$_3$) δ [ppm] = 140.0, 139.7, 133.4, 129.0, 128.9, 128.5, 127.7, 127.0. GC-MS calculated for C$_{12}$H$_9$Cl (M)$^+$ 188.04, found 188.0.
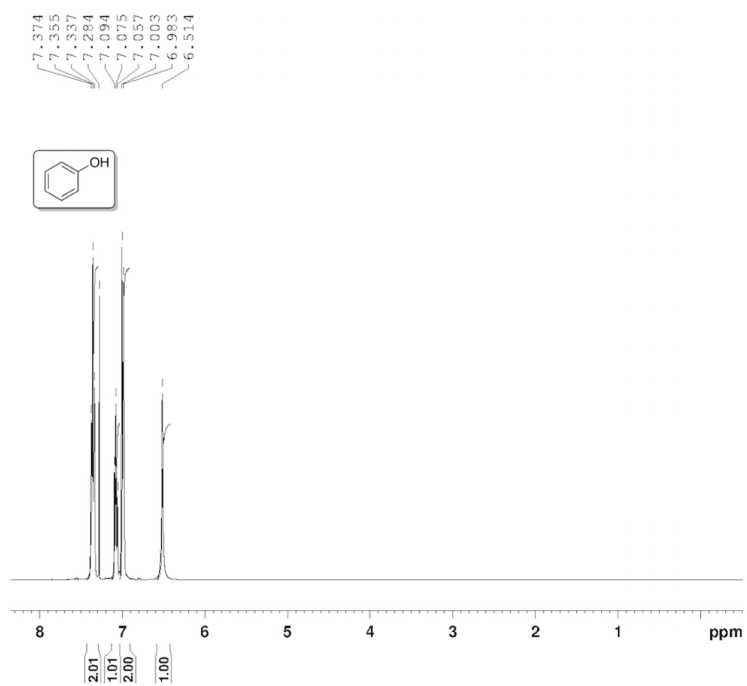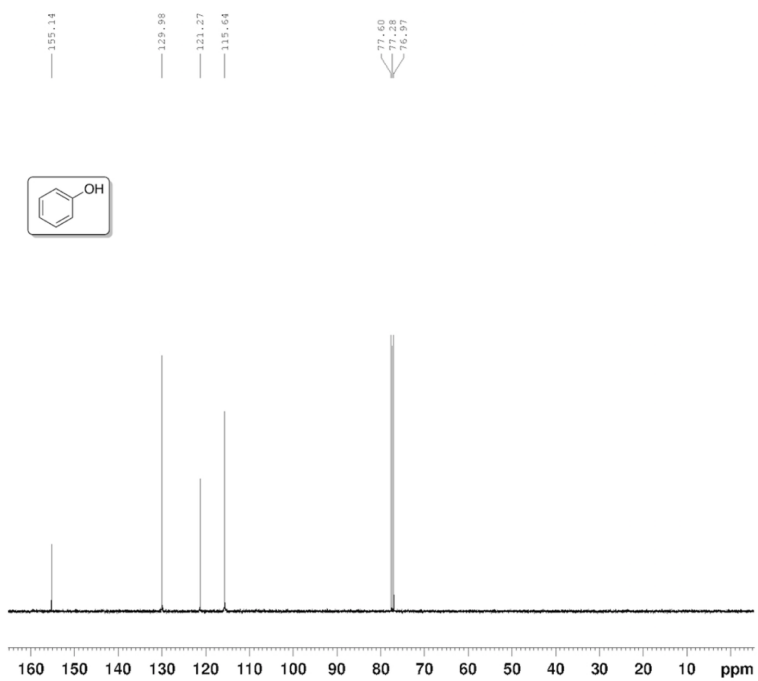
3,4,4'-trichloro-1,1'-biphenyl ^{1}H-NMR (400 MHz, CDCl$_3$) δ [ppm] = 7.65 (s, 1H), 7.53-7.43 (m, 5H), 7.39 (d, J = 8.4 Hz, 1H); ^{13}C-NMR (100 MHz, CDCl$_3$) δ [ppm] = 140.0, 137.2, 134.4, 133.0, 131.8, 130.8, 129.2, 128.8, 128.2, 126.2. GC-MS calculated for C$_{12}$H$_7$Cl$_3$ (M)$^+$ 255.96, found 256.0.

3,3',4,4'-tetrachloro-1,1'-biphenyl ^{1}H-NMR (400 MHz, CDCl$_3$) δ [ppm] = 7.62 (d, J = 8.0 Hz, 2H), 7.53-7.35 (m, 4H); ^{13}C-NMR (100 MHz, CDCl$_3$) δ [ppm] = 138.7, 133.5, 132.8, 131.5, 128.9, 126.4. GC-MS calculated for C$_{12}$H$_6$Cl$_4$ (M)$^+$ 289.92, found 290.0.

2,2',6,6'-tetrachloro-1,1'-biphenyl ^{1}H-NMR (400 MHz, CDCl$_3$) δ [ppm] = 7.45 (d, J = 8.0 Hz, 4H), 7.34 (t, J = 8.0 Hz, 2H); ^{13}C-NMR (100 MHz, CDCl$_3$) δ [ppm] = 135.5, 135.4, 130.5, 128.5. GC-MS calculated for C$_{12}$H$_6$Cl$_4$ (M)$^+$ 289.92, found 290.0.

4.6 Characterization of compounds

Spectra of phenol

^{1}H-NMR

^{13}C-NMR

Spectra of anisole

¹H-NMR

7.403
7.384
7.366
7.284
7.061
7.043
7.013
6.993

3.880

8.0 7.5 7.0 6.5 6.0 5.5 5.0 4.5 4.0 3.5 3.0 2.5 2.0 1.5 1.0 0.5 ppm

2.00   3.00   3.12

¹³C-NMR

159.64

129.53
120.72
113.96

77.47
77.15
76.83

55.15

170 160 150 140 130 120 110 100 90 80 70 60 50 40 30 20 10 ppm
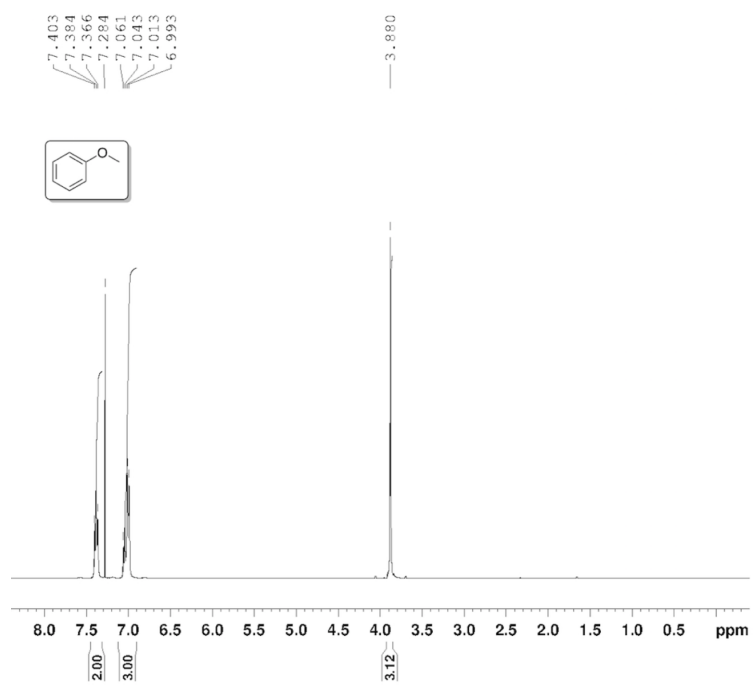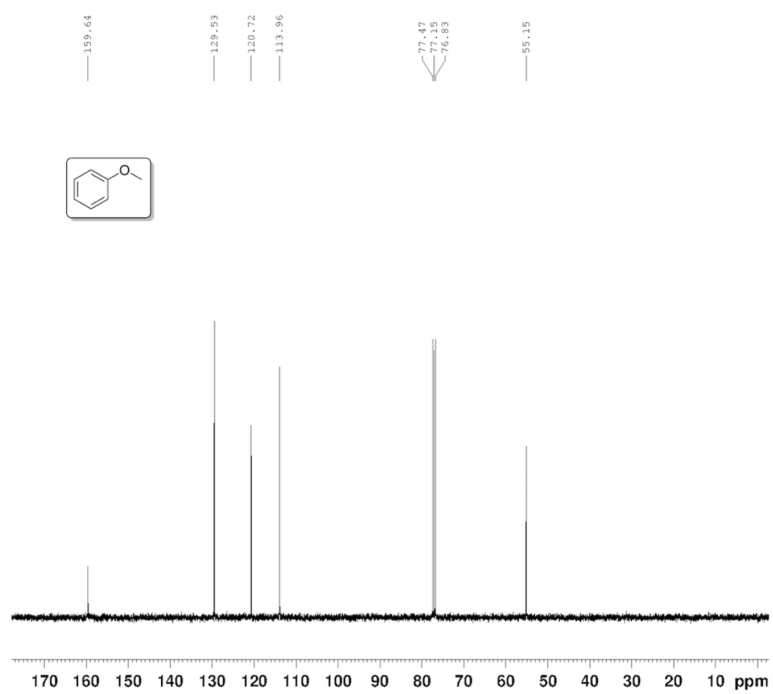
Spectra of benzoic acid

^{1}H-NMR
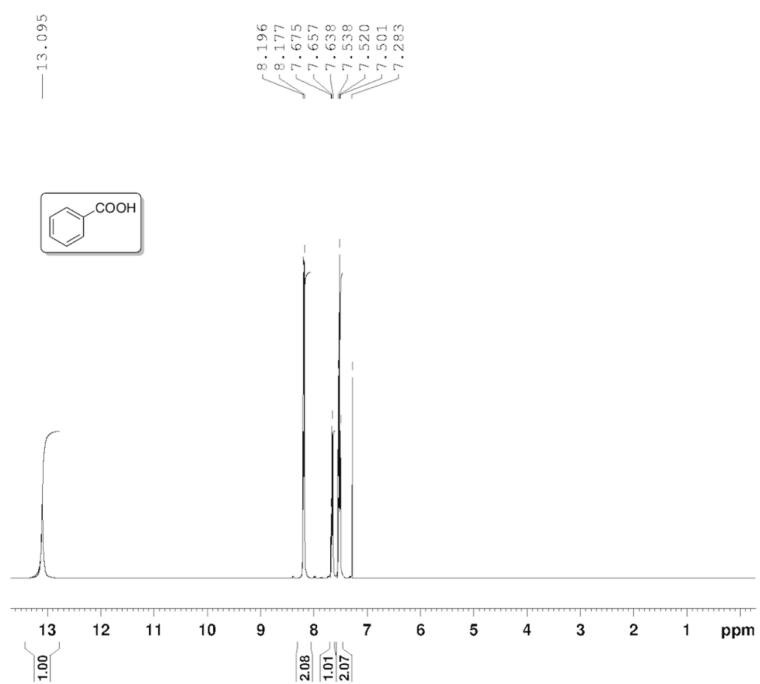
^{13}C-NMR
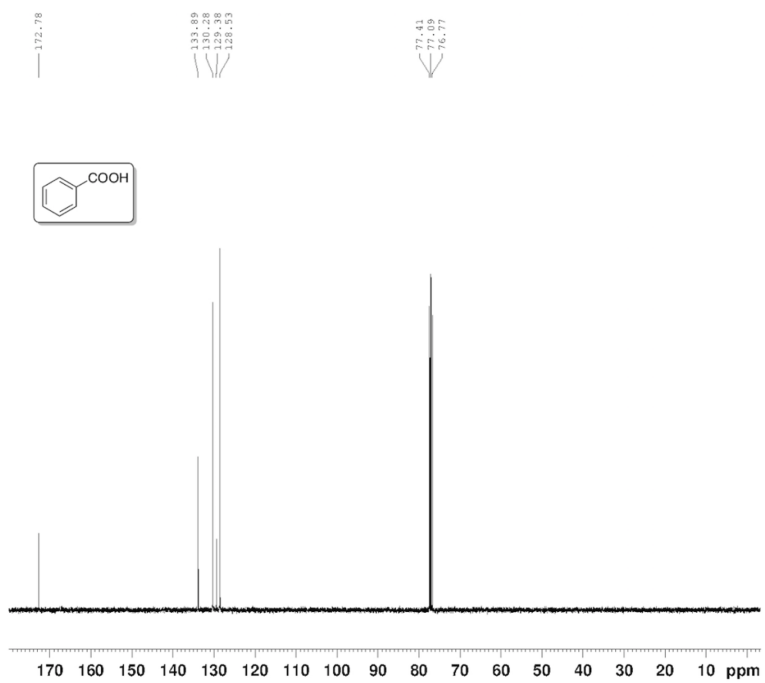
Spectra of aniline

^{1}H-NMR
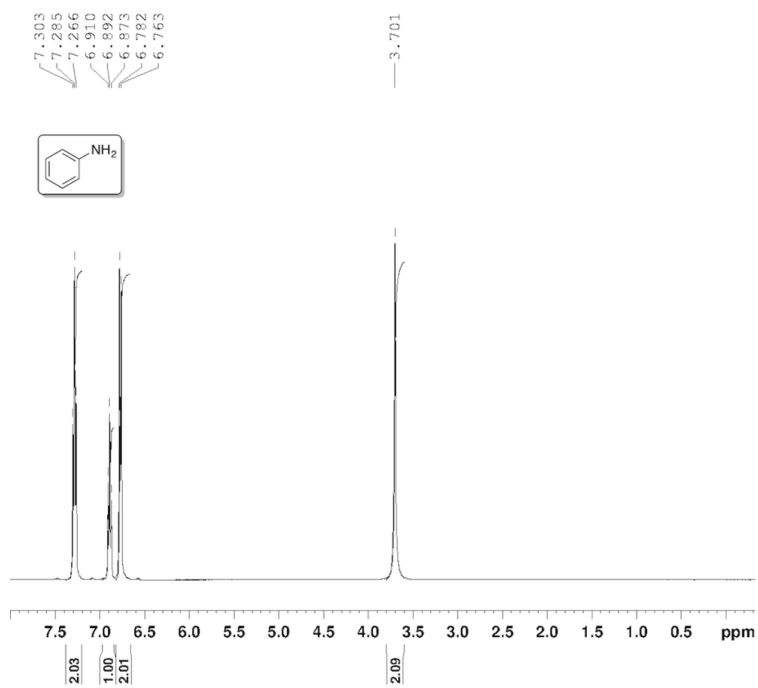
^{13}C-NMR
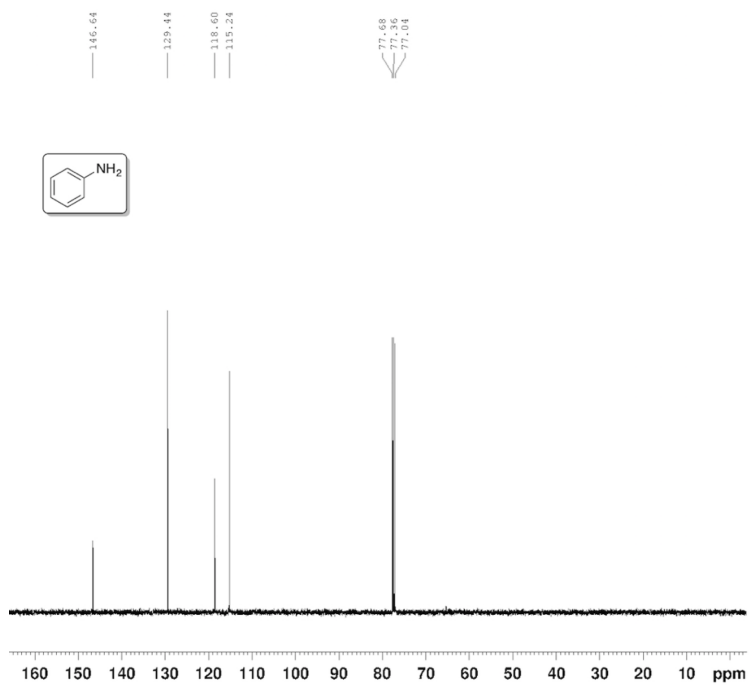
Spectra of 2-phenoxyacetic acid
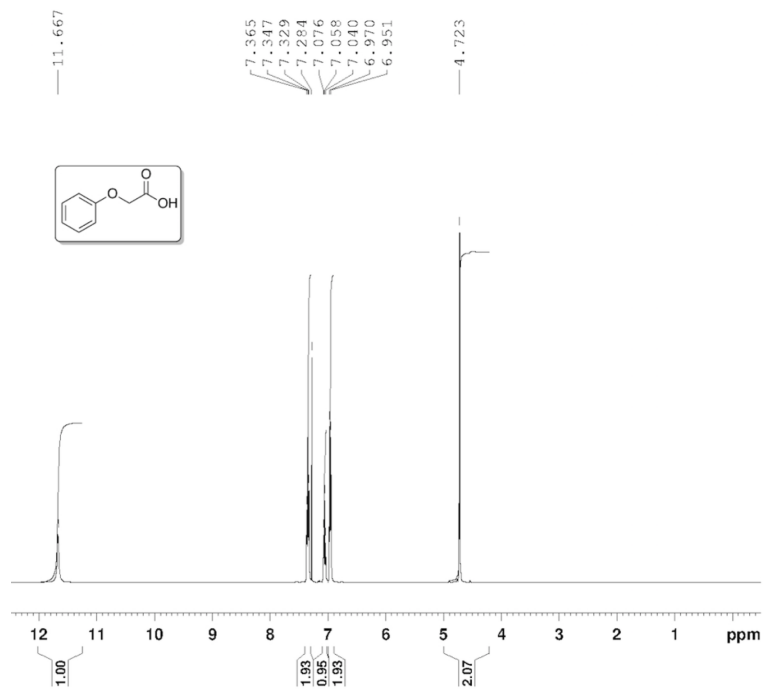
^{1}H-NMR

^{13}C-NMR
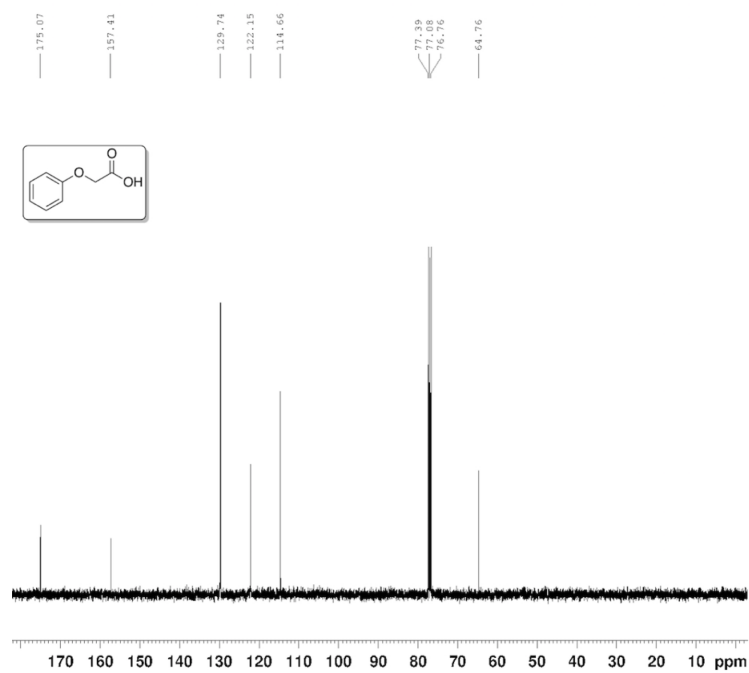
Spectra of 4-chloro-1,1'-biphenyl
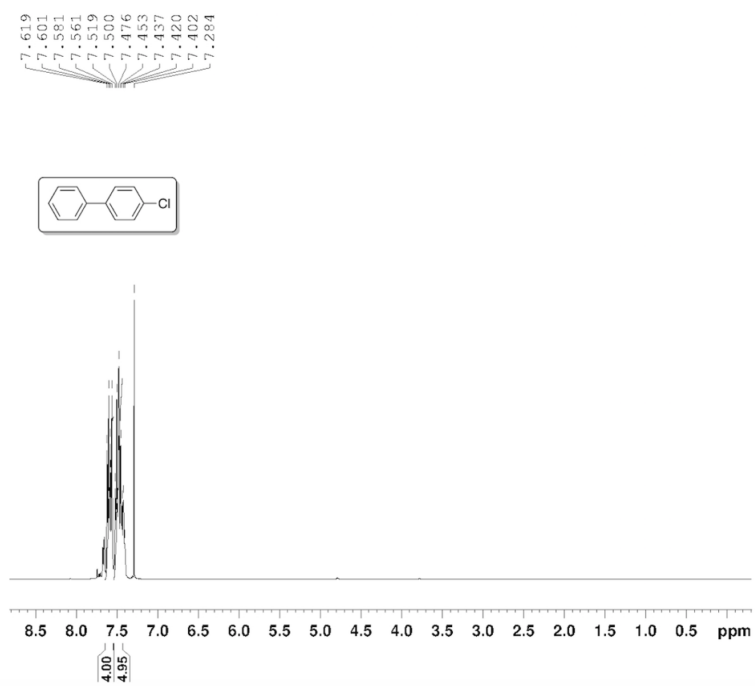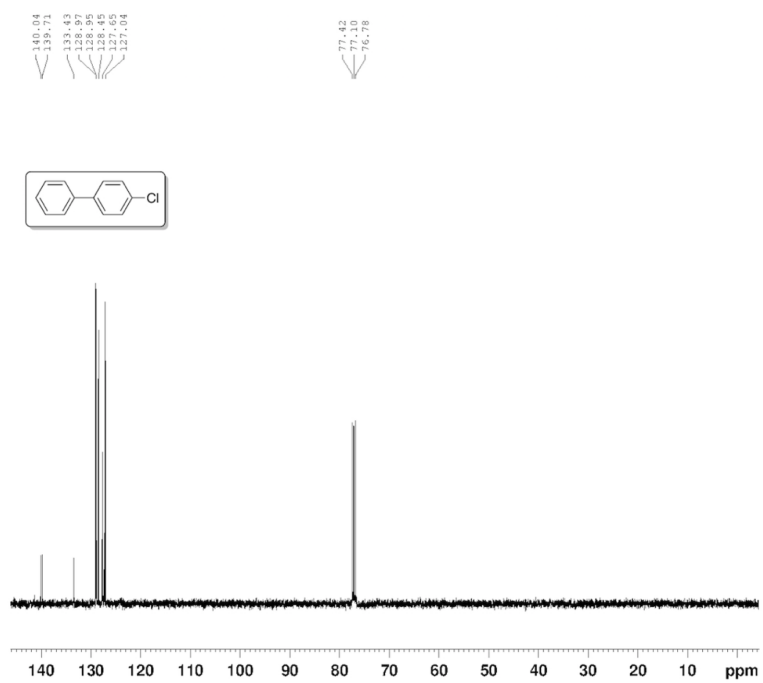
^{1}H-NMR

^{13}C-NMR

Spectra of 3,4,4'-trichloro-1,1'-biphenyl

^{1}H-NMR

7.649
7.532
7.511
7.495
7.474
7.448
7.428
7.401
7.380
7.284

1.07
5.00
1.09

8 7 6 5 4 3 2 1 0 ppm

^{13}C-NMR

139.97
137.20
134.35
133.03
131.84
130.83
129.21
128.81
128.21
126.19

77.37
77.05
76.73

140 130 120 110 100 90 80 70 60 ppm
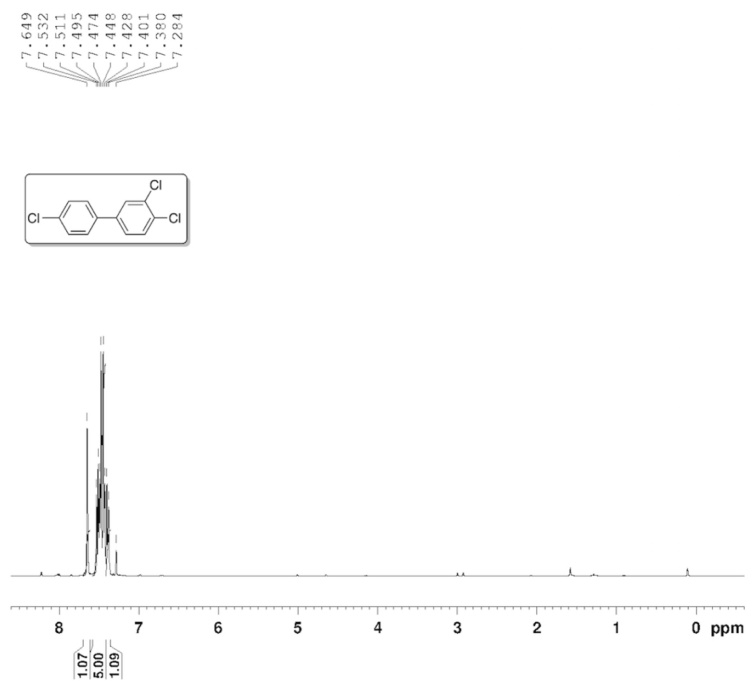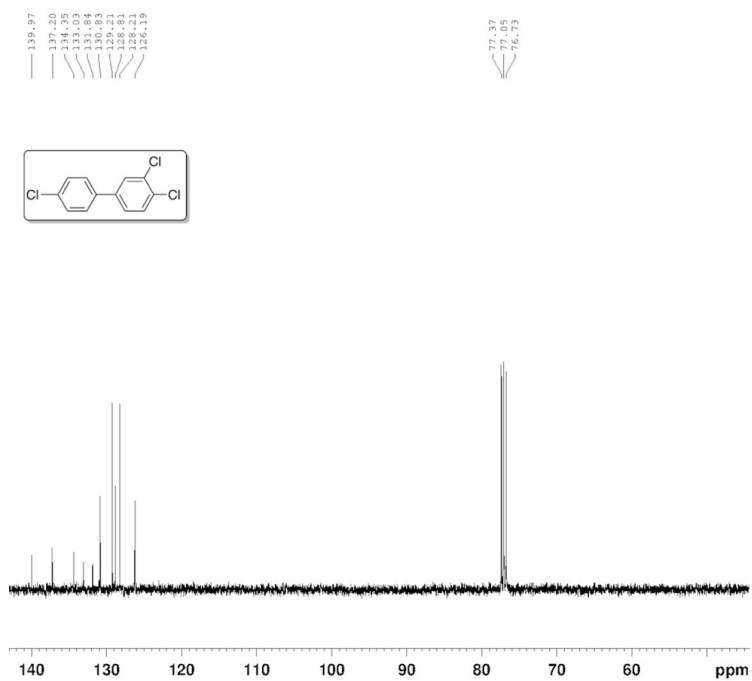
Spectra of 3,3',4,4'-tetrachloro-1,1'-biphenyl
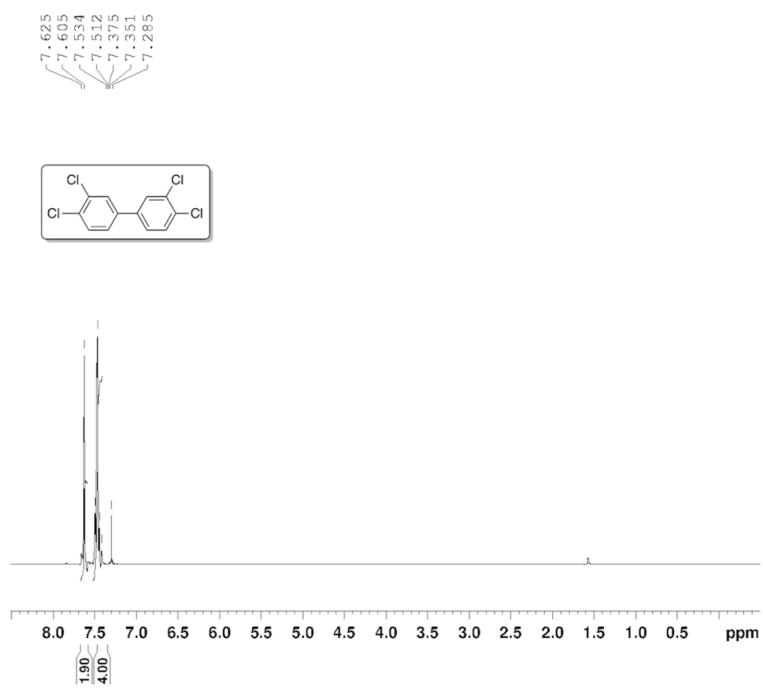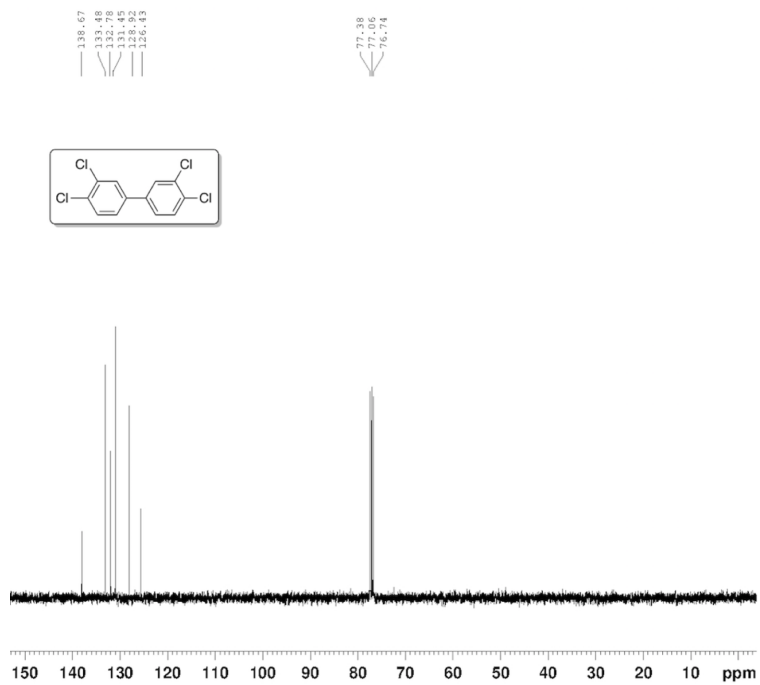
^{1}H-NMR

^{13}C-NMR

Spectra of 2,2',6,6'-tetrachloro-1,1'-biphenyl

^{1}H-NMR
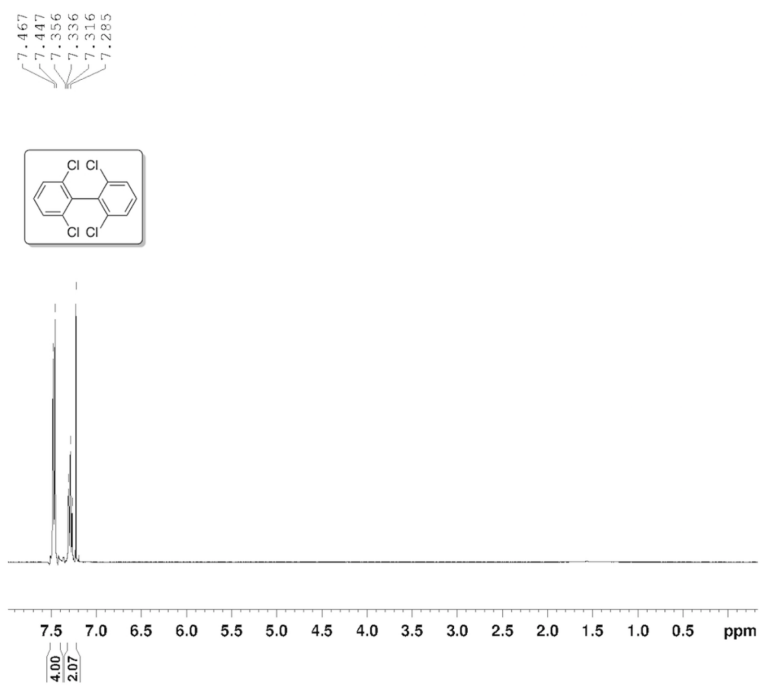
^{13}C-NMR
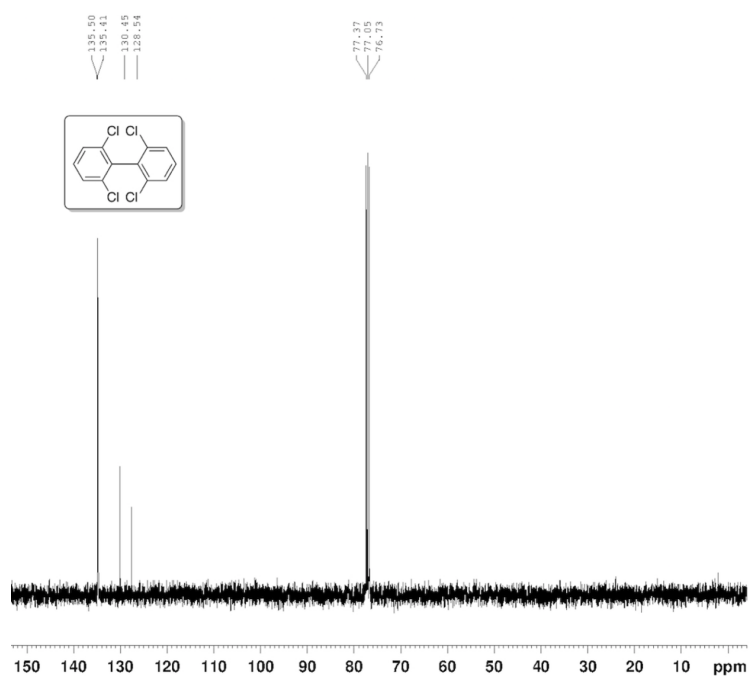
References

[1] Blanksby, S. J.; Ellison, G. B. Bond dissociation energies of organic molecules. *Accounts of Chemical Research* **2003**, *36*, 255–263.

[2] Jamieson, A. J.; Malkocs, T.; Piertney, S. B.; Fujii, T.; Zhang, Z. Bioaccumulation of persistent organic pollutants in the deepest ocean fauna. *Nature Ecology & Evolution* **2017**, *1*, 0051.

[3] Bartrons, M.; Catalan, J.; Penuelas, J. Spatial and temporal trends of organic pollutants in vegetation from remote and rural areas. *Scientific Reports* **2016**, *6*, 25446.

[4] Kelly, B. C.; Ikonomou, M. G.; Blair, J. D.; Morin, A. E.; Gobas, F. A. Food web–specific biomagnification of persistent organic pollutants. *Science* **2007**, *317*, 236–239.

[5] Pyo, A.; Kim, S.; Kumar, M. R.; Byeun, A.; Eom, M. S.; Han, M. S.; Lee, S. Palladium-catalyzed hydrodehalogenation of aryl halides using paraformaldehyde as the hydride source: high-throughput screening by paper-based colorimetric iodide sensor. *Tetrahedron Letters* **2013**, *54*, 5207–5210.

[6] Iranpoor, N.; Firouzabadi, H.; Azadi, R. Diphenylphosphinite ionic liquid (IL-OPPh2): A solvent and ligand for palladium-catalyzed silylation and dehalogenation reaction of aryl halides with triethylsilane. *Journal of Organometallic Chemistry* **2010**, *695*, 887–890.

[7] Navarro, O.; Marion, N.; Oonishi, Y.; Kelly, R. A.; Nolan, S. P. Suzuki- Miyaura, α-ketone arylation and dehalogenation reactions catalyzed by a versatile N-heterocyclic carbene- palladacycle complex. *The Journal of Organic Chemistry* **2006**, *71*, 685–692.

[8] You, T.; Wang, Z.; Chen, J.; Xia, Y. Transfer hydro-dehalogenation of organic halides catalyzed by ruthenium (II) complex. *The Journal of Organic Chemistry* **2017**, *82*, 1340–1346.

[9] Lázaro, G.; Polo, V.; Fernández-Alvarez, F. J.; García-Orduña, P.; Lahoz, F. J.; Iglesias, M.; Pérez-Torrente, J. J.; Oro, L. A. Catalytic hydrodechlorination of benzyl chloride promoted by Rh–N-heterocyclic carbene catalysts. *ChemSusChem* **2015**, *8*, 495–503.

[10] Fujita, K.-i.; Owaki, M.; Yamaguchi, R. Chemoselective transfer hydrodechlorination of aryl chlorides catalyzed by Cp* Rh complexes. *Chemical Communications* **2002**, 2964–2965.

[11] Mochizuki, K.; Suzuki, M. Photochemical dehalogenation mediated by macrocyclic nickel (II) complexes. *Inorganic Chemistry Communications* **2011**, *14*, 902–905.

[12] Chan, K. S.; Liu, C. R.; Wong, K. L. Cobalt porphyrin catalyzed hydrodehalogenation of aryl bromides with KOH. *Tetrahedron Letters* **2015**, *56*, 2728–2731.

[13] Czaplik, W. M.; Grupe, S.; Mayer, M.; von Wangelin, A. J. Practical iron-catalyzed dehalogenation of aryl halides. *Chemical Communications* **2010**, *46*, 6350–6352.

[14] Guo, H.; Kanno, K.-i.; Takahashi, T. Iron-catalyzed dechlorination of aryl chlorides. *Chemistry Letters* **2004**, *33*, 1356–1357.

[15] Papazi, A.; Kotzabasis, K. Rational management of dichlorophenols biodegradation by the microalga Scenedesmus obliquus. *PLOS One* **2013**, *8*, e61682.

[16] Papazi, A.; Andronis, E.; Ioannidis, N. E.; Chaniotakis, N.; Kotzabasis, K. High yields

of hydrogen production induced by meta-substituted dichlorophenols biodegradation from the green alga Scenedesmus obliquus. *PLOS One* **2012**, *7*, e49037.

[17] Čvančarová, M.; Křesinová, Z.; Filipová, A.; Covino, S.; Cajthaml, T. Biodegradation of PCBs by ligninolytic fungi and characterization of the degradation products. *Chemosphere* **2012**, *88*, 1317–1323.

[18] Zhang, H.; Jiang, X.; Lu, L.; Xiao, W. Biodegradation of polychlorinated biphenyls (PCBs) by the novel identified cyanobacterium Anabaena PD-1. *PLOS One* **2015**, *10*, e0131450.

[19] Zhang, H.; Hu, C.; Jia, X.; Xu, Y.; Wu, C.; Chen, L.; Wang, F. Characteristics of γ-hexachlorocyclohexane biodegradation by a nitrogen-fixing cyanobacterium, Anabaena azotica. *Journal of Applied Phycology* **2012**, *24*, 221–225.

[20] Kopinke, F.-D. Comment on Critical review of Pd-based catalytic treatment of priority contaminants in water. *Environmental Science & Technology* **2012**, *46*, 11467–11468.

[21] Zhuang, Y.; Ahn, S.; Seyfferth, A. L.; Masue-Slowey, Y.; Fendorf, S.; Luthy, R. G. Dehalogenation of polybrominated diphenyl ethers and polychlorinated biphenyl by bimetallic, impregnated, and nanoscale zerovalent iron. *Environmental Science & Technology* **2011**, *45*, 4896–4903.

[22] Goswami, A.; Rathi, A. K.; Aparicio, C.; Tomanec, O.; Petr, M.; Pocklanova, R.; Gawande, M. B.; Varma, R. S.; Zboril, R. In situ generation of Pd–Pt core–shell nanoparticles on reduced graphene oxide (Pd@ Pt/rGO) using microwaves: applications in dehalogenation reactions and reduction of olefins. *ACS Applied Materials & Interfaces* **2017**, *9*, 2815–2824.

[23] Rong, H.; Cai, S.; Niu, Z.; Li, Y. Composition-dependent catalytic activity of bimetallic nanocrystals: AgPd-catalyzed hydrodechlorination of 4-chlorophenol. *ACS Catalysis* **2013**, *3*, 1560–1563.

[24] Shiraishi, Y.; Takeda, Y.; Sugano, Y.; Ichikawa, S.; Tanaka, S.; Hirai, T. Highly efficient photocatalytic dehalogenation of organic halides on TiO2 loaded with bimetallic Pd–Pt alloy nanoparticles. *Chemical Communications* **2011**, *47*, 7863–7865.

[25] Sutton, A. D.; Burrell, A. K.; Dixon, D. A.; Garner, E. B.; Gordon, J. C.; Nakagawa, T.; Ott, K. C.; Robinson, J. P.; Vasiliu, M. Regeneration of ammonia borane spent fuel by direct reaction with hydrazine and liquid ammonia. *Science* **2011**, *331*, 1426–1429.

[26] Davis, B. L.; Dixon, D. A.; Garner, E. B.; Gordon, J. C.; Matus, M. H.; Scott, B.; Stephens, F. H. Efficient regeneration of partially spent ammonia borane fuel. *Angewandte Chemie International Edition* **2009**, *121*, 6944–6948.

[27] Hausdorf, S.; Baitalow, F.; Wolf, G.; Mertens, F. O. A procedure for the regeneration of ammonia borane from BNH-waste products. *International Journal of Hydrogen Energy* **2008**, *33*, 608–614.

[28] Yu, C.; Fu, J.; Muzzio, M.; Shen, T.; Su, D.; Zhu, J.; Sun, S. CuNi nanoparticles assembled on graphene for catalytic methanolysis of ammonia borane and hydrogenation of nitro/nitrile compounds. *Chemistry of Materials* **2017**, *29*, 1413–1418.

[29] Zhan, W.-W.; Zhu, Q.-L.; Xu, Q. Dehydrogenation of ammonia borane by metal nanoparticle catalysts. *ACS Catalysis* **2016**, *6*, 6892–6905.

[30] Goksu, H.; Ho, S. F.; Metin, O.; Korkmaz, K.; Mendoza Garcia, A.; Gultekin, M. S.; Sun, S. Tandem dehydrogenation of ammonia borane and hydrogenation of nitro/nitrile compounds catalyzed by graphene-supported nipd alloy nanoparticles. *ACS Catalysis* **2014**, *4*, 1777–1782.

[31] Yu, C.; Guo, X.; Xi, Z.; Muzzio, M.; Yin, Z.; Shen, B.; Li, J.; Seto, C. T.; Sun, S. AgPd nanoparticles deposited on WO2. 72 nanorods as an efficient catalyst for one-pot conversion of nitrophenol/nitroacetophenone into benzoxazole/quinazoline. *Journal of the American Chemical Society* **2017**, *139*, 5712–5715.

[32] Yu, C.; Guo, X.; Shen, M.; Shen, B.; Muzzio, M.; Yin, Z.; Li, Q.; Xi, Z.; Li, J.; Seto, C. T. Maximizing the catalytic activity of nanoparticles through monolayer assembly on nitrogen-doped graphene. *Angewandte Chemie International Edition* **2018**, *57*, 451–455.

[33] Metin, Ö.; Mendoza-Garcia, A.; Dalmızrak, D.; Gültekin, M. S.; Sun, S. FePd alloy nanoparticles assembled on reduced graphene oxide as a catalyst for selective transfer hydrogenation of nitroarenes to anilines using ammonia borane as a hydrogen source. *Catalysis Science & Technology* **2016**, *6*, 6137–6143.

[34] Ho, S. F.; Mendoza-Garcia, A.; Guo, S.; He, K.; Su, D.; Liu, S.; Metin, Ö.; Sun, S. A facile route to monodisperse MPd (M= Co or Cu) alloy nanoparticles and their catalysis for electrooxidation of formic acid. *Nanoscale* **2014**, *6*, 6970–6973.

[35] Yang, H. B.; Miao, J.; Hung, S.-F.; Chen, J.; Tao, H. B.; Wang, X.; Zhang, L.; Chen, R.; Gao, J.; Chen, H. M. Identification of catalytic sites for oxygen reduction and oxygen evolution in N-doped graphene materials: Development of highly efficient metal-free bifunctional electrocatalyst. *Science Advances* **2016**, *2*, e1501122.

[36] Shui, J.; Wang, M.; Du, F.; Dai, L. N-doped carbon nanomaterials are durable catalysts for oxygen reduction reaction in acidic fuel cells. *Science Advances* **2015**, *1*, e1400129.

Chapter 5

AgPd Nanoparticles Coupled to WO$_{2.72}$ Nanorods for the Synthesis of Benzoxazole†

5.1 Abstract

Using nanoparticles (NPs) to catalyze multiple chemical reactions in one-pot and to achieve high-yield syntheses of functional molecules/materials is an important direction in NP chemistry, catalysis and applications. In this chapter, we report a nanocomposite of AgPd NPs anchored on $WO_{2.72}$ nanorods (NRs) (denoted as $AgPd/WO_{2.72}$) as a general catalyst for formic acid dehydrogenation and transfer hydrogenation from Ar-NO_2 to Ar-NH_2 that further reacts with aldehydes to form benzene-fused heterocyclic compounds. The $AgPd/WO_{2.72}$ catalysis is Ag/Pd dependent and $Ag_{48}Pd_{52}$ is the most active composition for the multiple chemical reactions. The high activity of $AgPd/WO_{2.72}$ arises from strong interfacial interaction between AgPd and $WO_{2.72}$, resulting in AgPd lattice expansion and electron polarization from AgPd to $WO_{2.72}$. The syntheses proceed in one-pot reactions among formic acid, 2-nitrophenol (or 2-nitroaniline, or 2-nitrothiophenol) and aldehydes in dioxane/water (2/1 = v/v) at 80-90 °C, leading to one-pot syntheses of benzoxazoles, benzimidazoles and benzothiazoles that are key ring structures present in functional compounds for pharmaceutical, optical and polymer applications.

5.2 Introduction

Benzene-fused heterocycles, are common core structures found in compounds prepared for biomedical, sensor and optical applications.[1–5] Some typical examples of these structures are benzoxazoles where X = O, NH or S (Figure 5.1). Once properly functionalized for polymer formation, the ring structure is also a key component of a class of rigid organic polymers, such as polybenzozaxoles, that are important for ballistic fiber, flame retardant and electronic textile applications.[6–9] Conventional chemistry leading to the synthesis of benzoxazoles often requires long reaction times (up to 24 h), harsh reaction conditions (over 130 °C), reactive additives (H_2O_2), and toxic solvents.[10–14] These conditions can make it challenging to prepare aromatic ring structures with controlled functionalization to tune their chemical and physical properties. Ideally, the syntheses could proceed using a

one-pot reaction with easily available precursors in a green chemistry environment without compromising the synthetic yield and selectivity.
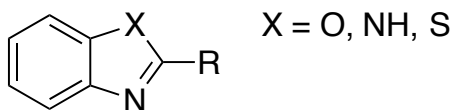

Figure 5.1 The schematic illustration of $Ag_{48}Pd_{52}/WO_{2.72}$-catalyzed one-pot syntheses of benzoxazoles (where X = O, NH, S).

Catalytic dehydrogenation of small molecules to release hydrogen (H_2) is an attractive approach to organic hydrogenation reactions without using pure H_2 as a reactant.[15,16] The common H_2 storage materials explored for H_2 formation or hydrogenation reactions include conventional alcohols and hydrides.[17–19] Recently, ammonia borane (H_3NBH_3) and formic acid (HCOOH) have attracted a lot of attention as H_2 storage materials.[20–30] HCOOH as a H_2 carrier is especially appealing since it is easily available from oxidation of biomass, or hydrogenation of CO_2. Recently, AgPd and AuPd alloy nanoparticles (NPs) were found to be active and stable for HCOOH dehydrogenation into H_2 and CO_2, and to initiate transfer hydrogenation to RNO_2 to give RNH_2.[31–36] Especially when AgPd NPs were coupled to oxygen-deficient $WO_{2.72}$, they catalyzed one-pot reactions among HCOOH, nitrophenol and aldehydes in H_2O/dioxane, providing a clean and safe method for preparing benzoxazoles.[32]

Despite the exciting synthetic potential demonstrated in the $AgPd/WO_{2.72}$ catalyzed one-pot reactions to yield benzoxazoles, there are two questions that remain unanswered: 1) why are these $AgPd/WO_{2.72}$ nanocomposites more active than AgPd NPs (AgPd is still active but with lower efficiency)? 2) can this one-pot strategy be extended to produce other aromatic analogues without significantly changing the reaction conditions? This paper aims to answer these two questions by studying what makes $AgPd/WO_{2.72}$ more active than simpler AgPd NPs, and by demonstrating that the one-pot synthesis can indeed be applied not only to benzoxazoles, but also to other structures where X = NH and S (Figure 5.1). The reactions provide a general approach to C-X bond formation and high yield production of benzene-fused heterocyclic compounds.
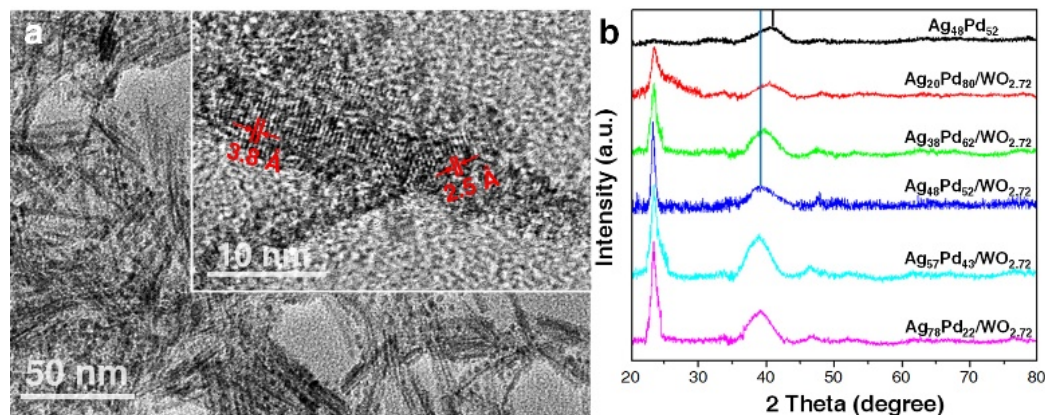
5.3   Results and discussion

Figure 5.2 (a) TEM image of the $Ag_{48}Pd_{52}/WO_{2.72}$ nanocomposite. Inset: HRTEM image of $Ag_{48}Pd_{52}/WO_{2.72}$. (b) XRD pattern of the $Ag_{48}Pd_{52}/WO_{2.72}$ and $Ag_{48}Pd_{52}$ NPs synthesized without $WO_{2.72}$. Inset: XRD patterns of $Ag_{78}Pd_{22}/WO_{2.72}$, $Ag_{57}Pd_{43}/WO_{2.72}$, $Ag_{48}Pd_{52}/WO_{2.72}$, $Ag_{38}Pd_{61}/WO_{2.72}$ and $Ag_{20}Pd_{80}/WO_{2.72}$.

The $AgPd/WO_{2.72}$ catalyst contains AgPd NPs perched on $WO_{2.72}$ nanorods (NRs), as shown in Figure 5.2a. $WO_{2.72}$ NRs were prepared by reacting WCl_4 with oleic acid (OA) and oleylamine (OAm) in 1-octadecene (ODE) at 280 °C,[37] while $AgPd/WO_{2.72}$ was obtained by growing AgPd NPs at 180 °C in the presence of the $WO_{2.72}$ NRs.[38] Under these reaction conditions, the molar ratios of Ag/Pd and the mass ratios of $AgPd/WO_{2.72}$ were controlled by varying the amounts of the Ag- and Pd-precursors and WCl_4, and were determined using inductively coupled plasma-atomic emission spectroscopy (ICP-AES). We prepared $Ag_{78}Pd_{22}/WO_{2.72}$, $Ag_{57}Pd_{43}/WO_{2.72}$, $Ag_{48}Pd_{52}/WO_{2.72}$, $Ag_{38}Pd_{61}/WO_{2.72}$ and $Ag_{20}Pd_{80}/WO_{2.72}$, with a fixed ratio of AgPd to $WO_{2.72}$ of 3:5 mol/mol. Representative TEM images of $Ag_{48}Pd_{52}/WO_{2.72}$ (Figure 5.2a) show that the NPs have an average diameter of 2.3 ± 0.1 nm and perch on 40×5 nm $WO_{2.72}$ NRs. High-resolution TEM (HRTEM) images of the composite (Inset in Figure 5.2a) show that the $WO_{2.72}$ NRs have a good crystalline structure with an interfringe distance of 3.8 Å, which corresponds to the (010) interplanar spacing of monoclinic $WO_{2.72}$ (3.78 Å, JCPDS NO. 65-1291). The $Ag_{48}Pd_{52}$ NPs attached to the $WO_{2.72}$ NRs have an interfringe distance of 2.5 Å, which is larger

than the (111) interplanar spacing of 2.3 Å observed for independent $Ag_{48}Pd_{52}$ NPs. X-ray diffraction (XRD) of the $Ag_{48}Pd_{52}$ NPs exhibit a wide (111) peak around 40° (Figure 5.2b). Once attached to $WO_{2.72}$, the (111) peak shifts to a smaller angle, indicating that AgPd NPs coupled to $WO_{2.72}$ have their lattice expanded. The (111) peaks of $AgPd/WO_{2.72}$ show Ag/Pd-composition-dependent shifts (Figure 5.2b) and the corresponding lattice parameters lie along the theoretical line based on Vegard's law, confirming the formation of an alloy structure of AgPd, not a core/shell structure. As a comparison, $WO_{2.72}$ does not show obvious pattern changes. X-ray photoelectron spectroscopy (XPS) was further used to characterize the AgPd NPs, $WO_{2.72}$ NRs and the $AgPd/WO_{2.72}$ composite structure (Figure 5.3a-b). Once attached to $WO_{2.72}$, the Ag 3d and Pd 3d binding energies of the AgPd NPs increase slightly. The Ag 3d peaks shift less (from 368.1/374.1 eV to 368.2/374.2 eV) than the Pd 3d ones (from 336.4/341.8 eV to 336.8/342.1 eV). In contrast, the binding energy of W 4f in the composite structure is down-shifted (Figure 5.3c). These observations indicate that the electron density of AgPd is decreased in the composite structure, and that Pd is affected more than Ag by the $AgPd-WO_{2.72}$ interactions.[39–43]

The interaction between AgPd and $WO_{2.72}$ induces charge polarization from AgPd to $WO_{2.72}$, which should increase the Lewis acidity of the AgPd NP, and the Lewis basicity of $WO_{2.72}$, facilitating AgPd binding of electrons and $WO_{2.72}$ absorption of protons. We first studied the CO binding properties of the AgPd surface via the CO stripping test (Figure 5.3d). From Pd to AgPd, the CO stripping peak is negatively shifted and broadened, indicating that CO is oxidized more easily on the AgPd surface than on the Pd surface. Once coupled with $WO_{2.72}$, the CO stripping peak is much weaker and more negatively shifted, demonstrating the improved CO-tolerance on the AgPd surface. We then evaluated the catalytic properties of $AgPd/WO_{2.72}$ for formic acid (FA) dehydrogenation. We found that the conditions, previously optimized in aqueous solution (10 mL of 900 mM FA, 323 K), were still suitable for the current catalyst system. Gas chromatography (GC) analyses show that the gas mixture consists of only CO_2 and H_2, and no CO is present. Using a NaOH trap to remove CO_2 from the gas mixture, we obtained the H_2 volume. Our studies show
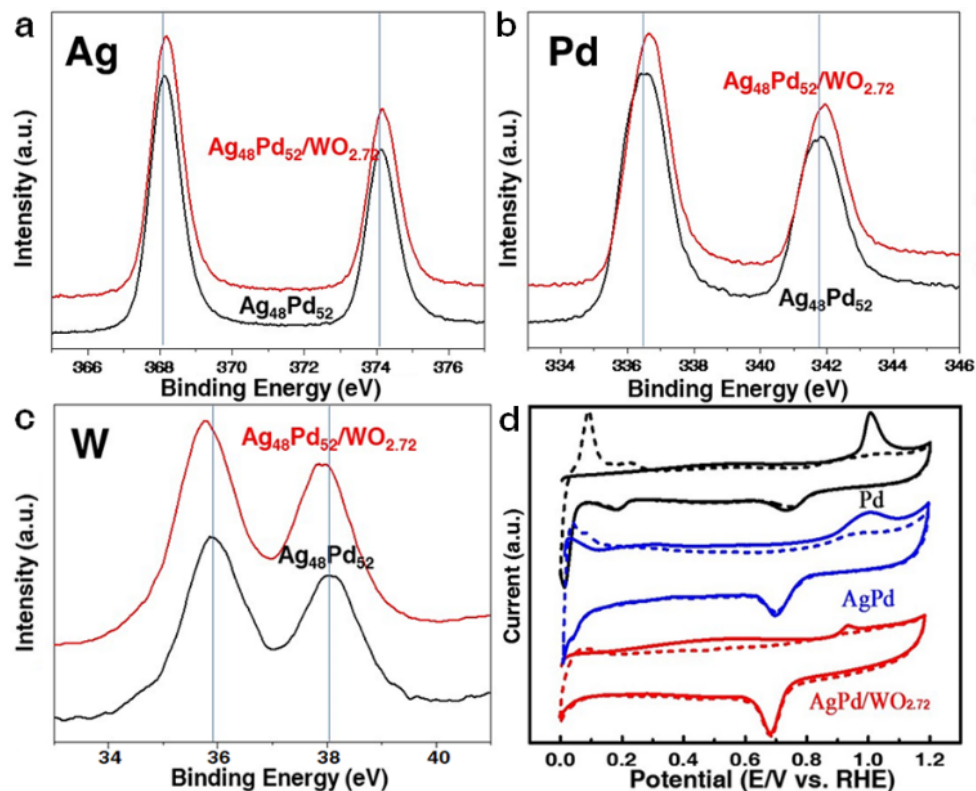
Figure 5.3 (a-c) XPS spectra of $Ag_{48}Pd_{52}/WO_{2.72}$ and $Ag_{48}Pd_{52}$ (Ag 3d, Pd 3d and W 4f). (d) CO stripping voltammetry of the $Ag_{48}Pd_{52}/WO_{2.72}$ composites, $Ag_{48}Pd_{52}$ and commercial Pd obtained in 0.1 M $HClO_4$ with a scan rate of 20 mV/s. The solid line is from the first scanning cycle and the dashed line is from the second scanning cycle.

that $AgPd/WO_{2.72}$ catalyzes FA decomposition in a CO-free pathway, and that the strong $AgPd-WO_{2.72}$ interaction makes AgPd more electrophilic, favoring the activation of FA to generate HCOO* via O-H bond cleavage or *COOH via C-H bond cleavage.[40–49] CO_2 and H_2 are formed via the AgPd-promoted decomposition of HCOO* and *COOH, which essentially blocks the CO-forming pathway.

$Ag_{48}Pd_{52}$-catalyzed dehydrogenation of FA was evaluated at 323 K with [AgPd] = 3.1 mM. Figure 5.4a shows that 3/5 molar ratio is necessary to reach optimum catalytic activity. Adding more $Ag_{48}Pd_{52}$ and $WO_{2.72}$ does not lead to the continued increase of TOF, rather it decreases its value due to apparent over-loading of the catalyst. At [FA] = 900 mM and $[AgPd]/WO_{2.72}$ = 3/5 mol/mol, it shows the best activity with a TOF value reaching 1718 h^{-1}. This TOF is among the highest ever reported for Pd-based catalysts.[50–56] We

also tested the effects of different inorganic supports, such as conventional carbon (C), silica (SiO2), graphene (G), or commercial WO_3 and $WO_{2.9}$ on the $Ag_{48}Pd_{52}$ catalysis at the 3/5 [AgPd]/[support] ratios (Figure 5.4b). These composites are all less active than $Ag_{48}Pd_{52}/WO_{2.72}$, suggesting that AgPd coupling to $WO_{2.72}$ favors the dehydrogenation of FA.
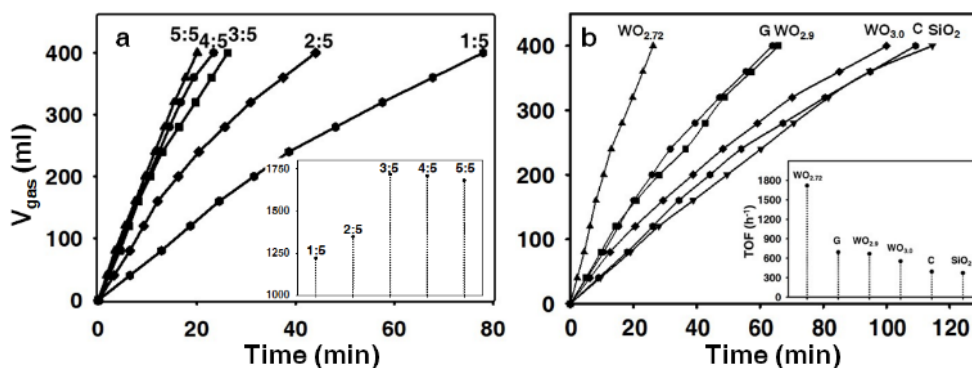
Figure 5.4 (a) Plot of time vs volume of gas generated from FA dehydrogenation catalyzed by nanocomposites with different $Ag_{48}Pd_{52}/WO_{2.72}$ molar ratio ([AgPd] = 3.1 mM, [FA] = 900 mM, T = 323 K). Inset: The dehydrogenation TOF values of nanocomposites with different $Ag_{48}Pd_{52}/WO_{2.72}$ molar ratios. (b) Plot of time vs. volume of gas generated from FA dehydrogenation catalyzed by $Ag_{48}Pd_{52}$ on different supports ([AgPd] = 3.1 mM, [FA] = 900 mM, T = 323 K). Inset: TOF values of $Ag_{48}Pd_{52}$ on different supports.

$Ag_{48}Pd_{52}/WO_{2.72}$ could further catalyze transfer hydrogenation from HCOOH to $R-NO_2$ to give $R-NH_2$ at 50 °C. Using nitrobenzene as a model substrate, we optimized the reaction conditions: 1 mmol nitrobenzene, 3.0 mmol FA, 3 mol% $Ag_{48}Pd_{52}/WO_{2.72}$ in 9 mL H_2O/dioxane (1:2 = v/v). Under these conditions the dehydrogenation of FA and hydrogenation of nitrobenzene were complete within 30 mins, and aniline was isolated in a 98% yield. Using similar reaction conditions, a variety of substituted nitrobenzene derivatives could be reduced to the corresponding anilines in yields above 90% within 2 hours.

We further extended this reaction to a one-pot synthesis of benzoxazoles starting from 2-nitrophenol and an aldehyde (Table 5.1). Various benzoxazoles (entries 1-8) were obtained in >90% yield at 80 °C within 8 h. The electronic properties of substituents at either the para- or meta-positions of the benzaldehyde had little influence on the reaction outcome. However, substituents at the ortho position decreased the yield somewhat (entries 9-10),

likely due to steric hinderance. The good yield (91%) of the thiophene derivative (entry 11) shows that the reaction is tolerant to substrates containing a sulfur atom. However, replacing the aromatic aldehyde with an aliphatic aldehyde does lower the yield (entry 12).

Table 5.1 $Ag_{48}Pd_{52}/WO_{2.72}$-catalyzed one-pot condensation of 2-nitrophenol with various aldehydes[a]
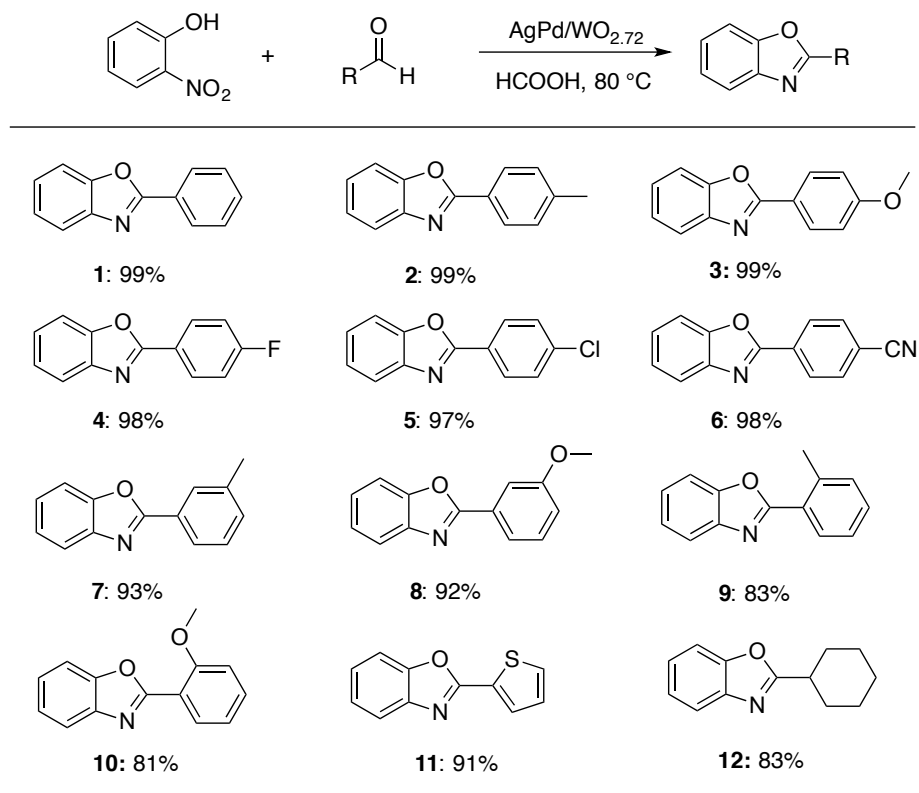
[a] Reaction conditions: 2-nitrophenol (1 mmol), aldehyde (1.2 mmol), $Ag_{48}Pd_{52}/WO_{2.72}$ (3 mol%), dioxane (6 mL), water (3 mL) and FA (4 mmol), 8 h.

To determine if other steps in this multi-step reaction, in addition to FA dehydrogenation and reduction of the nitro group, were dependent on the structure and composition of the catalyst, we examined the synthesis of 2-phenylbenzoxazole starting from 2-aminophenol and benzaldehyde. The reaction was performed using the same conditions as shown in Table 5.1, and we used GC-MS to monitor the concentrations of the 2-aminophenol starting material, the imine intermediate, and the benzoxazole product. The most efficient catalyst for synthesis of 2-phenylbenzoxazole starting from 2-aminophenol is $Ag_{48}Pd_{52}/WO_{2.72}$

(Figure 5.5a). 2-Aminophenol was almost completely consumed after 3 h, and the reaction was essentially complete after 7 h. Figure 5.5b shows the accumulation and subsequent consumption of the imine intermediate (black circles) formed by dehydration of the amino group of 2-aminophenol with benzaldehyde. This intermediate quickly accumulates during the first two hours of the reaction, before it is transformed more slowly to the product. Other AgPd-catalysts were not as efficient as $Ag_{48}Pd_{52}/WO_{2.72}$ for both the condensation of 2-aminophenol and benzaldehyde to give the imine intermediate, and also the cyclization and dehydrogenation of the intermediate to give the final benzoxazole product. Among the catalysts studied, Ag is the least active catalyst for both of these processes. Taken together, these synthetic data indicate that; 1) FA dehydrogenation, transfer hydrogenation from $Ar-NO_2$ to $Ar-NH_2$, and $Ar-NH_2$ reaction with aldehydes to form benzoxazoles are all dependent on the AgPd composition and identity of the solid support of the catalyst, 2) $Ag_{48}Pd_{52}/WO_{2.72}$ is the most effective catalyst for all of these reaction steps, and 3) the reactions are not significantly affected by the electronic character of substituents on the aldehyde, but are influenced by the steric characteristics of the aldehyde. The $Ag_{48}Pd_{52}/WO_{2.72}$ catalyst was not only active, but also stable under the one-pot reaction conditions. For example, in the formation of 2-phenylbenzoxazole, after the reaction was complete the catalyst was precipitated by adding ethyl acetate, isolated and purified by washing with water/methanol, and re-used. After 5 rounds of catalyst reuse, the catalyst showed little drop in activity, and the yield of the final product remained above 95% for all five reactions. In addition, the catalyst showed no obvious changes in morphology.

The $AgPd/WO_{2.72}$ catalyzed one-pot reaction was not limited to the formation of benzoxazoles, but could also be extended to the synthesis of other benzene-fused heterocycles (Figure 5.6a). By replacing 2-nitrophenol with 2-nitroaniline, N-methyl-2-nitroaniline or 2-nitrothiophenol, we obtained the corresponding benzimidazoles or benzothiazole in >83% yield using the same one-pot reaction conditions (compounds 13-15). By raising the reaction temperature from 80 to 90 °C, the yields were further improved to >94% (compounds 13-15 in parentheses). It is notable that the yield of 2-phenylbenzothiazole remains high
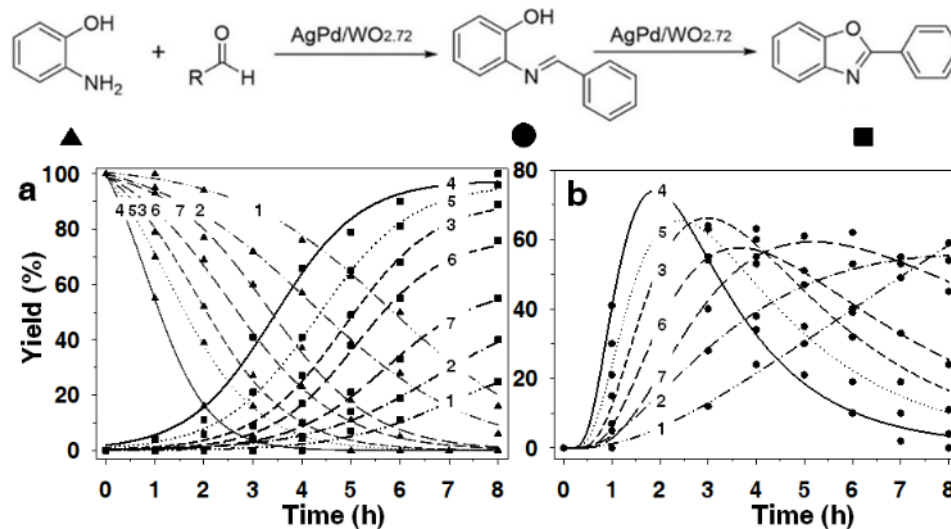
Figure 5.5 $Ag_xPd_y/WO_{2.72}$-catalyzed condensation of 2-aminophenol and benzaldehyde. (a) Time-dependent formation of 2-phenylbenzoxazole (rectangles) starting from 2-aminophenol (triangles). (b) Time-dependent formation and consumption of the imine intermediate (circles). Note: (1) Ag, (2) $Ag_{78}Pd_{22}$, (3) $Ag_{57}Pd_{43}$, (4) $Ag_{48}Pd_{52}$, (5) $Ag_{39}Pd_{61}$, (6) $Ag_{20}Pd_{80}$ and (7) Pd.

at 94%. The $AgPd/WO_{2.72}$ catalyst is not negatively affected by the thiol group in the 2-nitrothiophenol starting material. This outcome is different than what has been reported previously for other Pd-based nanocatalysts, which are typically poisoned by thiols.[57–60] This observation suggests that the presence of the $WO_{2.72}$ helps to protect the AgPd catalyst from poisoning.

The one-pot reaction could be further extended to prepare phenylene-bis-benzoxazole (compound 16) and 2,6-diphenyl-benzobis(oxazole) (compound 17) from 2-nitrophenol/ terephthalaldehyde and 4,6-dinitroresorcinol/benzaldehyde under the same 80 °C reaction conditions with >90% yields, making the reaction very promising for fabricating linear - conjugated polymers (Figure 5.6b). By elevating the temperature to 100 °C, the reaction was also suitable for condensation of two equivalents of 2-nitrophenol with thiophene-2,5-dicarbaldehyde to give 2,5-bis(benzoxazol-2-yl)thiophene (compounds 18), the known commercial fluorescent brightener 185. This brightener is normally prepared from the reaction
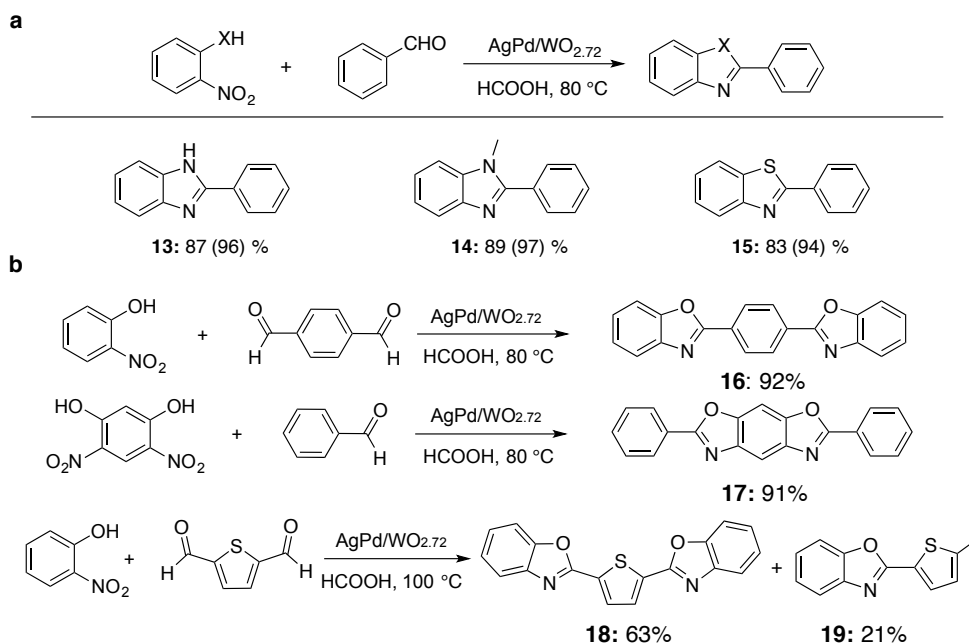
Figure 5.6 (a) $Ag_{48}Pd_{52}/WO_{2.72}$-catalyzed synthesis of 2-phenylbenzimidazole, 1-methyl-2-phenylbenzimidazole and 2-phenylbenzothiazole. Reaction conditions: substrate (1 mmol), benzaldehyde (1.2 mmol), $Ag_{48}Pd_{52}/WO_{2.72}$ (3 mol%), dioxane (6 mL), water (3 mL) and FA (4 mmol), 8 h. The yields in parentheses were obtained at 90 °C. (b) $Ag_{48}Pd_{52}/WO_{2.72}$-catalyzed synthesis of phenylene-bis-benzoxazole, 2,6-diphenyl-benzobis(oxazole) and 2,5-bis(benzoxazol-2-yl)thiophene.

between 2-aminophenol and thiophene-2,5-dicarboxylic acid in toluene and N-methyl-2-pyrrolidone at 185 °C with boric acid as an additive. Compared with this conventional approach, our one-pot reaction is milder and produces the brightener in a modestly good yield. This 63% yield is somewhat lower than what we have observed for the other reactions reported herein. This reduced yield is not due to poisoning of the catalyst by the sulfur atom of thiophene. Rather, it is caused by reduction of one of the aldehyde groups in thiophene-2,5-dicarbaldehyde to the corresponding methyl group (compound 19).

5.4   Conclusion

In this chapter, we extensively studied the $AgPd/WO_{2.72}$ catalyst and its general use for the one-pot syntheses of benzene-fused heterocyclic compounds. Our studies first examined

the $WO_{2.72}$ NR-mediated growth of AgPd NPs resulting in the formation of $AgPd/WO_{2.72}$ composites. The interfacial interaction between AgPd and $WO_{2.72}$ leads to the desired alloy NP lattice expansion and charge polarization from AgPd to $WO_{2.72}$. This interaction enhances the $AgPd/WO_{2.72}$ catalysis of FA dehydrogenation at a temperature of 50 °C, with TOF = 1718 h^{-1}, Ea = 31 kJ/mol. The dehydrogenation reaction is Ag/Pd dependent, and $Ag_{48}Pd_{52}/WO_{2.72}$ is found to be the most active catalyst to produce H_2 and CO_2 via a pathway that does not produce CO. The power of the $AgPd/WO_{2.72}$ catalyst is further demonstrated by the transfer hydrogenation from FA to $Ar\text{-}NO_2$ to give $Ar\text{-}NH_2$ at 50 °C, and to the reaction of $Ar\text{-}NH_2$ with an aldehyde at 80-90 °C to yield benzoxazoles. In the one-pot synthesis of benzoxazoles, the catalysis is not affected by the electronic character of substituents on the aldehyde, but is sensitive to steric hinderance on the aldehyde. In addition, the one-pot reaction can be extended to prepare various benzoazoles with the 5-member ring containing C-O, C-NH, or C-S bonds. The $AgPd/WO_{2.72}$-catalyzed one-pot reaction offers a general approach to benzene-fused heterocyclic compounds for pharmaceutical and functional polymer applications.

5.5 Experimental section

Synthesis of $WO_{2.72}$ NRs   81 mg WCl_4 (0.25 mmol), 5 mL ODE, 3 mL OAm were first mixed in a 20 mL vial through sonication to form a dark brown solution, and transferred into a 100 mL four-neck round bottom flask. 10 mL ODE and 6 mL OAc were then added into the flask. The mixture solution was first heated to 120 °C in a gentle Ar flow and magnetic stirring for 30 min to remove air and moisture from the reaction system. The clear dark green solution was heated to 280 °C in 30 min (when the reaction temperature reached 200 °C, the Ar gas was switched to form an Ar blanket over the reaction system and the solution started to turn to blue). The reaction solution was kept at 280 °C for 10 h before it was cooled to room temperature. The product was separated from the solution by adding 80 mL ethanol and centrifuging at 9500 rpm for 8 min. Then 20 mL hexane was

added to re-disperse the synthesized NRs and centrifugation (6000 rpm, 4 min) was applied to precipitate any undispersed. The product in the dispersion was then precipitated by adding 35 mL ethanol followed by centrifugation. The NRs were purified again with 15 mL hexane and 35 mL ethanol, and after separation by centrifugation, was dispersed in hexane for further use.

Synthesis of AgPd/WO$_{2.72}$ nanocomposites   Under a gentle nitrogen flow, 0.084 g of AgOAc (0.5 mmol), 0.15 g of Pd(acac)$_2$ (0.5 mmol) and 0.34 g of WO$_{2.72}$ NRs (1.5 mmol) were magnetically stirred in 4.5 mL of OAc, 0.5 mL of OAm, and 10 mL of ODE. The mixture was heated to 80 °C to generate a homogeneous solution and kept at this temperature for 1 h. Then the solution was heated to 180 °C at a rate of 5-7 °C/min. The reaction was allowed to proceed for 20 min and cooled to room temperature. 100 mL of isopropanol was added, and the product was separated by centrifugation at 9500 rpm for 15 min to remove the organic impurities and precursor residues. The product was redispersed in 10 mL of hexane and then recollected by adding 40 mL of ethanol and centrifugation (9500 rpm, 8 minutes). The products were washed twice with hexane/ethanol (v/v = 1:15) and then suspended in 30 mL of acetic acid and the suspension was stirring at 60 °C for 10 h. 30 mL of ethanol was added and the mixture was centrifuged at 9500 rpm for 8 minutes. This ethanol washing procedure was repeated three times, yielding Ag$_{48}$Pd$_{52}$/WO$_{2.72}$, which were dispersed in hexane for future use. The composition of AgPd/WO$_{2.72}$ was controlled by the molar ratio of metal precursors. For instance, with the total amount of Ag/Pd-precursors fixed at 1.0 mmol, Ag$_{78}$Pd$_{22}$/WO$_{2.72}$, Ag$_{57}$Pd$_{43}$/WO$_{2.72}$, Ag$_{48}$Pd$_{52}$/WO$_{2.72}$, Ag$_{38}$Pd$_{62}$/WO$_{2.72}$ and Ag$_{20}$Pd$_{80}$/WO$_{2.72}$ were formed from the Ag/Pd-precursors at the Ag/Pd ratios of 3:1, 2:1, 1:1, 1:2 and 1:3 respectively.

Decomposition of FA   A two-necked reaction flask (25 mL) containing a Teflon-coated stir bar was placed on a magnetic stirrer and thermostated to 50.0 ± 1 °C by using a constant temperature bath. A gas burette filled with water was connected to one neck of the flask (the other neck was sealed) to measure the volume of gas mixture evolved from the

reaction. 9.64 mL of aqueous suspension of the catalyst was transferred into the reaction flask, and 0.36 mL (9 mmol) of FA was added into the stirred (800 rpm) solution. The volume of gas mixture evolved was measured by recording the volume of water displaced. The reaction was considered to cease when gas generation was no longer observed.

NaOH trap experiments To quantify the molar ratio of CO_2 to H_2 in the gas mixture generated during the $AgPd/WO_{2.72}$ catalyzed dehydrogenation of aqueous FA solution (10 mL of 900 mM), the gas burette system was modified by placing a NaOH trap (10 M NaOH solution) between the jacketed reactor and gas burette. The gas generated during the reaction was passed through the NaOH trap and CO_2 was captured, leaving only H_2. The gas volume change observed before and after the NaOH trap experiment was used to quantify CO_2 and H_2.

General procedure for the catalytic tandem reactions for producing primary amines $Ar\text{-}NO_2$ (1 mmol), $Ag_{48}Pd_{52}/WO_{2.72}$ (3 mmol%), dioxane (6 mL) and water (3 mL) were stirred for 5 min in a 25 mL flask at 50 °C. Next, FA (4 mmol) was added to the reaction mixture, and the flask was sealed by a balloon. The solution was stirred at 800 rpm at 50 °C for different reaction times. The progress of the reaction and the yield of the amine compounds were determined by GC-MS with benzyl ether as the internal standard.

General procedure for catalytic one-pot synthesis of benzoazoles 2-Nitrobenzene substrate (1 mmol), aldehyde (1.2 mmol), $Ag_{48}Pd_{52}/WO_{2.72}$ (3 mol%), dioxane (6 mL) and water (3 mL) were stirred for 5 min in a 25 mL flask at 80 °C. Next, FA (4 mmol) was added to the reaction mixture, and the flask was sealed by a balloon. The solution was stirred at 800 rpm at 80 °C for 8 h. After completion of the reaction, a small amount of ethyl acetate was added and the catalyst was removed by centrifugation at 9500 rpm and washed three times with water or methanol. Then, the catalyst was allowed to dry for further use. The solvent was removed under vacuum and the residue was purified by flash column chromatography (hexane/ethyl acetate = 8:1) to give the product.

Catalyst stability test for multi-step tandem reactions   After each model reaction, the catalyst was separated, washed with water/methanol and weighed. Then the same reagents were added to the reaction system according to the feeding ratio. The process was repeated for the next round of reaction.

5.5.1   Characterization data of products

2-phenyl-benzoxazole (1)   ^{1}H-NMR (400 MHz, CDCl$_3$) δ [ppm] = 8.30-8.28 (m, 2H), 7.82-7.80 (m, 1H), 7.63-7.56 (m, 4H), 7.40-7.38 (m, 2H). ^{13}C-NMR (100 MHz, CDCl$_3$) δ [ppm] = 163.3, 150.6, 142.7, 132.0, 129.6, 128.4, 128.2, 126.3, 125.0, 121.3, 110.9. HRMS [M+H]$^+$ calculated for C$_{13}$H$_{10}$NO: 196.0764 found 196.0758.

2-(p-tolyl)-benzoxazole (2)   ^{1}H-NMR (400 MHz, CDCl$_3$) δ [ppm] = 8.15-8.12 (m, 2H), 7.82-7.79 (m, 1H), 7.68 -7.62 (m, 1H), 7.44-7.38 (m, 4H), 2.45 (s, 3H). ^{13}C-NMR (100 MHz, CDCl$_3$) δ [ppm] = 163.5, 151.6, 144.5, 144.3, 130.9, 128.3, 126.4, 125.7, 125.4, 121.3, 111.1, 21.9. HRMS [M+H]$^+$ calculated for C$_{14}$H$_{12}$NO: 210.0921 found 210.0914.

2-(4-methoxyphenyl)-benzoxazole (3)   ^{1}H-NMR (400 MHz, CDCl$_3$) δ [ppm] = 8.22-8.19 (m, 2H), 7.88-7.86 (m, 1H), 7.58-7.54 (m, 1H), 7.38-7.34 (m, 2H), 7.07-7.05 (m, 2H), 3.92 (s, 3H). ^{13}C-NMR (100 MHz, CDCl$_3$) δ [ppm] = 163.4, 162.4, 151.0, 142.5, 129.9, 124.7, 124.4, 119.8, 119.4, 115.0, 110.5, 55.47. HRMS [M+H]$^+$ calculated for C$_{14}$H$_{12}$NO$_2$: 226.0870 found 226.0861.

2-(4-fluorophenyl)-benzoxazole (4)   ^{1}H-NMR (400 MHz, CDCl$_3$) δ [ppm] = 8.29-8.24 (m, 2H), 7.79-7.75 (m, 1H), 7.60-7.55 (m, 1H), 7.38-7.34 (m, 2H), 7.24-7.19 (m, 2H). ^{13}C-NMR (100 MHz, CDCl$_3$) δ [ppm] = 166.7, 163.8, 162.4, 150.9, 142.3, 130.0, 125.4, 123.7, 120.1, 116.6, 110.6. HRMS [M+H]$^+$ calculated for C$_{13}$H$_9$NOF: 214.0670 found 214.0663.

2-(4-chlorophenyl)benzo[d]oxazole (5)   ^{1}H-NMR (400 MHz, CDCl$_3$) δ [ppm] = 8.23-8.21 (m, 2H), 7.81-7.79 (m, 1H), 7.62-7.59 (m, 1H), 7.55-7.51 (m, 2H), 7.41-7.37 (m, 2H).

^{13}C-NMR (100 MHz, CDCl$_3$) δ [ppm] = 162.3, 150.3, 142.3, 138.0, 129.4, 129.0, 125.8, 125.5, 124.9, 120.3, 110.9. HRMS [M+H]$^+$ calculated for C$_{13}$H$_9$NOCl: 230.0374 found 230.0381.

4-(benzo[d]oxazol-2-yl)benzonitrile (6) ^{1}H-NMR (400 MHz, CDCl$_3$) δ [ppm] = 8.41-8.38 (m, 2H), 7.87-7.83 (m, 3H), 7.66-7.64 (m, 1H), 7.46-7.43 (m, 2H). ^{13}C-NMR (100 MHz, CDCl$_3$) δ [ppm] = 161.0, 150.9, 141.9, 132.7, 131.2, 128.0, 126.2, 125.2, 120.6, 118.2, 114.8, 110.9. HRMS [M+H]$^+$ calculated for C$_{14}$H$_9$N$_2$O: 221.0717 found 221.0706.

2-(m-tolyl)-benzoxazole (7) ^{1}H-NMR (400 MHz, CDCl$_3$) δ [ppm] = 8.13-8.07 (m, 2H), 7.81-7.79 (m, 1H), 7.62 -7.60 (m, 1H), 7.46-7.40 (m, 1H), 7.39-7.37 (m, 3H), 2.49 (s, 3H). ^{13}C-NMR (100 MHz, CDCl$_3$) δ [ppm] = 163.6, 151.0, 142.3, 139.0, 132.6, 129.0, 128.4, 127.2, 125.2, 125.0, 124.7, 120.1, 110.7, 22.5. HRMS [M+H]$^+$ calculated for C$_{14}$H$_{12}$NO: 210.0921 found 210.0925.

2-(3-methoxyphenyl)-benzoxazole (8) ^{1}H-NMR (400 MHz, CDCl$_3$) δ [ppm] = 7.82-7.80 (m, 1H), 7.62-7.60 (m, 2H), 7.48-7.44 (m, 1H), 7.40-7.37 (m, 1H), 7.13-7.12 (m, 2H), 7.11-7.10 (m, 1H), 3.95 (s, 3H). ^{13}C-NMR (100 MHz, CDCl$_3$) δ [ppm] = 163.2, 160.2, 151.0, 142.3, 130.2, 128.6, 125.4, 124.7, 120.3, 120.2, 118.5, 112.2, 110.8, 55.4. HRMS [M+H]$^+$ calculated for C$_{14}$H$_{12}$NO$_2$: 226.0870 found 226.0863.

2-(o-tolyl)-benzoxazole (9) ^{1}H-NMR (400 MHz, CDCl$_3$) δ [ppm] = 8.22-8.20 (m, 1H), 7.86-7.83 (m, 1H), 7.64 -7.61 (m, 1H), 7.47-7.36 (m, 5H), 2.85 (s, 3H). ^{13}C-NMR (100 MHz, CDCl$_3$) δ [ppm] = 163.7, 150.5, 142.2, 139.0, 132.1, 131.1, 130.2, 126.3, 126.2, 125.2, 124.6, 120.3, 110.7, 22.5. HRMS [M+H]$^+$ calculated for C$_{14}$H$_{12}$NO: 210.0921 found 210.0928.

2-(2-methoxyphenyl)-benzoxazole (10) ^{1}H-NMR (400 MHz, CDCl$_3$) δ [ppm] = 8.18-8.15 (m, 1H), 7.86-7.84 (m, 1H), 7.63-7.60 (m, 1H), 7.55-7.51 (m, 1H), 7.38-7.29 (m, 2H), 7.15-7.10 (m, 2H), 4.05 (s, 3H). ^{13}C-NMR (100 MHz, CDCl$_3$) δ [ppm] = 161.9, 158.7, 150.4, 142.4, 133.1, 131.5, 125.1, 124.4, 120.8, 120.3, 116.4, 112.3, 110.6, 55.4. HRMS [M+H]$^+$ calculated for C$_{14}$H$_{12}$NO$_2$: 226.0870 found 226.0872.

2-(thiophen-2-yl)benzo[d]oxazole (11) ^{1}H-NMR (400 MHz, CDCl$_3$) δ [ppm] = 7.96-7.93 (m, 1H), 7.82-7.80 (m, 1H), 7.62-7.60 (m, 2H) 7.39-7.37 (m, 2H), 7.23-7.20 (m, 1H). ^{13}C-NMR (100 MHz, CDCl$_3$) δ [ppm] = 159.3, 150.7, 143.1, 132.1, 130.1, 129.8, 128.3, 125.4, 124.8, 120.3, 110.6. HRMS [M+H]$^+$ calculated for C$_{11}$H$_8$NOS: 202.0328 found 202.0334.

2-cyclohexyl-benzoxazole (12) ^{1}H-NMR (400 MHz, CDCl$_3$) δ [ppm] = 7.71-7.69 (m, 1H), 7.50-7.47 (m, 1H), 7.31-7.29 (m, 2H), 3.04-2.94 (m, 1H), 2.10-2.07 (m, 2H), 1.92-1.88 (m, 2H), 1.80-1.77 (m, 3H), 1.51-1.36 (m, 3H). ^{13}C-NMR (100 MHz, CDCl$_3$) δ [ppm] = 170.2, 150.5, 140.7, 124.5, 124.3, 119.8, 110.7, 38.9, 31.0, 25.4, 25.1. HRMS [M+H]$^+$ calculated for C$_{13}$H$_{16}$NO: 202.1234 found 202.1225.

2-phenyl-1H-benzo[d]imidazole (13) ^{1}H-NMR (400 MHz, d^{6-}DMSO) δ [ppm] = 12.89 (s, 1H), 8.19-8.17 (m, 2H), 7.68-7.66 (m, 1H), 7.57-7.47 (m, 4H), 7.24-7.17 (m, 2H). ^{13}C-NMR (100 MHz, d^{6-}DMSO) δ [ppm] = 151.2, 143.8, 135.0, 130.1, 129.8, 128.9, 126.4, 122.5, 121.6, 118.8, 111.3. HRMS [M+H]$^+$ calculated for C$_{13}$H$_{11}$N$_2$: 195.0924 found 195.0929.

1-methyl-2-phenyl-1H-benzo[d]imidazole (14) ^{1}H-NMR (400 MHz, CDCl$_3$) δ [ppm] = 7.86-7.85 (m, 1H), 7.81-7.79 (m, 2H), 7.56-7.54 (m, 3H), 7.44-7.42 (m, 1H), 7.36-7.34 (m, 2H), 3.90 (s, 3H) ^{13}C-NMR (100 MHz, CDCl$_3$) δ [ppm] = 153.9, 143.2, 136.8, 130.4, 129.9, 129.6, 128.9, 122.9, 122.6, 120.1, 109.8, 31.9. HRMS [M+H]$^+$ calculated for C$_{14}$H$_{13}$N$_2$: 209.1080 found 209.1074.

2-phenylbenzo[d]thiazole (15) ^{1}H-NMR (400 MHz, CDCl$_3$) δ [ppm] = 8.20-8.18 (m, 3H), 7.92-7.90 (m, 1H), 7.53-7.45 (m, 4H), 7.40-7.38 (m, 1H) ^{13}C-NMR (100 MHz, CDCl$_3$) δ [ppm] = 168.2, 154.2, 135.3, 133.6, 131.0, 129.1, 127.7, 126.3, 125.3, 123.3, 121.7. HRMS [M+H]$^+$ calculated for C$_{13}$H$_{10}$NS: 212.0536 found 212.0529.

1,4-bis(benzo[d]oxazol-2-yl)benzene (16) ^{1}H-NMR (400 MHz, CDCl$_3$) δ [ppm] = 8.25 (s, 4H), 7.77-7.73 (m, 4H), 7.41-7.38 (m, 4H). ^{13}C-NMR (100 MHz, CDCl$_3$) δ [ppm]

= 162.8, 151.2, 141.6, 131.0, 128.3, 125.1, 123.6, 119.1, 109.7. GC-MS calculated for $C_{20}H_{12}N_2O_2$: 312.09 found 312.1.

2,6-diphenylbenzo[1,2-d:5,4-d']bis(oxazole) (17) ^{1}H-NMR (400 MHz, CDCl$_3$) δ [ppm] = 8.18-8.17 (m, 4H), 7.66-7.63 (m, 6H), 7.35 (s, 2H). ^{13}C-NMR (100 MHz, CDCl$_3$) δ [ppm] = 163.1, 138.1, 133.8, 130.8, 129.4, 128.7, 127.5, 120.6, 110.8. GC-MS calculated for $C_{20}H_{12}N_2O_2$: 312.09 found 312.1.

2,5-bis(benzo[d]oxazol-2-yl)thiophene (18) ^{1}H-NMR (400 MHz, CDCl$_3$) δ [ppm] = 7.98 (s, 2H), 7.82-7.77 (m, 4H), 7.44-7.42 (m, 4H). ^{13}C-NMR (100 MHz, CDCl$_3$) δ [ppm] = 152.7, 150.0, 141.6, 131.9, 128.3, 124.3, 123.5, 119.7, 110.8. GC-MS calculated for $C_{18}H_{10}N_2O_2S$: 318.05 found 318.1.

5.6   Characterization of compounds

Spectra of 2-phenyl-benzoxazole (1)
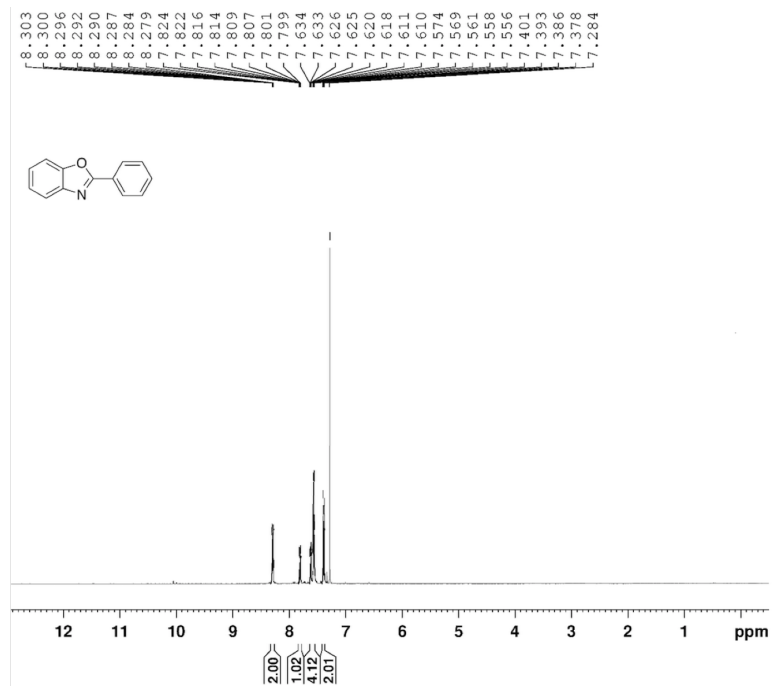
^{1}H-NMR

^{13}C-NMR
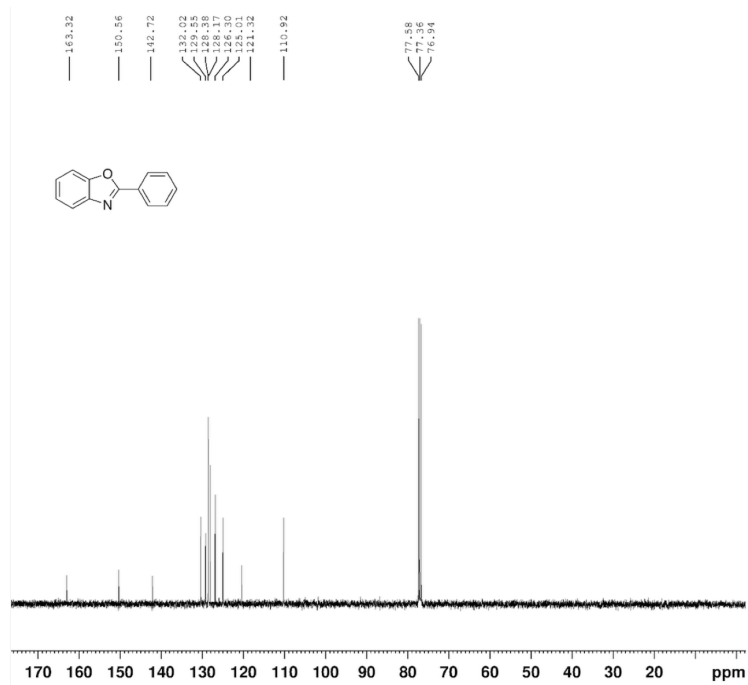
Spectra of 2-(p-tolyl)-benzoxazole (2)
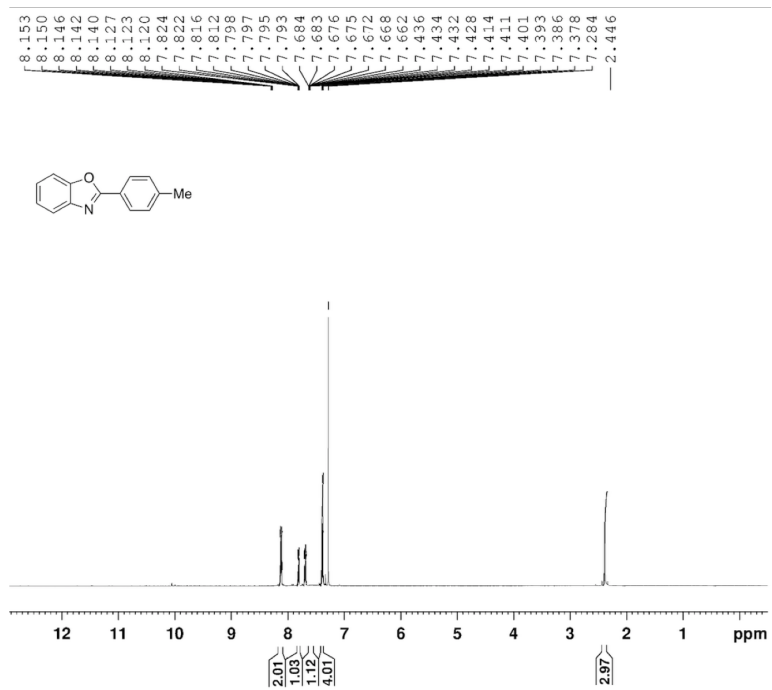
^{1}H-NMR

^{13}C-NMR
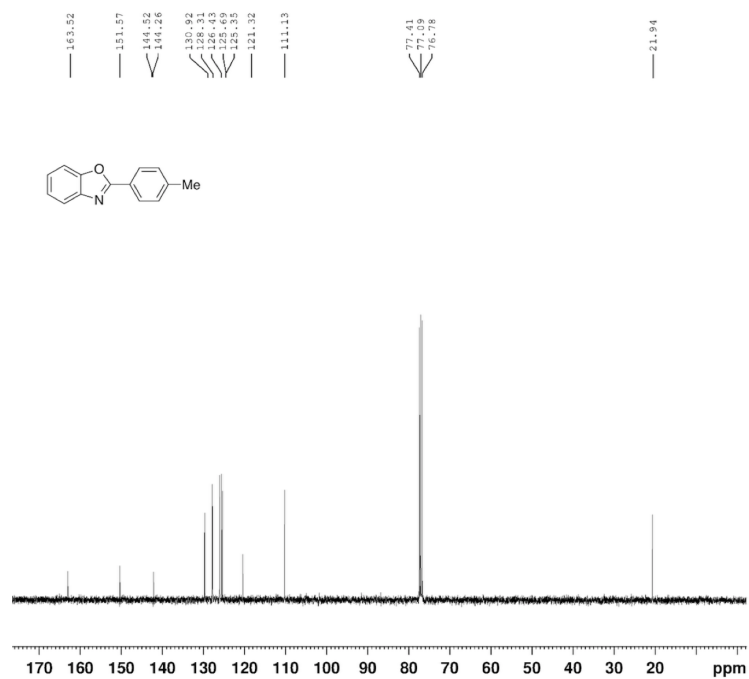
Spectra of 2-(4-methoxyphenyl)-benzoxazole (3)
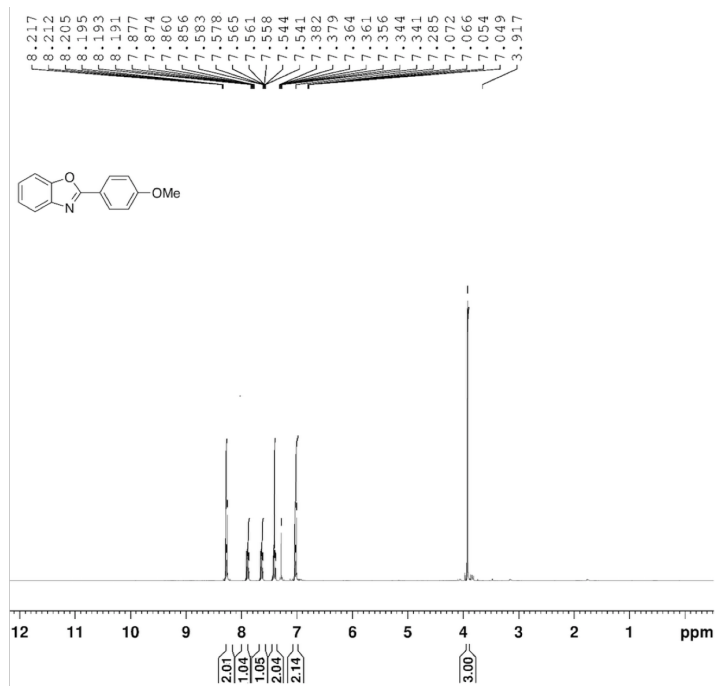
^{1}H-NMR

^{13}C-NMR
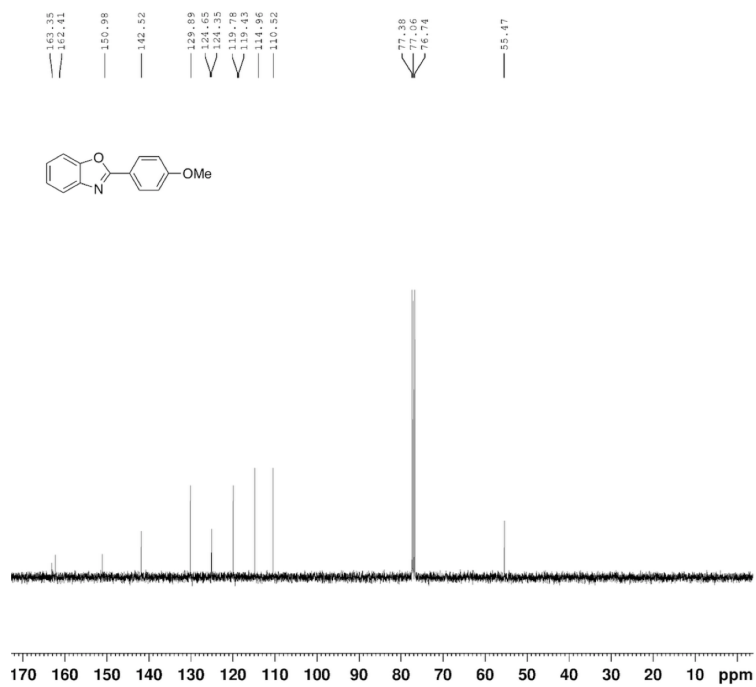
Spectra of 2-(4-fluorophenyl)-benzoxazole (4)
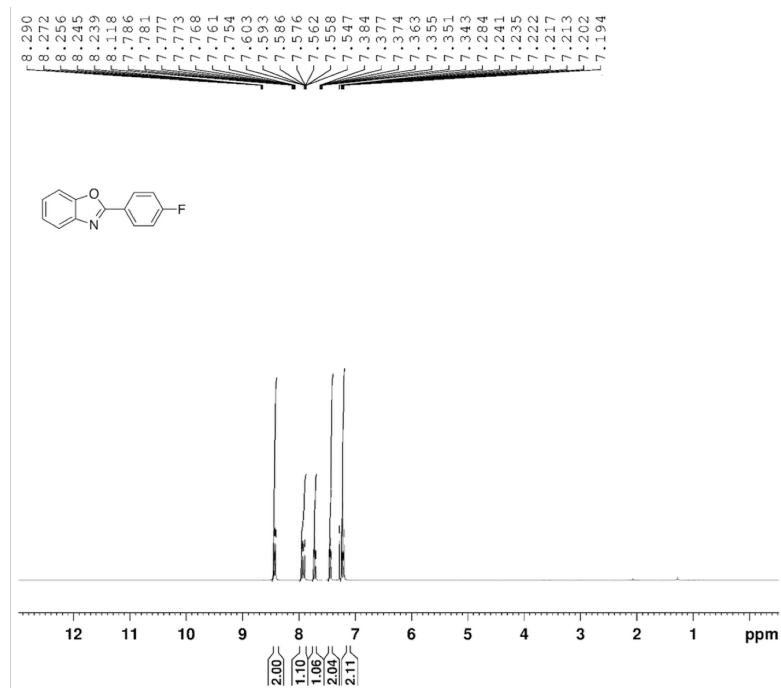
^{1}H-NMR

^{13}C-NMR

2-(4-chlorophenyl)benzo[d]oxazole (5)

^{1}H-NMR

8.230
8.225
8.213
8.208
7.808
7.802
7.799
7.794
7.786
7.616
7.608
7.603
7.599
7.593
7.545
7.540
7.535
7.522
7.518
7.512
7.413
7.402
7.394
7.387
7.379
7.369
7.284

2.00
1.01
1.01
2.00
2.09

^{13}C-NMR

162.34
150.33
142.26
137.98
129.43
129.01
125.81
125.54
124.90
120.29
110.91
77.34
77.03
76.71

4-(benzo[d]oxazol-2-yl)benzonitrile (6)

^{1}H-NMR

8.412 8.408 8.403 8.391 8.386 8.383 7.868 7.864 7.859 7.854 7.850 7.847 7.844 7.843 7.838 7.836 7.831 7.830 7.662 7.660 7.656 7.654 7.646 7.641 7.639 7.637 7.459 7.454 7.451 7.443 7.435 7.433 7.428 7.284

2.00 3.17 1.10 1.99

^{13}C-NMR

160.96 150.93 141.89 132.73 131.17 128.00 126.20 125.16 120.60 118.20 114.77 110.91 77.35 77.23 77.03 76.71

2-(m-tolyl)-benzoxazole (7)

^{1}H-NMR

8.130
8.093
8.074
7.814
7.805
7.801
7.797
7.791
7.618
7.612
7.608
7.603
7.595
7.459
7.440
7.421
7.400
7.388
7.381
7.374
7.365
7.284

2.486

2.00
0.99
1.05
1.07
3.10

3.09

^{13}C-NMR

163.56
150.98
142.28
138.99
132.56
129.02
128.42
127.15
125.18
124.97
124.72
120.11
110.70

77.38
77.06
76.74

22.47

2-(3-methoxyphenyl)-benzoxazole (8)

^{1}H-NMR

7.820
7.813
7.812
7.810
7.805
7.804
7.797
7.796
7.623
7.616
7.609
7.608
7.601
7.600
7.475
7.455
7.435
7.395
7.387
7.380
7.372
7.284
7.128
7.125
7.121
7.119
7.107
7.105
7.100
7.098
3.946

1.02 2.00 1.07 1.06 2.08 1.04   3.06

^{13}C-NMR

163.19
160.16
150.98
142.31
130.18
128.59
125.36
124.74
120.33
120.22
118.54
112.19
110.81
77.38
77.06
76.74
55.41

2-(o-tolyl)-benzoxazole (9)

^{1}H-NMR

^{13}C-NMR
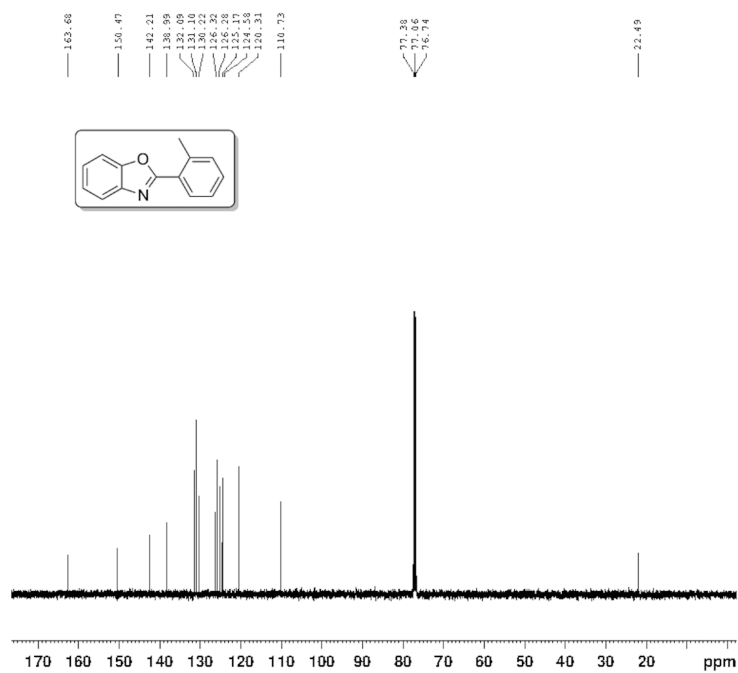
2-(2-methoxyphenyl)-benzoxazole (10)
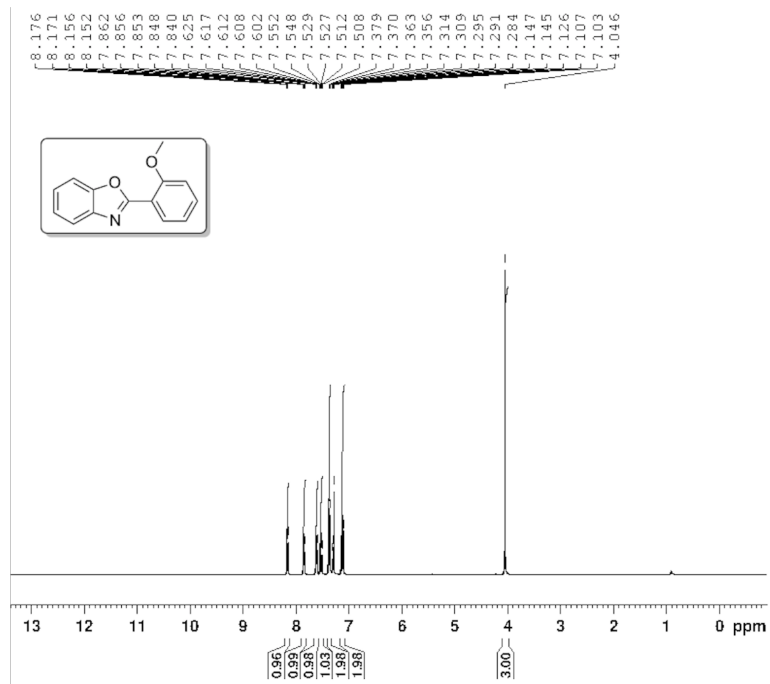
¹H-NMR

¹³C-NMR
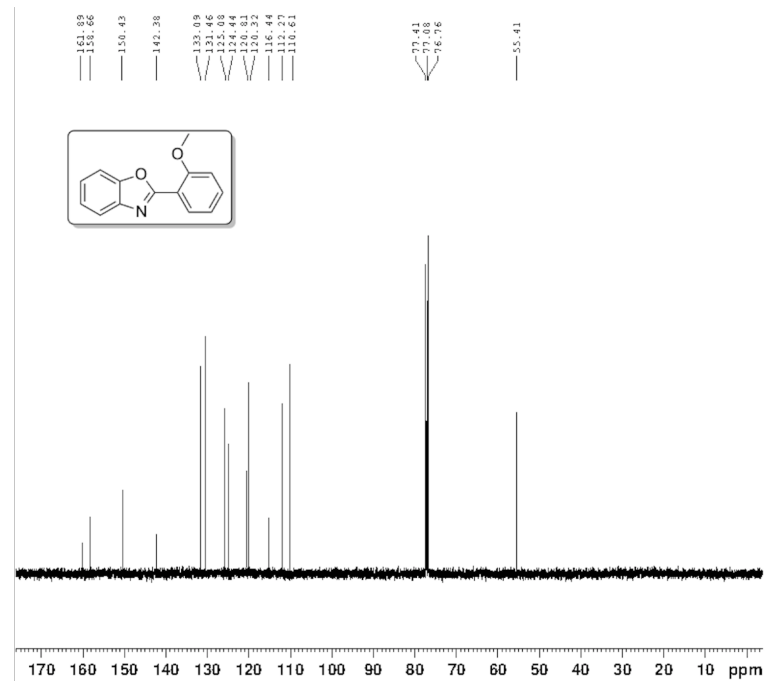
2-(thiophen-2-yl)benzo[d]oxazole (11)
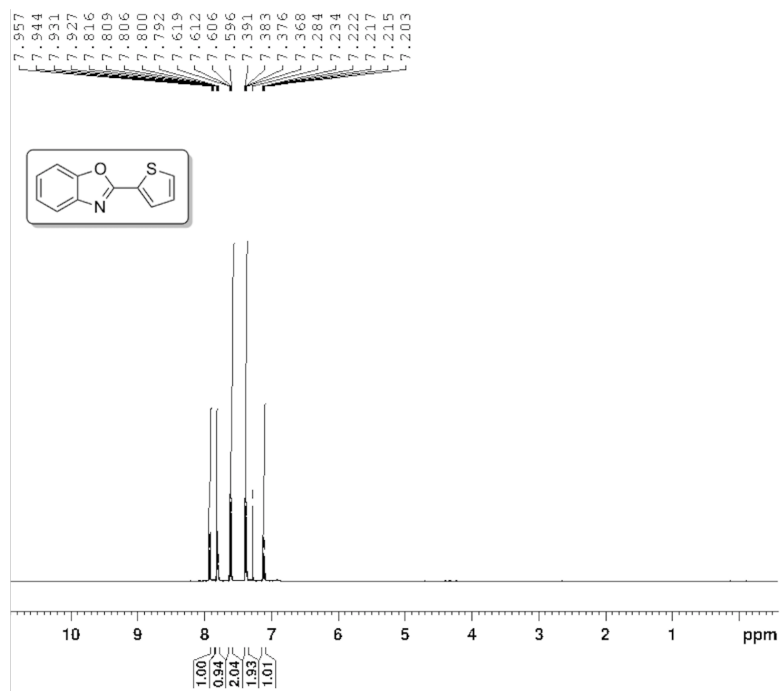
^{1}H-NMR

^{13}C-NMR
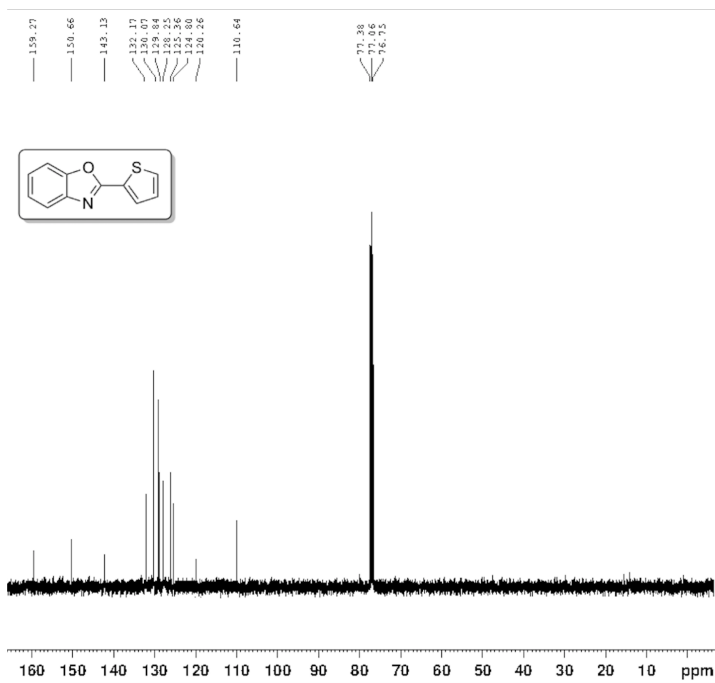
2-cyclohexyl-benzoxazole (12)
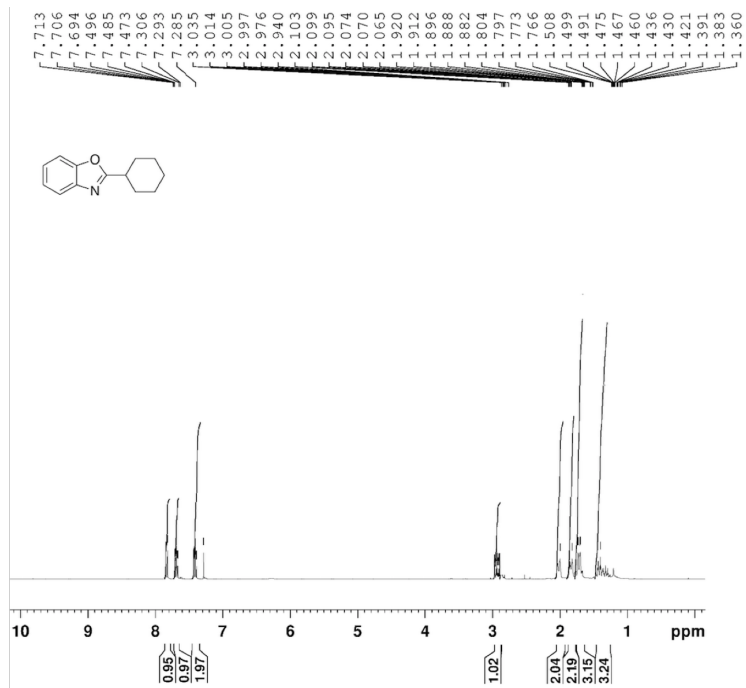
^{1}H-NMR

^{13}C-NMR
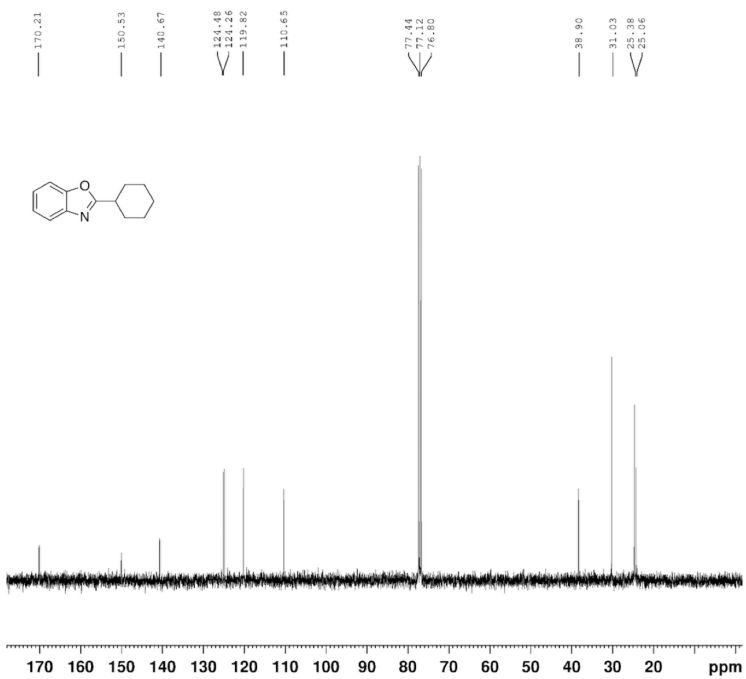
2-phenyl-1H-benzo[d]imidazole (13)
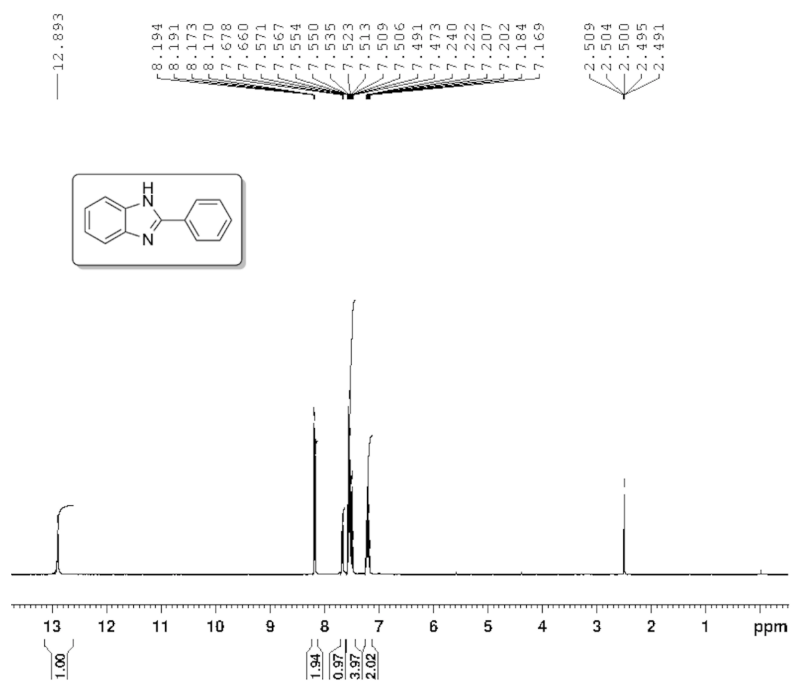
^{1}H-NMR

^{13}C-NMR
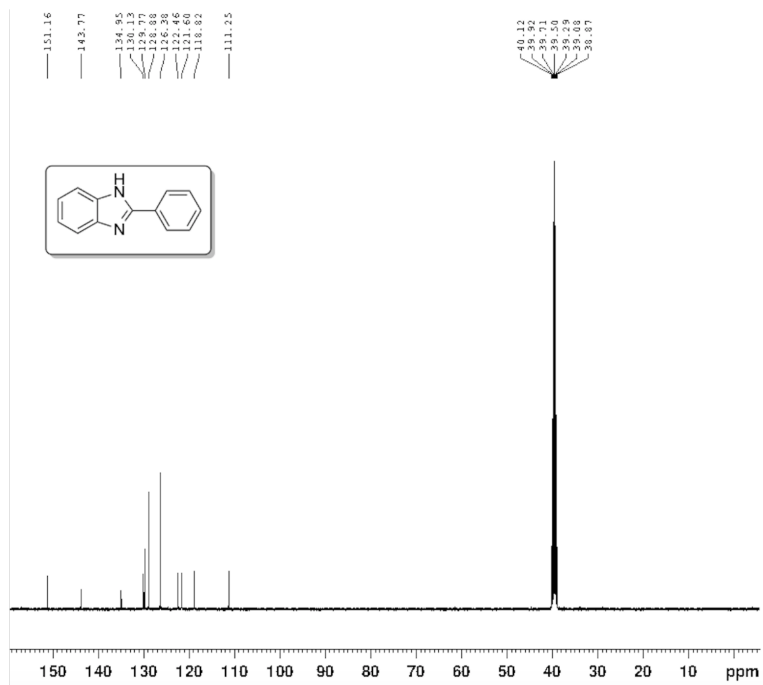
1-methyl-2-phenyl-1H-benzo[d]imidazole (14)
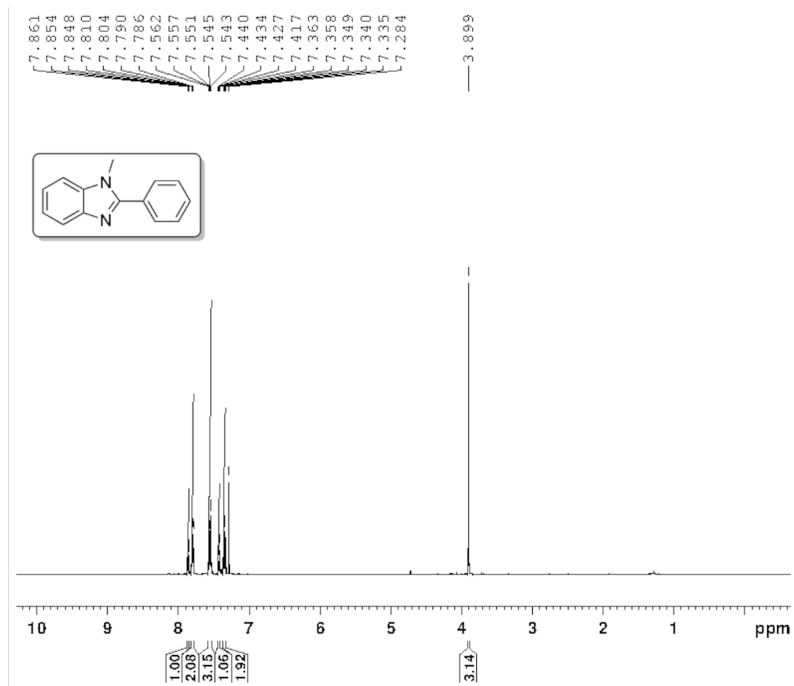
^{1}H-NMR

^{13}C-NMR
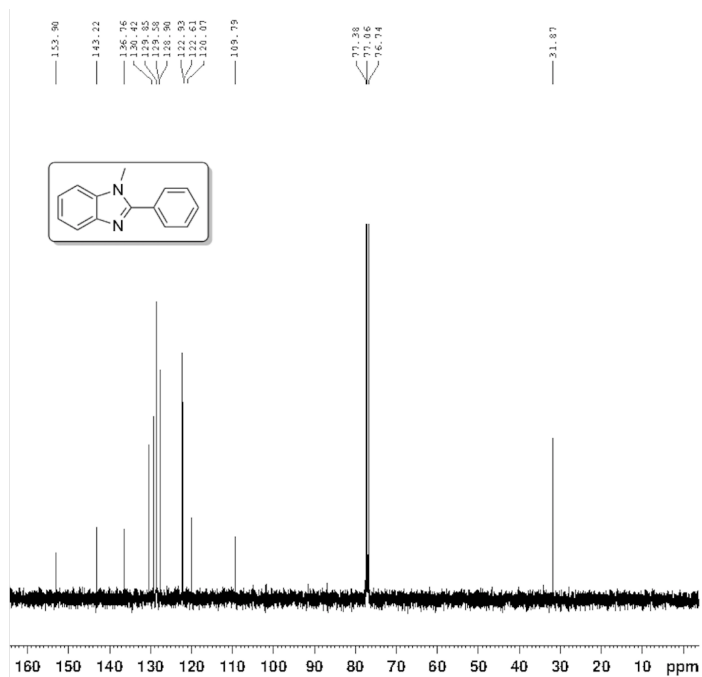
2-phenylbenzo[d]thiazole (15)
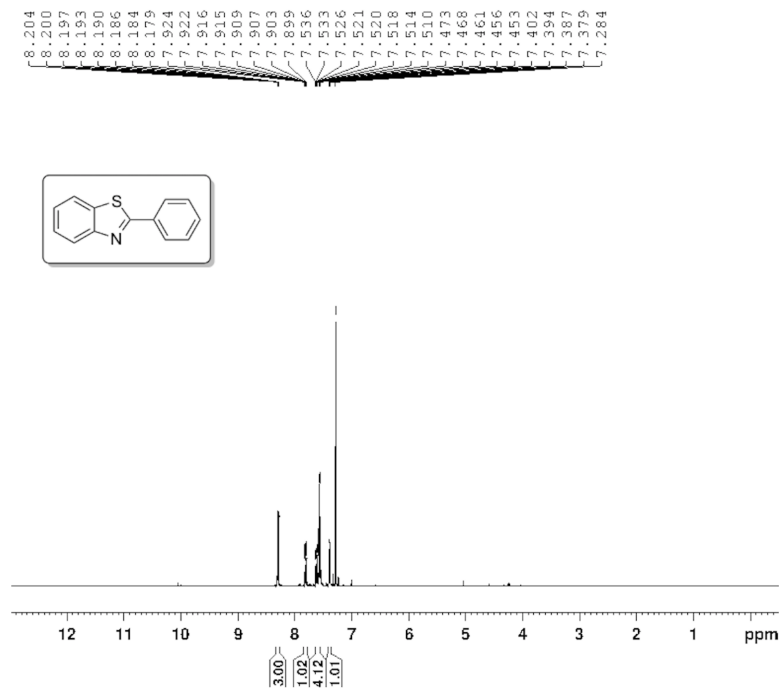
^{1}H-NMR

^{13}C-NMR
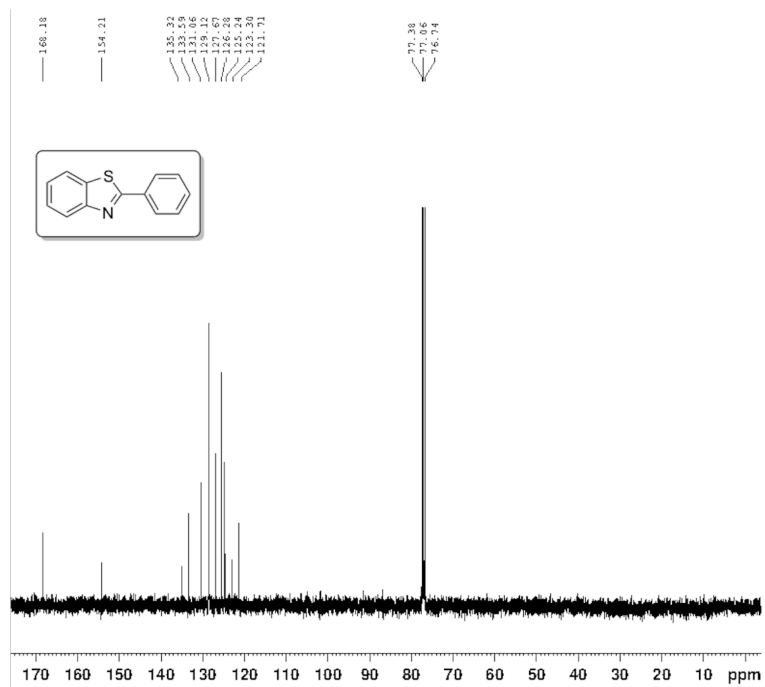
1,4-bis(benzo[d]oxazol-2-yl)benzene (16)

^{1}H-NMR

8.247
7.774
7.764
7.763
7.755
7.750
7.747
7.741
7.740
7.731
7.728
7.412
7.403
7.398
7.389
7.387
7.385
7.383
7.379
7.378
7.375
7.284

^{13}C-NMR

162.77
151.23
141.61
130.98
128.32
125.13
123.66
119.14
109.73
77.39
77.07
76.76
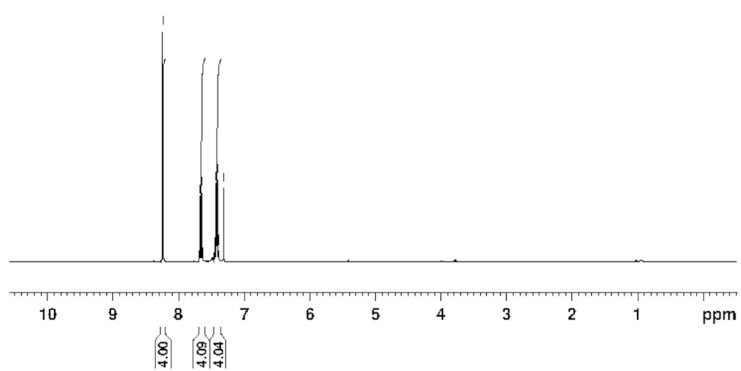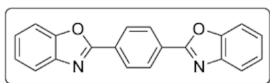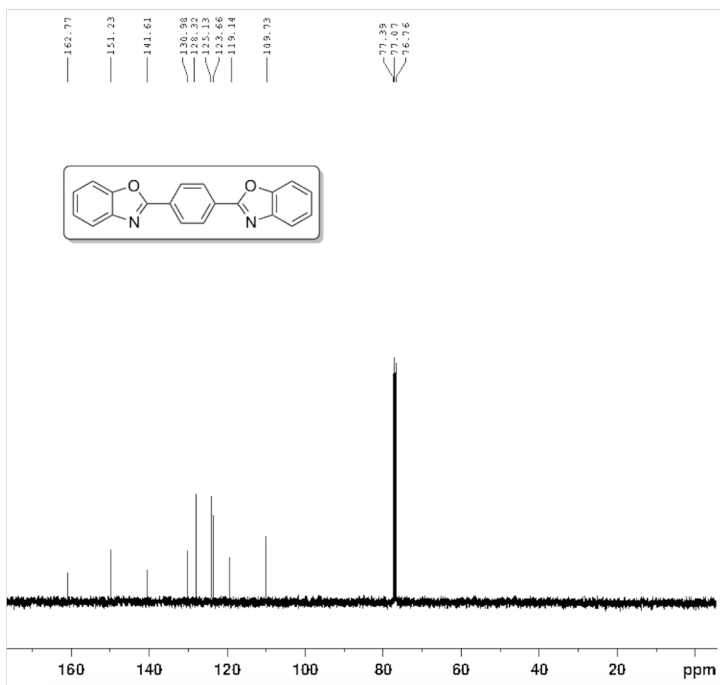
2,6-diphenylbenzo[1,2-d:5,4-d']bis(oxazole) (17)
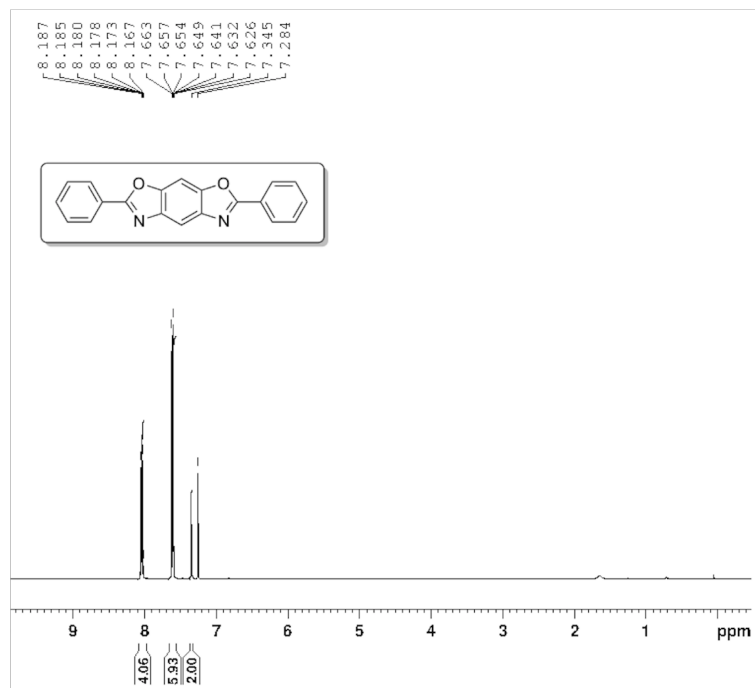
^{1}H-NMR

^{13}C-NMR
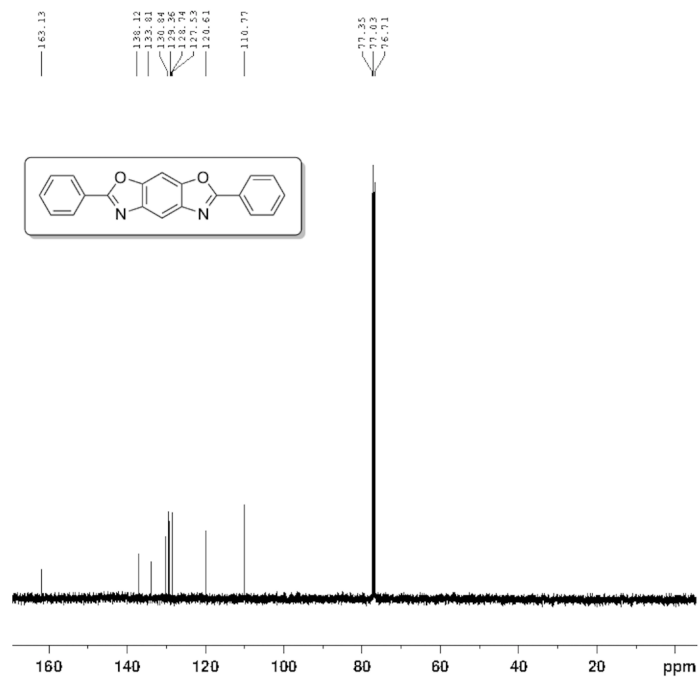
2,5-bis(benzo[d]oxazol-2-yl)thiophene (18)

^{1}H-NMR
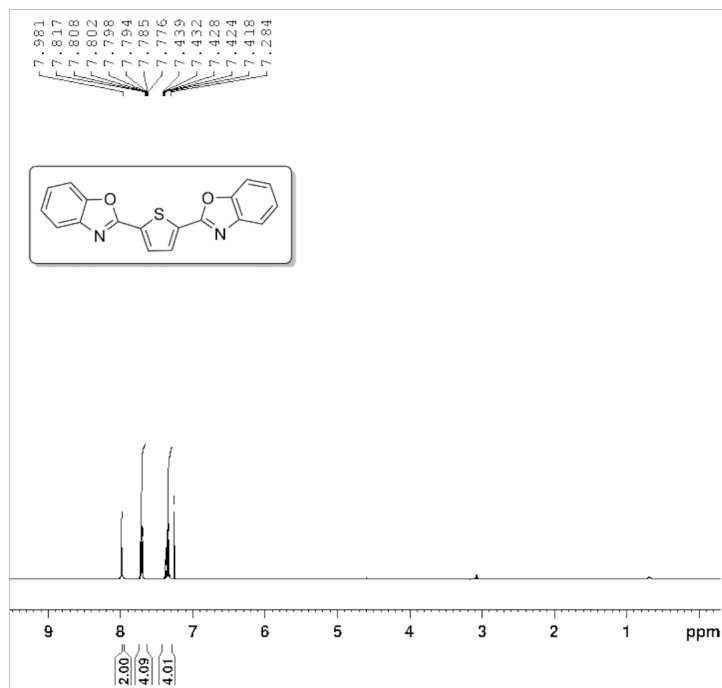
^{13}C-NMR
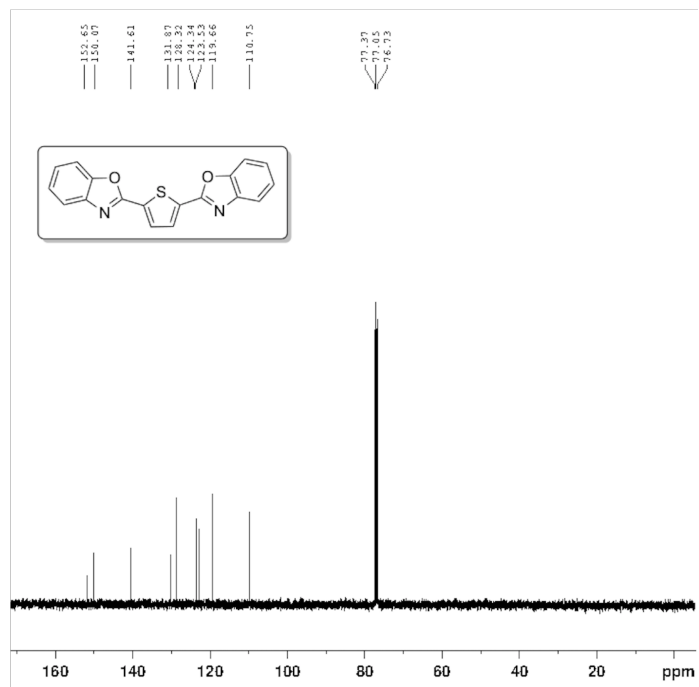
References

[1] Ghosh, T.; Lehmann, M. Recent advances in heterocycle-based metal-free calamitics. *Journal of Materials Chemistry C* **2017**, *5*, 12308–12337.

[2] Noel, S.; Cadet, S.; Gras, E.; Hureau, C. The benzazole scaffold: a SWAT to combat Alzheimer's disease. *Chemical Society Reviews* **2013**, *42*, 7747–7762.

[3] Amaike, K.; Muto, K.; Yamaguchi, J.; Itami, K. Decarbonylative C–H coupling of azoles and aryl esters: unprecedented nickel catalysis and application to the synthesis of muscoride A. *Journal of the American Chemical Society* **2012**, *134*, 13573–13576.

[4] Ai, W.; Zhou, W.; Du, Z.; Du, Y.; Zhang, H.; Jia, X.; Xie, L.; Yi, M.; Yu, T.; Huang, W. Benzoxazole and benzimidazole heterocycle-grafted graphene for high-performance supercapacitor electrodes. *Journal of Materials Chemistry* **2012**, *22*, 23439–23446.

[5] Wu, J.; Liu, W.; Ge, J.; Zhang, H.; Wang, P. New sensing mechanisms for design of fluorescent chemosensors emerging in recent years. *Chemical Society Reviews* **2011**, *40*, 3483–3495.

[6] Rabbani, M. G.; Islamoglu, T.; El-Kaderi, H. M. Benzothiazole-and benzoxazole-linked porous polymers for carbon dioxide storage and separation. *Journal of Materials Chemistry A* **2017**, *5*, 258–265.

[7] Luo, S.; Liu, J.; Lin, H.; Kazanowska, B. A.; Hunckler, M. D.; Roeder, R. K.; Guo, R. Preparation and gas transport properties of triptycene-containing polybenzoxazole

(PBO)-based polymers derived from thermal rearrangement (TR) and thermal cyclode-hydration (TC) processes. *Journal of Materials Chemistry A* **2016**, *4*, 17050–17062.

[8] Hao, X.; Zhu, J.; Jiang, X.; Wu, H.; Qiao, J.; Sun, W.; Wang, Z.; Sun, K. Ultra-strong polyoxyzole nanofiber membranes for dendrite-proof and heat-resistant battery separators. *Nano letters* **2016**, *16*, 2981–2987.

[9] Zhang, K.; Liu, J.; Ishida, H. An ultrahigh performance cross-linked polybenzoxa-zole via thermal conversion from poly (benzoxazine amic acid) based on smart o-benzoxazine chemistry. *Macromolecules* **2014**, *47*, 8674–8681.

[10] Tang, L.; Guo, X.; Yang, Y.; Zha, Z.; Wang, Z. Gold nanoparticles supported on titanium dioxide: an efficient catalyst for highly selective synthesis of benzoxazoles and benzimidazoles. *Chemical Communications* **2014**, *50*, 6145–6148.

[11] Khalafi-Nezhad, A.; Panahi, F. Ruthenium-catalyzed synthesis of benzoxazoles using acceptorless dehydrogenative coupling reaction of primary alcohols with 2-aminophenol under heterogeneous conditions. *ACS Catalysis* **2014**, *4*, 1686–1692.

[12] Cao, X.; Cheng, X.; Bai, Y.; Liu, S.; Deng, G.-J. Transition-metal free 2-arylbenzoxazole formation from aryl amides and cyclohexanones. *Green Chemistry* **2014**, *16*, 4644–4648.

[13] Jin, X.; Liu, Y.; Lu, Q.; Yang, D.; Sun, J.; Qin, S.; Zhang, J.; Shen, J.; Chu, C.; Liu, R. Formation of C [double bond, length as m-dash] N bonds by the release of H 2: a new strategy for synthesis of imines and benzazoles. *Organic & biomolecular chemistry* **2013**, *11*, 3776–3780.

[14] Wu, M.; Hu, X.; Liu, J.; Liao, Y.; Deng, G.-J. Iron-catalyzed 2-arylbenzoxazole forma-tion from o-nitrophenols and benzylic alcohols. *Organic letters* **2012**, *14*, 2722–2725.

[15] Gianotti, E.; Taillades-Jacquin, M.; Rozière, J.; Jones, D. J. High-purity hydrogen

generation via dehydrogenation of organic carriers: a review on the catalytic process. *ACS Catalysis* **2018**, *8*, 4660–4680.

[16] Sordakis, K.; Tang, C.; Vogt, L. K.; Junge, H.; Dyson, P. J.; Beller, M.; Laurenczy, G. Homogeneous catalysis for sustainable hydrogen storage in formic acid and alcohols. *Chemical reviews* **2017**, *118*, 372–433.

[17] Lu, Z.; Cherepakhin, V.; Demianets, I.; Lauridsen, P. J.; Williams, T. Iridium-based hydride transfer catalysts: from hydrogen storage to fine chemicals. *Chemical Communications* **2018**,

[18] Shen, Y.; Zhan, Y.; Li, S.; Ning, F.; Du, Y.; Huang, Y.; He, T.; Zhou, X. Hydrogen generation from methanol at near-room temperature. *Chemical science* **2017**, *8*, 7498–7504.

[19] Zhang, S.; Yang, F.; Zhou, L.; Zhang, Y.; Wu, Z.; Zhang, Z.; Wang, Y. A novel multilayer fin structure for heat transfer enhancement in hydride-based hydrogen storage reactor. *International Journal of Energy Research* **2018**,

[20] Li, S.-j.; Ping, Y.; Yan, J.-M.; Wang, H.-L.; Wu, M.; Jiang, Q. Facile synthesis of AgAuPd/graphene with high performance for hydrogen generation from formic acid. *Journal of Materials Chemistry A* **2015**, *3*, 14535–14538.

[21] Zhu, Q.-L.; Song, F.-Z.; Wang, Q.-J.; Tsumori, N.; Himeda, Y.; Autrey, T.; Xu, Q. A solvent-switched in situ confinement approach for immobilizing highly-active ultrafine palladium nanoparticles: boosting catalytic hydrogen evolution. *Journal of Materials Chemistry A* **2018**, *6*, 5544–5549.

[22] Zhong, W.; Liu, Y.; Deng, M.; Zhang, Y.; Jia, C.; Prezhdo, O. V.; Yuan, J.; Jiang, J. C 2 N-supported single metal ion catalysts for HCOOH dehydrogenation. *Journal of Materials Chemistry A* **2018**, *6*, 11105–11112.

[23] Song, J.; Gu, X.; Cheng, J.; Fan, N.; Zhang, H.; Su, H. Remarkably boosting catalytic H2 evolution from ammonia borane through the visible-light-driven synergistic electron effect of non-plasmonic noble-metal-free nanoparticles and photoactive metal-organic frameworks. *Applied Catalysis B: Environmental* **2018**, *225*, 424–432.

[24] Liu, H.; Huang, B.; Zhou, J.; Wang, K.; Yu, Y.; Yang, W.; Guo, S. Enhanced electron transfer and light absorption on imino polymer capped PdAg nanowire networks for efficient room-temperature dehydrogenation of formic acid. *Journal of Materials Chemistry A* **2018**, *6*, 1979–1984.

[25] Guo, X.; Yu, C.; Yin, Z.; Sun, S.; Seto, C. T. Hydrodehalogenation of polyhalogenated aromatics catalyzed by NiPd nanoparticles supported on nitrogen-doped graphene. *ChemSusChem* **2018**,

[26] others,, et al. Maximizing the catalytic activity of nanoparticles through monolayer assembly on nitrogen-doped graphene. *Angewandte Chemie International Edition* **2018**, *57*, 451–455.

[27] Xiao, L.; Jun, Y.-S.; Wu, B.; Liu, D.; Chuong, T. T.; Fan, J.; Stucky, G. D. Carbon nitride supported AgPd alloy nanocatalysts for dehydrogenation of formic acid under visible light. *Journal of Materials Chemistry A* **2017**, *5*, 6382–6387.

[28] Sun, Q.; Wang, N.; Bing, Q.; Si, R.; Liu, J.; Bai, R.; Zhang, P.; Jia, M.; Yu, J. Subnanometric hybrid Pd-M (OH) 2, M= Ni, Co, clusters in zeolites as highly efficient nanocatalysts for hydrogen generation. *Chem* **2017**, *3*, 477–493.

[29] Cheng, J.; Gu, X.; Liu, P.; Zhang, H.; Ma, L.; Su, H. Achieving efficient room-temperature catalytic H2 evolution from formic acid through atomically controlling the chemical environment of bimetallic nanoparticles immobilized by isoreticular amine-functionalized metal-organic frameworks. *Applied Catalysis B: Environmental* **2017**, *218*, 460–469.

[30] Jo, S.; Verma, P.; Kuwahara, Y.; Mori, K.; Choi, W.; Yamashita, H. Enhanced hydrogen production from ammonia borane using controlled plasmonic performance of Au nanoparticles deposited on TiO 2. *Journal of Materials Chemistry A* **2017**, *5*, 21883–21892.

[31] Liu, H.; Liu, X.; Yu, Y.; Yang, W.; Li, J.; Feng, M.; Li, H. Bifunctional networked Ag/AgPd core/shell nanowires for the highly efficient dehydrogenation of formic acid and subsequent reduction of nitrate and nitrite in water. *Journal of Materials Chemistry A* **2018**, *6*, 4611–4616.

[32] Yu, C.; Guo, X.; Xi, Z.; Muzzio, M.; Yin, Z.; Shen, B.; Li, J.; Seto, C. T.; Sun, S. AgPd nanoparticles deposited on WO2. 72 nanorods as an efficient catalyst for one-pot conversion of nitrophenol/nitroacetophenone into benzoxazole/quinazoline. *Journal of the American Chemical Society* **2017**, *139*, 5712–5715.

[33] Zhang, Q.; Li, S.-S.; Zhu, M.-M.; Liu, Y.-M.; He, H.-Y.; Cao, Y. Direct reductive amination of aldehydes with nitroarenes using bio-renewable formic acid as a hydrogen source. *Green Chemistry* **2016**, *18*, 2507–2513.

[34] Jagadeesh, R. V.; Banerjee, D.; Arockiam, P. B.; Junge, H.; Junge, K.; Pohl, M.-M.; Radnik, J.; Brückner, A.; Beller, M. Highly selective transfer hydrogenation of functionalised nitroarenes using cobalt-based nanocatalysts. *Green Chemistry* **2015**, *17*, 898–902.

[35] Javaid, R.; Kawasaki, S.-i.; Suzuki, A.; Suzuki, T. M. Simple and rapid hydrogenation of p-nitrophenol with aqueous formic acid in catalytic flow reactors. *Beilstein journal of organic chemistry* **2013**, *9*, 1156.

[36] Jouannin, C.; Dez, I.; Gaumont, A.-C.; Taulemesse, J.-M.; Vincent, T.; Guibal, E. Palladium supported on alginate/ionic liquid highly porous monoliths: Application to 4-nitroaniline hydrogenation. *Applied Catalysis B: Environmental* **2011**, *103*, 444–452.

[37] Xi, Z.; Erdosy, D. P.; Mendoza-Garcia, A.; Duchesne, P. N.; Li, J.; Muzzio, M.; Li, Q.; Zhang, P.; Sun, S. Pd nanoparticles coupled to WO2. 72 nanorods for enhanced electrochemical oxidation of formic acid. *Nano letters* **2017**, *17*, 2727–2731.

[38] Zhang, S.; Metin, Ö.; Su, D.; Sun, S. Monodisperse AgPd alloy nanoparticles and their superior catalysis for the dehydrogenation of formic acid. *Angewandte Chemie* **2013**, *125*, 3769–3772.

[39] Wang, H.; Fan, R.; Miao, J.; Chen, J.; Mao, S.; Deng, J.; Wang, Y. Oxygen vacancies on the surface of H x WO 3- y for enhanced charge storage. *Journal of Materials Chemistry A* **2018**, *6*, 6780–6784.

[40] Cheng, H.; Klapproth, M.; Sagaltchik, A.; Li, S.; Thomas, A. Ordered mesoporous WO 2.83: selective reduction synthesis, exceptional localized surface plasmon resonance and enhanced hydrogen evolution reaction activity. *Journal of Materials Chemistry A* **2018**, *6*, 2249–2256.

[41] Martínez-García, A.; Vendra, V. K.; Sunkara, S.; Haldankar, P.; Jasinski, J.; Sunkara, M. K. Tungsten oxide-coated copper oxide nanowire arrays for enhanced activity and durability with photoelectrochemical water splitting. *Journal of Materials Chemistry A* **2013**, *1*, 15235–15241.

[42] Kuo, C.-H.; Lamontagne, L. K.; Brodsky, C. N.; Chou, L.-Y.; Zhuang, J.; Sneed, B. T.; Sheehan, M. K.; Tsung, C.-K. The effect of lattice strain on the catalytic properties of Pd nanocrystals. *ChemSusChem* **2013**, *6*, 1993–2000.

[43] Bai, H.; Su, N.; Li, W.; Zhang, X.; Yan, Y.; Li, P.; Ouyang, S.; Ye, J.; Xi, G. W 18 O 49 nanowire networks for catalyzed dehydration of isopropyl alcohol to propylene under visible light. *Journal of Materials Chemistry A* **2013**, *1*, 6125–6129.

[44] Tsuji, M.; Shimamoto, D.; Uto, K.; Hattori, M.; Ago, H. Enhancement of catalytic activity of AgPd@ Pd/TiO 2 nanoparticles under UV and visible photoirradiation. *Journal of Materials Chemistry A* **2016**, *4*, 14649–14656.

[45] Jiang, Y.; Fan, X.; Xiao, X.; Qin, T.; Zhang, L.; Jiang, F.; Li, M.; Li, S.; Ge, H.; Chen, L. Novel AgPd hollow spheres anchored on graphene as an efficient catalyst for dehydrogenation of formic acid at room temperature. *Journal of Materials Chemistry A* **2016**, *4*, 657–666.

[46] others„ et al. A photoactive bimetallic framework for direct aminoformylation of nitroarenes. *Green Chemistry* **2016**, *18*, 1019–1022.

[47] Song, J.; Huang, Z.-F.; Pan, L.; Zou, J.-J.; Zhang, X.; Wang, L. Oxygen-deficient tungsten oxide as versatile and efficient hydrogenation catalyst. *ACS catalysis* **2015**, *5*, 6594–6599.

[48] Ping, Y.; Yan, J.-M.; Wang, Z.-L.; Wang, H.-L.; Jiang, Q. Ag 0.1-Pd 0.9/rGO: an efficient catalyst for hydrogen generation from formic acid/sodium formate. *Journal of Materials Chemistry A* **2013**, *1*, 12188–12191.

[49] Yamazoe, S.; Masutani, Y.; Teramura, K.; Hitomi, Y.; Shishido, T.; Tanaka, T. Promotion effect of tungsten oxide on photo-assisted selective catalytic reduction of NO with NH3 over TiO2. *Applied Catalysis B: Environmental* **2008**, *83*, 123–130.

[50] Zhong, H.; Iguchi, M.; Song, F.-Z.; Chatterjee, M.; Ishizaka, T.; Nagao, I.; Xu, Q.; Kawanami, H. Automatic high-pressure hydrogen generation from formic acid in the presence of nano-Pd heterogeneous catalysts at mild temperatures. *Sustainable Energy & Fuels* **2017**, *1*, 1049–1055.

[51] Jeon, H.-j.; Chung, Y.-M. Hydrogen production from formic acid dehydrogenation over Pd/C catalysts: Effect of metal and support properties on the catalytic performance. *Applied Catalysis B: Environmental* **2017**, *210*, 212–222.

[52] Yang, X.; Pachfule, P.; Chen, Y.; Tsumori, N.; Xu, Q. Highly efficient hydrogen generation from formic acid using a reduced graphene oxide-supported AuPd nanoparticle catalyst. *Chemical Communications* **2016**, *52*, 4171–4174.

[53] Cheng, J.; Gu, X.; Sheng, X.; Liu, P.; Su, H. Exceptional size-dependent catalytic activity enhancement in the room-temperature hydrogen generation from formic acid over bimetallic nanoparticles supported by porous carbon. *Journal of Materials Chemistry A* **2016**, *4*, 1887–1894.

[54] Cheng, J.; Gu, X.; Liu, P.; Wang, T.; Su, H. Controlling catalytic dehydrogenation of formic acid over low-cost transition metal-substituted AuPd nanoparticles immobilized by functionalized metal–organic frameworks at room temperature. *Journal of Materials Chemistry A* **2016**, *4*, 16645–16652.

[55] Bi, Q.-Y.; Lin, J.-D.; Liu, Y.-M.; He, H.-Y.; Huang, F.-Q.; Cao, Y. Dehydrogenation of formic acid at room temperature: Boosting palladium nanoparticle efficiency by coupling with pyridinic-nitrogen-doped carbon. *Angewandte Chemie International Edition* **2016**, *55*, 11849–11853.

[56] others,, et al. Experimental and computational studies of formic acid dehydrogenation over PdAu: influence of ensemble and ligand effects on catalysis. *Journal of Materials Chemistry A* **2016**, *4*, 14141–14147.

[57] Luo, Z.; Castleman Jr, A.; Khanna, S. N. Reactivity of metal clusters. *Chemical reviews* **2016**, *116*, 14456–14492.

[58] Xu, B.; Gonella, G.; DeLacy, B. G.; Dai, H.-L. Adsorption of anionic thiols on silver nanoparticles. *The Journal of Physical Chemistry C* **2015**, *119*, 5454–5461.

[59] Moreno, M.; Ibanez, F. J.; Jasinski, J. B.; Zamborini, F. P. Hydrogen reactivity of palladium nanoparticles coated with mixed monolayers of alkyl thiols and alkyl amines for sensing and catalysis applications. *Journal of the American Chemical Society* **2011**, *133*, 4389–4397.

[60] Garcia-Martinez, J. C.; Scott, R. W.; Crooks, R. M. Extraction of monodisperse palladium nanoparticles from dendrimer templates. *Journal of the American Chemical Society* **2003**, *125*, 11190–11191.

Chapter 6

Carbon-Supported AuPd Nanoparticles as Catalysts for the Synthesis of Polybenzoxazoles†

6.1 Abstract

Using nanoparticles (NPs) to catalyze chemical reactions for the formation of functional polymers with controlled polymerization and properties is a new and important field of materials research. In this article, we report an AuPd NP system as an active and stable catalyst for the preparation of polybenzoxazole (PBO) in a one-pot reaction of formic acid, 1,5-diisopropoxy-2,4-dinitrobenzene, and terephthaldehyde. The polymerization reaction is AuPd NP size- and composition-dependent and 8 nm $Au_{39}Pd_{61}$ NPs are the best catalyst for the formation of PBO (Mw = 3.6 kDa). The highly pure PBO shows excellent thermal stability up to 600 °C and improved chemical and mechanical stability under challenging environmental conditions compared to commercial PBO (Zylon®, Mw = 40 kDa). The reported NP-catalyzed one-pot reaction to polymerization is not limited to the formation of PBO, but can be extended as a general approach to rigid organic polymers that are important for ballistic fiber, anti-flame, smart-textile and ionic/separation membrane applications.

6.2 Introduction

Advances in nanoparticle (NP) synthesis have motivated extensive research into defining the tuning knobs that can be used to control the physical and chemical properties of NPs.[1–6] An excellent example is the study of NP catalysts where NP structural and morphological effects are employed to promote chemical reactions in much milder and greener reaction conditions than conventional catalysts for sustainable chemical and energy applications.[7–12] However, compared to the broad use of NPs for catalyzing reactions for the syntheses of small molecules,[13–18] there is no report to use NPs as a catalyst to promote reactions leading to controlled polymerization.

Herein we report an example using synergistic effects of AuPd NPs to catalyze a one-pot reaction of small molecules to form highly pure PBO. PBO is a sub-class of polybenzoazoles. The highly aromatic nature and conjugated structure of alternating benzoxazole and phenyl

rings provides the polymer with superior thermal and mechanical stability.[19–22] These characteristics make PBO fibers exceptional candidates for use as body armor, flame retardant materials, smart electronic textiles, and ionic/separation membranes.[23–26] However, PBOs are conventionally made by condensing diaminobenzene diol and terephthalic acid with polyphosphoric acid as both solvent and catalyst. As a result, they are inevitably contaminated with phosphoric acid (PA) units that can catalyze the hydrolysis of benzoxazole ring upon its exposure to humid and lighted environments (Figure 6.1), causing unexpected and fast degradation of the mechanical integrity of the polymer fibers.[27–29]
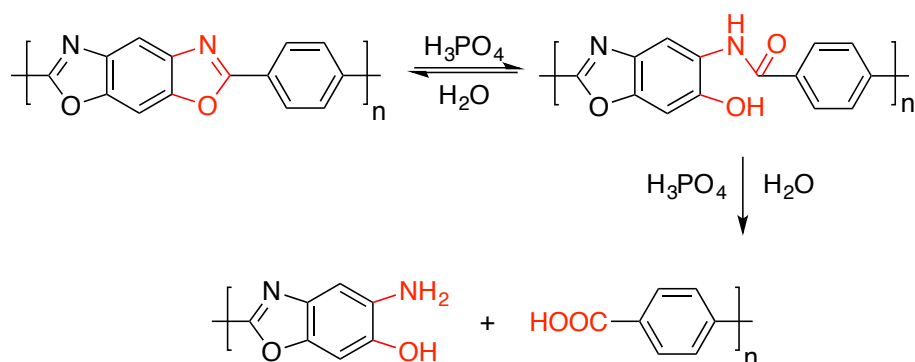
Figure 6.1 Hydrolysis and ring opening of benzoxazole catalyzed by phosphoric acid.

Our new AuPd NP catalyzed one-pot polymerization to PBO is NP size- and composition-dependent, and among the 4, 6, 8, 10 nm AuPd NPs studied, 8 nm $Au_{39}Pd_{61}$ NPs are the most efficient in catalyzing the reaction to the highest degree of polymerization (Mw = 3.6 kDa). Compared to the commercial PBO, Zylon® (Mw = 40 kDa), our lighter PBO has not only comparable thermal stability (over 600 °C), but also much improved chemical and mechanical stability against water- and organic solvent-induced polymer degradation. Molecular Mechanics (MM) and Density Functional Theory (DFT) simulations reveal that both surface strain and surface geometry of the NPs contribute to the size-dependent polymerization. Our studies show a general approach to NP-controlled catalysis applied to polymerization. This method can be extended to prepare other rigid organic polymers that are important for ballistic fibers, smart textiles, flame retardants, and membrane applications.
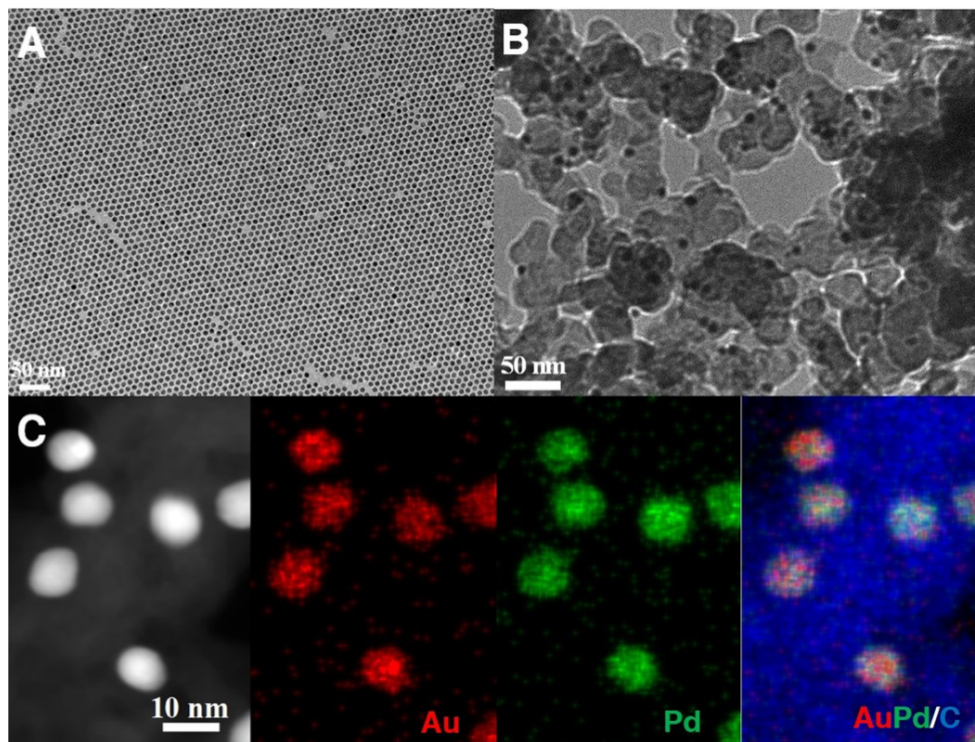
Figure 6.2 Preparation and characterization of AuPd alloy NPs. (A) TEM image of 8 nm Au NPs. (B) TEM image of 8.2±0.4 nm $Au_{39}Pd_{61}$ NPs deposited on C. (C) HAADF-STEM image of the $Au_{39}Pd_{61}$/C and elemental mapping of NPs to show Au (red) and Pd (green) distribution within the NPs.

6.3   Results and discussion

Recently, AuPd alloy NPs were studied as stable catalysts to dehydrogenate formic acid into H_2 for hydrogenation reactions.[30–33] These AuPd NPs were previously prepared by co-reduction methods, under which it is difficult to control both sizes and compositions of the NPs. We modified the synthesis and developed a unique seed-mediated growth-diffusion method to prepare AuPd NPs with well-controlled sizes and compositions. In our synthesis, 4, 6, 8 and 10 nm Au NPs were first prepared as described.[34] Then, in the presence of Au seeding NPs, a controlled amount of $Pd(acac)_2$ was reduced in oleylamine and oleic acid (v/v = 50/1) at 260 °C to yield AuPd NPs. We further deposited these AuPd NPs onto a Ketjen carbon support (C) and annealed the supported NPs, NPs/C, under forming gas at 500 °C for 10 min to obtain catalytically active AuPd alloy NPs. Figure 6.2 shows
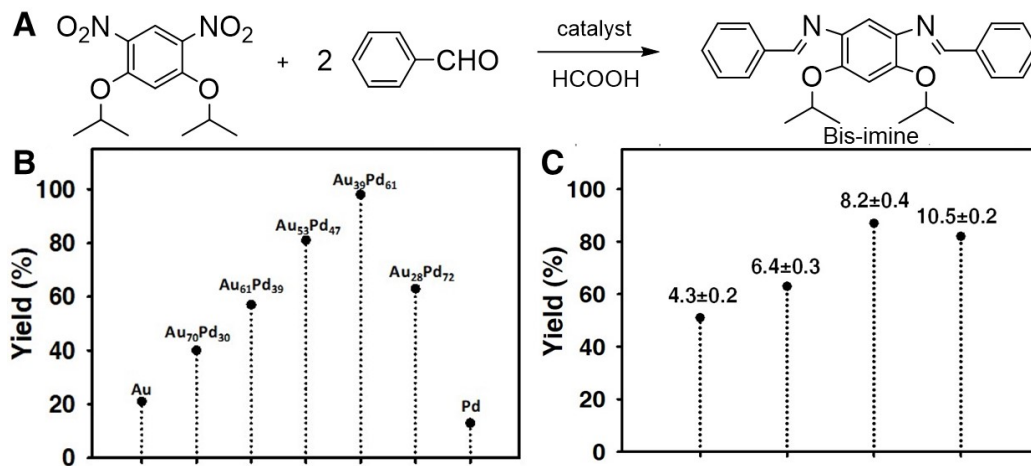
Figure 6.3 Au$_{39}$Pd$_{61}$-catalyzed reaction between 1,5-diisopropoxy-2,4-dinitrobenzene and benzaldehyde. (A) A new synthetic route for producing a bis-imine via the condensation of 1,5-diisopropoxy-2,4-dinitrobenzene and benzaldehyde. (B) The yields of bis-imine with different compositions of 8 nm AuPd supported on C. Reaction conditions: AuPd/C (2.5 mol%), 1,5-diisopropoxy-2,4-dinitrobenzene (1 mmol), benzaldehyde (2.1 mmol), NMP (3 mL), and FA (10 mmol), 80 °C, 6 h. (C) The yields of bis-imine with four different sizes of Au$_{39}$Pd$_{61}$/C as tandem catalyst. Reaction conditions: Au$_{39}$Pd$_{61}$/C (2.5 mol%), 1,5-diisopropoxy-2,4-dinitrobenzene (1 mmol), benzaldehyde (2.1 mmol), NMP (3 mL), and FA (10 mmol), 80 °C, 6 h.

representative TEM images of 8 nm Au seeding NPs (Figure 6.2A) and 8.2±0.4 nm AuPd/C (Figure 6.2B). Starting from 4, 6, 8, 10 nm Au NPs, we obtained 4.3±0.2, 6.4±0.3, 8.2±0.4, 10.5±0.2 nm Au$_{39}$Pd$_{61}$ alloy NPs, showing a very small NP size increase after the alloy formation. For simplicity of presentation, these AuPd NPs are denoted as 4, 6, 8, 10 nm NPs in this paper. The alloy structure of the NPs was characterized by high-resolution TEM (HRTEM), high angle annular dark field (HAADF) scanning transmission electron microscopy (STEM) and elemental mapping (Figure 6.2C), and X-ray diffraction analysis. From these analyses, we conclude that homogenous alloy AuPd NPs with a face-centered cubic structure are obtained.
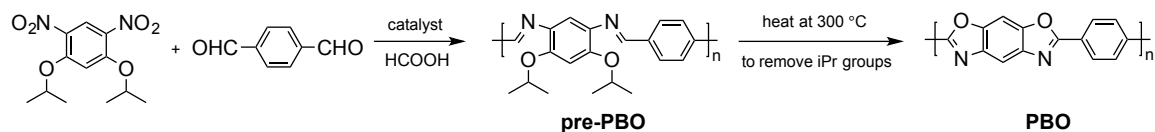
Figure 6.4 A new synthetic route for producing PBO.

The controls achieved in preparing AuPd NPs allow us to study size- and composition-dependent catalysis for reactions leading to the formation of small subunits of PBO. In this test, we studied FA-induced reduction of 1,5-diisopropoxy-2,4-dinitrobenzene, and the subsequent condensation of the 1,5-diisopropoxy-2,4-aminobenzene product with benzaldehyde to form (1E,1'E)-N, N'-(4,6-diisopropoxy-1,3-phenylene)-bis(1-phenylmethanimine) (denoted as bis-imine) in N-methyl pyrrolidone (NMP) solvent (Figure 6.3A). We attached isopropyl groups to the oxy-nitrobenzene structure to ensure that both reactants and products are soluble.[35] The results of the AuPd-catalyzed reactions are summarized in Figure 6.3B and C, from which we conclude that 8 nm $Au_{39}Pd_{61}$ NPs are the most active catalyst for the reduction/condensation reaction (Figure 6.3A).
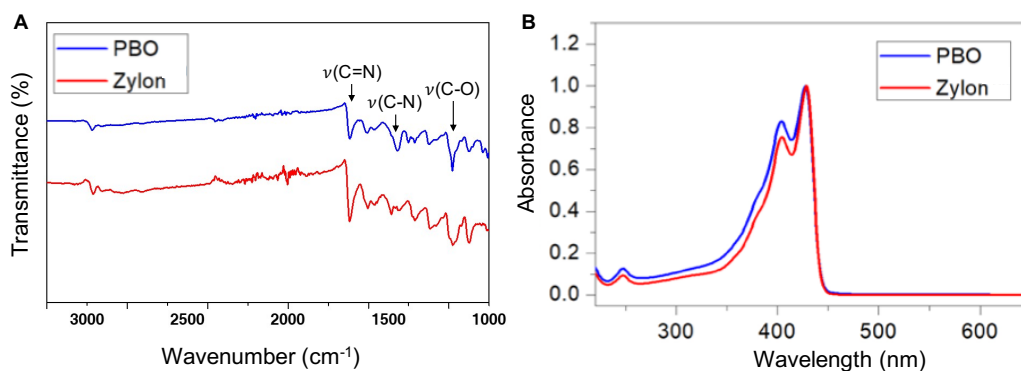
Figure 6.5 Conversion from pre-PBO to PBO. (A) FT-IR spectra of PBO and Zylon[®]. (B) UV-Vis spectra of PBO and Zylon[®].

The 8 nm $Au_{39}Pd_{61}$/C (2.5 mol%) was used to catalyze FA-induced reduction of 1,5-diisopropoxy-2,4-dinitrobenzene and subsequent condensation with terephthalaldehyde in NMP to form poly(p-phenylene-(4,6-diisopropoxy-1,3-phenylene) diethanimine), denoted as pre-PBO, which was further subject to heating treatment at 300 °C under a N_2 atmosphere for 6 h to remove isopropyl groups and to promote ring closure for the formation of PBO (Figure 6.4). Thermal gravimetric analysis (TGA) under a N_2 atmosphere showed that the pre-PBO has a weight loss of 25.7%, which agrees well with the calculated weight loss of 27.3% for the pre-PBO/PBO conversion. IR spectra of the newly prepared PBO show characteristic benzoxazole C=N, C-N, and C-O vibration peaks at approximately

1620, 1360, and 1054 cm^{-1}, respectively, which are similar to that of the commercial PBO, Zylon® (Figure 6.5A). UV-Vis absorption spectra taken in methane sulfonic acid solutions of PBO and Zylon® show the nearly identical absorption peaks (Figure 6.5B), indicating the highly aromatic nature and conjugated structure of alternating benzoxazole and phenyl rings within PBO and Zylon®.[36] The two split absorption peaks of 404 nm and 428 nm for PBO are induced by intermolecular interactions, consistent with that of the Zylon® sample.[37] A more interesting aspect of this reaction is that the degree of polymerization is dependent on the size of the AuPd NPs. Among 4, 6, 8 and 10 nm AuPd NPs tested, pre-PBO was formed with a molecular weight (Mw) of 2.1, 2.4, 3.6 and 3.0 kDa, respectively, as measured by gel permeation chromatography (GPC) (Figure 6.6). The 8 nm NPs induced the highest degree of polymerization in the one-pot reaction process. ICP-AES measurements show that the PBO synthesized using our method is metal- and PA-free. As a comparison, Zylon® contains 0.5% (by weight) of P, which means that there is one PA group for every 25 repeating PBO units.

NP	Mn	Mw	PDI
4 nm AuPd/C	1309	2094	1.67

NP	Mn	Mw	PDI
6 nm AuPd/C	1375	2440	1.77

NP	Mn	Mw	PDI
8 nm AuPd/C	1436	3558	2.40

NP	Mn	Mw	PDI
10 nm AuPd/C	1419	3020	2.19
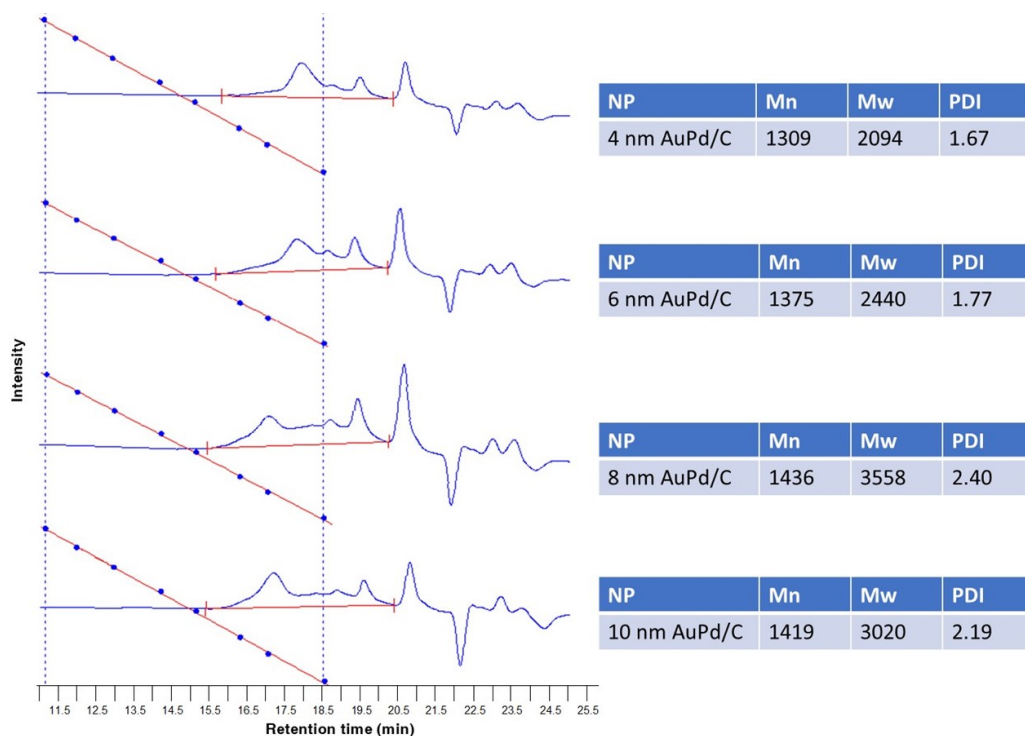
Figure 6.6 The GPC chromatograms of pre-PBOs formed using different AuPd NPs.
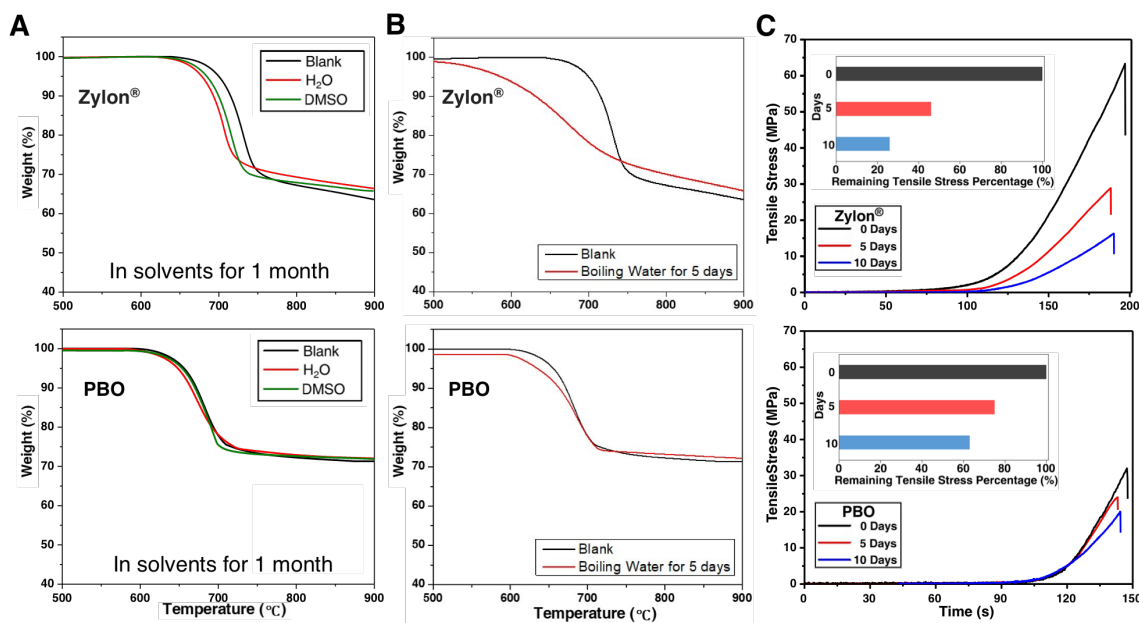
Figure 6.7 The thermal stability and mechanical properties of the as-prepared PBO. (A) TGA data for Zylon® and PBO after immersing in H_2O or DMSO at ambient temperature for 1 month. (B) TGA data for Zylon® and PBO after immersing in boiling water for 5 days. (C) Tensile strength of Zylon® and PBO as a function of time at a rate of 0.1 mm/min before and after immersing in boiling water for 5 days and 10 days, inset: the remaining tensile stress versus the pristine tensile strength of samples.

A large concern on Zylon® has been its long-term field stability. Here we tested the stability of PBO and Zylon® by exposing them to different environmental conditions and measuring their thermal and mechanical stability changes. Thermal stability of the PBO and Zylon® powders were assessed using TGA under a N_2 atmosphere (Figure 6.7). Our pristine PBO (Mw = 3.6 kDa) displays an onset decomposition temperature at 600 °C, whereas Zylon® (Mw = 40 kDa) has it at 650 °C. After immersion in water or DMSO under ambient conditions for a month, the Zylon® sample had a significantly reduced (35 °C or 45 °C decrease) onset decomposition temperature, whereas our PBO remained fairly constant (only 16 °C or 14 °C decrease) (Figure 6.7A). After the samples were immersed in boiling water for 5 days, the onset decomposition temperature of Zylon® was reduced to 500 °C, while the PBO was at 570 °C (Figure 6.7B). The difference in PBO and Zylon® thermal stability was also observed in 5% (T_5) and 20% (T_{20}) mass loss temperatures. Zylon®

suffered a significant depression of T_5 (587 °C) and T_{20} (689 °C) than the PBO (T_5/T_{20} at 635 °C/693 °C). Tensile stress measurements on 7.6 μm thick PBO and 10.5 μm thick Zylon® films revealed that the Zylon® film was subject to a larger stress change than the PBO one after immersion in boiling water, and after 10-days of immersion in boiling water, the PBO film retained higher mechanical stress (20 MPa) than the Zylon® one (16 MPa) (Figure 6.7C and the inset). Our studies demonstrate that highly pure PBO, even at a significantly lower degree of polymerization than Zylon®, can show much improved thermal and mechanical stability.
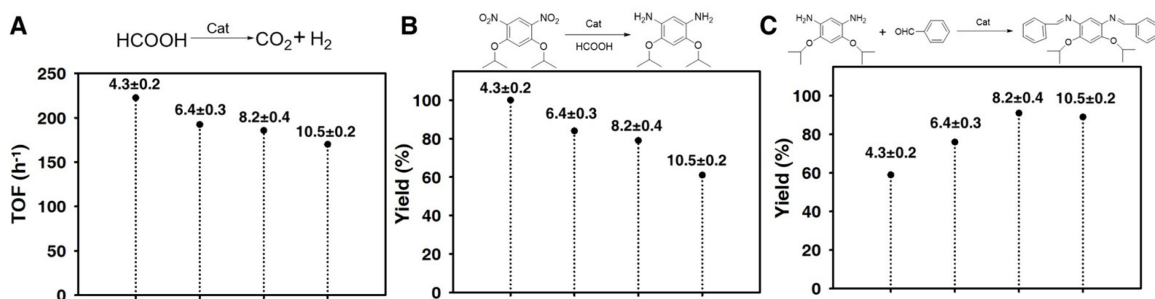
Figure 6.8 (A) The TOF values for FA dehydrogenation catalyzed by $Au_{39}Pd_{61}/C$ with AuPd in four different sizes: 10, 8, 6 and 4 nm. Reaction conditions: $Au_{39}Pd_{61}/C$ (2.5 mol%), NMP (3 mL), and FA (10 mmol), 80 °C, 1 h. (B) The AuPd NP size dependent yields of 1,5-diisopropoxy-2,4-diaminobenzene synthesized by the $Au_{39}Pd_{61}/C$-catalyzed dehydrogenation of FA and the hydrogenation of 1,5-diisopropoxy-2,4-dinitrobenzene. Reaction conditions: $Au_{39}Pd_{61}/C$ (2.5 mol%), 1,5-diisopropoxy-2,4-dinitrobenzene (1 mmol), NMP (3 mL), and FA (10 mmol), 80 °C, 2 h. (C) The AuPd NP size dependent yields of bis-imine formed by the $Au_{39}Pd_{61}/C$-catalyzed condensation of 1,5-diisopropoxy-2,4-diaminobenzene and benzaldehyde. Reaction conditions: $Au_{39}Pd_{61}/C$ (2.5 mol%), 1,5-diisopropoxy-2,4-diaminobenzene (1 mmol), benzaldehyde (2.1 mmol), NMP (3 mL), 80 °C, 3 h.

To understand why the formation of PBO in the one-pot reaction depends on the size of AuPd NPs, we analyzed the model reaction of FA-induced reduction of 1,5-diisopropoxy-2,4-dinitrobenzene and the amine condensation with benzaldehyde (Figure 6.3A) in three reaction steps: FA dehydrogenation, reduction of the nitro groups, and condensation of the diamine with aldehyde. From the NP size-dependent dehydrogenation of FA (Figure 6.8A), we can see that the 4 nm NP catalyst provides the highest initial TOF value. As the

size increases, the activity drops and the TOF decreases from 223 to 170 h^{-1}. A similar trend is observed for the hydrogenation of 1,5-diisopropoxy-2,4-dinitrobenzene (Figure 6.8B). However, for the condensation of two equivalents of benzaldehyde with 1,5-diisopropoxy-2,4-diaminobenzene, larger NPs (8 and 10 nm) are more efficient, and 8 nm NPs are the best catalyst for the reaction (Figure 6.8C), which is consistent with what we observed in Figure 6.3C and in the PBO synthesis.
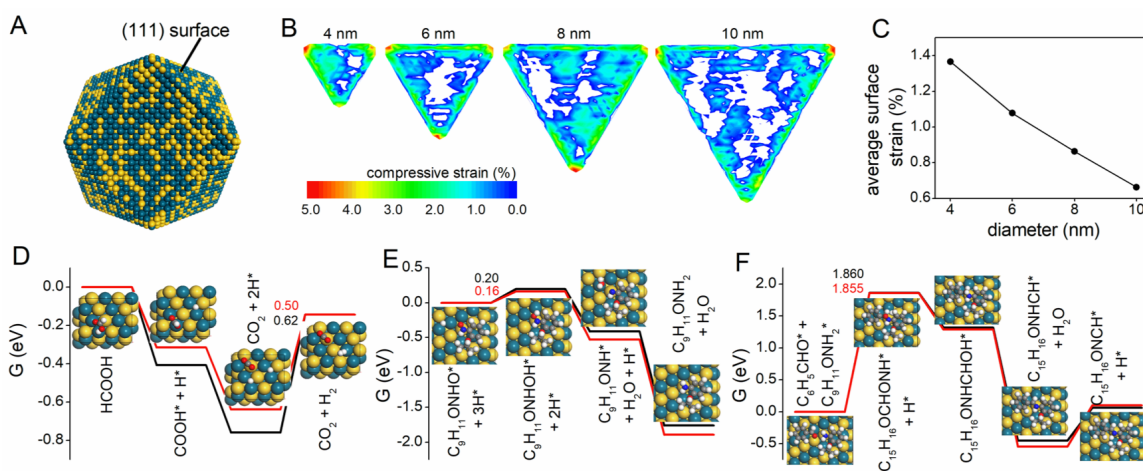
Figure 6.9 Strain distributions on the $Au_{39}Pd_{61}$ NPs and free energy diagrams of the three reaction steps. (A) Atomistic model of $Au_{39}Pd_{61}$ NP. (B) Color-coded strain distribution on the (111) facets of AuPd NPs with different diameters. (C) Average surface compression on the NPs as a function of their diameter. (D) Free energy diagram for the FA dehydrogenation on the (111) surface of the NP under zero strain (black) and 2% compression (red). (E) Free energy diagram for the hydrogenation of 1,5-diisopropoxy-2,4-dinitrobenzene on the NP under zero (black) and 2% compression (red). (F) Free energy diagram for the condensation of 1,5-diisopropoxy-2,4-diaminobenzene and benzaldehyde on the NP under zero (black) and 2% compression (red). The adsorption geometries are shown in the insets: yellow, cyan, gray, blue, red, and white spheres represent Au, Pd, C, N, O, and H atoms, respectively.

FA dehydrogenation on metal surfaces has been studied by DFT,[38] which indicates that H* binds too strongly on pure Pd (111), but too weakly on pure Au (111). Using combined classical MM[39] and DFT simulations, we can elucidate the observed size-dependent polymerization on the AuPd NPs. From the strain distribution on the $Au_{39}Pd_{61}$ NP (111) surface (Figure 6.9A), we find that the smaller NPs exhibit a higher degree of compression

(Figure 6.9B), and the average surface compression on 4, 6, 8, and 10 nm $Au_{39}Pd_{61}$ NPs is 1.37, 1.08, 0.86, and 0.66%, respectively (Figure 6.9C). The free energy diagrams are calculated to estimate the overpotential for each reaction step (Figure 6.9D-F). We find that on an AuPd slab without the compressive strain, the metal surface binds H* too strongly, resulting in a high overpotential of 0.62 V; on an AuPd surface with 2% compression, the overpotential is lowered to 0.5 V. Since 4 nm NPs have the largest surface compression of 1.37%, they should be the most active catalyst for FA dehydrogenation. In the -NO_2 hydrogenation reaction step, migration of surface H* towards O-NO is the only endothermic reaction step (Figure 6.9E); the surface compression decreases the migration energy barrier and promotes the hydrogenation reaction. Thus, the smaller the NPs (4 nm in the study), the higher the activity. In the condensation reaction step, the formation of the C-N bond is the rate-determining step, which is also enhanced by the surface compression thanks to weakened adsorption of the amino and carbonyl groups (Figure 6.9F). On the other hand, the condensation reaction involves two large molecules (amine and aldehyde), requiring larger NPs for the reaction (Figure 6.10). Otherwise, the reactants are too close to the under-coordinated edge sites, lowering the reaction activity.[40] By taking both strain and geometric factors into consideration, we conclude that 8 nm NPs are the most active for catalyzing the condensation and further polymerization reactions.

6.4   Conclusion

We report a new NP-based catalytic approach to synthesize functional polymers with controlled polymerization, purity and properties. Using the rigid organic polymer PBO as the model system, we have demonstrated that AuPd alloy NPs are especially efficient catalyzing multiple chemical reactions in one-pot, including FA dehydrogenation, nitro-hydrogenation and amine/aldehyde condensation, to form PBO. The AuPd NPs show both size and composition dependent catalytic polymerization, and 8 nm $Au_{39}Pd_{61}$ NPs are the most efficient
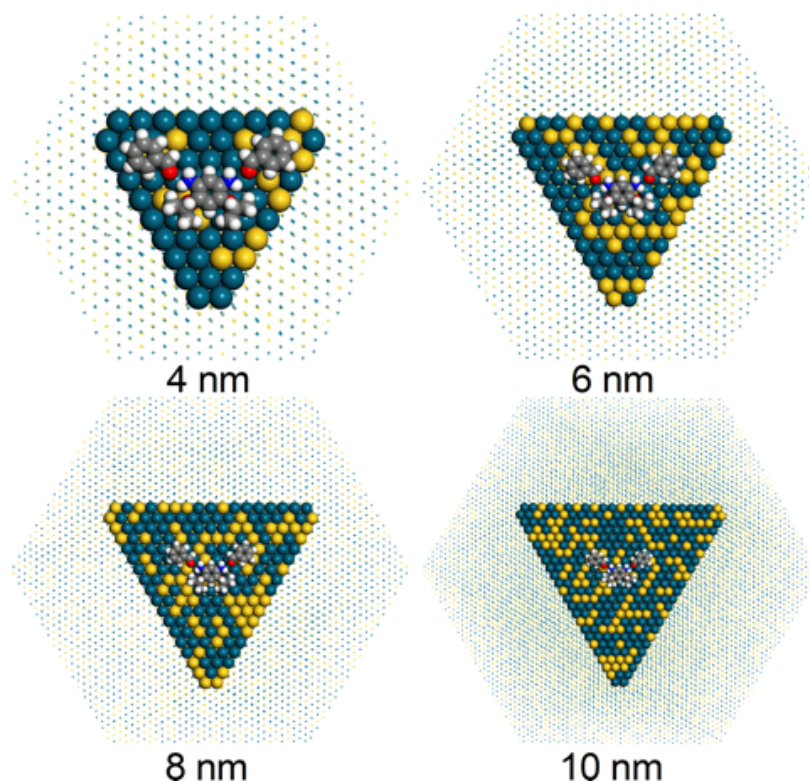
Figure 6.10 Atomic structures of the DFT optimized amino and carbonyl groups on the MM optimized AuPd TO (111) surfaces. Yellow, cyan, gray, blue, red, and white spheres represent Au, Pd, C, N, O, and H atoms, respectively.

catalyst for the formation of PBO (Mw = 3.6 kDa). The PBO shows excellent thermal stability up to 600 °C, which is comparable to commercial PBO (Zylon®, Mw = 40 kDa). More importantly, this lighter PBO exhibits much improved chemical and mechanical stability compared to Zylon® after exposure to water and DMSO under either ambient or boiling conditions. Our new synthesis solves the long-standing PBO purity and degradation problems by demonstrating that the AuPd NP catalyzed one-pot reaction is key to obtaining highly pure PBO, and chemical purity is essential for the PBO to maintain its thermomechanical stability. The NP catalyzed reaction is not limited to the formation of PBO, and we are actively working to extend this method as a general approach to highly pure rigid organic polymers for broad ballistic fiber, anti-flame, smart-textile and ionic/separation membrane applications.

6.5   Experimental section

Synthesis of 4 nm Au seeds   0.2 g HAuCl$_4$ was dissolved in 10 mL of tetralin and 10 mL of OAm at 4 °C under Ar flow and vigorous magnetic stirring. 0.5 mmol of BBA was dissolved in 1 mL of tetralin and 1 mL of OAm via sonication. The solution was then injected into the HAuCl$_4$ solution. The mixed solution was then stirred for 1 h at 45 °C before 40 mL of acetone was added to collect Au NPs via centrifugation (8500 rpm, 8 min). The product was dispersed in 20 mL hexane, precipitated out by adding 40 mL of ethanol and centrifugation, and re-dispersed in hexane.

Synthesis of 6 nm Au seeds   0.2 g HAuCl$_4$ was dissolved in 10 mL of tetralin and 10 mL of OAm at 4 °C under Ar flow and vigorous magnetic stirring. 0.5 mmol of BBA was dissolved in 1 mL of tetralin and 1 mL of OAm via sonication. The solution was then injected into the HAuCl$_4$ solution. The mixed solution was then stirred for 1 h at 4 °C before 40 mL of acetone was added to collect Au NPs via centrifugation (8500 rpm, 8 min). The product was dispersed in 20 mL hexane, precipitated out by adding 40 mL of ethanol and centrifugation, and re-dispersed in hexane.

Synthesis of 8 nm Au seeds   30 mg of 6 nm Au NPs was added to a solution made from 10 mL ODE, 10 mL OAm and 0.1 g HAuCl$_4$ at room temperature under Ar flow and vigorous magnetic stirring. The reaction solution was then heated to 80 °C at 5 °C/min and kept at this temperature for 2 h. The reaction solution was cooled down to room temperature and the 8 nm Au NP product was separated as described in the synthesis of 6 nm Au NPs.

Synthesis of 10 nm Au seeds   30 mg of 8 nm Au NPs was added to a solution made from 10 mL ODE, 10 mL OAm and 0.12 g HAuCl$_4$ at room temperature under Ar flow and vigorous magnetic stirring. The reaction solution was then heated to 80 °C at 5 °C/min and kept at this temperature for 2 h. The reaction solution was cooled down to room

temperature and the 8 nm Au NP product was separated as described in the synthesis of 6 nm Au NPs.

Seed-mediated synthesis of Au$_{39}$Pd$_{61}$/C from 4 to 10 nm 76 mg of Pd(acac)$_2$, 15 mL OAm, and 0.30 mL OAc were mixed under N$_2$ at 70 °C for 30 min to form a clear solution. Then 18 mg of Au seeds from 4 to 10 nm dispersed in 2 mL hexane was dropped into the solution. The solution was heated to 260 °C at 2 °C/min and kept at 260 °C for 1 h before it was cooled to room temperature. The Au$_{39}$Pd$_{61}$ NPs were separated by adding 100 mL ethanol and centrifuging at 9500 rpm for 8 min. The product was purified by dispersing in hexane and flocculating with ethanol, and precipitating by centrifugation (9500 rpm, 8 min). The purification process was repeated once, and the final NP product was redispersed into hexane for further use. 10 mg of Au$_{39}$Pd$_{61}$ NPs were dissolved in hexane in a 20 mL vial and 20 mg of Ketjen carbon support was carefully added to it. This colloidal mixture was sonicated for 2 h. The reaction mixture was then cooled down to room temperature. 30 mL of ethanol was added, and the mixture was centrifuged at 8000 rpm for 8 mins. This procedure was repeated twice. The Au$_{39}$Pd$_{61}$/C NPs were recovered by adding acetone. Acetone was evaporated and the resultant Au$_{39}$Pd$_{61}$/C NPs were weighed, followed by annealing under 95% Ar + 5% H$_2$ at 500 °C for 10 mins, which gave Au$_{39}$Pd$_{61}$/C NPs with different sizes for further study.

Synthesis of 1,5-diisopropoxy-2,4-dinitrobenzene To a mixture of potassium carbonate (5.5 g, 40 mmol) and 2-propanol (40 mL), 1,5-difluoro-2,4 dinitrobenzene (2.04 g, 10 mmol) was added while stirring under nitrogen. After reacting for 2 days at room temperature, a generated precipitate was filtered and then rinsed several times with water. The obtained solid was dried at 80 °C for 12 h in a vacuum to provide a yellow powder (2.243 g, 79%).

Synthesis of pre-PBO precursor   Under a nitrogen atmosphere, 1,5-diisopropoxy-2,4-dinitrobenzene (0.284 g, 1.0 mmol) was dissolved in NMP (3 mL), to which terephthalaldehyde (0.134 g, 1.0 mmol), formic acid (10 mmol) and AuPd/C (30 mg, 7%) were added, and then the mixture was stirred at 80 °C for 24 h. The solution was poured into 80 mL of methanol to produce a precipitate, which was filtered and rinsed several times with methanol. The obtained solid was then dried at 80 °C for 24 h in a vacuum to produce a dark purple powder (0.336 g, yield 93%).

Conversion of pre-PBO to PBO   The pre-PBO was heated at 300 °C under a N2 atmosphere for 6 h to ensure complete conversion to PBO.

Stability test of the PBO and Zylon at room temperature   The PBO (100 mg) and Zylon (100 mg) was immersed in different solvents (10 mL) and stored at room temperature for a month. After that, the solid was filtered and dried at 80 °C for 24 h under vacuum.

Stability test of the PBO and Zylon in boiling water   The PBO (100 mg) and Zylon (100 mg) was boiled in water at 100 °C for 5 days. After that, the solid was filtered and dried at 80 °C for 24 h under vacuum.

Fabrication of PBO films   The PBO or Zylon (500 mg) was dissolved in methanesulfonic acid at 80 °C for 5 h. The solution was then cast on a glass substrate to obtain a thin film, which was dried at 80 °C for 3 h and 130 °C for 3 h. The film was peeled off the glass substrate by immersing the substrate in water. The obtained film was dried at 80 °C for 12 h under vacuum for further mechanical tests.

DFT calculation   DFT calculations were performed using the Vienna ab initio Simulation Package (VASP) with the projector-augmented wave pseudopotentials. The exchange-correlation interaction was described by Perdew-Burke-Ernzerhof (PBE) functional. A plane-wave energy cutoff of 400 eV was used for all calculations. The Au/Pd (111) surface for FA dehydrogenation was modeled by a four-atomic-layer slab (64 atoms). For

the hydrogenation of nitro groups and the condensation of amino and carbonyl groups, a three-atomic-layer slab (144 atoms) was adopted. The adjacent computational slabs were separated by a 15 Å vacuum in the normal direction of the surface. The atoms in the top two layers were fully relaxed, while the rest of the atoms were fixed in the equilibrium positions. The Brillouin-zone was sampled with a $3 \times 3 \times 1$ k-mesh according to the Monkhorst-Pack scheme. The free energy of reaction intermediate was calculated as:

$$G = E_{DFT} + ZPE + \int C_P dT - TS \tag{6.1}$$

where E_{DFT} is the total energy of the surface with the intermediate. ZPE, C_P, and -TS are the zero-point energy, heat capacity, and entropy corrections calculated based on the molecular vibration analysis at T = 300 K. We assume that any changes in the vibrations of the metal surface caused by the adsorbate are minimal.

References

[1] Taloni, A.; Vodret, M.; Constantini, G.; Zapperi, S. Size effects on the fracture of microscale and nanoscale materials. *Nature Review Materials* **2018**, *3*, 211–224.

[2] Fenton, J. L.; Steimle, B. C.; Schaak, R. E. Tunable intraparticle frameworks for creating complex heterostructured nanoparticle libraries. *Science* **2018**, *360*, 513–517.

[3] Wu, L.; Willis, J. J.; McKay, I. S.; Diroll, B. T.; Qin, J.; Cargnello, M.; Tassone, C. J. High-temperature crystallization of nanocrystals into three-dimensional superlattices. *Nature* **2017**, *548*, 197.

[4] Zhang, C.; Macfarlane, R. J.; Young, K. L.; Choi, C. H. J.; Hao, L.; Auyeung, E.; Liu, G.; Zhou, X.; Mirkin, C. A. A general approach to DNA-programmable atom equivalents. *Nature materials* **2013**, *12*, 741.

[5] Pang, X.; Zhao, L.; Han, W.; Xin, X.; Lin, Z. A general and robust strategy for the synthesis of nearly monodisperse colloidal nanocrystals. *Nature nanotechnology* **2013**, *8*, 426.

[6] others,, et al. Gold nanocages covered by smart polymers for controlled release with near-infrared light. *Nature materials* **2009**, *8*, 935.

[7] others,, et al. Theory-guided Sn/Cu alloying for efficient CO 2 electroreduction at low overpotentials. *Nature Catalysis* **2019**, *2*, 55.

[8] Wu, C. H.; Liu, C.; Su, D.; Xin, H. L.; Fang, H.-T.; Eren, B.; Zhang, S.; Murray, C. B.;

Salmeron, M. B. Bimetallic synergy in cobalt–palladium nanocatalysts for CO oxidation. *Nature Catalysis* **2019**, *2*, 78.

[9] others„ et al. Steering post-C–C coupling selectivity enables high efficiency electroreduction of carbon dioxide to multi-carbon alcohols. *Nature Catalysis* **2018**, *1*, 421.

[10] others„ et al. Doping-induced structural phase transition in cobalt diselenide enables enhanced hydrogen evolution catalysis. *Nature communications* **2018**, *9*, 2533.

[11] De Luna, P.; Quintero-Bermudez, R.; Dinh, C.-T.; Ross, M. B.; Bushuyev, O. S.; Todorović, P.; Regier, T.; Kelley, S. O.; Yang, P.; Sargent, E. H. Catalyst electro-redeposition controls morphology and oxidation state for selective carbon dioxide reduction. *Nature Catalysis* **2018**, *1*, 103.

[12] Aslam, U.; Rao, V. G.; Chavez, S.; Linic, S. Catalytic conversion of solar to chemical energy on plasmonic metal nanostructures. *Nature Catalysis* **2018**, *1*, 656.

[13] Wang, H.; Gu, X.-K.; Zheng, X.; Pan, H.; Zhu, J.; Chen, S.; Cao, L.; Li, W.-X.; Lu, J. Disentangling the size-dependent geometric and electronic effects of palladium nanocatalysts beyond selectivity. *Science advances* **2019**, *5*, eaat6413.

[14] Hahn, G.; Kunnas, P.; de Jonge, N.; Kempe, R. General synthesis of primary amines via reductive amination employing a reusable nickel catalyst. *Nature Catalysis* **2019**, *2*, 71.

[15] Yang, X.; Sun, J.-K.; Kitta, M.; Pang, H.; Xu, Q. Encapsulating highly catalytically active metal nanoclusters inside porous organic cages. *Nature Catalysis* **2018**, *1*, 214.

[16] others„ et al. Carbon nitride supported Fe 2 cluster catalysts with superior performance for alkene epoxidation. *Nature communications* **2018**, *9*, 2353.

[17] Sun, Z.; Bottari, G.; Afanasenko, A.; Stuart, M. C.; Deuss, P. J.; Fridrich, B.; Barta, K. Complete lignocellulose conversion with integrated catalyst recycling yielding valuable aromatics and fuels. *Nature Catalysis* **2018**, *1*, 82.

[18] Jagadeesh, R. V.; Murugesan, K.; Alshammari, A. S.; Neumann, H.; Pohl, M.-M.; Radnik, J.; Beller, M. MOF-derived cobalt nanoparticles catalyze a general synthesis of amines. *Science* **2017**, *358*, 326–332.

[19] Lin, H.; Huang, Y.-D.; Wang, F. Synthesis and properties of poly [p-(2, 5-dihydroxy)-phenylenebenzobisoxazole] fiber. *International journal of molecular sciences* **2008**, *9*, 2159–2168.

[20] Afshari, M.; Sikkema, D. J.; Lee, K.; Bogle, M. High performance fibers based on rigid and flexible polymers. *Polymer Reviews* **2008**, *48*, 230–274.

[21] Hu, X.-D.; Jenkins, S. E.; Min, B. G.; Polk, M. B.; Kumar, S. Rigid-rod polymers: synthesis, processing, simulation, structure, and properties. *Macromolecular Materials and Engineering* **2003**, *288*, 823–843.

[22] So, Y.-H.; Heeschen, J. P.; Bell, B.; Bonk, P.; Briggs, M.; DeCaire, R. Study of the mechanism for poly (p-phenylene) benzoxazole polymerization a remarkable reaction pathway to make rigid-rod polymers. *Macromolecules* **1998**, *31*, 5229–5239.

[23] Luo, S.; Zhang, Q.; Zhu, L.; Lin, H.; Kazanowska, B. A.; Doherty, C. M.; Hill, A. J.; Gao, P.; Guo, R. Highly selective and permeable microporous polymer membranes for hydrogen purification and CO2 removal from natural gas. *Chemistry of Materials* **2018**, *30*, 5322–5332.

[24] Hao, X.; Zhu, J.; Jiang, X.; Wu, H.; Qiao, J.; Sun, W.; Wang, Z.; Sun, K. Ultrastrong polyoxyzole nanofiber membranes for dendrite-proof and heat-resistant battery separators. *Nano letters* **2016**, *16*, 2981–2987.

[25] Kolhe, N. B.; Asha, S.; Senanayak, S. P.; Narayan, K. n-Type field effect transistors based on rigid rod and liquid crystalline alternating copoly (benzobisoxazole) imides containing perylene and/or naphthalene. *The Journal of Physical Chemistry B* **2010**, *114*, 16694–16704.

[26] Park, H. B.; Jung, C. H.; Lee, Y. M.; Hill, A. J.; Pas, S. J.; Mudie, S. T.; Van Wagner, E.; Freeman, B. D.; Cookson, D. J. Polymers with cavities tuned for fast selective transport of small molecules and ions. *Science* **2007**, *318*, 254–258.

[27] Kanbargi, N.; Hu, W.; Lesser, A. J. Degradation mechanism of poly (p-phenylene-2, 6-benzobisoxazole) fibers by 31P solid-state NMR. *Polymer Degradation and Stability* **2017**, *136*, 131–138.

[28] Froimowicz, P.; Zhang, K.; Ishida, H. Intramolecular hydrogen bonding in benzoxazines: when structural design becomes functional. *Chemistry–A European Journal* **2016**, *22*, 2691–2707.

[29] Park, E. S.; Sieber, J.; Guttman, C.; Rice, K.; Flynn, K.; Watson, S.; Holmes, G. Methodology for detecting residual phosphoric acid in polybenzoxazole fibers. *Analytical chemistry* **2009**, *81*, 9607–9617.

[30] Yang, Y.; Xu, H.; Cao, D.; Zeng, X. C.; Cheng, D. Hydrogen production via efficient formic acid decomposition: engineering the surface structure of Pd-based alloy catalysts by design. *ACS Catalysis* **2018**, *9*, 781–790.

[31] Yu, W.-Y.; Mullen, G. M.; Flaherty, D. W.; Mullins, C. B. Selective hydrogen production from formic acid decomposition on Pd–Au bimetallic surfaces. *Journal of the American Chemical Society* **2014**, *136*, 11070–11078.

[32] Metin, Ö.; Sun, X.; Sun, S. Monodisperse gold–palladium alloy nanoparticles and their composition-controlled catalysis in formic acid dehydrogenation under mild conditions. *Nanoscale* **2013**, *5*, 910–912.

[33] Gu, X.; Lu, Z.-H.; Jiang, H.-L.; Akita, T.; Xu, Q. Synergistic catalysis of metal–organic framework-immobilized Au–Pd nanoparticles in dehydrogenation of formic acid for chemical hydrogen storage. *Journal of the American Chemical Society* **2011**, *133*, 11822–11825.

[34] Zhu, W.; Michalsky, R.; Metin, O.; Lv, H.; Guo, S.; Wright, C. J.; Sun, X.; Peterson, A. A.; Sun, S. Monodisperse Au nanoparticles for selective electrocatalytic reduction of CO2 to CO. *Journal of the American Chemical Society* **2013**, *135*, 16833–16836.

[35] Fukumaru, T.; Saegusa, Y.; Fujigaya, T.; Nakashima, N. Fabrication of poly (p-phenylenebenzobisoxazole) film using a soluble poly (o-alkoxyphenylamide) as the precursor. *Macromolecules* **2014**, *47*, 2088–2095.

[36] Feng, D.; Wang, S.; Zhuang, Q.; Guo, P.; Wu, P.; Han, Z. Joint theoretical and experimental study of the UV absorption spectra of polybenzoxazoles. *Journal of molecular structure* **2004**, *707*, 169–177.

[37] DiCésare, N.; Belletête, M.; Leclerc, M.; Durocher, G. Intermolecular interactions in conjugated oligothiophenes. 2. quantum chemical calculations performed on crystalline structures of terthiophene and substituted terthiophenes. *The Journal of Physical Chemistry A* **1999**, *103*, 803–811.

[38] Yoo, J. S.; Zhao, Z.-J.; Nørskov, J. K.; Studt, F. Effect of boron modifications of palladium catalysts for the production of hydrogen from formic acid. *ACS Catalysis* **2015**, *5*, 6579–6586.

[39] Zhou, X.; Johnson, R.; Wadley, H. Misfit-energy-increasing dislocations in vapor-deposited CoFe/NiFe multilayers. *Physical Review B* **2004**, *69*, 144113.

[40] Ruban, A.; Hammer, B.; Stoltze, P.; Skriver, H. L.; Nørskov, J. K. Surface electronic structure and reactivity of transition and noble metals. *Journal of Molecular Catalysis A: Chemical* **1997**, *115*, 421–429.